

**Ministry of Education and Science of the Russian Federation
Saint Petersburg National Research University of Information
Technologies, Mechanics, and Optics**

***NANOSYSTEMS:
PHYSICS, CHEMISTRY, MATHEMATICS***

2021, volume 12(4)

Наносистемы: физика, химия, математика

2021, том 12, № 4



NANOSYSTEMS:

PHYSICS, CHEMISTRY, MATHEMATICS

ADVISORY BOARD MEMBERS

Chairman: V.N. Vasiliev (*St. Petersburg, Russia*),
V.M. Buznik (*Moscow, Russia*); V.M. Ievlev (*Voronezh, Russia*), P.S. Kop'ev (*St. Petersburg, Russia*), N.F. Morozov (*St. Petersburg, Russia*), V.N. Parmon (*Novosibirsk, Russia*),
A.I. Rusanov (*St. Petersburg, Russia*),

EDITORIAL BOARD

Editor-in-Chief: I.Yu. Popov (*St. Petersburg, Russia*)

Section Co-Editors:

Physics – V.M. Uzdin (*St. Petersburg, Russia*),

Chemistry, material science – V.V. Gusarov (*St. Petersburg, Russia*),

Mathematics – I.Yu. Popov (*St. Petersburg, Russia*).

Editorial Board Members:

V.M. Adamyan (*Odessa, Ukraine*); O.V. Al'myasheva (*St. Petersburg, Russia*);
A.P. Alodjants (*Vladimir, Russia*); S. Bechta (*Stockholm, Sweden*); J. Behrndt (*Graz, Austria*);
M.B. Belonenko (*Volgograd, Russia*); A. Chatterjee (*Hyderabad, India*); A.V. Chizhov
(*Dubna, Russia*); A.N. Enyashin (*Ekaterinburg, Russia*), P.P. Fedorov (*Moscow, Russia*);
E.A. Gudilin (*Moscow, Russia*); V.K. Ivanov (*Moscow, Russia*), H. Jónsson (*Reykjavik, Iceland*);
A.A. Kiselev (*Durham, USA*); Yu.S. Kivshar (*Canberra, Australia*); S.A. Kozlov
(*St. Petersburg, Russia*); P.A. Kurasov (*Stockholm, Sweden*); A.V. Lukashin (*Moscow, Russia*);
I.V. Melikhov (*Moscow, Russia*); G.P. Miroshnichenko (*St. Petersburg, Russia*);
I.Ya. Mittova (*Voronezh, Russia*); Nguyen Anh Tien (*Ho Chi Minh, Vietnam*); V.V. Pankov
(*Minsk, Belarus*); K. Pankrashkin (*Orsay, France*); A.V. Ragulya (*Kiev, Ukraine*);
V. Rajendran (*Tamil Nadu, India*); A.A. Rempel (*Ekaterinburg, Russia*); V.Ya. Rudyak
(*Novosibirsk, Russia*); D Shoikhet (*Karmiel, Israel*); P Stovicek (*Prague, Czech Republic*);
V.M. Talanov (*Novocherkassk, Russia*); A.Ya. Vul' (*St. Petersburg, Russia*);
A.V. Yakimansky (*St. Petersburg, Russia*), V.A. Zagrebnov (*Marseille, France*).

Editors:

I.V. Blinova; A.I. Popov; A.I. Trifanov; E.S. Trifanova (*St. Petersburg, Russia*),
R. Simoneaux (*Philadelphia, Pennsylvania, USA*).

Address: ITMO University, Kronverkskiy pr., 49, St. Petersburg 197101, Russia.

Phone: +7(812)607-02-54, **Journal site:** <http://nanojournal.ifmo.ru/>,

E-mail: nanojournal.ifmo@gmail.com

AIM AND SCOPE

The scope of the journal includes all areas of nano-sciences. Papers devoted to basic problems of physics, chemistry, material science and mathematics inspired by nanosystems investigations are welcomed. Both theoretical and experimental works concerning the properties and behavior of nanosystems, problems of its creation and application, mathematical methods of nanosystem studies are considered.

The journal publishes scientific reviews (up to 30 journal pages), research papers (up to 15 pages) and letters (up to 5 pages). All manuscripts are peer-reviewed. Authors are informed about the referee opinion and the Editorial decision.

CONTENT

MATHEMATICS

- K.J. Gowtham, Narahari Narasimha Swamy
On Sombor energy of graphs 411
- U. Baltaeva, Y. Alikulov, I.I. Baltaeva, A. Ashirova
Analog of the Darboux problem for a loaded integro-differential equation involving the Caputo fractional derivative 418
- A.G. Belolipetskaia, I.Y. Popov
Dirac operator with different potentials on edges of quantum graph: resonance asymptotics 425

PHYSICS

- N.N. Konobeeva, M.B. Belonenko
Influence of a magnetic field on the propagation of ultrashort optical pulses in anisotropic optical media with carbon nanotubes 430
- M.A. Buntat, A.H.A. Rosol, M.F.M. Rusdi,
A.A. Latif, M. Yasin, S.W. Harun
Ti₃C₂T_x thin film as a saturable absorber for passively generating Q-switched pulses in thulium-doped fiber laser cavity 436
- Ratna Chakrabarty, S. Roy, T. Pathak, D. Ghosh, N.K. Mandal
Design of 2:4 and 3:8 decoder circuit using QCA technology 442
- D.R. Roopa, C.M. Subhan, K. Fakruddin,
P. Pardhasaradhi, B.T.P. Madhav, G. Srilekha
Influence of silver and gold nano particles on luminance properties of n-hexyloxy-cynobiphenyl liquid crystal through image analysis 453
- A.M. Vorobiev
Resonance asymptotics for quantum waveguides with semitransparent multi-perforated wall 462

CHEMISTRY AND MATERIAL SCIENCE

- Sh.O. Omarov
The effect of hydrolysis duration on the phase composition, texture, aggregation and agglomeration of ZrO₂ nanoparticles 472

Nitika, Anu Rana, Vinod Kumar Study of magnetic and optical transitions in MFe₂O₄ (M= Co, Zn, Fe, Mn) with spinel structure	481
B.V. Vasil'ev, R.Yu. Smyslov, D.A. Kirilenko, A.N. Bugrov Synthesis and magnetic properties of cobalt ferrite nanoparticles formed under hydro and solvothermal condition	492
D.S. Yasyrkina, S.V. Kuznetsov, A.A. Alexandrov, S.Kh. Batygov, V.V. Voronov, P.P. Fedorov Preparation and X-ray luminescence of Ba_{4±x}Ce_{3±x}F_{17±x} solid solutions	505
A. Ioshin, E. Polyakov, I. Volkov, E. Denisov Properties of Prussian Blue filled membrane mini-reactor in Cs(I) adsorption processes	512
A.P. Safronov, T.V. Terziyan, A.V. Petrov, I.V. Beketov Tuning of interfacial interactions in poly(isoprene) ferroelastomer by surface modification of embedded metallic iron nanoparticles	520
Runjun Sarma, Monoj Kumar Das, Lakshi Saikia, Anand Ramteke, Ratul Saikia Conjugation of curcumin with Ag nanoparticles for improving its bioavailability and study of the bioimaging response	528
Information for authors	536

On Sombor energy of graphs

K. J. Gowtham, Narahari Narasimha Swamy

Dept. of Mathematics, University College of Science, Tumkur University, Tumakuru,
Karnataka State, Pin 572 103, India

gowtham.k.j@yahoo.com, narahari_nittur@yahoo.com

DOI 10.17586/2220-8054-2021-12-4-411-417

The concept of Sombor index $SO(G)$ was recently introduced by Gutman in the chemical graph theory. It is a vertex-degree-based topological index and is denoted by $SO(G)$. This paper introduces a new matrix for a graph G , called the Sombor matrix, and defines a new variant of graph energy called Sombor energy $ES(G)$ of a graph G . The striking feature of this new matrix is that it is related to well-known degree-based topological indices called forgotten indices. When $ES(G)$ values of some molecules containing hetero atoms are correlated with their total π -electron energy, we got a good correlation with the correlation coefficient $r = 0.976$. Further, we found some bounds and characterizations on the largest eigenvalue of $S(G)$ and Sombor energy of graphs.

Keywords: Sombor index, Sombor energy, forgotten index.

Received: 30 May 2021

Revised: 1 July 2021

Final revision: 20 July 2021

1. Introduction

Spectral graph theory plays an important role in analyzing the matrices of graphs with the help of matrix theory and linear algebra. Now, spectral graph theory has attracted the attention of both pure and applied mathematicians whose benefit lies far from the spectral graph theory, which may be surprised because graph energy is a special kind of matrix norm. They will then recognize that the concept of graph energy (under different names) is encountered in several seemingly unrelated areas of their own expertise. The eigenvalues are closely related to almost all major invariants of a graph, linking one extremal property to another, they play a central role in the fundamental understanding of graphs [1]. In 1978, Gutman related the Graph energy and total π -electron energy in a molecular graph; it was defined as, the sum of absolute values of the eigenvalues of the associated adjacency matrix of a graph G [2]. Later, many matrices were defined based on distance and adjacency among the vertices, degree of the vertices involved in forming the graph structure like: Zagreb matrix [3], Randić matrix [4], distance matrix [5], Seidel matrix [6], Laplacian matrix [7], Seidel Laplacian matrix [8], signless Laplacian matrix [9], Seidel signless Laplacian matrix [10], degree sum matrix [11], etc.

Topological indices are mainly categorized into two types: namely degree-based indices and distance-based indices. Some of the well-known degree-based indices are first Zagreb index, second Zagreb index, forgotten index, hyper Zagreb index, Randić index, harmonic index, geometric-arithmetic index, redefined third Zagreb index, inverse sum index, etc. The details on degree-based topological indices we refer to [12–14]. Recently, Gutman et al. [15] defined new degree-based indices, called the Sombor index, which is one of the trending areas in the present graph-theoretical research. The details of this new index we refer to [16–25]. In [26], the chemical applicability of Sombor indices had been studied. The wide application of Sombor indices motivated us to define the Sombor matrix and Sombor energy of the graph.

2. Preliminaries

In this paper, we considered simple, finite, undirected, and connected graphs. A graph G involves a vertex set $V = V(G) = \{v_1, v_2, \dots, v_n\}$ and $E = E(G)$ as its edge set. If two vertices have a common edge, then they are known as adjacent vertices. Likewise, if two edges have a common end vertex, then it is called an adjacent edge. The number of edges incident to a vertex v is called the degree of that vertex v and it is denoted by, d_v .

The first and second Zagreb indices of a graph G [2] is defined as,

$$M_1(G) = \sum_{uv \in E(G)} (d_u + d_v) = \sum_{u \in V(G)} d_u^2 \quad \text{and} \quad M_2(G) = \sum_{uv \in E(G)} (d_u d_v) \quad (1)$$

respectively.

Followed by the above definition, Furtula and Gutman introduced the forgotten topological index [27], defined as:

$$F(G) = \sum_{uv \in E(G)} (d_u^2 + d_v^2) = \sum_{u \in V(G)} d_u^3. \quad (2)$$

In [15] Gutman defined new degree based topological index called Sombor index, denoted by $SO(G)$ and defined as:

$$SO(G) = \sum_{uv \in E(G)} \sqrt{(d_u^2 + d_v^2)}, \quad (3)$$

In the next section, we introduce a new matrix for a graph G and a new graph invariant based on this matrix.

3. Sombor matrix and Sombor energy of graph

Definition 3.1. The Sombor matrix of a graph G with a vertex set $V = V(G) = \{v_1, v_2, v_3, \dots, v_n\}$ and edge set $E = E(G)$ is defined as $S(G) = (s_{ij})_{n \times n}$, where:

$$s_{ij} = \begin{cases} \sqrt{d_u^2 + d_v^2}, & uv \in E(G); \\ 0, & \text{otherwise;} \end{cases}$$

where d_u denotes the degree of the vertex u .

The Sombor polynomial of a graph G is defined as:

$$P_{S(G)}(\lambda) = |\lambda I - S(G)|,$$

where I is an $n \times n$ unit matrix.

Since $S(G)$ is real symmetric matrix, all roots of $P_{S(G)}(\lambda) = 0$ are real. Hence, they can be arranged as $\lambda_1 \geq \lambda_2 \geq \lambda_3 \cdots \geq \lambda_n$. The Sombor energy of graph G is given by

$$ES(G) = \sum_{i=1}^n |\lambda_i|.$$

4. Chemical applicability of $ES(G)$

The development of Huckel molecular orbital theory is mainly concentrated on conjugated, all carbon compounds. The range of those compounds can be studied if hetero atoms are considered. This can be done by comparing energy values for hetero compounds. To this end, we need to adjust Coulomb (α) and resonance integral (β) values for hetero atoms using the relations:

$$\alpha' = \alpha + h\beta \quad \text{and} \quad \beta' = k\beta,$$

where h and k are correction values which are different and depending on what atom is in conjugation. So, we can take more than one value for α for a hetero atom but depends on the number of electrons hetero atom donates to π -system.

Consider, the secular matrix of the compound urea:

$$\begin{bmatrix} \alpha - E & 1.131\beta & \beta & 0 \\ 1.131\beta & \alpha + 1.5\beta - E & 0 & 0 \\ \beta & 0 & \alpha + \beta - E & 0 \\ 0 & 0 & 0 & \alpha + 1.5\beta - E \end{bmatrix}$$

By substituting appropriate values of α and β for urea in the above matrix and expanding the secular determinant, π -electron energy for urea can be calculated [28, 29] we found the close resemblance between secular matrix of hetro molecule and Sombor matrix $S(G)$ of corresponding molecular graph G . Further, we calculated $ES(G)$ with dataset of total π -electron energy values of hetero atoms which are found in [30]. From Fig. 1 we found that $ES(G)$ has good correlation hetero atoms, as mentioned in Fig. 2, with correlation coefficient $r = 0.976$ and $r^2(\text{adjusted}) = 0.952$.

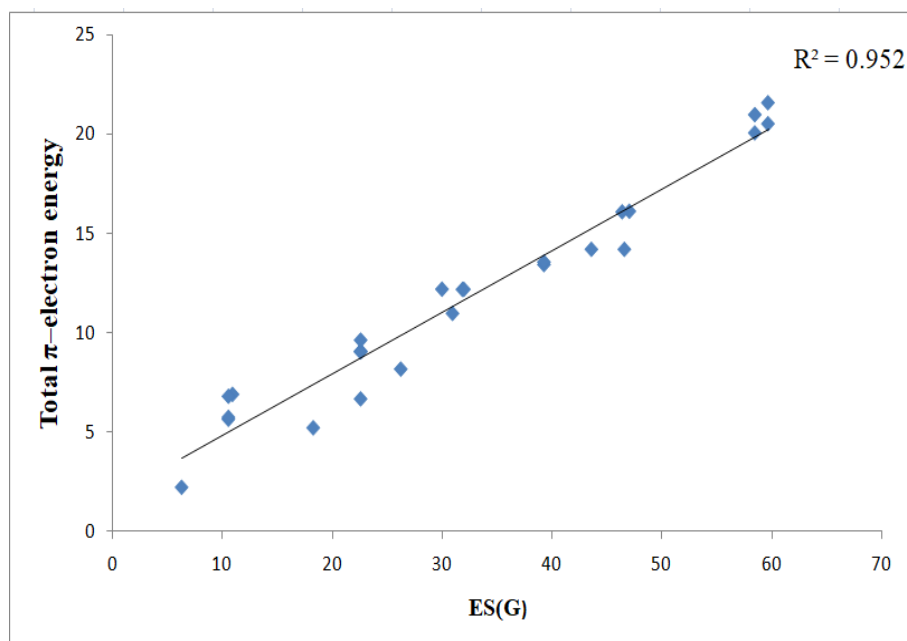


FIG. 1. Correlation of $ES(G)$ with the total π -electron energy of molecules containing hetero atoms

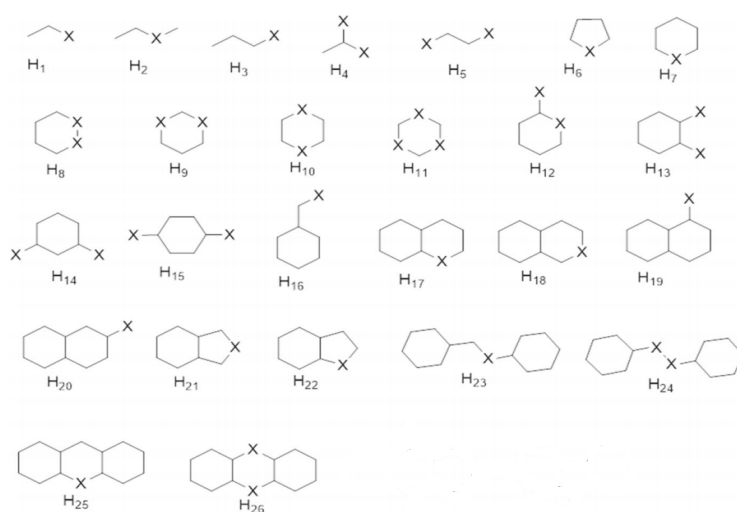


FIG. 2. Molecules containing hetero atoms. (H₁=Vinyl chloride like systems, H₂=Butadiene perturbed at C₂, H₃=Acrolein like systems, H₄=1,1-Dichloro-ethylene like systems, H₅=Glyoxal like and 1,2-Dichloro-ethylene like systems, H₆=Pyrrole like systems, H₇=Pyridine like systems, H₈=Pyridazine like systems, H₉=Pyrimidine like systems, H₁₀=Pyrazine like systems, H₁₁=S-Triazine like systems, H₁₂=Aniline like systems, H₁₃=O-Phenylene-diamine like systems, H₁₄=m-Phenylene-diamine like systems, H₁₅=p-Phenylene-diamine like systems, H₁₆=Benzaldehyde like systems, H₁₇=Quinoline like systems, H₁₈=Iso-quinoline like systems, H₁₉=1-Naphthalein like systems, H₂₀=2-Naphthalein like systems, H₂₁=Iso-indole like systems, H₂₂=Indole like systems, H₂₃=Benzyldine-aniline-like systems, H₂₄=Azobenzene like systems, H₂₅=Acridine like systems, H₂₆=Phenazine like systems)

5. Some result on Sombor matrix

Theorem 5.1. Let G be graph with vertex set $V(G)$ and edge set $E(G)$ with the Sombor matrix $S(G)$. If

$$P_{S(G)} = c_0\lambda^n + c_1\lambda^{n-1} + c_2\lambda^{n-2} + \dots + c_n$$

is the characteristic polynomial of $S(G)$, then

- i. $c_2 = -F(G)$,
- ii. $c_3 = -2 \sum_{\Delta} \prod_{uv \in E(\Delta)} \sqrt{d_u^2 + d_v^2}$,

where Δ is a triangle in the graph G .

Proof. i. From the definition of $P_{S(G)}$, we have:

$$c_2 = \sum_{1 \leq i < j \leq n} \begin{vmatrix} 0 & s_{ij} \\ s_{ji} & 0 \end{vmatrix} = - \sum_{1 \leq i < j \leq n} s_{ij}^2 = \sum_{uv \in E(G)} d_u^2 + d_v^2 = -F(G).$$

ii. From the definition of $P_{S(G)}$, we have:

$$c_3 = - \sum_{1 \leq i < j \leq n} \begin{vmatrix} 0 & s_{ij} & s_{ik} \\ s_{ji} & 0 & s_{jk} \\ s_{ki} & s_{kj} & 0 \end{vmatrix} = - \sum_{1 \leq i < j < k \leq n} s_{ij}s_{jk}s_{ki} = -2 \sum_{\Delta} \prod_{uv \in E(\Delta)} \sqrt{d_u^2 + d_v^2}.$$

□

Lemma 5.2. [Newton’s identity] Given an $n \times n$ matrix A , let $P(\lambda) = c_0\lambda^n + c_1\lambda_{n-1} + c_2\lambda_{n-2} + \dots + c_n$ be the characteristic polynomial of A , then the coefficient $c_3 = \frac{1}{6} [-(\text{Tr}(A))^3 + 3 \text{Tr}(A) \text{Tr}(A^2) - 2 \text{Tr}(A^3)]$.

Theorem 5.3. Let $S(G) = (s_{ij})_{n \times n}$ be the Sombor matrix of a graph G and be its $\lambda_1 \geq \lambda_2 \geq \dots \geq \lambda_n$ eigenvalues, then:

- i. $\sum_{i=1}^n \lambda_i^2 = 2F(G)$,
- ii. $\sum_{i=1}^n \lambda_i^3 = 3 \sum_{\Delta} \prod_{uv \in E(\Delta)} \sqrt{d_u^2 + d_v^2}$,

where Δ is a triangle in the graph G

Proof.

i. $\sum_{i=1}^n \lambda_i^2 = \text{Tr}(S(G)^2) = \sum_{i=1}^n \sum_{j=1}^n s_{ij}s_{ji} = \sum_{i=1}^n s_{ii}^2 + \sum_{i \neq j} s_{ij}s_{ji} = 2 \sum_{i < j} s_{ij}^2 = 2 \sum_{uv \in E(G)} d_u^2 + d_v^2 = 2F(G).$

ii. We know that, $\text{Tr}(S(G)^3) = \sum_{i=1}^n \lambda_i^3$. The result follows by equating the coefficient c_3 values given in Theorem 5.1, Lemma 5.2 and using the facts $\text{Tr}(S(G)) = 0$ and $\text{Tr}(S(G)^2) = 2F(G)$. We get the required result.

□

6. Bounds for the largest eigenvalue

Theorem 6.1. If G is any graph with n vertices with $S(G) = (s_{ij})_{n \times n}$ being its Sombor matrix and $\lambda_1 \geq \lambda_2 \geq \dots \geq \lambda_n$ are its eigenvalues, then

$$\lambda_1 \leq \sqrt{2(n-1)F(G)}.$$

Proof. Taking $a_i = \lambda_i$ and $b_i = 1$ for $i = 1, 2, 3, \dots, n$ in Cauchy–Schwarz inequality we get:

$$\left(\sum_{i=2}^n \lambda_i \right)^2 \leq (n-1) \sum_{i=2}^n \lambda_i^2.$$

On solving we get:

$$\begin{aligned} (-\lambda_1)^2 &\leq (n-1)(2F(G) - \lambda_1^2) \\ \implies \lambda_1 &\leq \sqrt{2(n-1)F(G)}. \end{aligned}$$

□

7. Bounds for Sombor energy

Now we obtain some bounds on the Sombor energy of graphs. To this end, we make use of the following classical inequalities

Lemma 7.1. [Diaz–Metcalf Inequality] Let (a_1, a_2, \dots, a_n) and (b_1, b_2, \dots, b_n) be positive real numbers, satisfying the condition $ra_i \leq b_i \leq Ra_i$ for $1 \leq i \leq n$. Then:

$$\sum_{i=1}^n b_i^2 + rR \sum_{i=1}^n a_i^2 \leq (r + R) \sum_{i=1}^n a_i b_i.$$

Equality holds if and only if $b_i = Ra_i$ or $b_i = ra_i$ for $1 \leq i \leq n$.

Lemma 7.2. Let a_1, a_2, \dots, a_n be non-negative real numbers, then:

$$n \left(\frac{1}{n} \sum_{i=1}^n a_i - \left(\prod_{i=1}^n a_i \right)^{1/n} \right) \leq n \sum_{i=1}^n a_i - \left(\sum_{i=1}^n \sqrt{a_i} \right)^2 \leq n(n-1) \left(\frac{1}{n} \sum_{i=1}^n a_i - \left(\prod_{i=1}^n a_i \right)^{1/n} \right).$$

7.1. Lower bounds for the Sombor energy

Theorem 7.3. Let G be any graph with n vertices and let P be the absolute value of the determinant of Sombor matrix $S(G)$, then:

$$\sqrt{2F(G) + n(n-1)P^{2/n}} \leq ES(G).$$

Proof.

$$[ES(G)]^2 = \left(\sum_{i=1}^n |\lambda_i| \right)^2 = \sum_{i=1}^n |\lambda_i|^2 + \sum_{i \neq j} |\lambda_i| |\lambda_j| = 2F(G) + \sum_{i \neq j} |\lambda_i| |\lambda_j|.$$

Clearly we have:

$$\frac{1}{n(n-1)} \sum_{i \neq j} |\lambda_i| |\lambda_j| \geq \prod_{i \neq j} (|\lambda_i| |\lambda_j|)^{1/(n(n-1))} = \left| \prod_{i=1}^n \lambda_i \right|^{2/n} = P^{2/n} \implies \sum_{i \neq j} |\lambda_i| |\lambda_j| \geq n(n-1)P^{2/n},$$

therefore

$$\sqrt{2F(G) + n(n-1)P^{2/n}} \leq ES(G).$$

□

Theorem 7.4. Let G be a graph with n vertices. Then

$$\frac{2F(G) + n|\lambda_1||\lambda_n|}{|\lambda_n| + |\lambda_1|} \leq ES(G),$$

where, $|\lambda_1|$ and $|\lambda_n|$ are maximum and minimum of the absolute value of eigenvalues of $S(G)$. Equality will be attained if and only if for each $1 \leq i \leq n$, either $|\lambda_i| = |\lambda_1|$ or $|\lambda_i| = |\lambda_n|$.

Proof. substituting $b_i = |\lambda_i|$, $a_i = 1$, $r = |\lambda_n|$ and $R = |\lambda_1|$ in lemma 7.1, we have

$$\begin{aligned} \sum_{i=1}^n |\lambda_i|^2 + |\lambda_n||\lambda_1| \sum_{i=1}^n 1 &\leq (|\lambda_1| + |\lambda_n|) ES(G) \\ \implies \frac{2F(G) + n|\lambda_1||\lambda_n|}{|\lambda_1| + |\lambda_n|} &\leq ES(G). \end{aligned}$$

□

7.2. Upper bound for Sombor index

Theorem 7.5. *If G is a graph with n vertices, then*

$$ES(G) \leq \sqrt{nF(G)}.$$

Proof. Put $a_i = 1$ and $b_i = |\lambda_i|$ in Cauchy–Schwarz inequality, we get

$$[ES(G)]^2 \leq n \left(\sum_{i=1}^n |\lambda_i| \right)^2 = nF(G).$$

Simplifying the above equation we get the required result. □

Theorem 7.6. *If G is a graph with n vertices, then:*

$$ES(G) \leq \sqrt{n \left\{ 2F(G) + [\text{Det}(N(G)^2)]^{1/n} \right\} - 2F(G)},$$

where $|\text{Det}(N(G))|$ is absolute value of the determinant of Sombor matrix $S(G)$.

Proof. Substituting $a_i = \lambda_i^2$ for $i = 1, 2, \dots, n$ in lemma 7.2, we have:

$$n \left(\frac{1}{n} \sum_{i=1}^n \lambda_i^2 - \left(\prod_{i=1}^n \lambda_i^2 \right)^{1/n} \right) \leq n \sum_{i=1}^n \lambda_i^2 - \left(\sum_{i=1}^n \lambda_i \right)^2.$$

Using results in theorem 5.1, we get:

$$n \left(\frac{1}{n} 2F(G) - |\text{Det}(S(G))|^{1/n} \right) \leq n 2F(G) - (ES(G))^2.$$

On simplifying above equation we arrive the required result. □

8. Conclusion

Recently, Gutman introduced a new vertex-degree-based topological index, called the Sombor index $SO(G)$ in chemical graph theory. In this paper, we have introduced a new matrix for a graph G , called the Sombor matrix, and defined a new variant of graph energy called the Sombor energy $ES(G)$ of a graph G . The striking feature of this new matrix is that it is related to the well-known degree-based topological indices called forgotten indices. When $ES(G)$ values of some molecules containing hetero atoms are correlated with their total π -electron energy, we obtained a good correlation with the correlation coefficient $r = 0.952$. Further, bounds (lower and upper) and characterizations on the largest eigenvalue of $S(G)$ and Sombor energy of graphs have been studied.

References

- [1] Boregowda H.S., Jummanaver R.B. Neighbors degree sum energy of graphs. *J. Appl. Math. Comput.*, 2021, <https://doi.org/10.1007/s12190-020-01480-y>.
- [2] Gutman I., Trinajstić N. Graph theory and molecular orbitals. Total π -electron energy of alternant hydrocarbons. *Chem. Phys. Lett.*, 1972, **17**, P. 535–538.
- [3] Jafari Rad N., Jahanbani A., Gutman I. Zagreb Energy and Zagreb Estrada Index of Graphs. *MATCH Commun. Math. Comput. Chem.*, 2018, **79**, P. 371–386.
- [4] Rajendra P., Randić. Color Energy of a Graph. *Int. Journal of Computer Applications*, 2017, **171**, P. 1–5.
- [5] Aouchiche M., Hansen P. Distance spectra of graphs: a survey. *Linear Algebra Appl.*, 2014, **458**, P. 301–386.
- [6] Brouwer A., Haemers W. *Spectra of Graphs*, Springer, Berlin, 2012.
- [7] Mohar B. The Laplacian spectrum of graphs. In: Alavi, Y., Chartrand, G., Ollermann, O.R., Schwenk, A.J. (eds.) *Graph Theory, Combinatorics and Applications*, Wiley, New-York, 1991, **2**, P. 871–898.
- [8] Ramane H.S., Jummanaver R.B., Gutman I. Seidel Laplacian energy of graphs. *Int. J. Appl. Graph. Theory*, 2017, **2**, P. 74–82.
- [9] Cvetković D., Rowlinson P., Simić S.K. Eigenvalue bounds for the signless Laplacian. *Publ. Inst. Math. (Beograd)*, 2007, **81**, P. 11–27.
- [10] Ramane H.S., Gutman I., Patil J.B., Jummanaver R.B. Seidel signless Laplacian energy of graphs. *Math. Interdiscip. Res.*, 2017, **2**, P. 181–192.
- [11] Ramane H.S., Revankar D.S., Patil J.B. Bounds for the degree sum eigenvalues and degree sum energy of a graph. *Int. J. Pure Appl. Math. Sci.*, 2013, **6**, P. 161–167.
- [12] Das K.C., Trinajstić N. Comparison between first geometric–arithmetic index and atom–bond connectivity index. *Chem. Phys. Lett.*, 2010, **497**, P. 149–151.

- [13] Graovac A., Gutman I., Trinajstić N. Total π -Electron Energy. In: *Topological Approach to the Chemistry of Conjugated Molecules*, 1977, **4**, P. 48–78.
- [14] Gutman I. Degree-based topological indices. *Croat. Chem. Acta*, 2013, **86**, P. 351–361.
- [15] Gutman I. Geometric approach to degree-based topological indices: Sombor indices. *MATCH Commun. Math. Comput. Chem.*, 2021, **86**, P. 11–16.
- [16] Das K.C., Cevik A.S., Cangul I.N., Shang Y. On Sombor Index. *Symmetry*, 2021, **13**, 140.
- [17] Cruz R., Gutman I., Rada J. Sombor index of chemical graphs. *Applied Mathematics and Computation*, Elsevier, 2021, **399**, 126018.
- [18] Deng H., Tang Z., Wu R. Molecular trees with extremal values of Sombor indices. *Int. J. Quantum. Chem.*, 2021, **121** (11), e26622.
- [19] Gutman I. Some basic properties of Sombor indices. *Open J. Discret. Appl. Math.*, 2021, **4**, P. 1–3.
- [20] Horoldagva B., Xu C. On Sombor index of graphs. *MATCH Commun. Math. Comput. Chem.*, 2021, **86**, P. 703–713.
- [21] Kulli V.R., Gutman I. Computation of Sombor Indices of Certain Networks. *Int. Journal of Applied Chemistry*, 2021, **8**, P. 1–5.
- [22] Liu H., You L., Tang Z., Liu J.B. On the reduced Sombor index and its applications. *MATCH Commun. Math. Comput. Chem.*, 2021, **86**, P. 729–753.
- [23] Milovanović I., Milovanović E., Matejić M. On some mathematical properties of Sombor indices. *Bull. Int. Math. Virtual Inst.*, 2021, **11**, P. 341–353.
- [24] Réti T., Doslić T., Ali A. On the Sombor index of graphs. *Contrib. Math.*, 2021, **3**, P. 11–18.
- [25] Wang Zh., Mao Y., Li Y., Furtula B. On relations between Sombor and other degree-based indices. *J. Appl. Math. Comput.*, 2021, doi:10.1007/s12190-021-01516-x.
- [26] Redžepović I. Chemical applicability of Sombor indices. *J. Serb. Chem. Soc.*, 2021, **86** (5), P. 445–457.
- [27] Furtula B., Gutman I. A forgotten topological index. *J. Math. Chem.*, 2015, **53**, P. 1184–1190.
- [28] Ramachandran K.I., Deepa G., Namboori K. *Computational Chemistry and Molecular Modelling: Principles and Applications*. Springer, Berlin, 2008.
- [29] Yates K. *Huckel Molecular Orbital Theory*. Academic Press, New York, 1978.
- [30] Coulson C.A., Streitwieser J. *Dictionary of π -Electron Calculations*. Freeman, San Francisco, 1965.

Analog of the Darboux problem for a loaded integro-differential equation involving the Caputo fractional derivative

U. Baltayeva^{1,2,*}, Y. Alikulov³, I. I. Baltayeva², A. Ashirova⁴

¹Khorezm Mamun Academy, Markaz-1, 220900, Khiva, Uzbekistan

²Urgench State University, Kh.Alimdjani str. 14, 220100, Urgench, Uzbekistan

³Tashkent University of Information Technologies named after Muhammad Al-Khwarizmi, Amir Temur str. 108, 100200 Tashkent, Uzbekistan

⁴Urganch branch of Tashkent University of Information Technology named after Muhammad al-Khwarizmi, Al Khorezmi str. 110, 220100 Urgench, Uzbekistan

umida.baltayeva@mail.ru, yolqin-aliqulov@mail.ru, iroda-b@mail.ru, anorgul@mail.ru

PACS 02.30.Jr

DOI 10.17586/2220-8054-2021-12-4-418-424

In this paper, we prove the unique solvability of an analogue problem Darboux for a loaded integro-differential equation with Caputo operator by method of integral equations. The problem is equivalently reduced to a system of integral equations, which is unconditionally and uniquely solvable.

Keywords: integro-differential equations, Caputo fractional derivative, loaded equation, nonlocal problem, Bessel function.

Received: 9 June 2021

Revised: 17 July 2021

1. Introduction and formulation of the problem

In recent years, the range of problems under consideration for partial differential equations, as well as for equations of hyperbolic, parabolic and mixed types, has significantly expanded. Along with the study of the main boundary value problems for such equations, since the 1970's, much attention of researchers is paid to the formulation and study of nonlocal boundary value problems. This is explained by the fact that many practically important problems associated with the dynamics of soil moisture, with the process of particle diffusion in turbulent plasma with cooling an inhomogeneous curved rod, modeling the process of laser radiation lead to nonlocal problems [1, 2].

In prior research to date, mainly nonlocal boundary value problems for second-order equations have been studied.

Equations of the third and higher order, which, according to similar equations of the second order, have very important applications, were considered in the works of Berdyshev A. S. [3], Sabitov K. B. [4], Zikirov O. S. and Kholikov D. K. [5], Kh. Belakroum, A. Ashyralyev, A. Guezane-Lakoud [6], Khashimov A. R., Smetanová D. [7], as well as in [8, 9].

On the other side, in connection with intensive research on problems of optimal control of the agro economical system, long-term forecasting and regulating the level of ground waters and soil moisture, problems of mathematical biology: population dynamics and problems of mathematical economics, it has become necessary to investigate a new class of equations called as "loaded equations". Such equations were investigated for the first time by A. Knezer (1914), L. Lichtenstein (1931). However, they did not use the term "loaded equation". This terminology was introduced by A. M. Nakhushhev (1976), where the most general definition of the loaded equation is given and various loaded equations are classified in detail [1].

We can cite by many examples as which emphasized the development of the theory of the loaded equation in the last several decades. As we know [1], mathematical models of nonlocal physics-biological fractal processes represented by loaded integro-differential equations or loaded differential equations especially with integro-differential operators [1, 9].

How we know, there has been a significant development in nonlocal problems for fractional differential equations or inclusions (we can see [10] and their literature). Very recently, in the works [11], [12] authors investigated the fractional order integro-differential equations with nonlocal conditions. However, to the best of our knowledge, the nonlocal problems for fractional integro-differential equations in the Caputo derivative sense have not been discussed extensively [10].

Based on the above, the main aim of this paper is to formulate and investigate the unique solvability of a boundary-value problem type of Darboux (Cauchy-Goursat) for a third-order loaded partial differential equation of hyperbolic type, with the Caputo operators. For investigating this problem, we reduce the boundary-value problem for the loaded

equation to a new non-local problem for the fractional order integro-differential equation [8, 9]. Taking into account the unique solvability of non-local problems, we prove the solvability of the local boundary-value problem for the loaded equation.

We consider the following linear loaded [13] integro-differential equation:

$$\frac{\partial}{\partial x} (u_{xx} - u_{yy} + au_x + bu_y + cu) = cD_{0x}^\alpha u(x, 0), \tag{1}$$

where $cD_{0x}^\alpha f(x)$ is a fractional differential operator of Caputo type [14], $0 < \alpha < 1$, a, b, c are given real parameters.

Let Ω be a characteristic triangle bounded by the segment AB the axis OX and two characteristics

$$AC : x + y = 0, \quad BC : x - y = 1$$

of equation (1) for $y < 0$, $I = \{(x, y) : 0 < x < 1, y = 0\}$.

Problem D₁. (Darboux) Find a regular solution $u(x, y)$ of the equation (1) in Ω , which is continuous in $\bar{\Omega}$, has continuous derivatives $u_x(u_y)$, up to $AB \cup AC$, and satisfies the boundary-value conditions:

$$u_y(x, 0)|_{y=0} = \varphi_1(x), \quad 0 \leq x < 1, \tag{2}$$

$$u(x, -x) = \psi_1(x), \quad \left. \frac{\partial u(x, y)}{\partial n} \right|_{y=-x} = \psi_2(x), \quad 0 \leq x \leq \frac{1}{2}, \tag{3}$$

where $\varphi_1(x)$, $\psi_1(x)$ and $\psi_2(x)$ are given functions.

2. Representation of solution of the equation

One of the most important aspect of the investigation of the boundary-value problem, is shown by the following theorem.

Theorem 1. Any regular solution of equation (1) is represented in the form:

$$u(x, y) = z(x, y) + w(x), \tag{4}$$

where $z(x, y)$ is a solution to the equation:

$$\frac{\partial}{\partial x} (z_{xx} - z_{yy} + az_x + bz_y + cz) = 0, \tag{5}$$

$w(x)$ is a solution of the following integro-differential equation

$$w'''(x) + aw''(x) + cw'(x) - cD_{0x}^\alpha w(x) = cD_{0x}^\alpha z(x, 0). \tag{6}$$

Proof. Let $z(x, y)$ be a regular solution of the equation (5), $w(x)$ is a solution of the equation (6). Then, we must prove that the function represented by formula (4) will be solution of the equation (1). Thus, in (1), $u(x, y)$ instead of $z(x, y) + w(x)$ taking into account (5) and (6), it is easy to verify that the relation:

$$\begin{aligned} \frac{\partial}{\partial x} (u_{xx} + au_{xx} + bu_y + cu) - cD_{0x}^\alpha u(x, 0) &= \frac{\partial}{\partial x} (z_{xx} + az_x + bz_y + cz) + \\ &+ w'''(x) + aw''(x) + cw'(x) - cD_{0x}^\alpha w(x) - cD_{0x}^\alpha z(x, 0) = 0, \end{aligned}$$

that is, represented by formula (4), is a solution of the equation (1) for $y > 0$. Then, vice versa, let $u(x, y)$ be a regular solution of the equation (1), and $w(x)$ be a certain solution of the following integro-differential equation:

$$w'''(x) + aw''(x) + cw'(x) = cD_{0x}^\alpha u(x, 0). \tag{7}$$

Let us prove the validity of the relation (4).

Consequently, the function:

$$u(x, y) = z(x, y) + \left(-\frac{2}{a}\right) \int_0^x \left(\left(x - t + \frac{2}{a}\right) e^{-\frac{a}{2}(x-t)} - \frac{2}{a} \right) cD_{0t}^\alpha u(t, 0) dt,$$

is a solution of the equation (1), as for equation with right side at $a^2 = 4c \neq 0$, where $z(x, y)$ is a solution of the equation (5), and the function:

$$u(x, y) = -\frac{2}{a} \int_0^x \left(\left(x - t + \frac{2}{a}\right) e^{-\frac{a}{2}(x-t)} - \frac{2}{a} \right) cD_{0t}^\alpha u(t, 0) dt,$$

is a partial solution to the equation (1). Hence, (1) highlights the validity of the representation (4), i.e. $u(x, y) = z(x, y) + w(x)$.

It follows from the latter representation that $u(x, 0) = z(x, 0) + w(x)$. Thus, from equation (7), it provides:

$$w'''(x) + aw''(x) + cw'(x) - cD_{0x}^\alpha w(x) - cD_{0x}^\alpha z(x, 0) = 0,$$

and the function $z(x, y) = u(x, y) - w(x)$, satisfies equation: (5) for $y > 0$. In cases $a^2 > 4c$ and $a^2 < 4c$ respectively. Analogously, it was proved in the case for $y < 0$. Theorem 1 is thus proved.

Remark 1. Taking into account, that the function $z(x) = \tilde{a}e^{\sqrt{\lambda}x} + \tilde{b}e^{-\sqrt{\lambda}x} + \tilde{c}$ satisfies the equation (5), for the investigation of the problem D_1 , we can assume without loss of generality that

$$w(0) = w'(0) = w''(0) = 0. \quad (8)$$

Denoting $w'(x) = y(x)$ in the equation (6) we have:

$$y''(x) + ay'(x) + cy(x) - \frac{1}{\Gamma(1-\alpha)} \int_0^x (x-t)^{-\alpha} y(t) dt = cD_{0x}^\alpha z(x, 0). \quad (9)$$

The characteristic equation, corresponding to the homogeneous equation, has the form

$$k^2 + ak + c = 0. \quad (10)$$

Let us introduce the notation $\Delta = a^2 - 4c$:

1) If $\Delta = 0$ then, the equation (10) has two real roots, moreover they are equal. Thus, at $a^2 > 4c$ the equation (9) equivalent to the following form:

$$\begin{aligned} y(x) - \frac{1}{\Gamma(1-\alpha)} \int_0^x y(t) dt \int_t^x (x-s)(s-t)^{-\alpha} e^{-\frac{\alpha}{2}(x-s)} ds = \\ = l_1(0)e^{-\frac{\alpha}{2}x} + l_2(0)xe^{-\frac{\alpha}{2}x} + \int_0^x (x-t)e^{-\frac{\alpha}{2}(x-t)} cD_{0x}^\alpha z(t, 0) dt, \end{aligned} \quad (11)$$

where $l_1(0)$ and $l_2(0)$ are unknown constants to be defined. In equation (9) at $s = t + (x-t)v$, with respect to $y'(0) = y(0) = 0$, we obtain the Volterra integral equation relative to $y(x)$:

$$y(x) - \int_0^x K_1(x, t)y(t) dt = \int_0^x (x-t)e^{-\frac{\alpha}{2}(x-t)} cD_{0x}^\alpha z(t, 0) dt, \quad (12)$$

where:

$$K_1(x, t) = \frac{(x-t)^{2-\alpha}}{\Gamma(1-\alpha)} \int_0^1 v^{-\alpha} (1-v) e^{-\frac{\alpha}{2}(x-t)(1-v)} dv.$$

Solving the next integral equation (12) we obtain:

$$y(x) = \int_0^x \left(K_1(x, t) + \int_t^x R_1(x, s)K_1(s, t) ds \right) z'(t, 0) dt, \quad (13)$$

where $R_1(x, s)$ is the resolvent of the kernel $K_1(x, t)$.

Hence, by virtue of the (8), (13) and the designation $w'(x) = y(x)$, after some transformation, we have:

$$w(x) = \int_0^x K(x, t)z'(t, 0) dt, \quad (14)$$

where:

$$K(x, t) = \int_t^x \left\{ K_1(s, t) + \int_t^s R_1(s, z) K_1(z, t) dz \right\} ds.$$

Similarly we can receive in the cases 2) $a^2 > 4c$, and 3) $a^2 < 4c$.

3. The main results

Theorem 2. If $\psi_1'(0) + 2\varphi_1(0) = \sqrt{2}\psi_2(0)$, and $\varphi_1(x) \in C^1[0, 1] \cap C^2(0, 1)$,

$$\psi_1(x) \in C^1\left[0, \frac{1}{2}\right] \cap C^3\left(0, \frac{1}{2}\right), \quad \psi_2(x) \in C[0, 1/2] \cap C^2(0, 1/2), \tag{15}$$

then there exists a unique solution to the problem D_1 in the domain Ω .

Proof. Firstly, by virtue of the representation (4) and in view of (8), the equation (1) and boundary-value conditions (2), (3), are reduced to the form (5):

$$z_y(x, 0) = \varphi_1(x), \quad 0 \leq x < 1, \tag{16}$$

$$z(x, -x) = \psi_1(x) - \int_0^x K(x, t)z'(t, 0)dt, \quad 0 \leq x \leq \frac{1}{2}, \tag{17}$$

$$\frac{\partial z(x, -x)}{\partial n} = \psi_2(x) - \frac{1}{\sqrt{2}} \int_0^x K'(x, t)z'(t, 0)dt, \quad 0 \leq x \leq \frac{1}{2}. \tag{18}$$

Since, problem D_1 was reduced to the equivalent non-local problem for a third order equation of mixed type (5), we may conclude that Problem D_1 has a unique solution, as a direct result of the unique solvability of the non-local problem.

Bearing in mind [15], after integration of the equation (5), with respect to x , we have the following form:

$$z_{xx} - z_{yy} + az_x + bz_y + cz = \tilde{\omega}(y), \quad y < 0, \tag{19}$$

where $\tilde{\omega}(y)$ is arbitrary continuous function.

First, we find the main functional relations on I deduced from the domain Ω . We introduce the following notation:

$$z(x, y)|_{y=0} = \tau(x), \quad (x, 0) \in \bar{I}, \tag{20}$$

where $\tau(x)$ is unknown function.

The solution of the Cauchy problem for the equation (19) with the conditions (2), (20) can be represented in the form:

$$\begin{aligned} z(x, y) = & \frac{1}{2} \left[\tau(x - y)\exp\left(-\frac{a - b}{2}y\right) + \tau(x + y)\exp\left(-\frac{a + b}{2}y\right) \right] - \\ & - \frac{1}{2} \exp\left(\frac{b}{2}y\right) \int_{x-y}^{x+y} \left(\frac{b}{2} J_0 \left[\sqrt{\lambda((x - \xi)^2 - y^2)} \right] - \lambda y \hat{J}_1 \left[\sqrt{\lambda((x - \xi)^2 - y^2)} \right] \right) \times \\ & \times \exp\left(-\frac{a}{2}(x - \xi)\right) \tau(\xi) d\xi + \\ & + \frac{1}{2} \exp\left(\frac{b}{2}y\right) \int_{x-y}^{x+y} J_0 \left[\sqrt{\lambda((x - \xi)^2 - y^2)} \right] \exp\left(-\frac{a}{2}(x - \xi)\right) \varphi_1(\xi) d\xi + \\ & + \frac{1}{2} \int_0^y \tilde{\omega}(\eta) d\eta \int_{x-y+\eta}^{x+y-\eta} J_0 \left[\sqrt{\lambda((x - \xi)^2 - (y - \eta)^2)} \right] d\xi, \\ & \lambda = \frac{1}{4} (4c^2 - a^2 - b^2), \end{aligned} \tag{21}$$

where $J_0[z]$, $J_1[z]$ is Bessel function, $\hat{J}_1[z] = J_1[z]/z$.

Then using condition (18) from (21), taking account of $\tau'(0) + \varphi_1(0) = \sqrt{2}\psi_2(0)$ and considering of the property of the Bessel functions and by replacing the argument x for $-y$ in the relation, we get the following functional relation, transferred from the domain Ω to I :

$$\tilde{\omega}(y) + \lambda_2 \int_0^y L(\eta, y)\tilde{\omega}(\eta) d\eta = \Phi'(y), \tag{22}$$

$$L(\eta, y) = \int_{\eta-2y}^{-\eta} \left[\hat{J}_1[z(-y, y; \xi, \eta)] - \frac{1}{2} J_2[z(-y, y; \xi, \eta)] \right] d\xi, \tag{23}$$

$$\begin{aligned} \Phi(y) &= \sqrt{2}\psi_2(-y) - w'(-y) + \frac{a-b}{4}\tau(-2y)\exp\left(-\frac{a-b}{2}y\right) - \\ & - \frac{1}{2}\exp\left(\frac{a+b}{2}y\right) \int_{-2y}^0 [p_0(\xi, y)\tau(\xi) + p_1(\xi, y)\varphi_1(\xi)] d\xi - \\ & - \left[\varphi_1(0) + \frac{2\lambda y + a - b}{4}\tau(0) + \tau'(0)\right] \exp\left(\frac{a+b}{2}y\right), \\ z(x, y; \xi, \eta) &= \sqrt{\lambda\left((x-\xi)^2 - (y-\eta)^2\right)}, \quad z(x, y; \xi, 0) = z(x, y; \xi). \end{aligned}$$

Both $p_0(\xi, y), p_1(\xi, y)$ are known continuous functions. Hence, if we reckon the right-hand side known, with regards the properties of the special functions, and the theory of the integral equations of the Volterra type, the solution of the equation (22) can be written in the form:

$$\tilde{\omega}(y) = \Phi'(y) + \int_0^y R_2(y, t)\Phi'(t)dt, \tag{24}$$

here $R_2(y, t)$ is the resolvent of the kernel $L(\eta, y)$.

Further, from (21) bearing mind (17), $\tau(0) = \psi_1(0)$, we deduce the next functional relation, transferred from the Ω to I :

$$\begin{aligned} \tau(x) &+ \int_0^x \tilde{p}_0\left(\frac{x}{2}, \xi\right) \exp\left(-\frac{a}{2}(x-\xi)\right) \tau(\xi) d\xi - \\ &- \int_0^x J_0\left[z\left(\frac{x}{2}, -\frac{x}{2}; \xi\right)\right] \exp\left(-\frac{a}{2}(x-\xi)\right) \varphi_1(\xi) d\xi = \\ &= -\psi_1(0)\exp\left(-\frac{a}{2}x\right) + 2\exp\left(-\frac{a-b}{4}x\right) \times \\ &\times \left\{ \psi_1\left(\frac{x}{2}\right) - \omega\left(\frac{x}{2}\right) - \frac{1}{2} \int_0^{-\frac{x}{2}} \tilde{\omega}(\eta) d\eta \int_{x+\eta}^{-\eta} J_0[z(x, -x; \xi, \eta)] d\xi \right\}. \end{aligned} \tag{25}$$

The equality (25) with regards (24), is equivalent to the system of integral equation with shift. We can easily obtain the Volterra integral equation with shift regarding the unknown function $\tau'(y)$, transferred from the domain Ω to I . Hence, taking account of (15) and based on the general theory of integral equations, one can easily be sure that equation has a unique solution.

Thus, solution of the problem D_1 in the domain Ω in view of (14), (24) and (25) is determined uniquely according to the formula (4). Therefore, we can conclude that, there exists a regular solution of problem D_1 . Thus, the constructed solution of the problem D_1 is unique. Indeed, let $\varphi_1(x) = \psi_1(x) = \psi_2(x) = 0$, then from (14) (respectively (24) and (25)), we have $w(x) = 0$ and $\tau(x) = 0$. It follows from this and (21) that $z(x, y) \equiv 0$ in $\bar{\Omega}$. Consequently, the homogeneous boundary value problem has no nontrivial solutions, i.e. from formulas (4), we have $u(x, y) \equiv 0$ in the domain Ω , Q.E.D.

Thus, we have proved that Problem D_1 is uniquely solvable.

For example, let $a = c = 0$ in the equation (1), in that case, the kernel of the equation (12) has the form $K_1(x, t) = \frac{(x-t)^{2-\alpha}}{\Gamma(3-\alpha)}$ and we can find the resolvent of the kernel as:

$$R_1(x, t) = \sum_{i=1}^n \frac{(x-t)^{(3-\alpha)i-1}}{\Gamma((3-\alpha)i)}.$$

If we can choose the given functions taking into account the conditions of Theorem 2, applying $z(x, y) = x - y$, then we obtain the solution of the problem (6) and (8) in the form:

$$w(x) = \frac{x^{4-\alpha}}{\Gamma(5-\alpha)} + \sum_{i=1}^{\infty} \frac{x^{4-\alpha+(3-\alpha)i}}{\Gamma(5-\alpha+(3-\alpha)i)}, \quad 0 < \alpha < 1.$$

Consequently, we can find the exact solution to the problem (1), (2) and (3), which is represented in the Fig. 1.

Similarly, we can prove solvability of this analogous problem Darboux D_2 .

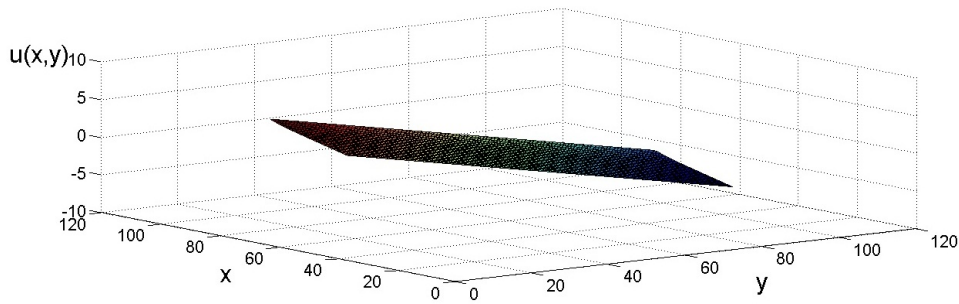


FIG. 1. Exact solution to the problem (1), (2) and (3)

Problem D₂. Find a regular solution $u(x, y)$ equation (1) in Ω , which has continuous derivatives $u_x(u_y)$, up to $AB \cup BC(BC)$, and satisfies the conditions (2):

$$u(x, x - 1) = \psi_3(x), \quad \left. \frac{\partial u(x, y)}{\partial n} \right|_{y=x-1} = \psi_4(x), \quad \frac{1}{2} \leq x \leq 1, \tag{26}$$

where $\psi_3(x)$ and $\psi_4(x)$ are given real-valued functions.

Theorem 3. If $\psi'_3(1) = -\sqrt{2}\psi_4(1) + 2\varphi'_2(0)$, and the conditions (15) and:

$$\psi_3(x) \in C^1 [1/2, 1] \cap C^3 (1/2, 1), \psi_4(x) \in C [1/2, 1] \cap C^2 (1/2, 1)$$

are satisfied, then there exists a unique solution to the problem D_2 in the domain Ω .

Theorem 3 is proved in the same way as the Theorem 2. That is, by virtue of the Theorem 1, equation (1) and the conditions (2), (16), in view of (8), are reduced to the form (5), (16) and:

$$z(x, x - 1) = \psi_3(x) - w(x), \quad 0 \leq x \leq \frac{1}{2}, \tag{27}$$

$$\left. \frac{\partial z(x, y)}{\partial n} \right|_{y=x-1} = \psi_4(x) - \frac{1}{\sqrt{2}}w'(x), \quad 0 \leq x \leq \frac{1}{2}, \tag{28}$$

where $w(x)$ expressed in terms of (14).

Since, problem D_2 was reduced to the equivalent non-local problem. The equation (5) can be represented in the form (19). Thus, using the solution of the Cauchy problem (21), taking into account (18):

$$\tau(1) = \psi_3(1), \quad \tau(x) = \psi_3(1) - \int_x^1 \tau'(t)dt, \quad \psi'_3(1) = -\sqrt{2}\psi_4(1) + 2\varphi'_1(0),$$

we obtain the first functional relation, transferred from the Ω to I . On the other side, the relation (25) between the functions $\tau(x)$ and $\varphi_1(x)$ transferred from the Ω to I is correctly. Further, conducting an analogous reasoning to that of $\tau(x)$, from the main functional relations with regards of conditions of the problem, we can find the $\tau(x)$ and $w(x)$. The subsequent investigations are performed by analogy with problem D_1 .

4. Conclusion

One of the directions of the modern theory of partial differential equations, which has been rapidly developing in recent years, is the theory of nonlocal problems. In this paper, we investigated solvability of problems for linear loaded integro-differential equations. Taking into account Theorem 1, our problem reduced to nonlocal problems for partial differential equations with conditions (16)–(18) and (16), (27)–(28). Attention to such problems is not due to only theoretical interest, but also practical necessity. Mathematical modeling a number of physical and biological processes is of interest to modern natural science as nanosciences, nano-engineering.

We should note that the problem under consideration has investigated the equation with a wave operator which appears in problems of nanophysics and is present in some micro and nanoflow models of spinodal decomposition models, and also described flow in thin viscous layers subjected to ultrasonic acoustic field and etl [17–21].

Results [22] show that for tension bars in small length scales, nonlocal effects would have significant influences on the study of nano-structures and nonlocal theory could potentially play a useful role in analysis related to nanotechnology applications [22]. In prior studies [23], nonlocal differential problem, supplemented with non-standard boundary conditions, is highlighted and shown to lead to mathematically well-posed problems of nano-engineering.

The theoretical predictions, exhibiting stiffening nonlocal behaviors, are therefore appropriate to significantly model a wide range of small-scale devices of nanotechnological interest [23].

In the work [24] researchers considered a general form of fractional integro-differential equations arising in nano-transistors, which were described with loaded differential equation.

As noted in other studies [25, 26], many important materials used in modern technologies (such as nanotechnology) are viscoelastic and anisotropic. In mathematical modeling of processes taking place in viscoelastic materials, there is a so-called system with memory, whose behavior is not completely determined by the state at the moment, but depends on the systems of entire history, and therefore, describes an integro-differential equation which contains the corresponding integral with respect to the time variable. The equation (1), taking into account the integro-differential operator is basic in the linear theory of viscoelastic anisotropic media [26].

References

- [1] Nakhushiev A.M. *Equations of mathematical biology*. Vishaya shkola, Moscow, 1995, 301 p.
- [2] Serbina L. I. *Nonlocal mathematical models of movement in watertransit systems*. Moscow, Nauka, 2007.
- [3] Berdyshev A. S. The basis property of a system of root functions of a nonlocal problem for a third-order equation with a parabolic-hyperbolic operator. *Diff Equat*, 2000, **36**, P. 417–422.
- [4] Sabitov K.B. Nonlocal problem for a parabolic-hyperbolic equation in a rectangular domain. *Math Notes*, 2011, **89**, P. 562–567.
- [5] Zikirov O. S. A nonlocal boundary value problem for third order linear partial differential equation of composite type. *Math. Model. And Anal.*, 2009, **14**(3), P. 407–421.
- [6] Belakroum Kh., Ashyralyev A., Guezane-Lakoud A. Stability of boundary-value problems for third-order partial differential equations. *Electronic Journal of Differential Equations*, 2017, **2017**(53), P. 1–11.
- [7] Khashimov A. R., Smetanov D. Nonlocal Problem for a Third-Order Equation with Multiple Characteristics with General Boundary Conditions. *Axioms*, 2021, **10**(2), P. 110.
- [8] Fedorov Valery E. and Efimova Elena S. Nonlocal boundary value problems for a third order equation of a composite type. AIP Conference Proceedings, 2021, 2328, 020009.
- [9] Baltaeva U. I. The loaded parabolic-hyperbolic equation and its relation to non-local problems. *Nanosystems physics, chemistry, mathematics*, 2017, **8**(4), P. 413–419.
- [10] JinRong Wang, Yong Zhou, Wei Wei, Honglei Xu. Nonlocal problems for fractional integrodifferential equations via fractional operators and optimal controls. *Computers and Mathematics with Applications*, 2011, **62**(3), P. 1427–1441.
- [11] Chang Y.K., Kavitha V., Mallika Arjunan M. Existence and uniqueness of mild solutions to a semilinear integrodifferential equation of fractional order. *Nonlinear Anal.*, 2009, **71**, P. 5551–5559.
- [12] Jin Rong Wang, Yong Zhou A. class of fractional evolution equations and optimal controls. *Nonlinear Anal.*, 2011, **12**, P. 262–272.
- [13] Islomov B, Baltaeva U. I. Boundary value problems for a third-order loaded parabolic-hyperbolic equation with variable coefficients. *Electronic Journal of Differential Equations*, 2015, **221**, P. 1–10.
- [14] Atangana A. *Derivative with a New Parameter*, Editor(s): Abdon Atangana. Chapter 1 – History of derivatives from Newton to Caputo Academic Press, 2016, P. 1–24.
- [15] Baltaeva U. Solvability of the analogs of the problem Tricomi for the mixed type loaded equations with parabolic-hyperbolic operators. *Boundary Value Probl.*, 2014, **211**.
- [16] Abdullaev O. K., Islomov B. I. Gellerstedt Type Problem for the Loaded Parabolic-Hyperbolic Type Equation with Caputo and Erdelyi-Kober Operators of Fractional Order. *Russ Math.*, 2020, **64**, P. 29–42.
- [17] Kirillova S. A., Almjashev V. I., Gusarov V. V. Spinodal decomposition in the SiO₂TiO₂ system and hierarchically organized nanostructures formation. *Nanosystems: Physics, Chemistry, Mathematics*, 2012, **3**(2), P. 100–115.
- [18] Antonov N. M., Popov I. Yu., Gusarov V. V. Model of spinodal decomposition of phases under hyperbolic diffusion. *Physics of the Solid State*, 1999, **41**(5), P. 824–826.
- [19] Lobanov I. S., Nikiforov D. S., Popov I. Y. et al. Model of time-dependent geometric graph for dynamical Casimir effect. *Indian J. Phys.*, 2020.
- [20] Melikhov I. F., Popov I. Y. Model of cell membrane in ultrasonic field. *Chinese Journal of Physics*, 2020, **65**, P. 334–340.
- [21] Agarwal P., Baltaeva U., Alikulov Y. Solvability of the boundary-value problem for a linear loaded integro-differential equation in an infinite three-dimensional domain. *Chaos, Solitons and Fractals*, 2020, **140**, P. 110108.
- [22] Tepe Aysegul, Artan, Reha, Application of Nonlocal Bars in Tension to Nanotechnology. *Journal of Computational and Theoretical Nanoscience*, 2009, **6**(3), P. 537–540.
- [23] Raffaele Barretta, Francesco Marotti de Sciarra, Marzia Sara Vaccaro On nonlocal mechanics of curved elastic beams. arXiv:2009.09188v1 [physics.app-ph] 19 Sep. 2020.
- [24] Avaji M., Dehcheshmeh S. S., Hafshejani J. S., Ghahfarokhi D.F. On the Solution of Linear and Nonlinear Fractional Integro-Differential Equations in Nano-Transistors. *Journal of Computational and Theoretical Nanoscience*, 2013, **10**, P. 510–513.
- [25] Baleanu D., Tenreiro Machado J. A., Guvenc Z. B. *New Trends in Nanotechnology and Fractional Calculus Applications*. Springer-Verlag, London, 2010.
- [26] Durdiev D. K., Durdiev U. D. The problem of kernel determination from viscoelasticity system integro-differential equations for homogeneous anisotropic media. *Nanosystems: Physics, Chemistry, Mathematics*, 2016, **7**(3), P. 405–409.

Dirac operator with different potentials on edges of quantum graph: resonance asymptotics

A. G. Belolipetskaia, I. Y. Popov

ITMO University, Kronverkskiy, 49, Saint Petersburg, 197101, Russia

annabel1502@mail.ru, popov1955@gmail.com

DOI 10.17586/2220-8054-2021-12-4-425-429

Asymptotics of resonances for the Dirac operator with different potentials on edges of a quantum graph with the Kirchhoff coupling conditions at vertices is studied. The results are obtained for a quantum graph that consists of a compact interior and a finite number of exterior edges of infinite length connected to the interior.

Keywords: quantum graph, Dirac operator, asymptotics, resonance.

Received: 18 July 2018

1. Introduction

In the past few decades, quantum graphs have become the subject of intense study. We will not describe in detail the history of the development of the theory of quantum graphs, but refer to works [1, 2]. In this article, we will study the Weyl asymptotics of resonances for the Dirac operator on a quantum graph with Kirchhoff coupling conditions at the vertices.

As for the Weyl asymptotics of resonances, almost all results were obtained for the Schrödinger operator acting on the edges of a quantum graph. For example, E. B. Davies and A. Pushnitski in prior research [3] obtained results for a quantum graph, on the edges of which the Schrödinger operator acts, and Kirchhoff constraints are used as the connection conditions at the vertices. Earlier, a similar problem with connection conditions at vertices of a general type was also investigated, the results can be seen, for example, in the articles [4, 5]. In addition to the above, results were also obtained by adding a magnetic field [6] to the system. We would like to obtain similar results for the Dirac operator acting on the edges of a quantum graph.

Resonances have attracted great attention over time. There are a number of works concerning the problem of resonances, particularly the completeness of resonance states which is related to the resonance asymptotics (see, e.g., [7–17]). The purpose of this paper is to investigate the asymptotics of the resonances of the Dirac operator on a quantum graph. The Dirac operator D at edge e has the domain $W_2^1(e) \otimes \mathbb{C}^2$, $W_2^1(e)$ is the Sobolev space. At j -th edge, it acts as follows:

$$D_j = -i \frac{d}{dx} \otimes \sigma_1 + a_j \otimes \sigma_3, \quad (1)$$

where $\sigma_1 = \begin{pmatrix} 0 & 1 \\ 1 & 0 \end{pmatrix}$, $\sigma_3 = \begin{pmatrix} 1 & 0 \\ 0 & -1 \end{pmatrix}$, $a_j \in \mathbb{R}$ is some constant, specific for each edge. As the conditions for the connection at the vertices, we will use the assumption of the continuity of the function f (1) and the Kirchhoff coupling conditions:

$$\sum_j \partial f_{e_j}(V) = 0, \quad (2)$$

where $\partial f_{e_j}(V) = f'_{e_j}(0)$ if the vertex V is the beginning of the edge e_j , and $\partial f_{e_j}(V) = -f'_{e_j}(\rho(e_j))$ if the vertex V is the end of the edge e_j and $\rho(e_j)$ is edge length e_j .

The main result about the asymptotics of resonances will be given for the function $N(R, F)$, which calculates the number of zeros of the function $F(k)$, taking into account their multiplicity, not exceeding the parameter R :

$$N(R, F) = \{\#k : F(k) = 0 \text{ and } |k| < R\}, \quad (3)$$

where the form of the function F will be described below.

2. Preliminary

As mentioned previously, we will consider a quantum graph consisting of the so-called inner and outer parts. The rigorous mathematical definitions for the inside and outside are taken from [3] and provided below.

Definition 2.1. An edge $e \in G$ is internal if it has finite length. Other-wise, the edge $e \in G$ is external.

Definition 2.2. A vertex $v \in G$ is interior if all edges outgoing from it are interior. Otherwise, the vertex $v \in G$ is external.

Definition 2.3. The interior of the quantum graph G is the quantum graph G_0 , which contains all the interior edges of the graph G and the vertices that are their ends.

Definition 2.4. The volume of the inner quantum graph is equal to the sum of the lengths of all inner edges.

It will be shown that the topological structure of a quantum graph affects the form of the asymptotics of resonances. In studying the asymptotics of resonances in a similar problem with the Schrödinger operator acting on the edges, the so-called balanced vertices play an important role. If the Dirac operator acts on the edges, then the balanced vertices also play an important role.

Definition 2.5. An outer vertex $v \in G$ is balanced if the number of inner and outer edges going out from it is equal. Otherwise, the vertex $v \in G$ is unbalanced.

Let us study in more detail the form of the system of differential equations (1) and coupling equations at the vertices (2). On each interior edge, the solution to the differential equation (1) is the following vector-function:

$$y_j(x) = b_j e^{i(\lambda - a_j)x} + c_j e^{-i(\lambda - a_j)x}, \quad (4)$$

and on each outer edge the solution (1) is the following function:

$$y_j(x) = d_j e^{i(\lambda - a_j)x}. \quad (5)$$

Strictly speaking, on the outer edge, the solution (1) has the form $y_j(x) = d_j e^{i(\lambda - a_j)x} + \tilde{d}_j e^{-i(\lambda - a_j)x}$, but within the framework of this problem, we assume that the boundary conditions at infinity of the outer edge are such that $\tilde{d}_j = 0$ for any outside edge.

When describing the formulation of the problem, we used the coupling conditions at the vertices described by the equations (2). The system of coupling conditions at the vertices can be written in matrix form:

$$A \cdot \varphi_A = 0, \quad (6)$$

where φ_A is a vector whose coordinates are the variables b_j, c_j, d_j and the values of the function f at the vertices are $f(V_j)$.

It is easy to see that the matrix A is determined ambiguously for a fixed quantum graph, namely, it is possible to change the order of the variables $b_j, c_j, d_j, f(V_j)$, as well as to change the order of the constraint equations at the vertices. The following function will be taken as the function F , which will be used to study the asymptotics of resonances (3):

$$F(\lambda) = \det(A), \quad (7)$$

where the matrix A can be any matrix describing the conditions of communication at the vertices of a quantum graph (6). This definition is correct, since the function is the determinant of the invariant up to a sign with respect to the permutation of rows and columns. In what follows, as a matrix A , it is more convenient to use the matrices A^+, A^- :

$$\begin{aligned} A^+ \cdot \varphi^+ &= 0, \\ A^- \cdot \varphi^- &= 0. \end{aligned} \quad (8)$$

In order to describe the form of the vectors φ^\pm and matrices A^\pm , we introduce auxiliary notation. Consider some vertex V_i . Suppose that it contains p interior edges e_{ij} , the solutions of which are characterized by the coefficients b_{ij}, c_{ij} (4). Suppose q of the inner edges e_{ik} emerges from the vertex, the solutions of which are characterized by the coefficients $\tilde{b}_{ik}, \tilde{c}_{ik}$ (4). And finally, suppose that r of outer edges e_{il} emerge from the vertex V_i , the solutions of which are characterized by the coefficients d_{il} (5). Then the vectors φ^\pm are equal to the following:

$$\varphi^\pm = (V_1^\pm, \dots, V_N^\pm)^T, \quad (9)$$

where N is the number of vertices in a quantum graph and V_i^\pm denotes the following:

$$\begin{aligned} V_i^+ &= (b_{i1}, \dots, b_{ip}, \tilde{c}_{i1}, \dots, \tilde{c}_{iq}, d_{i1}, \dots, d_{ir}, f(V_i)), \\ V_i^- &= (c_{i1}, \dots, c_{ip}, \tilde{b}_{i1}, \dots, \tilde{b}_{iq}, d_{i1}, \dots, d_{ir}, f(V_i)). \end{aligned} \quad (10)$$

Thus, we have decided on the order of the columns of the matrices A^\pm , it remains to choose a convenient order of the rows. The rows of the matrix are arranged as follows. Using the notation introduced above, suppose that the vertex V_i has the number of internal edges that enter it, is equal to p_i , the number of internal edges that go out of it is q_i , the number of external edges that go out of it, is equal to r_i . Then the first $p_1 + q_1 + r_1$ rows of the matrices A^\pm describe the equations characterizing the continuity of the function f at the vertex V_1 . The next line describes the Kirchhoff constraint equation at the vertex V_1 . In a similar way, $p_2 + q_2 + r_2 + 1$ lines describe the constraint equations at the vertex V_2 , and so on for all other vertices.

It is worth noting that, depending on the choice of the orientation of the inner edges of the quantum graph, the form of the matrices A , and as a consequence of the matrices A^\pm , will change. In this regard, the question arises whether the orientation of the zeros of the function $F(\lambda)$ will not be affected. It was shown in the [3] article that changing the orientation will not affect the zeros of $F(\lambda)$. And although this was proved for quantum graphs on whose edges the Schrödinger operator acts, we can also use this result, since the general form of the equation (4) coincides with the general form of the solution on the edges for the Schrödinger operator.

When investigating the asymptotics of resonances, we will use a theorem formulated below. A rigorous mathematical proof of this theorem can be found in [5].

Theorem 2.6. *Let $F(k) = \sum_{r=0}^n k^{v_r} a_r(k) e^{ik\sigma_r}$, where $v_r \in \mathbb{R}$, $a_r(k)$ are rational functions of the complex variable k with complex coefficients that do not vanish identically, and $\sigma_r \in \mathbb{R}$, $\sigma_0 < \sigma_1 < \dots < \sigma_n$. Suppose also that v_r are chosen so that $\lim_{k \rightarrow \infty} a_r(k) = \alpha_r$ is finite and non-zero for all r . There exists a compact set $\Omega \subset \mathbb{C}$, real numbers m_r and positive K_r , $r = 1, \dots, n$ such that the zeros of $F(k)$ outside Σ lie in one of n logarithmic strips, each one bounded between the curves $-Imk + m_r \log |k| = \pm K_r$. The counting function behaves in the limit $R \rightarrow \infty$ as:*

$$N(R, F) = \frac{\sigma_n - \sigma_0}{\pi} R + O(1). \tag{11}$$

3. Results

Before proceeding to the main results, we prove some auxiliary statements.

Lemma 3.1. *The following relation takes place:*

$$\begin{vmatrix} a_1 & 0 & \dots & 0 & -1 \\ 0 & a_2 & \dots & 0 & -1 \\ \dots & \dots & \ddots & \dots & \vdots \\ 0 & \dots & 0 & a_n & -1 \\ b_1 & b_2 & \dots & b_n & 0 \end{vmatrix} = \prod_{i=1}^n a_i \cdot \sum_{j=1}^n \frac{b_j}{a_j}. \tag{12}$$

To prove this, it is sufficient to add all $(j-)$ th columns multiplied by $\frac{1}{a_j}$ to the last column. As a result, one obtains the triangular determinant.

As you can see from the theorem 2.6, the coefficients before e in various powers of the function $F(\lambda)$ are of particular interest. For further convenience, we introduce several auxiliary variables:

$$\begin{aligned} e^+ &= \prod_{j=1}^M z_j, \\ e^- &= \prod_{j=1}^M z_j^{-1}, \\ z_j &= e^{i(\lambda - a_j)\rho(e_j)}, \end{aligned} \tag{13}$$

where $\rho(e_j)$ is the length of the edge e_j , M is the number of interior edges in the quantum graph. Next, we will calculate the coefficient in front of e^\pm of the function $F(\lambda)$.

Lemma 3.2. *The coefficient c^+ before e^+ of the function $F(\lambda) = \det(A^+)$ is as follows:*

$$\begin{aligned} c^+ &= \prod_{i=1}^N c_{V_i}, \\ c_{V_i} &= \sum_{V_i \in e_j} a_j - \sum_{V_i \in e_k} a_k + \lambda \cdot l, \end{aligned} \tag{14}$$

where e_j are inner edges, e_k are outer edges, l is a number equal to the difference between the number of outer and inner edges containing the vertex V_i .

Proof. According to the choice of the order of rows and columns for the matrix A^+ , it has the following form:

$$A^+ = \begin{pmatrix} \tilde{V}_1 & \cdots & \cdots & \cdots \\ \cdots & \tilde{V}_2 & \cdots & \cdots \\ \vdots & \vdots & \ddots & \vdots \\ \cdots & \cdots & \cdots & \tilde{V}_N \end{pmatrix}, \tag{15}$$

where the blocks \tilde{V}_i characterize the vertex V_i , have the size $(p_i + q_i + r_i + 1) \times (p_i + q_i + r_i + 1)$, where the designations p_i, q_i, r_i are taken from the description of the construction of the matrix A^+ , and contain the elements $z_j = e^{i(\lambda - a_j)\rho(e_j)}$. Moreover, by the construction of the matrix A^+ , the elements of z_j are contained only in the blocks \tilde{V}_j . Then, it is easy to see that the coefficient before e^+ in $\det(A^+)$ is the same as the coefficients before e^+ of the function F_V , which is equal to the following:

$$F_V = \prod_{i=1}^N \det \tilde{V}_i. \tag{16}$$

Recalling the description of the matrix A^+ , as well as the system of differential equations (4), (5) with matching conditions at the vertices (2), let us study in more detail the form of the block \tilde{V}_i :

$$\begin{pmatrix} z_{i1} & 0 & \cdots & \cdots & \cdots & \cdots & \cdots & \cdots & 0 & -1 \\ \cdots & \ddots & \cdots \\ \cdots & \cdots & z_{ip} & 0 & \cdots & \cdots & \cdots & \cdots & 0 & -1 \\ 0 & \cdots & 0 & 1 & 0 & \cdots & \cdots & \cdots & 0 & -1 \\ \cdots & \cdots & \cdots & \cdots & \ddots & \cdots & \cdots & \cdots & \cdots & \cdots \\ 0 & \cdots & \cdots & \cdots & 0 & 1 & 0 & \cdots & 0 & -1 \\ 0 & \cdots & \cdots & \cdots & \cdots & 0 & 1 & \cdots & \cdots & -1 \\ \cdots & \ddots & \cdots & \cdots \\ 0 & \cdots & \cdots & \cdots & \cdots & \cdots & \cdots & 0 & 1 & -1 \\ -z_{i1}\chi_{i1} & \cdots & -z_{ip}\chi_{ip} & -\chi_{j1} & \cdots & -\chi_{jq} & \chi_{k1} & \cdots & \chi_{kr} & 0 \end{pmatrix}, \tag{17}$$

where $\chi_{ij} = \lambda - a_{ij}$, the vertex V_i has p inner edges entering it, q inner edges leaving it, and r outer edges leaving it. Using lemma 3.1, we calculate $\det(\tilde{V}_i)$:

$$\begin{aligned} \det(\tilde{V}_i) &= \prod_{l=1}^p z_{il} \cdot \left(\sum_{l=1}^p (-\lambda + a_{il}) + \sum_{m=1}^q (-\lambda + a_{jm}) + \sum_{n=1}^r (\lambda - a_{kn}) \right) = \\ &= \prod_{l=1}^p z_{il} \cdot \left(\sum_{e_j \in G_0} a_j - \sum_{e_k \in G \setminus G_0} a_k + \lambda \cdot (r - p - q) \right) = \prod_{l=1}^p z_{il} \cdot c_{V_i}. \end{aligned}$$

After calculating $\det(\tilde{V}_i)$, it is easy to determine what F_V is equal to:

$$F_V = \prod_{i=1}^M z_i \cdot c_V, \tag{18}$$

where M is equal to the number of interior edges. From 18 it can be seen that $c^+ = \prod_{i=1}^N c_V$. Thus, the lemma is proved.

Note. It is worth mentioning similar coefficients for e^- . If solutions of the form $\tilde{d}_i e^{-i(\lambda - a_i)x}$ are considered on the outer edges, the coefficients will be similar to the results of the lemma 3.2 up to sign. In the case of considering solutions of the form $d_i e^{i(\lambda - a_i)x}$ on the outer edges, the coefficients will be similar to the results of the lemma 3.2 with the only difference that the sums over the outer and inner edges will not be subtracted, but added.

Now let us formulate a theorem, which is the main result of this article.

Theorem 3.3. Consider a quantum graph consisting of a compact interior and a finite number of edges of infinite length that are attached to the interior of the quantum graph. The edges of this quantum graph will be acted upon by the Dirac operator I . As the connection conditions at the vertices of the quantum graph, we will use the Kirchhoff connection conditions and the assumption of the continuity of the solution function on the quantum graph. Then the asymptotics of the resonance counting function as $R \rightarrow \infty$ is of the form:

$$N(R, F) = \frac{2W}{\pi}R + O(1), \quad (19)$$

where the variable W satisfies the following inequalities:

$$0 \leq W \leq V = \sum_{j=1}^N l_j. \quad (20)$$

It should be noted that $W < V$ is equivalent to the existence of an external balanced vertex V_i , in which the following relation holds:

$$\sum_{V_i \in e_j} a_j = \sum_{V_i \in e_k} a_k. \quad (21)$$

Proof. To prove the statement (20), we use the theorem 2.6. Then, using the notation from this theorem 2.6 and using the results of the lemma 3.2, we obtain $-V \leq \sigma_0 \leq 0, 0 \leq \sigma_n \leq V$, where $V = \sum_{j=1}^N l_j$. Consequently $0 \leq \sigma_n - \sigma_0 \leq 2V$ and by theorem 2.6 $N(R, F) = \frac{2W}{\pi}R + O(1)$, where $0 \leq W \leq V$, as required in the relation (20).

To prove the relation (21), note that for the inequality $W < V$ to hold, it is necessary and sufficient that at least one of the two inequalities $-V < \sigma_0$ or $\sigma_n < V$. That is, the coefficient before e^+ or e^- must be equal to 0. In lemma 3.2 the coefficient before e^+ of $F(\lambda)$ was determined. It is easy to see that the coefficient before e^+ is 0 if and only if there is an external balanced vertex for which the relation (21) holds.

Thus, the theorem is proved.

References

- [1] Berkolaiko G., Kuchment P. Introduction to quantum graphs. *American Mathematical Soc.*, 2013.
- [2] Exner P. et al. (ed.). *Analysis on Graphs and Its Applications: Isaac Newton Institute for Mathematical Sciences*, Cambridge, UK, January 8–June 29, 2007. American Mathematical Soc., 2008.
- [3] Davies E.B., Pushnitski A. Non-Weyl resonance asymptotics for quantum graphs. *Analysis and PDE*, 2011, **4**, P. 729–756.
- [4] Exner P., Lipovský J. Resonances from perturbations of quantum graphs with rationally related edges. *Journal of Physics A: Mathematical and Theoretical*, 2010, **43**, P. 105301.
- [5] Davies E.B., Exner P., Lipovsky J. Non-Weyl asymptotics for quantum graphs with general coupling conditions. *J. Phys. A: Math. Theor.*, 2010, **43**, P. 474013.
- [6] Exner P., Lipovsky J. Non-Weyl resonance asymptotics for quantum graphs in a magnetic field. *Phys. Lett. A*, 2011, **375**, P. 805–807.
- [7] Aslanyan A., Parnovski L., Vassiliev D. Complex resonances in acoustic waveguides. *Q. J. Mech. Appl. Math.*, 2000, **53**(3), P. 429–447.
- [8] Blinova I.V., Popov I.Y. Quantum graph with the Dirac operator and resonance states completeness. *Operator Theory: Adv. Appl.*, 2018, **268**, P. 111–124.
- [9] Christiansen T. Some upper bounds on the number of resonances for manifolds with infinite cylindrical ends. *Ann. Henri Poincare*, 2002, **3**, P. 895–920.
- [10] Edward J. On the resonances of the Laplacian on waveguides. *J. Math. Anal. Appl.*, 2002, **272**, P. 89–116.
- [11] Gerasimov D.A., Popov I.Y. Completeness of resonance states for quantum graph with two semi-infinite edges. *Compl. Var. Elliptic Eq.*, 2018, **63**, P. 996–1010.
- [12] Popov I.Y., Blinova I.V. Quantum graph in a magnetic field and resonance states completeness. *Operator Theory: Adv. Appl.*, 2020, **276**, P. 540–553.
- [13] Sjöstrand J., Zworski M. Complex scaling and the distribution of scattering poles. *J. Amer. Math. Soc.*, 1991, **4**, P. 729–769.
- [14] Blinova I.V., Popov I.Y., Popov A.I. Resonance states completeness for relativistic particle on a sphere with two semi-infinite lines attached. *Journal of King Saud University - Science*, 2020, **32**(1), P. 836–841.
- [15] Popov I.Y., Popov A.I. Quantum Dot with Attached Wires: Resonant States Completeness. *Reports on Mathematical Physics*, 2017, **80**(1), P. 1–10.
- [16] Popov I., Gerasimov D., Blinova I., Popov A. Incompleteness of resonance states for quantum ring with two semi-infinite edges. *Analysis and Mathematical Physics*, 2019, **9**(3), P. 1287–1302.
- [17] Duclos P., Exner P., Meller B. Open quantum dots: Resonances from perturbed symmetry and bound states in strong magnetic fields. *Rep. Math. Phys.*, 2001, **47**(2), P. 253–267.

Influence of a magnetic field on the propagation of ultrashort optical pulses in anisotropic optical media with carbon nanotubes

N. N. Konobeeva, M. B. Belonenko

Volgograd State University, University avenue, 100, Volgograd, 400062, Russia

yana_nn@volsu.ru, belonenko@volsu.ru

PACS 78.20.Fm, 73.63.Fg

DOI 10.17586/2220-8054-2021-12-4-430-435

In this paper, we investigate the interaction of ultrashort pulses with anisotropic optical media with carbon nanotubes in the presence of a magnetic field. Based on Maxwell's equations, taking into account the second polarization of the light wave, an effective equation for the vector potential of the electromagnetic field is obtained. The dependence of the pulse shape on the magnetic field is revealed, and the Fourier spectra of the pulse are analyzed.

Keywords: magnetic field, anisotropic media, carbon nanotubes.

Received: 2 June 2021

Revised: 30 June 2021

1. Introduction

To solve many practical problems, it is necessary to form a powerful electromagnetic pulse with specified characteristics. In this case, an important issue is the study of the pulse's behavior in a medium under the action of the strong external fields [1]. Note that the magnetic field can be used to control the properties of optical pulses, which is confirmed by the Faraday effect and the magneto-optical Kerr effect [2]. In this context, media containing carbon nanotubes with their stabilizing effect have a high potential for application in the development of optoelectronic devices [3]. We have studied the effect of external constant magnetic and alternating electric fields on the ultrashort pulse propagation in CNTs [4, 5], but without taking into account the anisotropy of the medium, which can have a significant effect on the character of pulse propagation. Therefore, the problem of the correct accounting the optically anisotropic properties of a nonlinear medium naturally arises. These properties can lead to various interesting effects, for example, the Zakharov–Benny resonance [6].

Since the works [7, 8], the stable propagation of optical pulses in the CNT array has been shown repeatedly. As an example, we cite recent papers on this topic [9, 10]. In previous studies, we took into account only one (linear) polarization of light, when the nanotube axis was parallel to the electric field vector. Here, we take into account the second polarization, as well as different values of the velocity components. In this work, we study the dynamics of a three-dimensional ultrashort optical pulse in a dielectric anisotropic crystal with CNTs under the action of a constant magnetic field.

2. Model and basic equations

We consider an array of carbon nanotubes immersed in an anisotropic dielectric medium (crystal). The OX, OY and OZ axes are aligned with the crystal axes. The CNT axis lies in the XOY plane and makes an angle α with the OX axis (Fig. 1). We investigate the propagation of three-dimensional ultrashort electromagnetic pulses in the array of zigzag carbon nanotubes. We consider only semiconductor carbon nanotubes to avoid the effects associated with intraband absorption. The magnetic field H is directed along the CNT axis. Under the action of the electric field E directed along the OX axis, a current begins to flow in the CNTs and a field appears along the other axis, the OY axis. Note, in this paper, we consider a positive crystal [11]. There are several ways to obtain well-oriented nanotubes in a dielectric matrix. It is important that the distance between CNTs is much greater than the distances between atoms. For example, one of the methods is induced anisotropy using external fields due to the Kerr effect. Moreover, we consider the pulse field to be much larger than the external field responsible for the anisotropy. Another method is media of polar molecules. It should be noted that our approach is a generalization, but it is also suitable for an isotropic medium.

The vector potential has the form: $\mathbf{A} = (A_x(x, y, z, t), A_y(x, y, z, t), 0)$, the electric current density is: $\mathbf{j} = (j_x(x, y, z, t), j_y(x, y, z, t), 0)$.

We write the three-dimensional wave equation for the electric field component directed at an angle to the CNT axis (taking into account the calibration: $\mathbf{E} = -\partial A/c\partial t$):

$$\frac{1}{c^2} \frac{\partial^2 A}{\partial t^2} = \frac{\partial^2 A}{\partial x^2} + \frac{\partial^2 A}{\partial y^2} + \frac{\partial^2 A}{\partial z^2} + \frac{4\pi}{c} j(A), \quad (1)$$

where c is the light velocity.

Next, we go over to a cylindrical coordinate system and rewrite equation (1) into two components of the vector potential:

$$\begin{aligned} \frac{1}{v_0^2} \frac{\partial^2 A_x}{\partial t^2} &= \frac{1}{r} \frac{\partial}{\partial r} \left(r \frac{\partial A_x}{\partial r} \right) + \frac{\partial^2 A_x}{\partial z^2} + \frac{1}{r^2} \frac{\partial^2 A_x}{\partial \varphi^2} + \frac{4\pi}{c} j_x(A_x, A_y), \\ \frac{1}{v_e^2} \frac{\partial^2 A_y}{\partial t^2} &= \frac{1}{r} \frac{\partial}{\partial r} \left(r \frac{\partial A_y}{\partial r} \right) + \frac{\partial^2 A_y}{\partial z^2} + \frac{1}{r^2} \frac{\partial^2 A_y}{\partial \varphi^2} + \frac{4\pi}{c} j_y(A_x, A_y), \end{aligned} \quad (2)$$

$$v_0 = c/n_x, \quad v_e = c/n_y,$$

r, z, φ are the cylindrical coordinates; n_x, n_y are the refractive indices for x polarization and for y polarization respectively, v_0 is the velocity of an ordinary ray, v_e is the velocity of an extraordinary ray. Earlier in [12, 13], we have shown that there is a damping of azimuthal harmonics during the propagation of an electromagnetic wave in an array of CNTs. Therefore, we neglect the derivative with respect to the angle.

The standard expression for the current density along the CNTs axis can be written as [14]:

$$j = 2e \sum_{s=1}^m \int v_s(p) \cdot f(p, s) dp, \quad (3)$$

where e is the electron charge, hereinafter $\hbar = 1$, the integration is carried out over the first Brillouin zone, p is the projection of the quasi-momentum of the conduction electron along the axis of the nanotube, $v_s(p) = \partial \varepsilon_s(p)/\partial p$ is the electron velocity, $f(p, s)$ is the Fermi distribution, $\varepsilon_s(p)$ is the dispersion law, which describes the properties of electrons of CNTs and takes into account a magnetic field [15]:

$$\varepsilon_s(p) = \pm \gamma_0 \sqrt{1 + 4 \cos(ap_z) \cos\left(\frac{\pi}{n} \left(s + \frac{\Phi}{\Phi_0}\right)\right) + 4 \cos^2\left(\frac{\pi}{n} \left(s + \frac{\Phi}{\Phi_0}\right)\right)}, \quad (4)$$

where $s = 1, 2, \dots, n$, CNTs type is $(n, 0)$, $\gamma_0 \approx 2.7$ eV, $a = 3b/2\hbar$, b is the distance between adjacent carbon atoms, Φ is the magnetic flux through the cross section of CNT, $\Phi_0 = h/e \approx 2.068 \cdot 10^{-15}$ Wb is the magnetic flux quantum [16]. Because the magnetic field is codirectional to the nanotube axis, then $\Phi = B \cdot S$, where S is the CNT cross-sectional area, B is the modulus of the magnetic induction vector.

Based on calculations in [14], we assume that the derivative with respect to the angle is zero. In this case, we obtain a system of the effective equations for the components of the vector potential, taking into account the transition to the cylindrical coordinate system:

$$\begin{cases} \frac{1}{r} \frac{\partial}{\partial r} \left(r \frac{\partial A_x}{\partial r} \right) + \frac{\partial^2 A_x}{\partial z^2} - \frac{1}{v_0^2} \frac{\partial^2 A_x}{\partial t^2} + \frac{4en_0\gamma_0 a \cdot \cos \alpha}{c} \sum_{q=1}^{\infty} b_q \sin(\tilde{A}) = 0, \\ \frac{1}{r} \frac{\partial}{\partial r} \left(r \frac{\partial A_y}{\partial r} \right) + \frac{\partial^2 A_y}{\partial z^2} - \frac{1}{v_e^2} \frac{\partial^2 A_y}{\partial t^2} + \frac{4en_0\gamma_0 a \cdot \sin \alpha}{c} \sum_{q=1}^{\infty} b_q \sin(\tilde{A}) = 0, \\ \tilde{A} = \frac{aeq(A_x \cos \alpha + A_y \sin \alpha)}{c}, \end{cases} \quad (5)$$

n_0 is the electron concentration:

$$b_q = \sum_s a_{sq} \int_{ZB} dp \cdot \cos(pq) \frac{\exp(-\varepsilon_s(p)/k_B T)}{1 + \exp(-\varepsilon_s(p)/k_B T)}, \quad (6)$$

k_B is the Boltzmann constant, T is the temperature, a_{sq} is the coefficients in the expansion of the electron dispersion law (4) as a Fourier series:

$$\varepsilon_s(p) = \frac{1}{2\pi} \sum_{s=1}^m \sum_{q=1}^{\infty} a_{sq} \cos(pq), \quad (7)$$

$$a_{sq} = \int_{ZB} dp \cdot \cos(pq) \varepsilon_s(p). \quad (8)$$

Note, due to a decrease in the coefficients b_q (6), with an increase in q , we can restrict ourselves to the first 15 nonvanishing terms [17].

The system of equations (5) is solved numerically. We use an explicit finite-difference three-layer scheme of the “cross” type with the following initial conditions:

$$\begin{aligned} A_x &= Q \cdot \exp\left(-\left(\frac{z}{l_z}\right)^2\right) \exp\left(-\frac{x^2 + y^2}{l_r^2}\right), \\ \frac{d}{dt}A_x &= \frac{2v_0Q}{l_z^2} \cdot \exp\left(-\left(\frac{z}{l_z}\right)^2\right) \exp\left(-\frac{x^2 + y^2}{l_r^2}\right), \\ A_y &= 0, \quad \frac{d}{dt}A_y = 0 \end{aligned} \quad (9)$$

where Q is the initial amplitude of the electromagnetic pulse, l_z , l_r determine the pulse width along the z and r directions, respectively, z_0 is the initial coordinate of the pulse center along the axis z .

3. Results and discussion

Further, we make numerical calculations at the following system parameters: CNT of type is (80, 0), coefficients b_q , are calculated at the temperature $T = 293$ K [18]. It should be noted some points of our model. The substrate field is not taken into account. Distances between adjacent carbon nanotubes are much larger than their diameter. The magnetic field is directed strictly along the axis of the nanotubes. We consider pulses from the near-IR, with a duration of 1 period, and a width of 2 wavelengths. Examples of the pulse producing, see in [19, 20].

The evolution of the electromagnetic field during its propagation over the sample in the presence of a constant magnetic field is shown in Fig. 2. We presented the field intensity I , which is determined according to the formula:

$$I = \frac{1}{c^2} \left(\frac{\partial A_x}{\partial t} \right)^2. \quad (10)$$

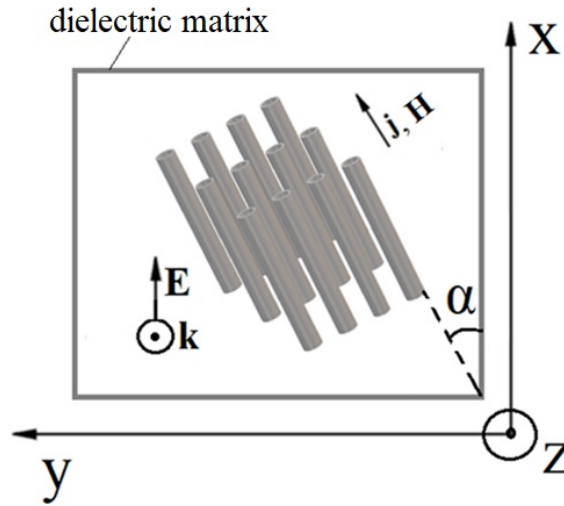


FIG. 1. The geometry of the problem

Figure 2 shows that dispersive spreading of the pulse is observed. Despite this, the pulse is localized in the propagation direction. The dispersion spreading of the pulse is essential here and it is associated with the fact that both field components (E_x and E_y) are taken into account in the problem. This is the most important difference between this problem and the problems considered earlier.

The dependence of the pulse width l_z (which is defined as the distance at which its intensity drops by half of the intensity at the center) is shown in Fig. 3.

The essential point here is that the pulse component that was initially excited is broadened least of all. It can be associated with the fact that nonlinear effects act there from the very beginning, which compensate for the spreading.

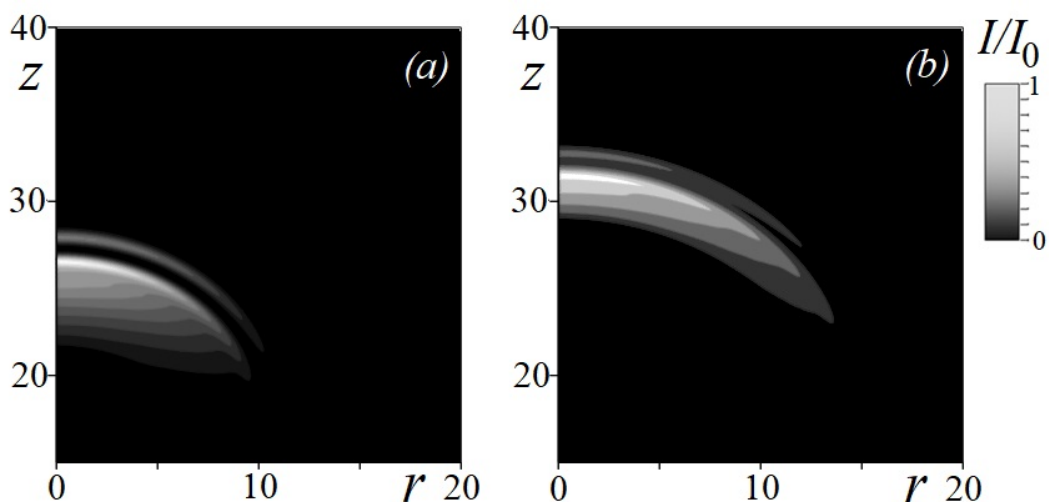


FIG. 2. Evolution of the pulse: a) $t = 6.5$; b) $t = 9.5$. The nondimensional unit along the r and z axes corresponds to $2 \cdot 10^{-5}$ m, in time 10^{-14} s. I_0 is the field intensity at $t = 0$.

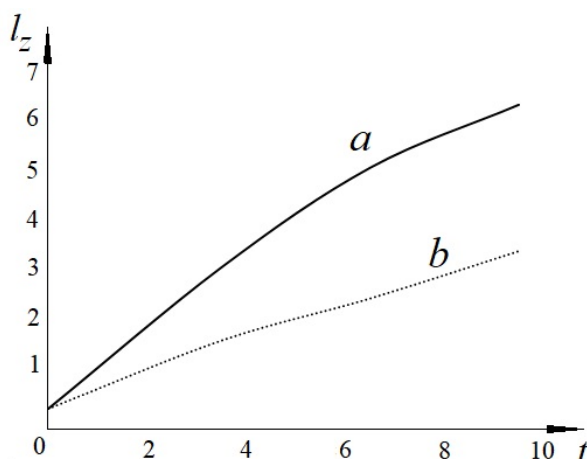


FIG. 3. Dependence of the pulse width on time: a) for the component E_y ; b) for the component E_x . The nondimensional unit along the vertical axis corresponds to $2 \cdot 10^{-5}$ m, in time 10^{-14} s.

At the same time, this dependence explain us why the broadening is much stronger than in previous works, for example [9, 12]. This is due to the presence of the second component of the electric field vector, which makes its own contribution.

The influence of the angle between the electric field E_x with the carbon nanotubes axis on the dynamics of the pulse propagation is shown in Fig. 4.

It can be seen, that the greater the magnetic field, the higher the field intensity for different angles of inclination of the CNT to the crystal axis.

The influence of the magnetic field on the pulse dynamics is presented in Fig. 5.

It follows from Figs. 4 and 5 that the amplitude and shape of the pulse can be controlled both by the angle at which the CNT array is located in the dielectric matrix, and by the magnitude of the magnetic field. It can be seen, that by choosing in a certain way the angle α and the magnitude of the magnetic field, we can control the longitudinal dispersion of the pulse.

Let us analyze the shape of the Fourier spectrum (ω is the angular frequency) of the pulse at a fixed time (Fig. 6).

Figure 6 shows, that for sharp angles, α , between the nanotube axis and the crystal axis, additional peaks appear in the Fourier spectrum. It indicates the generation of additional harmonics. Note, when the magnitude of the constant magnetic field increases, the number of these peaks also increases. By varying the magnitude of the external magnetic

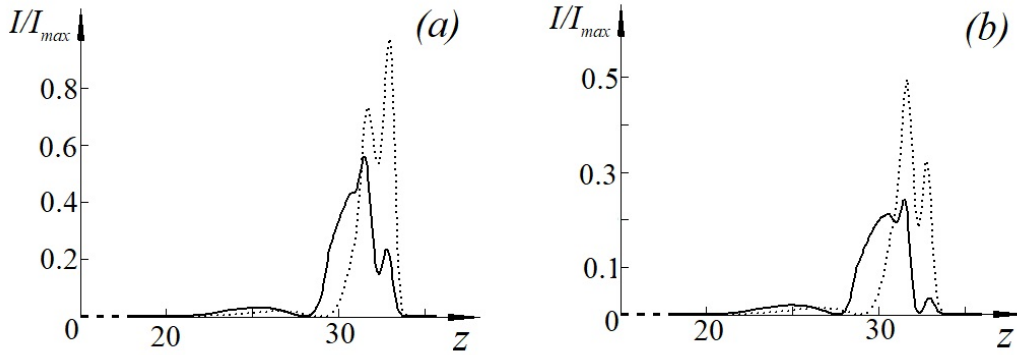


FIG. 4. Dependence of the electric field intensity E_x on the z coordinate for the time instant $t = 9.5$ (slices at $r = 0$): (a) $\alpha = 0.75$ rad; (b) $\alpha = 1.05$ rad. For the dashed line, the magnetic field is 2 times greater than for the solid one. The nondimensional unit along the z axis corresponds to $2 \cdot 10^{-5}$ m, the dimensionless unit on time is 10^{-14} s. I_{\max} is the maximum value of field intensity at $t = 9.5$.

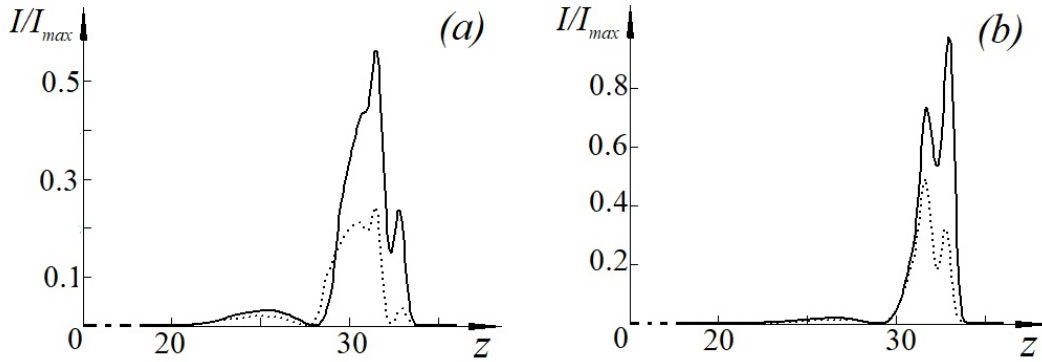


FIG. 5. Dependence of the electric field intensity E_x on the z coordinate for the time instant 9.5 (slices at $r = 0$). For the Fig. (b) the magnetic field is 2 times greater than for (a). The solid line corresponds to $\alpha = 0.75$ rad, the dashed line – $\alpha = 1.05$ rad. The nondimensional unit along the z -axis corresponds to $2 \cdot 10^{-5}$ m, the dimensionless unit on time is 10^{-14} s. I_{\max} is the maximum value of field intensity at $t = 9.5$ (at the following parameters: $\alpha = 0.75$ rad, $\Phi/\Phi_0 = n/2$).

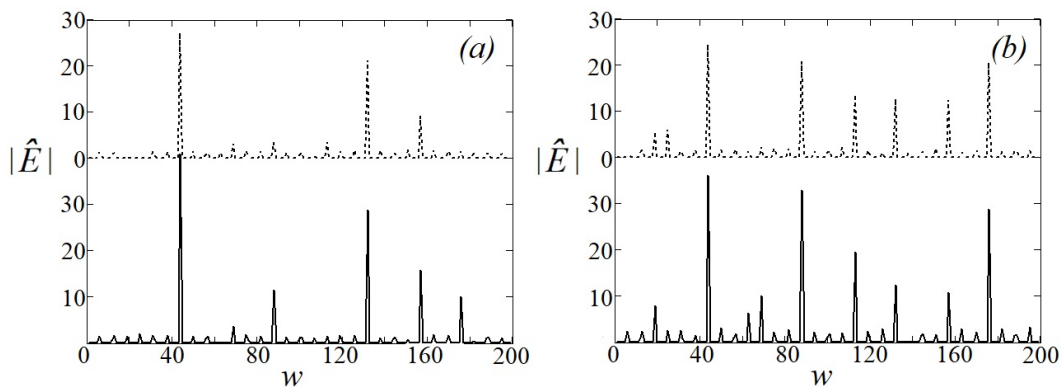


FIG. 6. Absolute values of Fourier spectra at time $t = 9.5 \cdot 10^{-14}$ s for several values of α and the magnetic field. For the Fig. (b) the magnetic field is 2 times greater than for (a). The dashed line corresponds to $\alpha = 1.05$ rad, the solid line corresponds to $\alpha = 0.75$ rad. The unit on the ω axis corresponds to 10^{13} s $^{-1}$, on the axis $|E| = 10^7$ V/m.

field (as well as the angle α), it is possible to achieve the effective generation of the second harmonic, or vice versa, to suppress this generation and make the generation of the third harmonic more efficient. It is also possible to control the generation of higher harmonics and harmonics at intermediate frequencies. This is undoubtedly important for practical applications, since it allows one to make a device on a single crystal for generating harmonics controlled by a magnetic field. We note another application. The value of the magnetic field applied to the sample can be determined from the harmonic output. That is this effect can be useful for optical magnetism sensors.

4. Conclusion

This study reports three key results, which have some practical applications in the harmonic generation:

- (1) A model of propagation of ultrashort optical pulses in an anisotropic optical media with carbon nanotubes in the presence of a magnetic field is proposed.
- (2) The magnitude of the magnetic field makes it possible to change both the amplitude and the shape of the pulse during its propagation over the sample.
- (3) The magnitude of the magnetic field effectively controls the output of optical harmonics.

Acknowledgements

N. N. Konobeeva acknowledges support from the Ministry of Science and Higher Education of the Russian Federation, RF President's Grants Council Grant No. MD-3173.2021.1.2 (agreement 075-15-2021-337 dated 20.04.2021).

References

- [1] Mihalache D. Localized structures in optical and matter-wave media: A selection of recent studies. *Rom. Rep. Phys.*, 2021, **73**, 403.
- [2] Kerr J. On rotation of the plane of polarization by reflection from the pole of a magnet. *Philosophical Magazine*, 1877, **3** (19), P. 321–343.
- [3] Sadykov N.R., Muratov E.T., Pilipenko I.A., Aporoski A.V. Wavefunctions and energy eigenvalues of charge carriers in zigzag carbon nanotubes and in armchair nanoribbons in the vicinity of Dirac point under the influence of longitudinal electric field. *Physica E: Low-Dimensional Systems and Nanostructures*, 2020, **120**, 114071.
- [4] Belonenko M.B., Glazov S.Y., Mescheryakova N.E. Effect of an AC electric field on the conductance of single-wall semiconductor-type carbon nanotubes. *Semiconductors*, 2010, **44** (9), P. 1211–1216.
- [5] Konobeeva N.N., Belonenko M.B. Dynamics of ultimately short electromagnetic pulses in chiral carbon nanotubes in the presence of an external field. *Technical Physics*, 2014, **59**, P. 1749–1752.
- [6] Sazonov S.V., Sobolevskii A.F. Continuous Stokes self-scattering of an optical pulse in a uniaxial crystal in the case of Zakharov—Benney resonance. *Quantum Electronics*, 2005, **35**, P. 1019–1026.
- [7] Belonenko M.B., Lebedev N.G., Popov A.S. Two-dimensional light bullets in an array of carbon nanotubes. *JETP Letters*, 2010, **91**, P. 461–465.
- [8] Leblond H., Mihalache D. Spatiotemporal optical solitons in carbon nanotube arrays. *Phys. Rev. A*, 2012, **86** (4), 043832.
- [9] Fedorov E.G., Zhukov A.V., et al. Propagation of three-dimensional bipolar ultrashort electromagnetic pulses in an inhomogeneous array of carbon nanotubes. *Phys. Rev. A*, 2018, **97** (4), 043814.
- [10] Fedorov E.G., Zhukov A.V., et al. External light control of three-dimensional ultrashort far-infrared pulses in an inhomogeneous array of carbon nanotubes. *Phys. Rev. B*, 2021, **103** (8), 085111.
- [11] Matveev A.N. *Optics*. Mir, Moscow, 1988, 446 p.
- [12] Konobeeva N.N., Fedorov E.G., et al. Stabilization of ultrashort pulses by external pumping in an array of carbon nanotubes subject to piezoelectric effects. *J. Appl. Phys.*, 2019, **126**, 203103.
- [13] Konobeeva N.N., Belonenko M.B. Propagation of three-dimensional extremely short optical pulses in germanene in the presence of an external electric field. *Optics and Spectroscopy*, 2017, **123**, P. 425–429.
- [14] Zhukov A.V., Bouffanais R., Fedorov E.G., Belonenko M.B. Three-dimensional electromagnetic breathers in carbon nanotubes with the field inhomogeneity along their axes. *J. Appl. Phys.*, 2013, **114**, 143106.
- [15] Eletsii A.V. Carbon nanotubes. *Physics-Uspeski*, 1997, **40**, P. 899–924.
- [16] Ovchinnikov A.A., Atrazhev V.V. Magnetic susceptibility of multilayered carbon nanotubes. *Physics of the Solid State*, 1998, **40**, P. 1769–1773.
- [17] Belonenko M.B., Demushkina E.V., Lebedev N.G. Electromagnetic solitons in a system of carbon nanotubes. *J. Rus. Las. Res.*, 2006, **27**, 457.
- [18] Zhukov A.V., Bouffanais R., et al. Collisions of three-dimensional bipolar optical solitons in an array of carbon nanotubes. *Phys. Rev. A*, 2016, **94**, 053823.
- [19] Ferray M., L'Huillier A., et al. Multiple-harmonic conversion of 1064 nm radiation in rare gases. *J. Phys. B: At. Mol. Opt. Phys.*, 1988, **21**, L31.
- [20] Chang Z., Rundquist A., et al. Generation of Coherent Soft X Rays at 2.7 nm Using High Harmonics. *Phys. Rev. Lett.*, 1997, **79**, 2967.

Ti₃C₂T_x thin film as a saturable absorber for passively generating Q-switched pulses in thulium-doped fiber laser cavity

M. A. Buntat¹, A. H. A. Rosol², M. F. M. Rusdi², A. A. Latif¹, M. Yasin³, S. W. Harun²

¹Fakulti Kejuruteraan Elektronik dan Kejuruteraan Komputer, Universiti Teknikal Malaysia Melaka, Hang Tuah Jaya, 76100 Durian Tunggal, Melaka, Malaysia, Malaysia

²Photonics Engineering Laboratory, Department of Electrical Engineering, Faculty of Engineering, University of Malaya, 50603 Kuala Lumpur, Malaysia

³Department of Physics, Faculty of Science and Technology, Airlangga University, Surabaya, Indonesia
yasin@fst.unair.ac.id, swharun@um.edu.my

PACS 42.60.Da, 42.70.Hj, 42.60.-v

DOI 10.17586/2220-8054-2021-12-4-436-441

We demonstrated a Q-switched thulium-doped fiber laser (TDFL) based on MXene Ti₃C₂T_x saturable absorber (SA) as Q-switcher. Ti₃C₂T_x was obtained using selective etching and embedded into polyvinyl alcohol (PVA) film. As the film was added into a TDFL cavity, a stable Q-switched pulse train operating at 1996 nm was produced within a single mode 1552 nm pump power range from 161.8 to 237.1 mW. When the pump power was varied within this range, the repetition rate increased from 19.6 to 33.3 kHz while the pulse width decreases from 6.71 to 3.55 μs. To the best of our knowledge, this is the first report of a Ti₃C₂T_x SA for passively generating Q-switched pulses in the 2 μm wavelength region.

Keywords: MXene Ti₃C₂T_x, Q-switching, thulium doped fiber, energy efficiency.

Received: 1 June 2021

Revised: 27 June 2021

1. Introduction

Mid-infrared light sources operating at around 2 μm have drawn a great deal of interest in recent years due to their potential applications in various areas, including biomedical diagnostic [1], atmospheric gas analysis [2], free-space communication [3], and THz generation [4]. To date, many laser sources have proposed and developed for operation in 2 μm region, including the quantum cascaded based solid-state lasers and thulium or holmium doped fiber lasers. In this regard, fiber-based laser systems are preferable, due to their numerous advantages: they are compact, alignment free, compact, low maintenance cost, and featuring excellent heat dissipation etc.

Thulium doped fiber (TDF) has a broad gain bandwidth, ranging from 1800 nm to 2100 nm, and thus, it offers opportunities for short pulse generation and wide tuneability. For instance, Q-switched TDF lasers (TDFLs) were widely proposed and demonstrated for various industrial and scientific applications, such as LIDAR [5], nonlinear frequency conversion [6] and supercontinuum generation in mid-infrared region [7]. They could be achieved passively by using an external controller such as modulator as Q-switcher to provide variability of laser performance including repetition rate and pulse duration. However, the modulator is a bulky component with complex electronics and thus would be a barrier towards robust and portable systems design. Therefore, the passive technique utilizing physical saturable absorber (SA) is preferable for Q-switching. This technique is more desirable due to its flexible design, inexpensiveness and less complexity.

Many SAs have been reported for use in pulse generation via Q-switching such as semiconductor saturable absorber mirror (SESAM) [8], carbon nanotube (CNT) [9, 10] and graphene [11, 12]. SESAM offers high stability during the high intensity of light but operating in narrow bandwidth regime. Due to this limitation, more research has focused on CNT and graphene, that can be fabricated in lower cost and operated in broad bandwidth regime. Recently, the groups of topological insulators, transition metal dichalcogenide, noble metal nanoparticle [13] and black phosphorus [14] have also been used as a Q-switcher.

Recently, a ternary metal carbide/nitride so-called MXene has also gained interest as a new member for 2D nanomaterial class [15]. It has a general formula of M_{n+1}X_nT_x, where M, X and T is a transition metal, carbon or nitrogen (with $n = 1, 2, 3, \dots$), and face-termination group likes oxygen or fluorine, respectively. MXene can be produced by selectively etching of MAX layer [16, 17]. The MXene has been previously utilized in various photonic and nanoscience applications due to its excellent optical, thermal and physical properties [18]. It has a small band gap size, excellent metallic conductivity, and hydrophilic nature of its surface, which are advantages for many applications. MXene also has an excellent saturable absorption characteristic, which is suitable for photonic diodes [19]. It is also reported that the MXene also exhibits the zero-bandgap structure, which has the potential to be used for the broadband

optical device [20]. Here, we proposed the use of Mxene $Ti_3C_2T_x$ film for realizing Q-switching operation in Thulium-doped fiber laser (TDFL). The Mxene $Ti_3C_2T_x$ obtained by a simple selective etching technique was mixed with polyvinyl alcohol (PVA) solution to fabricate the SA thin film. The film was slot in between two ferrules and inserted into a ring TDFL cavity to function as a Q-switcher.

2. Fabrication and characterization of SA

The MAX Ti_3AlC_2 and hydrofluoric acid were obtained respectively from Shanghai Winfay Industry Ltd and Merck KGaA while the PVA powder was purchased from Sigma Aldrich. We performed selective etching of $Ti_3C_2T_x$ with hydrofluoric acid to fabricate MXene $Ti_3C_2T_x$. The etching process was conducted at room temperature for six hours. Then, we obtained the sample of $Ti_3C_2T_x$ through vacuum-assisted filtration by polyvinyl difluoride filter membrane. It was dried with a vacuum oven at 80 °C for 24 hours for formation of clay. The powder was collected and put into a clean beaker. Next, 20 mg of $Ti_3C_2T_x$ powder was mixed with 10 mg of PVA powder and 40 ml of distilled water. The mixture was then agitated at room temperature for 24 hours. We used the ultrasonic bath for 2 hours to separate the agglomerate of $Ti_3C_2T_x$ particles by cavitation. Consequently, about 5 mL of the $Ti_3C_2T_x$ solution was placed inside a clean petri dish and left for 48 hours to dry. Finally, the dried MXene $Ti_3C_2T_x$ -film was peeled out for use as Q-switcher.

Figures 1(a) and (b) show the actual and FESEM images of the prepared $Ti_3C_2T_x$ PVA film, respectively. The FESEM image reveals that the $Ti_3C_2T_x$ elements are uniformly distributed in the polymer composite. The prepared $Ti_3C_2T_x$ thin film was then cut to a tiny piece and placed onto a fiber ferrule after depositing index-matching gel onto the fiber end as shown in Fig. 1(c). The ferrule was then linked to another clean ferrule via a fiber adaptor to assemble a transmissive type of SA as shown in Fig. 1(d). The nonlinear absorption of the MXene $Ti_3C_2T_x$ film was also characterized by utilizing a twin balance detection approach. It is worthy to note that the saturable intensity, saturable absorption, and non-saturable absorption of the film were measured to be about 20 MW/cm², 4.8 and 3.6 %, respectively.

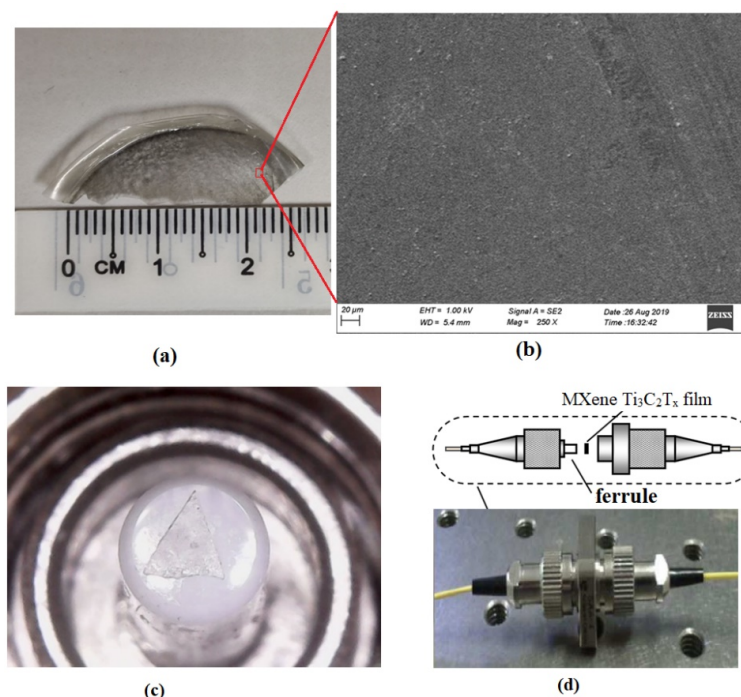


FIG. 1. $Ti_3C_2T_x$ PVA film (a) real image (b) FESEM image (c) the attachment of the film on the fiber ferrule, (b) construction of transmissive type SA

3. Cavity setup for Q-switched TDFL

A ring cavity TDFL was built to examine the performance of the proposed $Ti_3C_2T_x$ based SA as a Q-switcher, as illustrated in Fig. 2. The total cavity length was estimated to be around 13 m. In the experiment, a 5 m thulium-doped fiber (produced by Nufern) with a nominal absorption of about 27 and 9.3 dB/m at 793 and 1180 nm, respectively,

was used as the active medium. The TDF was pumped via wavelength division multiplexer (WDM) by a homemade erbium-ytterbium co-doped fiber laser (EYDFL) operating at 1552 nm up to a maximum power of 1.8 W. 10 % of the oscillating laser was coupled out from the laser cavity by a 10 dB output coupler. 90 % of the oscillating laser was retained within the ring cavity. The spectral and temporal characteristics of the Q-switched laser were analyzed utilizing a mid-infrared spectrometer (Miriad Technologies) and a 7.8 GHz photodetector (ELECTRO-OPTICS TECHNOLOGY, INC., ET-3500F) followed by a 350 MHz digital oscilloscope (GWINSTEK, GDS-3352), respectively. The electrical spectrum of the Q-switched TDFL was measured by a RF spectrum analyzer.

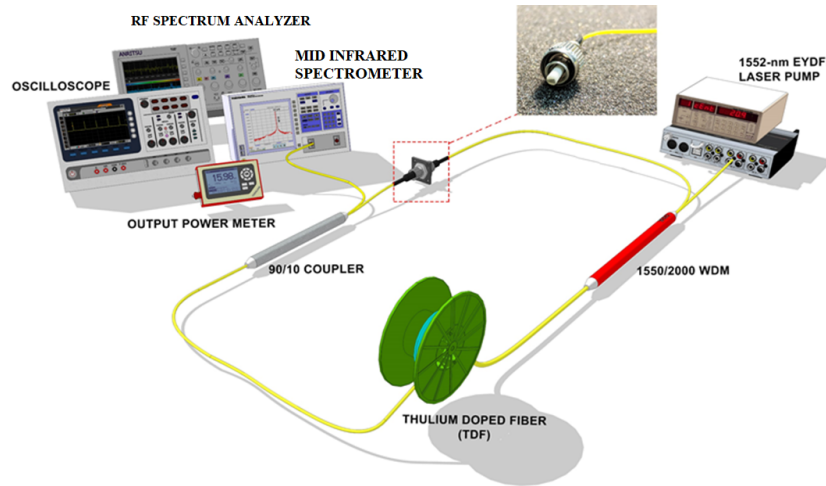


FIG. 2. Configuration of the proposed $\text{Ti}_3\text{C}_2\text{T}_x$ based Q-switched TDFL

4. Result and discussion

To prove that the Q-switching operation here was induced by $\text{Ti}_3\text{C}_2\text{T}_x$ thin film, we intentionally removed the thin film from the TDFL cavity. No Q-switching operation could be observed by the current laser setup even though the pump power was varied across the entire range and the cavity arrangement was manipulated. With the $\text{Ti}_3\text{C}_2\text{T}_x$, the Q-switching behavior was started in the laser as we tuned power of the 1552 nm pump power within a range from 161.8 to 237.1 mW. The characteristics of the Q-switching operation of the fiber laser is summarized in Fig. 3. Fig. 3(a) shows the spectral characteristic of the laser. The laser operated at 1996 nm due to the transition of thulium ions from $^3\text{F}_4$ to $^3\text{H}_6$ energy level as the TDF was pumped at a wavelength of approximately 1552 nm. Fig. 3(b) shows the measured oscilloscope trace within 1000 μs time scale when 1552 nm pump was fixed at the threshold of 161.8 mW. It shows a peak-to-peak period of 51 μs , which can be translated to the repetition rate of 19.6 kHz. It is observed that the pulse period reduces with the increase of pump power, corresponding to typical pulse behavior of Q-switched laser. Fig. 3(c) illustrates the RF spectrum of the Q-switched pulse train at the maximum pump power of 237.1 mW. The fundamental peak was obtained at 33.3 kHz, which corresponds to the repetition rate of the laser at 237.1 mW pump power. The signal to noise ratio (SNR) of the fundamental frequency is measured to be about 31 dB above the noise level, which indicates that stable Q-switched pulses were being produced. The stability of the Q-switching operation by $\text{Ti}_3\text{C}_2\text{T}_x$ film was further confirmed by the observation of many harmonics within a wideband RF spectrum.

The repetition rate and pulse width of the $\text{Ti}_3\text{C}_2\text{T}_x$ Q-switched fiber laser can be tuned by varying the 1552 nm pump power as shown in Fig. 4(a). The pulse repetition rate increases almost linearly from 19.6 kHz at threshold pump of 161.8 to 33.3 kHz at the maximum power of 237.1 mW. On the other hand, the pulse width decreases from 6.71 to 3.55 μs with the increase of pump power within the same range. This phenomenon is due to a strong pumping, which induced gain compression effect; a similar trend has been commonly observed in SA-based Q-switched fiber lasers. The relation between the average output power and pump power is presented in Fig. 4(b). The output power rises with pump and the maximum output power of 3.7 mW was obtained at 237.1 mW pump power. The slope efficiency of the laser was 1.84 %. No residual pump was also observed at 1552 nm, which indicates the pump light was fully absorbed by the active TDF. The pulse energy was calculated to be around 111 nJ at 237.1 mW pump power. The performance of the Q-switched laser could be improved by reducing the total cavity loss by optimizing the SA and gain medium parameters. Finally, a performance comparison between the previously demonstrated Q-switched TDFLs with SAs and our laser is presented in the Table 1. Comparatively, the laser generated in this work has lower pulse energy, which is mainly caused by its small output power. However, it is obvious from the table that our laser exhibited better

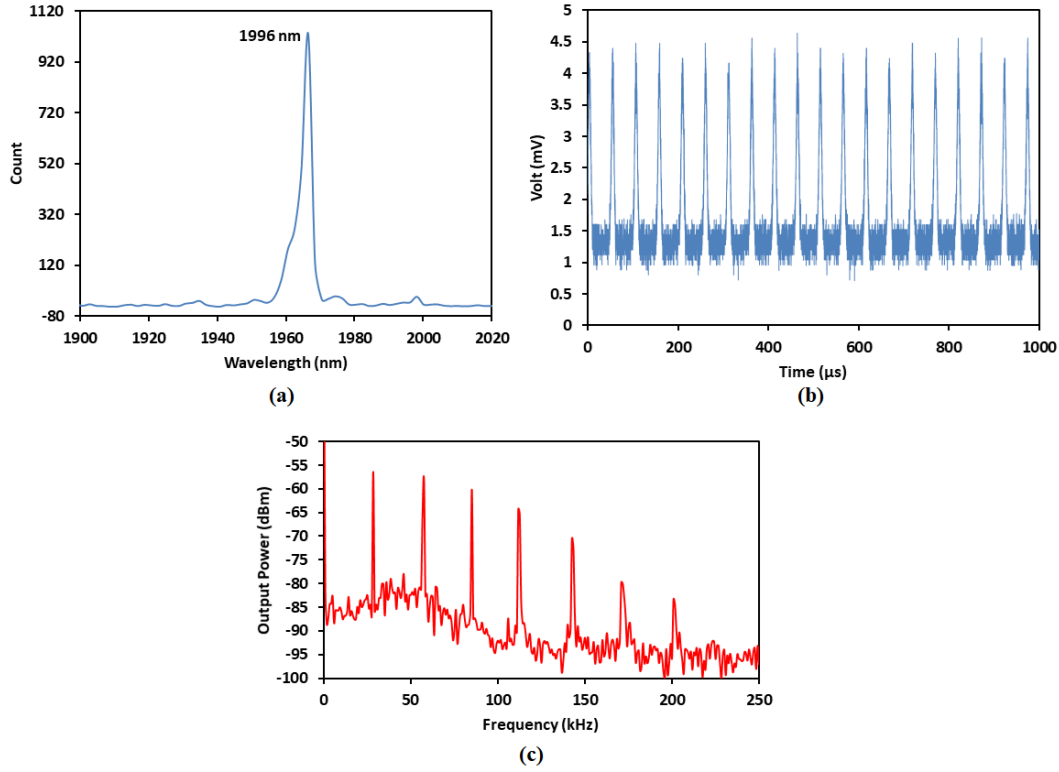


FIG. 3. (a) spectral (b) temporal and (c) frequency characteristics of the Q-switched TDFL with $Ti_3C_2T_x$ SA

TABLE 1. Comparison of proposed laser performance against other works on Q-switched TDFL

SAs	Center Wavelength (nm)	Max. Repetition Rate (kHz)	Minimum Pulse Width (μs)	Max Pulse Energy (nJ)	Reference
CNT	1890	7.2	3.2	—	[21]
Al_2O_3	1950	40.3	5.3	173.5	[22]
Antimony	1947	23.5	4.9	120.1	[23]
Alcohol	1885	66.7	1.5	930	[24]
$Ti_3C_2T_x$	1996	33.3	3.55	111	This work

performance than antimony in terms of repetition rate and pulse width. The proposed laser also operated at the longest wavelength in the thulium region at 1996 nm.

5. Conclusion

We have successfully generated a Q-switched pulses train in TDFL cavity using a newly developed Mxene $Ti_3C_2T_x$ based SA. The $Ti_3C_2T_x$ was prepared from MAX Ti_3AlC_2 based on a selective etching technique. It was then embedded into PVA to form a SA film. By incorporated the SA into TDFL cavity, a Q-switched pulse train operating at 1996 nm was produced with a tuneable repetition rate and pulse width. The repetition rate can be tuned from 19.6 to 33.3 kHz by changing the 1552 nm pump power from 161.8 to 237.1 mW. The pulse width decreases from 6.71 to 3.55 μs with the increase of pump power within the same range. This experiment demonstrated the promising potential of $Ti_3C_2T_x$ material as a kind of SA for pulse generation in 2-micron wavelength region.

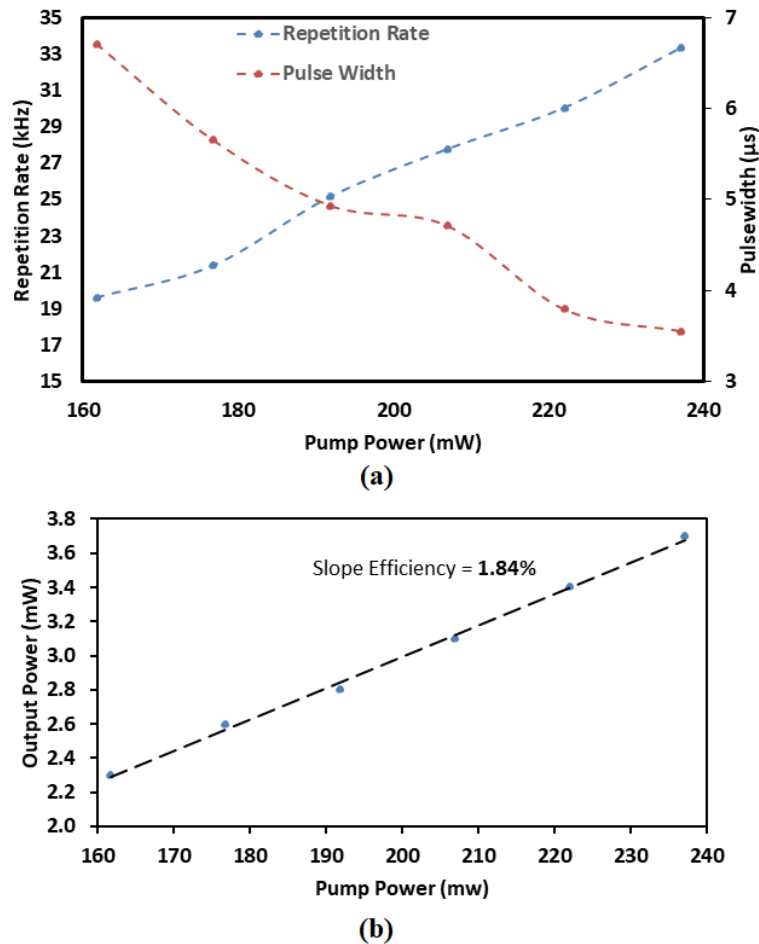


FIG. 4. (a) The repetition rate and pulse width, and (b) average output power performances of the laser at various pump power values

References

- [1] Amini-Nik S., et al. Ultrafast mid-IR laser scalpel: protein signals of the fundamental limits to minimally invasive surgery. *PLoS one*, 2010, **5** (9), e13053.
- [2] Werle P., et al. Near- and mid-infrared laser-optical sensors for gas analysis. *Optics and lasers in engineering*, 2002, **37** (2–3), P. 101–114.
- [3] Li Z., et al. Thulium-doped fiber amplifier for optical communications at $2 \mu\text{m}$. *Optics Express*, 2013, **21** (8), P. 9289–9297.
- [4] Yan D., et al. High-average-power, high-repetition-rate tunable terahertz difference frequency generation with GaSe crystal pumped by $2 \mu\text{m}$ dual-wavelength intracavity KTP optical parametric oscillator. *Photonics Research*, 2017, **5** (2), P. 82–87.
- [5] Henderson S.W., et al. Coherent laser radar at $2 \mu\text{m}$ using solid-state lasers. *IEEE transactions on geoscience and remote sensing*, 1993, **31** (1), P. 4–15.
- [6] Feaver R., Peterson R., Powers P. Longwave-IR optical parametric oscillator in orientation-patterned GaAs pumped by a $2 \mu\text{m}$ Tm, Ho: YLF laser. *Optics express*, 2013, **21** (13), P. 16104–16110.
- [7] Zhang M., et al. Mid-infrared Raman-soliton continuum pumped by a nanotube-mode-locked sub-picosecond Tm-doped MOPFA. *Optics express*, 2013, **21** (20), P. 23261–23271.
- [8] Zhang H., et al. Multi-wavelength dissipative soliton operation of an erbium-doped fiber laser. *Optics express*, 2009, **17** (15), P. 12692–12697.
- [9] Xu X., et al. Passively mode-locking erbium-doped fiber lasers with 0.3 nm Single-Walled Carbon Nanotubes. *Scientific reports*, 2014, **4**, 6761.
- [10] Zhou D.-P., et al. Tunable passively-switched erbium-doped fiber laser with carbon nanotubes as a saturable absorber. *IEEE Photonics Technology Letters*, 2010, **22** (1), P. 9–11.
- [11] Ismail M., et al. A Q-switched erbium-doped fiber laser with a graphene saturable absorber. *Laser Physics Letters*, 2013, **10** (2), 025102.
- [12] Zhang H., et al. Graphene mode locked, wavelength-tunable, dissipative soliton fiber laser. *Applied Physics Letters*, 2010, **96** (11), 111112.
- [13] Ahmad H., et al. 1.5-micron fiber laser passively mode-locked by gold nanoparticles saturable absorber. *Optics Communications*, 2017, **403**, P. 115–120.
- [14] Ismail E., et al. Black phosphorus crystal as a saturable absorber for both a Q-switched and mode-locked erbium-doped fiber laser. *RSC advances*, 2016, **6** (76), P. 72692–72697.
- [15] Naguib M., et al. Two-dimensional nanocrystals produced by exfoliation of Ti_3AlC_2 . *Advanced materials*, 2011, **23** (37), P. 4248–4253.

- [16] Ivanovskii A.L., Enyashin A.N. Graphene-like transition-metal nanocarbides and nanonitrides. *Russian Chemical Reviews*, 2013, **82** (8), P. 735.
- [17] Enyashin A.N., Ivanovskii A.L. Structural and electronic properties and stability of MXenes Ti_2C and Ti_3C_2 functionalized by methoxy groups. *The Journal of Physical Chemistry C*, 2013, **117** (26), P. 13637–13643.
- [18] Jiang X., et al. Broadband nonlinear photonics in few-layer MXene $Ti_3C_2T_x$ (T= F, O, or OH). *Laser & Photonics Reviews*, 2018, **12** (2), 1700229.
- [19] Dong Y., et al. Saturable absorption in 2D Ti_3C_2 MXene thin films for passive photonic diodes. *Advanced Materials*, 2018, **30** (10), 1705714.
- [20] Jhon Y.I., et al. Metallic MXene saturable absorber for femtosecond mode-locked lasers. *Advanced Materials*, 2017, **29** (40), 1702496.
- [21] Sakata H., Kimpara K., Takahashi N. Q-switched thulium-doped fibre ring lasers operating at 1.9 μm using multi-walled carbon nanotubes in UV-curing resin. *Electronics Letters*, 2015, **52** (1), P. 63–64.
- [22] Ahmad H., et al. Aluminized film as saturable absorber for generating passive Q-switched pulses in the two-micron region. *Journal of Light-wave Technology*, 2017, **35** (12), P. 2470–2475.
- [23] Rahman M.F., et al. Q-switched and mode-locked thulium-doped fiber laser with pure Antimony film Saturable absorber. *Optics Communications*, 2018, **421**, P. 99–104.
- [24] Ibarra-Escamilla B., et al. Passively Q-switched thulium-doped fiber laser using alcohol. *IEEE Photonics Technology Letters*, 2018, **30** (20), P. 1768–1771.

Design of 2:4 and 3:8 decoder circuit using QCA technology

Ratna Chakrabarty¹, S. Roy¹, T. Pathak¹, D. Ghosh¹, N. K. Mandal²

¹Institute of Engineering & Management, Department of Electronics & Communication Engineering, Salt Lake Electronics Complex, Sector V, Kolkata, 700091, India

²University of Engineering & Management, Department of Electronics & Communication Engineering, Salt Lake Electronics Complex, Sector V, Kolkata, 700091, India

ratna.chakrabarty@iemcal.com, soumyaruproy98@gmail.com, trambak.jaku@gmail.com, debanjanghosh.bwn@gmail.com, niranjanmandal54@gmail.com

DOI 10.17586/2220-8054-2021-12-4-442-452

Quantum Dot Cellular Automata is an emerging technology in the field of nanotechnology and has the potential to replace the existing CMOS technology. CMOS technology has its limitations in terms of high leakage current. However, QCA technology has higher speed of operation and very low power consumption. In this paper, designs for 2-4 and 3-8 decoder circuits have been made using a novel inverter circuit design which helps in decreasing the energy dissipation of the circuits. Finally, the proposed designs are compared to previously made designs. All the circuits in this paper have been simulated using QCA Designer software.

Keywords: QCA, decoders, laser ablation, majority voter, kink energy.

Received: 25 May 2021

1. Introduction

The QCA technology is a transistorless technology which is superior to the existing CMOS technology in terms of power consumption, area coverage and speed of operation. Many basic electronic components which are essential have been made using the QCA technology, namely adders [1–3], subtractors [1,3], multiplexers [4–7], decoders [8,9] and memory elements [10, 11]. This technology uses the Coulombic forces between charged particles. Unlike the CMOS technology, in QCA, they transfer the polarization of each cell [12]. Hence, polarization of QCA cell plays a very important role in choosing the perfect QCA device for use. There are two polarizations, $P = +1$ and -1 as shown in Fig. 1 which are treated as logic 1 and logic 0 respectively.

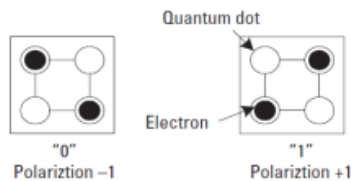


FIG. 1. QCA cell with the polarizations

The basic gate in this technology is a majority voter gate [13], as shown in Fig. 2, which can be programmed to act as an AND gate or an OR gate, depending on the control value given. Any one of the inputs can be used as a control input and the remaining two can act as normal inputs. When the control input is given as $+1$ the majority voter acts as a OR Gate and when the control input is given as -1 , the majority voter acts as an AND Gate.

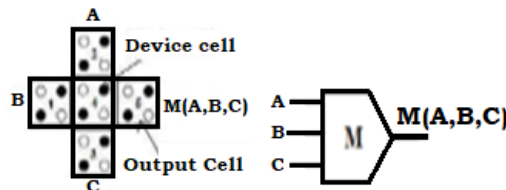


FIG. 2. Majority voter gate

One important aspect in this QCA technology is the concept of clocks shown in Fig. 3. They are used to synchronize the whole circuit and provide the direction of state transition. There are four clocks, namely clock 0, clock 1, clock 2 and clock 3 and each of them has four clocking zones, switch, hold, release and relax. During the switch phase, the inter-dot potential barrier becomes high and the cell becomes polarized based on the polarization state of its driver cell. In the hold phase, the barrier remains high as the cells preserve their state. In the release phase, the cells become unpolarized as the potential barrier decreases and in relax phase they remain unpolarized [12, 14].

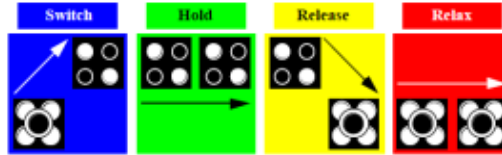


FIG. 3. The clocking zones

In the subsequent sections of the paper, we have designed a 2:4 decoder and a 3:8 decoder with an efficient architecture using QCA technology. The designs are made such that it can be scaled up from 2:4 to 3:8 to 4:16 decoders and so on. Finally, we compare it to the previous designs as mentioned in [15–18].

2. 2:4 Decoder circuit

Figure 4 is the proposed design of 2:4 decoder circuit using QCA Designer tool [19]. The whole circuit is designed in a single layer only. The design consists of 50 cells and occupies the area of 0.016 μm^2 . The output of this decoder is shown in Fig. 5 and the truth table is shown in Table 1.

TABLE 1. Truth table for 2:4 decoder

INPUT		OUTPUT			
S_1	S_0	I_0	I_1	I_2	I_3
0	0	1	0	0	0
0	1	0	1	0	0
1	0	0	0	1	0
1	1	0	0	0	1

It is evident from Fig. 6(a), that the polarization decreases as the temperature increases. For the output to be within tolerable ranges, the temperature of operation of the circuit is 1 to 9 K. Within that temperature frame, the lowest energy recorded is 0.0237 eV as shown in Fig. 6(b).

Calculation of kink energy is important in QCA-based design circuit. Kink energy is the energy difference between two neighboring or adjacent cells. Kink energy between two cells depends on the dimension of the QCA cell as well as the spacing between adjacent cells. It is independent of temperature. It is one of the most significant parameters for the stability of the design. The state having minimum Kink Energy is most stable state.

The kink energy (in Joule) between two electron charges is calculated using the formula:

$$U = \frac{kQ_1Q_2}{2},$$

where $k = 1/(4\pi\epsilon_0\epsilon_r) = 9 \times 10^{-9}$, $Q_1 = Q_2 = 1.6 \times 10^{-19}$ C – charge of an electron.

$$U = \frac{23.04 \times 10^{-29}}{r},$$

r – distance between the two charges.

$$U_T = \sum_i U_i,$$

U_T – summation of all the individual kink energies (in Joule).

For this calculation, the below postulates are considered.

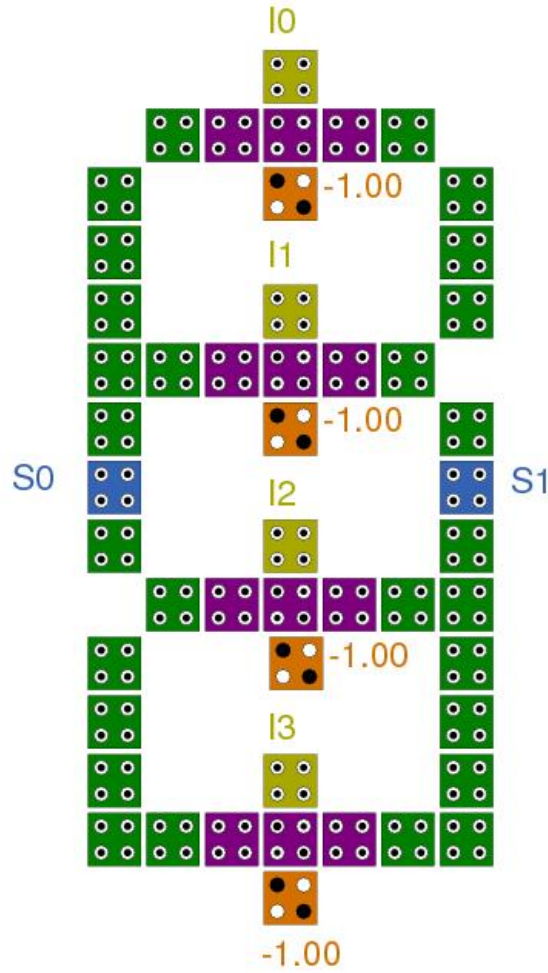


FIG. 4. Proposed 2:4 decoder

- (1) All cells are alike and the distance of end to end of each cell is 18 nm as shown in Fig. 7.
- (2) The space between two neighbouring cells (interspacing distance) is 2 nm.
- (3) The diameter of each quantum dot is 2.5 nm.
- (4) The distance between the two layers used for the design is 11.5 nm.

Below, a particular value of the two inputs is taken and the kink energy of all the corresponding output cells are calculated. Here, $S_1 = 1$ and $S_0 = 0$ is considered for the kink energy calculation. As per the truth table of 2:4 Decoder, for input $(S_1 S_0) = (10)$, the outputs are $I_0 = 0$, $I_1 = 0$, $I_2 = 1$ and $I_3 = 0$. The yellow cells are the output cells. As it can be observed from Fig. 8, the I_2 is only high and the rest are low. All the electrons (black dots) are arranged such that minimal possible energy configuration is achieved. Then the kink energies are calculated. Table 2 shows the kink energies for the proposed 2:4 decoder circuit.

3. 3:8 Decoder circuit

Figure 9 shows the 3 layered 3:8 decoder circuit. The 3:8 decoder can be derived from the 2:4 circuit. The three layers of the decoder circuit is shown in Fig. 10.

Figure 11 shows the simulated output for the 3:8 decoder circuit and Fig. 12 shows the polarization and energy dissipation graph with the temperature variation. Below, a particular value of the three inputs is taken and the kink energy of all the corresponding output cells are calculated. Here, $S_2 = 1$, $S_1 = 1$ and $S_0 = 0$ is considered for the kink energy calculation. As per the truth table of Table 3 of 3:8 Decoder, let the input $(S_2 S_1 S_0) = (110)$, the outputs are $I_0 = 0$, $I_1 = 0$, $I_2 = 0$, $I_3 = 0$, $I_4 = 0$, $I_5 = 0$, $I_6 = 1$ and $I_7 = 0$. The yellow cells are the output cells. As it can be observed from Fig. 13, the I_6 is only high and the rest are low. Again, all the electrons (black dots) are arranged such that minimal possible energy configuration is achieved just like the 2:4 decoder case. Then the kink energies are

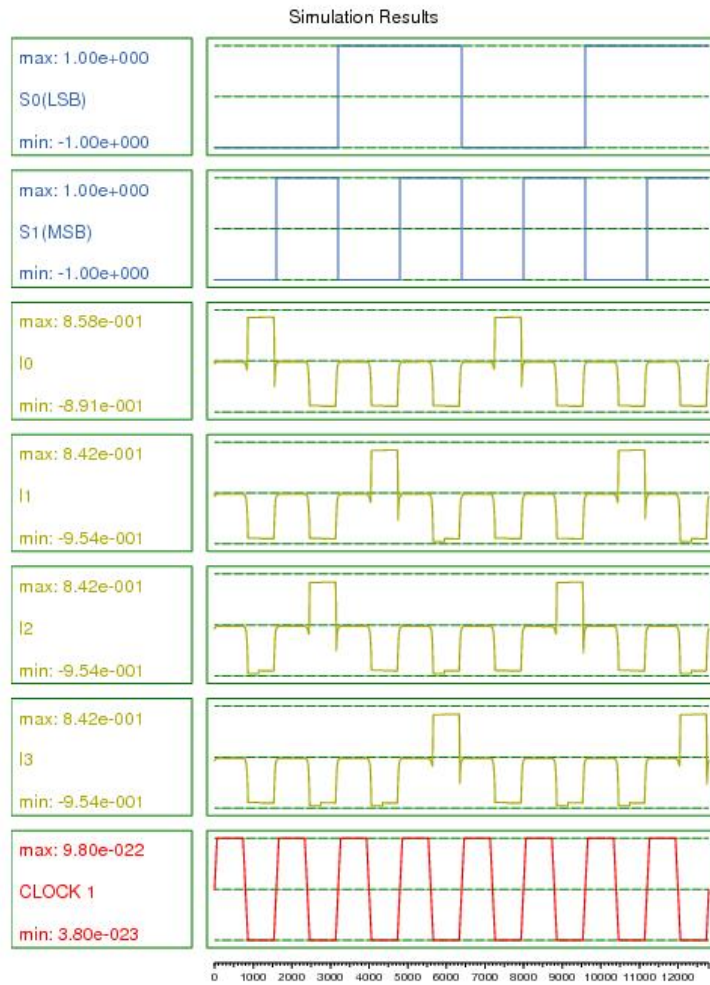


FIG. 5. Output of proposed 2:4 decoder circuit

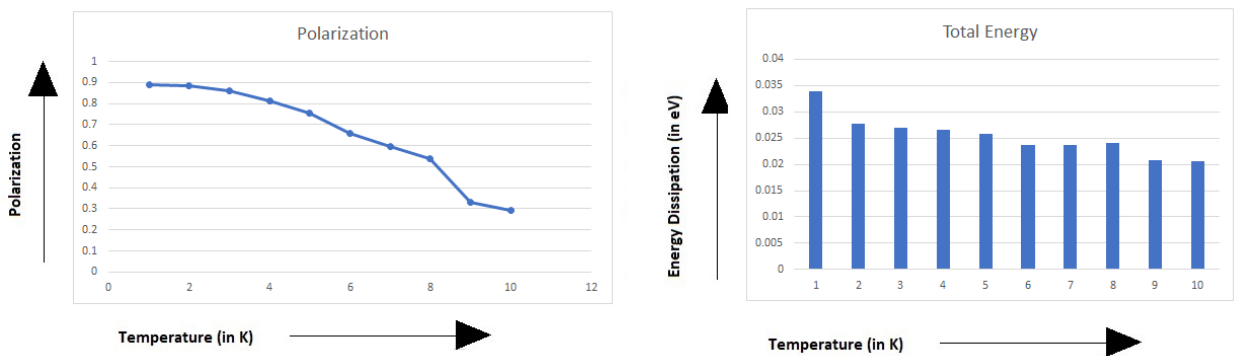


FIG. 6. Polarization (a) or energy dissipation (b) vs temperature

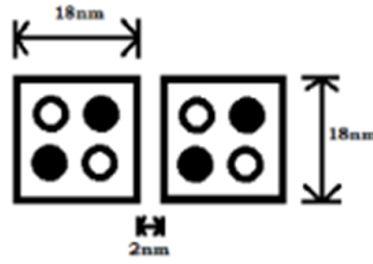


FIG. 7. Dimensions of the QCA cells

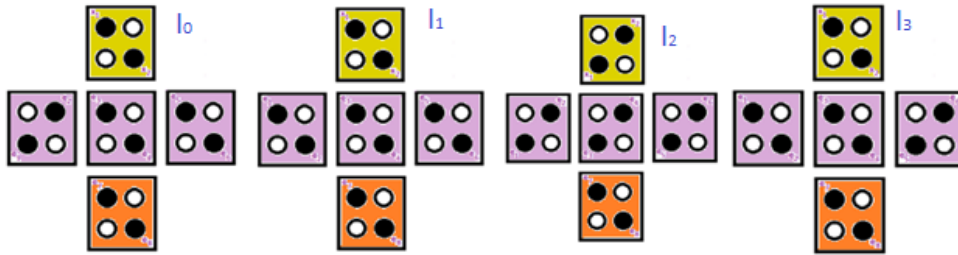
FIG. 8. Kink energy calculation diagram reference (from left to right I_0, I_1, I_2, I_3)

TABLE 2. Kink Energy for 2:4 decoder circuit

	$I_0 (\times 10^{-21})$		$I_1 (\times 10^{-21})$		$I_2 (\times 10^{-21})$		$I_3 (\times 10^{-21})$	
	x1	x2	x1	x2	x1	x2	x1	x2
U_{e1}	6.54	6.54	8.15	7.42	8.15	5.62	8.15	7.42
U_{e2}	10.08	10.08	7.42	8.15	14.81	8.15	7.42	8.15
U_{e3}	11.52	16.21	11.52	16.21	11.52	7.59	11.52	16.21
U_{e4}	7.59	11.52	7.59	11.52	16.21	11.52	7.59	11.52
U_{e5}	8.15	14.81	8.15	14.81	8.15	7.42	8.15	10.08
U_{e6}	5.62	8.15	5.62	8.15	7.42	8.15	6.54	10.08
U_{e7}	5.76	7.14	5.76	7.14	7.43	5.62	5.76	7.14
U_{e8}	4.62	5.76	4.62	5.76	5.62	4.70	4.62	5.76
Total (U_T)	59.88	80.21	58.83	79.16	79.31	58.77	59.75	76.36

calculated. Table 4 and 5 shows the kink energies for the proposed 3:8 decoder circuit. Now, I_1, I_2 and I_3 has 16 possible interactions with the electrons, so there are 16 rows in their case (Table 5), and the remaining have 8 rows (Table 4). From Fig. 13, it is also clear that due to the interaction of the output cell electrons with the main cell layer electrons, the calculations of kink energies for I_1, I_2 and I_3 are a bit complex.

4. Observation and results

Table 6 summarizes few of the parameters of the existing 2:4 decoders. It is a comparison between the already available decoder circuits and our proposed 2:4 decoder circuit design. In terms of cell count, layer separation and consumption of area proposed 2:4 decoder is better design compare to the 3 layered circuits proposed in [15] and [16]. Though the papers in [17] and [18] had designed a single layered circuit but number of cells and area requirement is more than the proposed design. Due to this single layer, the space occupied by our proposed circuit is much less. Also, this structure can be further extended to make a 3:8 decoder circuit. And, because of this single layered circuit, the

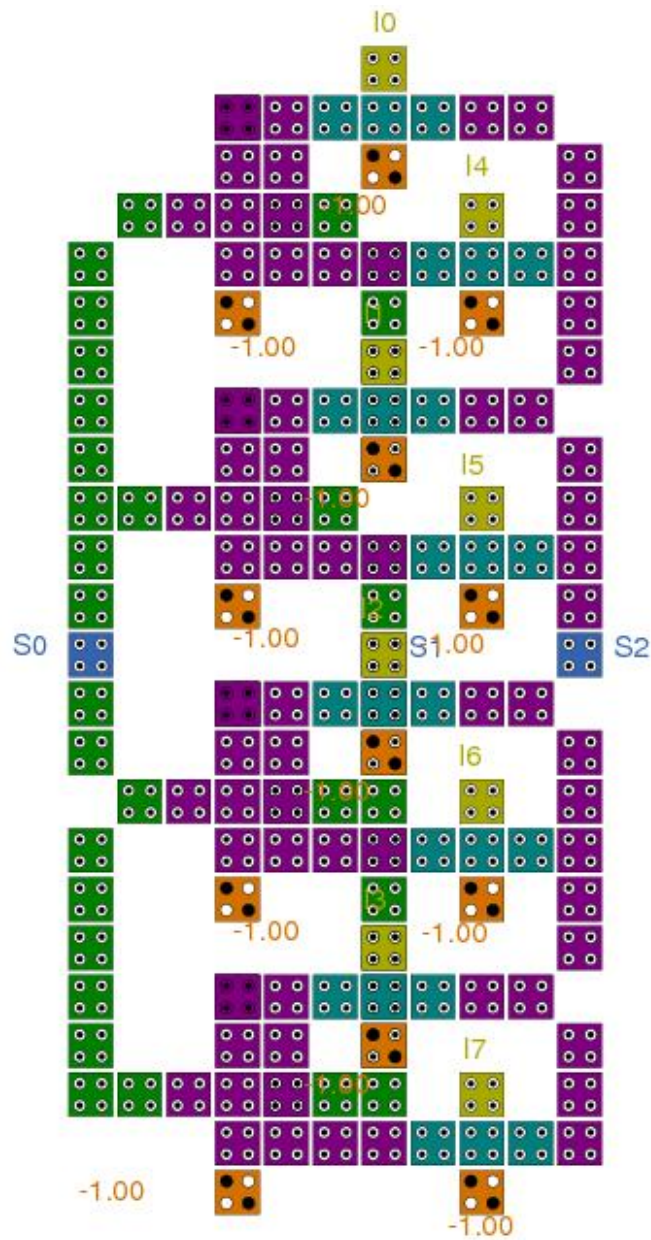


FIG. 9. Proposed 3:8 decoder (3 layered circuit)

cost of fabricating the circuit is much less. Table 7 shows the comparisons among the 3:8 decoders with the proposed decoder.

5. Conclusion

There are few decoder circuits designed in QCA. The work in [15] is slightly efficient design in terms of the cells count for the 3:8 decoder circuit but the layers used for the design and the consumption of area is same with the proposed design. The proposed design can be formed from 2:4 decoder and can be easily scaled up to form 3:8, 4:16 decoders and so on. Designing higher complex decoders will be easier with the proposed design.

TABLE 4. Kink energy for I_0, I_4, I_5, I_6, I_7

	$I_0 (\times 10^{-21})$		$I_4 (\times 10^{-21})$		$I_5 (\times 10^{-21})$		$I_6 (\times 10^{-21})$		$I_7 (\times 10^{-21})$	
	x1	x2								
U_{e1}	8.15	7.42	8.15	7.42	8.15	7.42	8.15	5.62	8.15	7.42
U_{e2}	7.42	8.15	7.42	8.15	7.42	8.15	14.81	8.15	7.42	8.15
U_{e3}	11.52	16.21	11.52	16.21	11.52	16.21	11.52	7.59	11.52	16.21
U_{e4}	7.59	11.52	7.59	11.52	7.59	11.52	16.21	11.52	7.59	11.52
U_{e5}	8.15	14.81	8.15	10.08	8.15	10.08	8.15	7.42	8.15	10.08
U_{e6}	7.59	8.15	6.54	10.08	6.54	10.08	7.42	8.15	6.54	10.08
U_{e7}	5.76	7.14	5.76	7.14	5.76	7.14	7.43	5.62	5.76	7.14
U_{e8}	4.62	5.76	4.62	5.76	4.62	5.76	5.62	4.7	4.62	5.76
Total (U_T)	60.8	79.16	59.75	76.36	59.75	76.36	79.31	58.77	59.75	76.36

TABLE 5. Kink energy for I_1, I_2, I_3

	$I_1 (\times 10^{-21})$		$I_2 (\times 10^{-21})$		$I_3 (\times 10^{-21})$	
	x1	x2	x1	x2	x1	x2
U_{e1}	8.15	7.42	6.54	6.54	8.15	7.42
U_{e2}	7.42	8.15	10.08	10.08	7.42	8.15
U_{e3}	11.52	16.21	11.52	16.21	11.52	16.21
U_{e4}	7.59	11.52	7.59	11.52	7.59	11.52
U_{e5}	8.15	14.81	8.15	14.81	8.15	14.81
U_{e6}	5.62	8.15	5.62	8.15	5.62	8.15
U_{e7}	5.76	7.14	5.76	7.14	5.76	7.14
U_{e8}	4.62	5.76	4.62	5.76	4.62	5.76
U_{e9}	9.04	7.25	9.04	7.25	9.04	7.25
U_{e10}	7.25	6.22	7.25	6.22	7.25	6.22
U_{e11}	9.33	9.33	9.33	9.33	9.33	9.33
U_{e12}	9.33	9.33	9.33	9.33	9.33	9.33
U_{e13}	6.22	7.25	6.22	7.25	6.22	7.25
U_{e14}	7.25	9.04	7.25	9.04	7.25	9.04
U_{e15}	4.26	4.9	4.26	4.9	4.26	4.9
U_{e16}	4.9	5.97	4.9	5.97	4.9	5.97
Total (U_T)	116.41	138.45	117.46	139.5	116.41	138.45

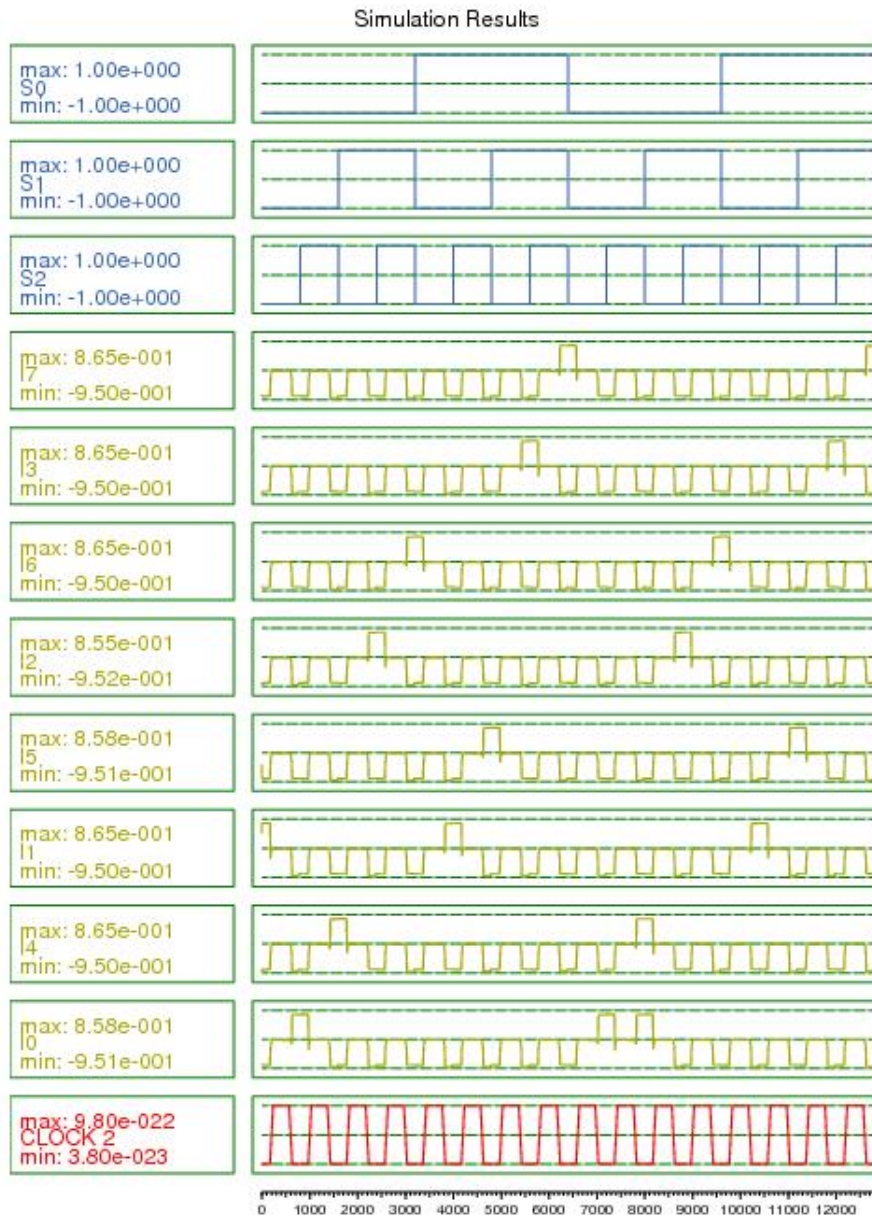


FIG. 11. Output of proposed 3:8 decoder circuit

TABLE 6. Observations for 2:4 decoders

Decoder circuit	No of cells	No of layers	Area (μm^2)
[15]	62	3	0.03
[16]	88	3	0.06
[17]	212	1	0.25
[18]	93	1	0.09
proposed	50	1	0.01

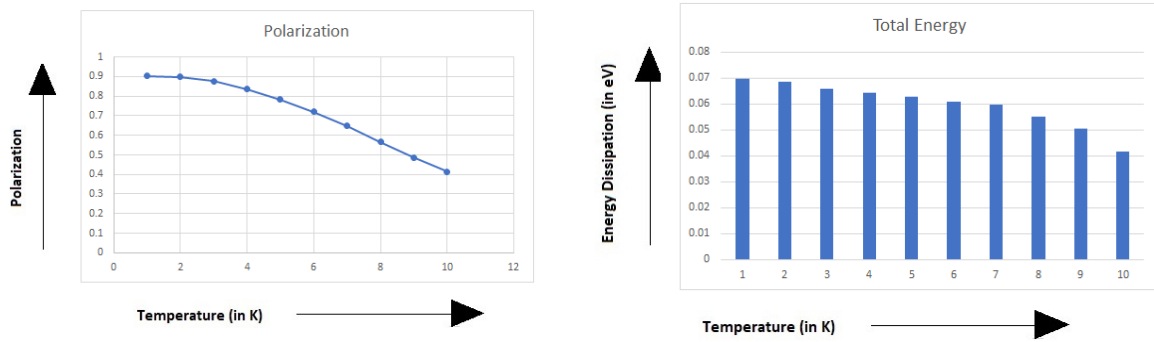


FIG. 12. Polarization (a) or energy dissipation (b) vs temperature

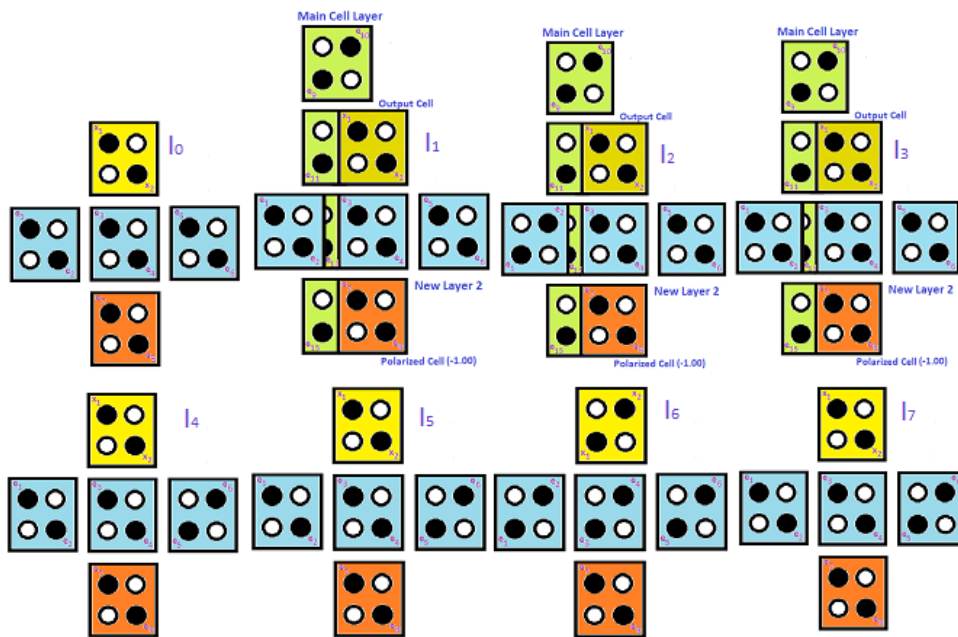


FIG. 13. Reference Diagram for kink energy calculation (I_0, I_1, I_2, I_3 (top row left to right); I_4, I_5, I_6, I_7 (bottom row left to right))

TABLE 7. Observations for 3:8 decoders

Decoder circuit	No of cells	No of layers	Area (μm^2)
[15]	136	3	0.04
[18]	312	1	0.1
proposed	168	3	0.04

References

- [1] Zoka S., Gholami M.A. Novel efficient full adder–subtractor in QCA nanotechnology. *Int. Nano Lett.*, 2019, **9**, P. 51–54.
- [2] Sen B., Rajoria A., Sikdar B.K. Design of Efficient Full Adder in Quantum-Dot Cellular Automata. *The Scientific World Journal*, 2013, 250802.
- [3] Jaiswal R., Sasamal T.N. Efficient design of full adder and subtractor using 5-input majority gate in QCA. *Tenth International Conference on Contemporary Computing (IC3)*, 2017, P. 1–6.
- [4] Aishwarya Tambe, Snehal Bhakre, Sankit Kassa. Design and Analysis of (2×1) and (4×1) Multiplexer Circuit in Quantum dot Cellular Automata Approach. *Int. Journal of Innovative Technology and Exploring Engineering*, 2019, **8** (6S3).
- [5] Firdous Ahmad. An Optimal Design of QCA Based $2n:1/1:2n$ Multiplexer/Demultiplexer and Its Efficient Digital Logic Realization. *Microprocessors and Microsystems*, 2018, **56**, P. 64–75.
- [6] Khan A., Mandal S., Nag S., Chakrabarty R. Efficient multiplexer design and analysis using quantum dot cellular automata. *IEEE Distributed Computing, VLSI, Electrical Circuits and Robotics (DISCOVER)*, 2016, P. 163–168.
- [7] Debarka Mukhopadhyay, Paramartha Dutta. Quantum Cellular Automata based Novel Unit 2:1 Multiplexer. *Int. Journal of Computer Applications*, 2012, **43** (2), P. 22–25.
- [8] Kianpour M., Sabbaghi-Nadooshan R. A Novel Modular Decoder Implementation in Quantum-Dot Cellular Automata (QCA). *Int. Conference on Nanoscience, Technology and Societal Implications*, Bhubaneswar, 2011, P. 1–5.
- [9] Mingliang Zhang, Wenqiang Li, et al. A Programmable Hamming Encoder/Decoder System Design with Quantum-dot Cellular Automata. *3rd Int. Conference on Electronic Information Technology and Computer Engineering*, 2019, P. 1338–1345.
- [10] Angizi S., Sarmadi S., Sayedsalehi S., Navi K. Design and evaluation of new majority gate-based RAM cell in quantum-dot cellular automata. *Microelectronics Journal*, 2015, **46** (1), P. 43–51.
- [11] Milad Bagherian Khosroshahy, Mohammad Hossein Moaiyeri, Keivan Navi, Nader Bagherzadeh. An energy and cost efficient majority-based RAM cell in quantum-dot cellular automata. *Results in Physics*, 2017, **7**, P. 3543–3551.
- [12] Radhouane Laajimi. Nanoarchitecture of Quantum-Dot Cellular Automata (QCA) Using Small Area for Digital Circuits. In *Advanced Electronic Circuit – Principles, Architectures and Applications on Emerging Technologies*, IntechOpen, London, 2018.
- [13] Naqvi S.R., Akram T., et al. A dynamically reconfigurable logic cell: from artificial neural networks to quantum-dot cellular automata. *Appl. Nanosci.*, 2018, **8**, P. 89–103.
- [14] Lent C.S., Tougaw P.D. A device architecture for computing with quantum dots. *Proceedings of the IEEE*, 1997, **85** (4), P. 541–557.
- [15] Abbasizadeh A., Mosleh M. Ultra dense 2-to-4 decoder in quantum-dot cellular automata technology based on MV32 gate. *ETRI Journal*, 2020, **42** (6), P. 912–921.
- [16] Seyedi S., Navimipour N.J. An Optimized Three-Level Design of Decoder Based on Nanoscale Quantum-Dot Cellular Automata. *Int. Journal of Theoretical Physics*, 2018, **57**, P. 2022–2033.
- [17] Kumar M., Sasamal T.N. An Optimal design of 2-to-4 Decoder circuit in coplanar Quantum-dot cellular automata. *Energy Procedia*, 2017, **117**, P. 450–457.
- [18] De D., Purkayastha T., Chattopadhyay T. Design of QCA based Programmable Logic Array using decoder. *Microelectronics Journal*, 2016, **55**, P. 92–107.
- [19] QCADesigner 2.0. URL: <https://qcadesigner.software.informer.com/2.0/>.

Influence of silver and gold nano particles on luminance properties of n-hexyloxy-cyanobiphenyl liquid crystal through image analysis

D. R. Roopa¹, C. M. Subhan², K. Fakruddin^{3,*}, P. Pardhasaradhi⁴, B. T. P. Madhav⁴, G. Srilekha⁴

¹Department of Physics, SJB Institute of Technology, Bengaluru, Karnataka, India

²Department of Physics, SV Degree and PG College, Anantapur, Andhra Pradesh, India

³Department of Physics, Ghousia College of Engineering, Ramanagaram, Karnataka, India

⁴Department of ECE, Koneru Lakshmaiah Education Foundation, Vaddeswaram, Guntur, India

*drfakruddin2008@gmail.com

PACS 42.70.Df, 42.79.Kr, 87.15.mq.

DOI 10.17586/2220-8054-2021-12-4-453-461

In this work, gold and silver nanoparticles are separately dispersed in n-hexyloxy-cyanobiphenyl (6O.CB) liquid crystal in the ratio 1:100. The optical textures of pure and nano-dispersed compounds are recorded by using polarizing optical microscope. Differential scanning calorimeter (DSC) is used to compute enthalpy and transition temperature values. Due to the dispersion of nanoparticles, the clearing temperature of the compounds are slightly reduced but there is no significant change in the nematic phase exhibited by pure 6O.CB. Further characterization is done by various spectroscopic techniques like scanning electron microscopy (SEM) and X-ray diffraction (XRD). The optical textures have been analyzed using MATLAB software for the evaluation of display parameters viz., Luminance, Luminance coefficient, Luminance uniformity and Contrast ratio.

Keywords: Liquid crystal, luminance, polarizing optical microscope, differential scanning calorimeter, scanning electron microscopy, X-ray diffraction.

Received: 26 June 2021

1. Introduction

Owing to the supreme properties of liquid crystals (LCs) like physical tuning and molecular designing, supramolecular hydrogen bonded liquid crystals (HBLCs) became most important materials in current research. Intermolecular hydrogen bonding between non-mesogenic-mesogenic materials, mesogenic-mesogenic materials or non-mesogenic-non-mesogenic materials produces the self-assembling of molecules, which induces new novel materials with different shapes and structures [1–11]. Further, these materials induce the new phases and physical properties. Such developments made hydrogen bonded LC's as essential materials for many applications such as optical storage devices, display devices, optical switches etc. Different types of HBLCs have been used by many authors in their research to derive different forms of applications.

Basically, display devices are specified in terms of chromaticity, i.e., black and white points. Where chromaticity is related to color information and black and white points, this represents luminance values [12, 13]. This type of specification includes the determination of display parameters obtained from the color information and luminance of the novel materials. There are several spectroscopic and experimental methods to measure the color information and luminance of the LCs [13–15]. In previous work, LC texture were utilized to calculate desired display parameters. Display parameters like luminance, luminance coefficient, luminance uniformity and contrast ratio have been estimated from the optical textures through MATLAB software [16–18] To compute the display parameters, LCs' textures are used as function of temperature.

2. Materials and methods

2.1. Synthesis of gold nanoparticles

The gold nanoparticles are synthesized from the citrate reduction process. The chemical ingredients for synthesis, the reducing agent trisodium citrate dehydrate ($\text{Na}_3\text{C}_6\text{H}_5\text{O}_7 \cdot 2\text{H}_2\text{O}$) 99% and hydrogen tetrachloroaurate (III) trihydrate ($\text{HAuCl}_4 \cdot 3\text{H}_2\text{O}$) ACS, 99.99% were purchased from Sigma Aldrich laboratories, USA and used as such. From Inductively Coupled Plasma Optical Spectrometry (ICPOS) report (ICAP6500 Thermo Fisher Scientific make), the amount of gold present in solution of 1 ml (1000 μl) of citrate capped gold nanoparticles is 96.75 μg . The author has dispersed very small amounts of citrate capped gold nanoparticles which contain the gold nanoparticles of amounts 4.83 μg , respectively.

2.2. Synthesis of silver nanoparticles

150 mg of silver nitrate (AgNO_3) is taken into 30 ml of distilled water and is mixed to the solution of 225 mg of tetraoctylammonium bromide (TOAB) in 24 ml of toluene. This solution is stirred continuously for one hour, and then 0.189 ml of dodecanethiol is added and so obtained homogeneous solution is further stirred for 30 minutes. In 24 ml of distilled water, 398 mg of sodium borohydride (NaBH_4) is dissolved and mixed with above obtained homogeneous solution.

This solution is stirred at room temperature for approximately three hours. From the solution, the organic phase is separated from aqueous solution and is reduced to 2 to 3 ml of solution by evaporating in a roto-evaporator under vacuum at room temperature. Next 50 ml of ethanol was added and the solution was centrifuged at 5000 rpm for one hour. The supernatant liquid, which is dodecane thiol protected silver nanoparticles, was dissolved in 1 ml of dichloromethane to get precipitated. This was washed with ethanol for many times for complete removal of organic material. 60 mg of thiol capped silver nanoparticles were obtained after this centrifugation process.

2.3. Homogeneous dispersion of gold and silver nano nanoparticles in LC compounds

LC compound 6O.CB was obtained from Sigma-Aldrich laboratories, USA and used without further purification. For homogeneous dispersion, gold and silver nanoparticles were dissolved in toluene and stirred in magnetic stirrer (Remi make) for 1 hour. Then, this solution was added to isotropic state of 100 mg of 6O.CB and the mixture is stirred well about 3 hours. Then the complex was cooled to room temperature which afforded 6O.CB with homogeneous dispersion of gold and silver nanoparticles. After cooling, 6O.CB mixtures were subjected to examination of both their textures and phase transition temperatures using polarizing optical microscope (POM) (SDTECHS make) attached with hot stage and differential scanning calorimetry (DSC) (Perkin Elmer Diamond DSC) along with the enthalpy values. The presence of gold and silver nanoparticles in 6O.CB is characterized by the experimental techniques Scanning Electron Microscope (SEM) and XRD.

2.4. POM (Polarising Optical Microscopy)

Due to change in local molecular order, the LC molecule is characterized into different LC phases with an increase in temperature. Determination and characterization of these mesophase will give very important information on the textures and pattern of the LCs. The thermal ranges of nematic phase are slightly changed due to the dispersion of gold and silver nanoparticles in LC compounds and the textures of the phase changes by the self-assembly of nanoparticles.

2.5. DSC Thermo grams

DSC gives complete and accurate information about thermal history of liquid crystal melting points at different rates of cooling and heating. In this instrument an accurately weighted sample which is placed in an aluminum pan crimped tightly closed with a sealing press and placed in the sample chamber of DSC. In this process the instructions are provided with each type of instrument for obtaining a good DSC scan.

Small values of enthalpy gives the mesophase transitions involved in pre- or post-transitional or second order transitions. While increasing the concentration of nanoparticles at the nematic phase transition, the clearing temperatures are reduced. This is the best complementary tool with the optical polarizing microscope. The DSC curve for the same is shown in Figs. 1 – 3.

2.6. Scanning Electron Microscope (SEM) Analysis

To estimate the morphology and chemical composition of nanoparticles, SEM acts as a wonderful tool with image magnification range from 10X to 300,000X and the resolution is almost down to few nanometers. In addition to the topographical information, the elements present in LC compounds as well as dispersed nanocomposites can be obtained from SEM analysis. In SEM, a very small amount of LC Nano-composite material sample is sufficient for characterization studies, and homogeneous dispersion of citrate capped gold nanoparticles in the respective LC compounds are studied from the different parts of the compounds which gives the similar Energy Dispersive Spectroscopy (EDS) data.

SEM detects the spatial variations in chemical compositions by generating high resolution images of the shape of the metal nanoparticles. The chemical composition of the elements in terms of the atomic percent and weight in the given LC Nano-composites and SEM images of LC compounds are well studied from SEM analysis. The SEM and EDS of 6O.CB with the dispersed gold nanoparticles is shown in Fig. 4. The SEM and EDS data of 6O.CB with the dispersed silver nanoparticles is shown in Fig. 5. Results from data of EDS reveal the presence of chemical compounds in sample. Carbon (C), sulfur (S), silver (Ag) and oxygen (O) elements are present in the 6O.CB with dispersed silver nanoparticle sample.

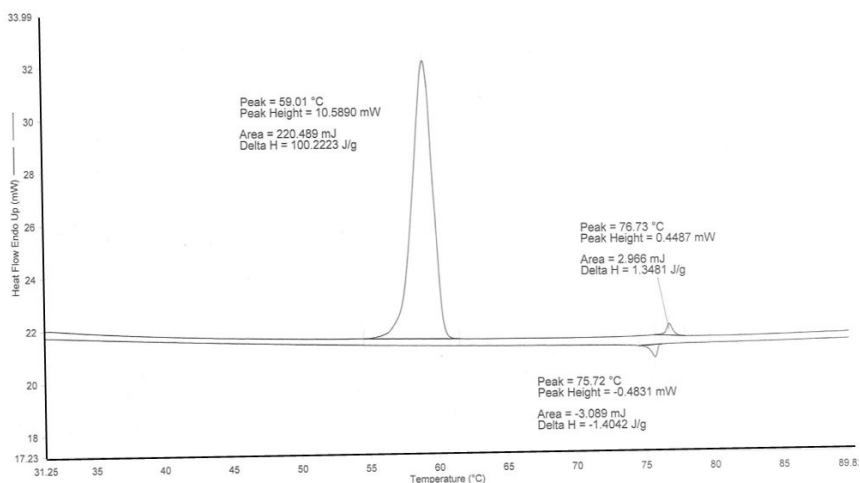


FIG. 1. DSC thermogram of 60.CB pure

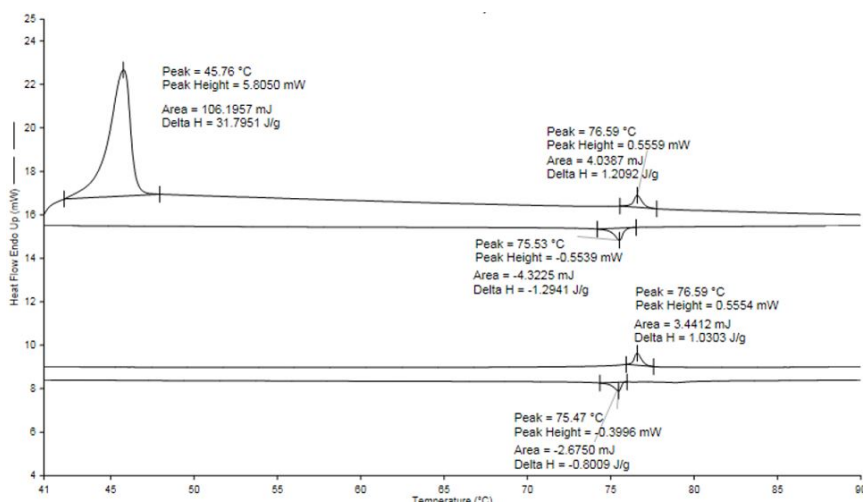


FIG. 2. DSC thermogram of 60.CB with gold nanoparticles

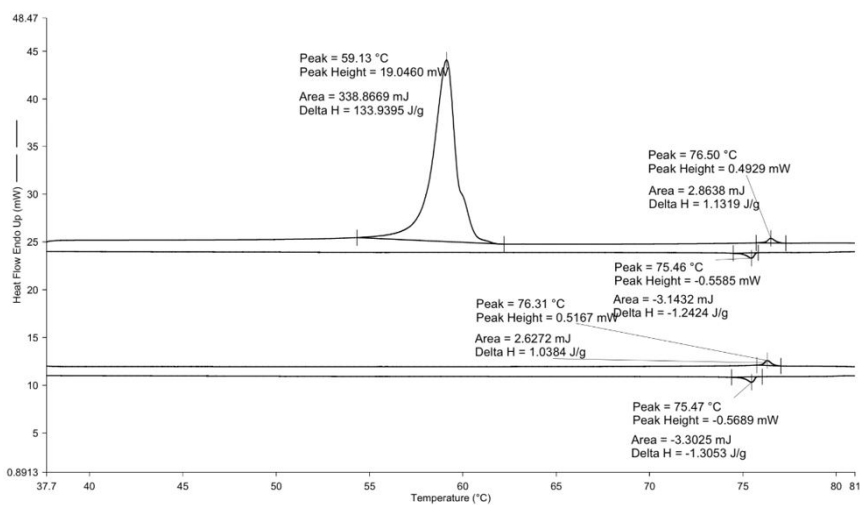


FIG. 3. DSC thermogram of 60.CB with silver nanoparticles

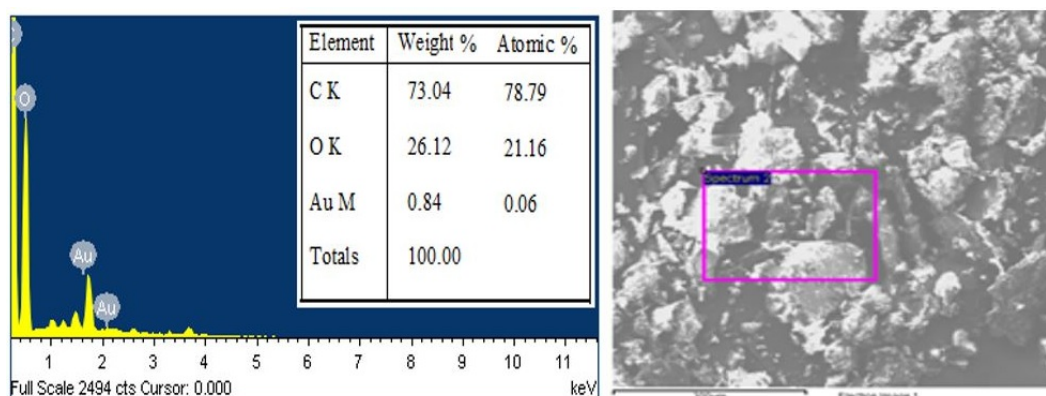


FIG. 4. SEM and EDS data of 6O.CB with the dispersed gold nanoparticles

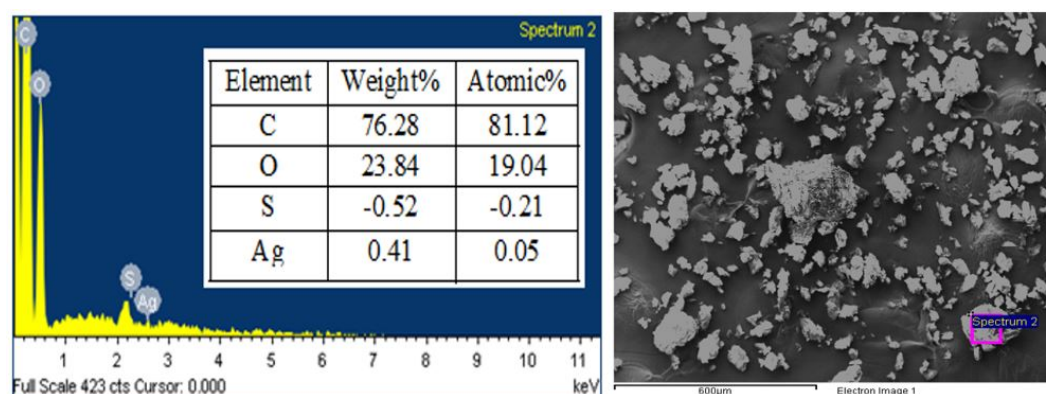


FIG. 5. SEM and EDS data of 6O.CB with the dispersed silver nanoparticles

2.7. X-Ray diffraction (XRD) studies

By utilizing XRD, the study of crystal structure of solids, defects, stresses, grain size and identity of the phases of LCs, by broadening of X-ray diffraction peaks. The Bragg's equation is given by:

$$\lambda = 2d \sin \theta.$$

Here, d is the inter-planar spacing, λ represents the wavelength of X-rays in which wavelength of the beam of X-rays varying from 0.07 to 0.2 nm and 2θ is angle of diffraction.

A good amount of powder sample is required for X-ray diffraction to give the collective information about the size of the nanoparticles dispersed in LC materials. An ideal powder sample will provide a similar diffraction pattern in the isotropic, nematic and smectic phases.

When there are no inhomogeneous strains in the LC sample, the size of the crystal t , can be measured from Scherrer's formula,

$$t = \frac{K\lambda}{\beta \cos \theta}.$$

K is Scherrer's constant and its value approaches to unity for a spherical crystal and 0.9 for LCs, λ is wavelength of X-rays, β is the full width half maxima (FWHM) height of a diffraction peak and θ is diffraction angle.

The XRD data is taken for the 6O.CB with homogeneous dispersion of the gold nanoparticles is shown in Fig. 6. In comparison of JCPDS data peaks were well resolved and are matched with JCPDS card no. 03-0652870 which is clearly evidenced the existence citrate capped Au nanoparticles in LC compound 6O.CB. By using Scherrer's Formula, $t = \frac{k\lambda}{\beta \cos \theta}$, grain size 33 nm, $\lambda = 1.54 \text{ \AA}$, $\beta = \text{FWHM}$, Peaks at 38.39° , 44.24° and 64.55° resembles the existence of citrate capped Au nanoparticles. The XRD data for 6O.CB with dispersion of silver nanoparticles is shown in Fig. 7.

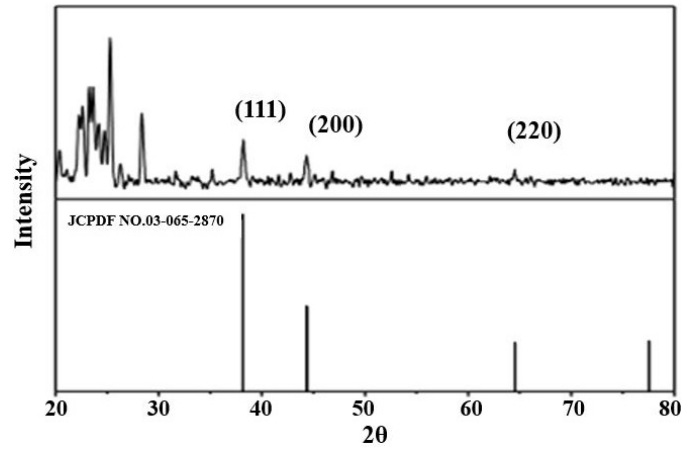


FIG. 6. XRD data of 6ocb pure and with the dispersion of gold nanoparticles

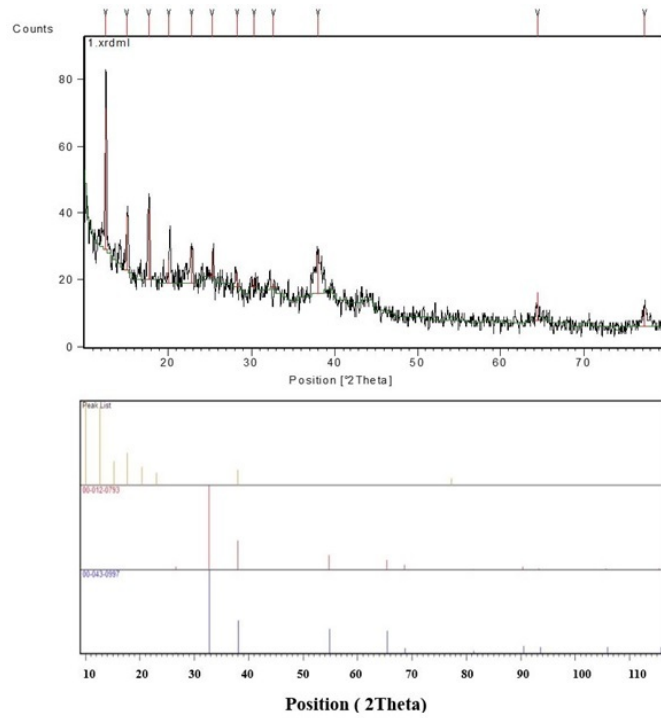


FIG. 7. XRD data of 6O.CB pure and with the dispersion of gold nanoparticles

3. Theory

The display device parameters of the LC compound images are calculated using MATLAB software [19]. The test image $I(m, n)$ is of the size $i \times j$ is recorded from POM with i number of pixels in vertical direction and j number of pixels in horizontal direction, where m and n are the spatial coordinates of the image. The total number of pixels can be computed as $N = i \cdot j$, where $0 \leq m \leq i, 0 \leq n \leq j$. The parameters for display device applications can thus be computed.

3.1. Luminance

The amount of light which is being transmitted or reflected from the object is being illuminated is called as luminance. In analysis of image, the weighted sum of intensities of color components (R, G, B) is referred as luminance and is defined as [20, 21]:

$$L = 0.2126 \cdot R + 0.152 \cdot G + 0.0722 \cdot B, \tag{1}$$

where L is luminance and R, G, B are the color components of the image.

3.2. Luminance coefficient

The ratio of luminance to the illuminance of the image is called as luminance coefficient. Where illuminance of the image is referred as intensity of the incident light [23]. It can be computed from the components of parallel polarisation where no sample is there in POM:

$$L_C = \frac{L}{(I_L)}, \quad (2)$$

where L_C is luminance coefficient and I_L is the illumination of the image.

3.3. Luminance uniformity

The percentage of luminance carried out from the one corner to another corner (pixel to pixel) of an image. The higher value of luminance uniformity provides the better consistency in brightness of the total image and which can be calculated as [22]:

$$\Delta L_U = [(L_{max} - L_{min}) - 1] \cdot 100, \quad (3)$$

where L_U is luminance uniformity.

3.4. Contrast ratio

The basic property of the display devices is contrast ratio. It is represented as the ratio between maximum to the minimum luminance of the recorded image from POM. Contrast in terms of luminance is defined as:

$$C_R = \frac{(L_{max} - L_{min})}{L_{max}}, \quad (4)$$

where C_R is contrast ratio and L_{max} and L_{min} are maximum and minimum luminance.

4. Results and discussions

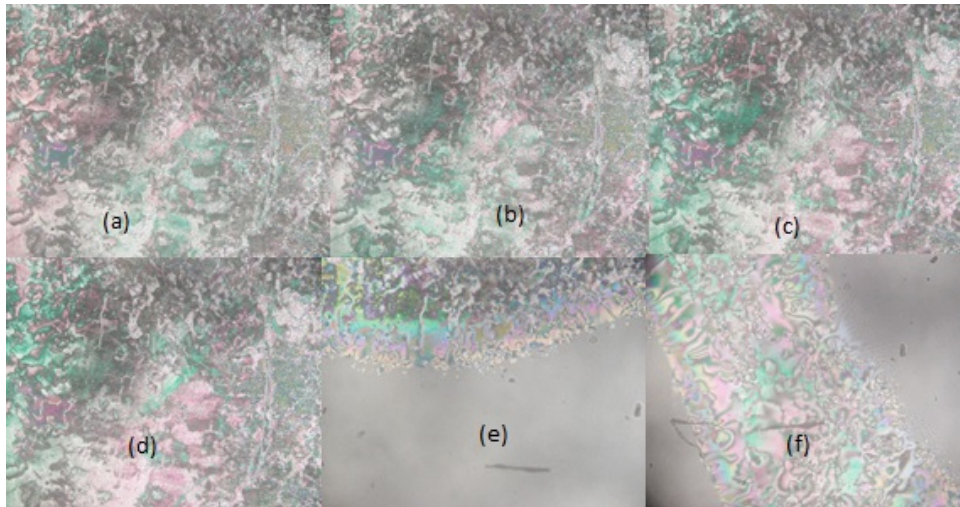


FIG. 8. 6O.CB pure Nematic phase textures at temperatures (a) 55 °C, (b) 60 °C, (c) 65 °C, (d) 66 °C, (e) 74.4 °C and (f) 74.7 °C

The nematic phase textures of the pure 6O.CB and dispersed with gold, silver nanoparticles are shown in Figs. 8 – 10.

From the Figs. 11 – 14 it is evident that the Luminance, Luminance coefficient, Luminance uniformity, and contrast ratio values are high at nematic phase for gold and silver nanoparticles as compared with pure 6O.CB. It is found that the percentage of increase in Luminance, Luminance coefficient, Luminance uniformity and contrast ratio for 6O.CB dispersed with gold nanoparticles are 8.57%, 9.813%, 31.52% and 27.96%. Correspondingly for 6O.CB dispersed with silver Nanoparticles are 14.89%, 27.93%, 83.29% and 39.85%. The higher luminance uniformity value offers well consistency in brightness of total image.

In our present studies silver nanoparticles dispersed in 6O.CB compound has higher value hence this may be a better material for display applications. Compare to gold silver nanoparticles dispersed in 6O.CB illustrates greater

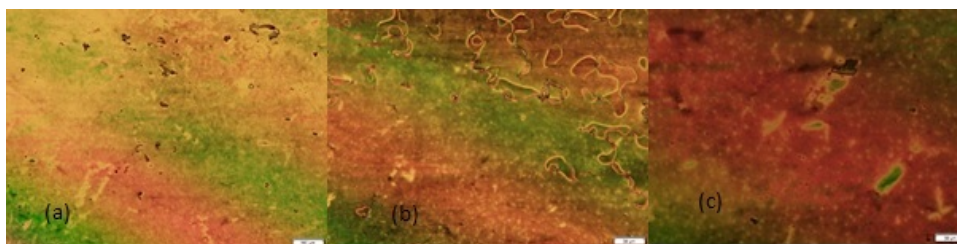


FIG. 9. 6O.CB with gold nanoparticles nematic phase textures at temperatures (a) 59.9 °C, (b) 67 °C and (c) 73.4 °C

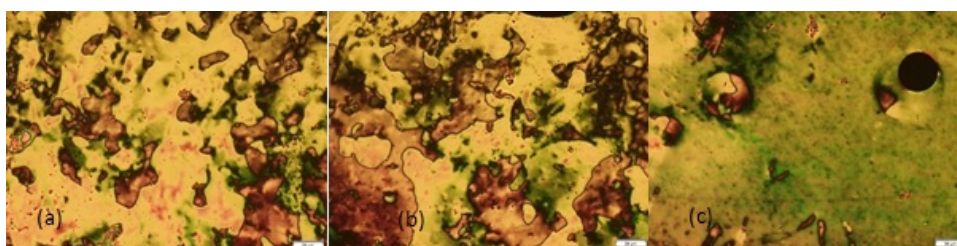


FIG. 10. 6O.CB with silver nanoparticles nematic phase textures at temperatures (a) 54.1 °C, (b) 56.5 °C and (c) 63.1 °C

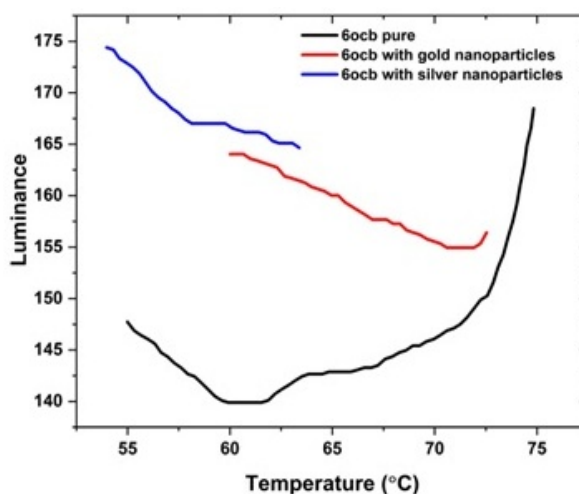


FIG. 11. Luminance values of the 6O.CB Pure and 6O.CB dispersed with gold, silver nano particles

values of above display parameters. This may be due to the fact that in visible region the reflection coefficient of silver is more than gold. For design of display devices luminance values play an important role. Higher the luminance the better is the compound for display device applications.

In alkoxy cyanobiphenyl liquid crystal compounds, good parallel molecular alignment exists in molecular structure due to the presence of oxygen atoms. Whereas in alkyl cyanobiphenyls in nematic phase there is imperfection in molecular arrangement [24]. Aligned molecules have the optical properties of uniaxial crystals this makes them exceptionally useful materials. Further the occurrence of oxygen atoms in molecular moiety increases the transition temperature.

By spectroscopic investigations, it is manifest that gold and silver nanoparticles are homogeneously dispersed in host 6O.CB liquid crystal compound. No variation in molecular structure and no substantial change in nematic phase due to the presence of gold and silver nanoparticles in mass material.

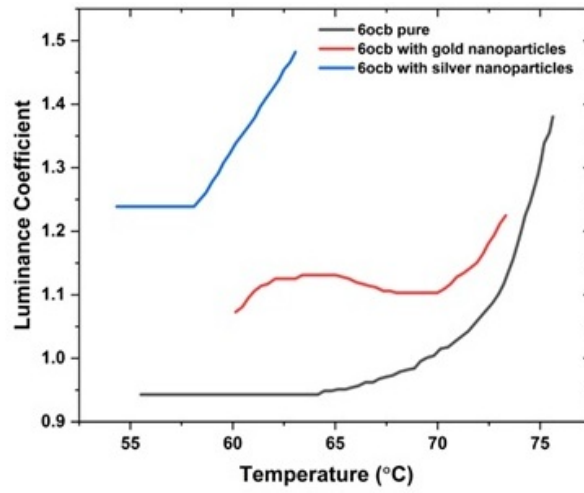


FIG. 12. Luminance uniformity values of the 60.CB Pure and 60.CB dispersed with gold, silver nano particles

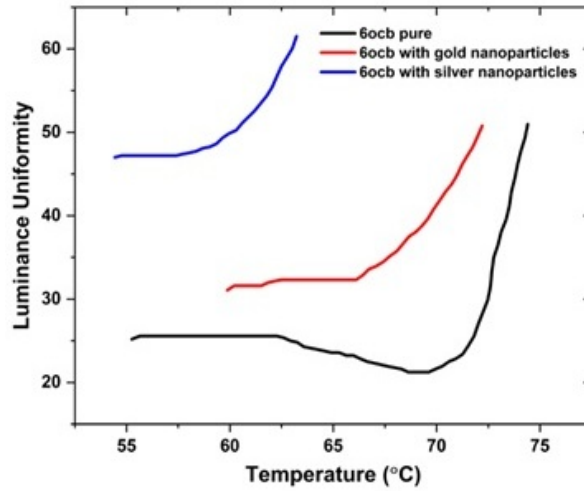


FIG. 13. Luminance Coefficient values of the 60.CB Pure and 60.CB dispersed with gold, silver nano particles

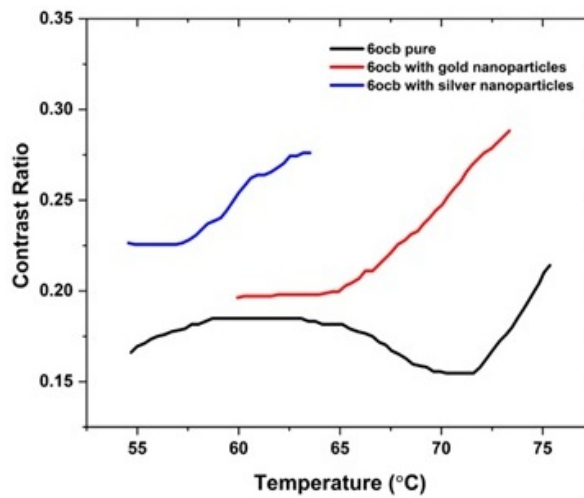


FIG. 14. Contrast Ratio values of the 60.CB Pure and 60.CB dispersed with gold, silver nanoparticles

5. Conclusion

Display device parameters as a function of temperature for 6O.CB Pure and 6O.CB dispersed with gold, silver nanoparticles are studied for LCD (Liquid Crystal Display) applications. The nematic transition temperatures are reduced by small amounts due to nano-dispersion. The conformation of gold and silver nanoparticles is evident by various spectroscopic techniques like SEM, and XRD studies. XRD studies confirm no alteration of structure of LCs by the dispersion of gold and silver nanoparticles. From the obtained parameters of luminance, luminance uniformity, luminance coefficient and contrast ratio, it is evident that the luminance values for the textures with dispersion of gold, silver nanoparticles have higher values than pure LC textures. It is concluded that nano-dispersed compounds are more suitable for display device applications as compared with pure LC.

References

- [1] Prasad M.M., Mohan M.M.L.N., Chalapathi P.V., Ashok Kumar A.V.N., Potukuchi D.M. Influence of spacer and flexible chain on polymorphism in complementary hydrogen bonded liquid crystal dimers, SA: nOBAs. *J Mol Liq.*, 2015, **207**, P. 294–308.
- [2] Sangameswari G., Prabu N.P.S., Mohan M. A detailed study of hydrogen bonded ferroelectric mesogens formed between alkyl and alkyloxy benzoic acids with carbonyl glutamic acid. *Liq Cryst.*, 2018, **45**, P. 431–449.
- [3] Ahmed H.A., Hagar M., Alaasar M., Naoum M. Wide nematic phases induced by hydrogen-bonding. *Liq Cryst.*, 2019, **46**(4), P. 550–559.
- [4] Martinez-Felipe A., Cook A.G., Wallage M.J., Imrie C.T. Hydrogen bonding and liquid crystallinity of low molar mass and polymeric mesogens containing benzoic acids: a variable temperature Fourier transform infrared spectroscopic study. *Phase Transitions*, 2014, **87**(12), P. 1191–1210.
- [5] Walker R., Pocięcha D., Abberley J.P., Martinez-Felipe A., Paterson D.A., Forsyth E., Lawrence G.B., Henderson P.A., Storey J.M.D., Gorecka E., Imrie C.T. Spontaneous chirality through mixing achiral components: a twist-bend nematic phase driven by hydrogen-bonding between unlike components. *Chem Comm.*, 2018, **54**, P. 3383–3386.
- [6] Goodby J.W., Pikin S.A., Robert Blinc, Clark N.A., Lagerwall S.T., Osipov M.A., Tadayoshi Sakurai, Yoshino K., Zeks B. *Ferro electric liquid crystal-principles properties and applications*. Gordon and Breech Science, Philadelphia, 1991.
- [7] Percec V. Bioinspired supramolecular liquid crystals. *Philos Trans R Soc A.*, 2006, **364**, P. 2709–2719.
- [8] Yang D.K., Wu S.T. *Liquid crystal materials in fundamentals of liquid crystal devices*. John Wiley and Sons, Ltd., Chichester (UK), 2006.
- [9] Sreehari Sastry S., Nageswara Rao C., Vishwam. T., Mallika K., Ha sie Tiong. Confirmation Studies of intermolecular hydrogen bonding through induced crystal G phase in nBA:7HB. *Liq Cryst.*, 2013, **40**(7), P. 932–941.
- [10] Martinez-Felipe A., Imrie C.T. The role of hydrogen bonding in the phase behaviour of supra molecular liquid crystal dimers. *J. Mol Struct.*, 2015, **1100**, P. 429–437.
- [11] Paterson D.A., Martinez-Felipe A., Jansze S.M., Antonius T.M.M., Storey J.M.D., Imrie C.T. New insights into the liquid crystal behaviour of hydrogen-bonded mixtures provided by temperature-dependent FTIR spectroscopy. *Liq Cryst.*, 2015, **42**, P. 928–939.
- [12] Rohehrig H. *Displays for medical imaging*, Chapter 2: Physical characterization and image quality, dissertation. Arizona, The University of Arizona, 2018.
- [13] Castellano J.A. *Handbook of display technology*. Academic Press Inc, San Diego (US), 1992.
- [14] Vimal T., Dharmendra P.S., Agrahari K., Srivatsava A., Manohar R. Analysis of optical properties and mechanism of photoluminescence enhancement of a quantum dot – ferroelectric liquid crystal composite. *Photonics Lett Poland*, 2016, **8**, P. 23–25.
- [15] Pathaka G., Agraharia K., Roya A., Srivatsava A., Strzeżysz O., Garbatb K., Manohara R. Dispersion of fluorescent dye in the nematic liquid crystal: enhanced photoluminescence and high birefringence. *Opto-electron rev.*, 2018, **26**, P. 317–324.
- [16] Chen J., Cranton W., Fihn M. *Handbook of Visual Display Technology*. Springer International Publishing, Switzerland, 2016.
- [17] Widdel H., Post D.L. *Color in electronic displays*. Plenum press, New York, 1992.
- [18] Sweet Khisa. *Characterization and calibration of a LCD display based on a limited set of color samples* (master Thesis). Saint-Étienne, University of Jean Monnet, 2010.
- [19] Gonzalez R.C., Woods R.E., Eddins S.L. *Digital image processing using MATLAB*. Knoxville (TN), Gatesmark Publishing, 2009.
- [20] tophlightco.com (internet). London (UK), lighting blog (cited 2015 June 18). Available from: <https://toplightco.com/blog/whats-the-difference-between-luminance-and-illuminance.html>
- [21] cs.stackexchange.com (internet). New York (US), Stackover flow (cited 2018 May 31). Available from: <https://cs.stackexchange.com/questions/92569/what-is-the-difference-between-luma-and-luminance.html>
- [22] displayalliance.com (internet). Amesbury (Essex), Mass Integrated, Inc (cited 2011 July 8). Available from: <http://www.displayalliance.com/glossary/luminanceuniformity.html>
- [23] Casol M., Fiorentin P., Scroccaro A. 16-th IMEKO TC4 Symposium- Exploring New Frontiers of Instrumentation and Methods for Electrical and Electronic Measurements. Florence, Italy, 2008, Sept 22–24.
- [24] Ghanadzade A., Beevers M.S. Effect of surface and molecular structure on the dielectric behaviour in thick layers of cyanobiphenyl liquid crystals. *Journal of Molecular Liquids*, 2002, **100**(1), P. 47–57.

Resonance asymptotics for quantum waveguides with semitransparent multi-perforated wall

A. M. Vorobiev

ITMO University, Kronverkskiy, 49, St. Petersburg, 197101, Russia

lenden31@yandex.ru

DOI 10.17586/2220-8054-2021-12-4-462-471

A pair of coupled quantum waveguides with a common semitransparent wall is considered. The wall has a finite number of small windows. We consider resonance states localized near each window. The presence of several windows forces one to describe their common influence differently from that of the single-window case. Using the “matching of asymptotic expansions” method, we derive formulas for resonances and resonance states.

Keywords: resonance, resonance state, waveguide, asymptotics, semitransparency.

Received: 5 June 2021

Revised: 12 August 2021

1. Introduction

There is a large class of mathematical and physical problems concerning to “systems with small coupling windows”, i.e., systems of connected quantum waveguides, Helmholtz resonators and other structures with perturbation caused by small windows on different boundaries. Such systems have long been of interest to physicists and mathematicians. Transport properties of waveguides and other additional phenomena caused by resonators are widely used in electrodynamics and theories of acoustic and electromagnetic waves.

Currently, scientists study such systems in the context of nanoelectronics. The development in this field has led to the creation of a new class of objects used in electronic devices – quantum threads (nanowhiskers), quantum dots, antidots and so on. Of course, “quantum” is a keyword here because studying mesoscopic systems (systems where the coherence of the phases of the electrons is preserved on a scale much larger than atomic) is absolutely impossible if we ignore quantum properties of the electron. Obviously, taking into account the quantum behavior of an electron requires the development of fundamentally new physical, and, most importantly, mathematical approaches.

When we consider mesoscopic systems, we actually mean studying wave propagation in waveguides and other structures. Properties of this propagation are described as spectral properties of corresponding mathematical operator. This is usually a Schrödinger operator. Laplace operator is also applicable for problems considering the ballistic mode. Resonance phenomena are widely used for development of new nanoelectronic devices.

Systems with small coupling windows were studied since the beginning of the 20th century [1, 2]. Currently, we use term “asymptotic analysis” for large class of problems including resonance phenomena. Great variety of electronic device caused great variety of systems in resonance problems. Different combinations of waveguides and resonators were considered [3–6], in addition to different geometry characteristics [7, 8], windows amount [9–11], and boundary conditions [12, 13].

The core of the mathematical approach in this work is “Matching asymptotic expansions of solutions of boundary problems”. This method was previously described in [14]. This method is intended for boundary problems of equations containing naturally occurring small parameter. It is very typical for mathematical physics problems, in particular for problems we described previously.

Semitransparency was studied by Ikebe, Shimada, Exner, Kreicirik, Popov in [15–20] in terms of spectral and scattering properties. Resonance asymptotics for such systems were studied in [21, 22].

2. Preliminaries

Let us consider the pair of quantum waveguides in two-dimensional Cartesian coordinates with widths d_- and d_+ .

The common wall of both waveguides is semitransparent and is coupled through small windows. Semitransparency was studied in [21] for the same system but with single window. In this work, we consider finite number of windows. We will rely on the results of that work but we won't describe in detail the preliminary calculations. So let's take a quick look at used formulas and assumptions.

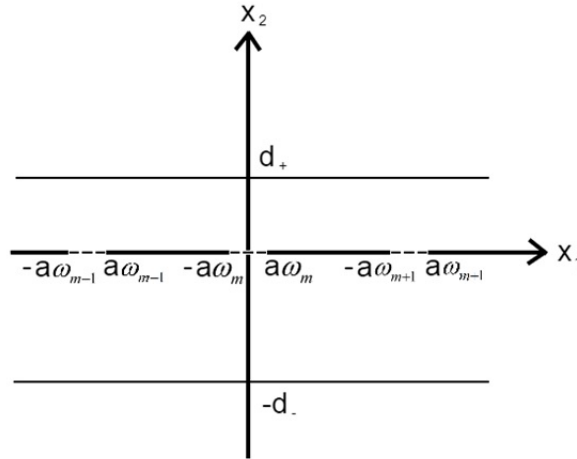


FIG. 1. Waveguides with common semitransparent wall (windows abscissas are relative to each center)

The wall semitransparency is described by the parameter α . Generally, $\alpha \in (0; +\infty)$, where zero value means no barrier and infinity means absolutely nontransparent barrier. Zero value is not included because actually it is not the case of the considered problem.

Boundary conditions on the walls are the key point: we choose the Dirichlet conditions on non-common walls but semitransparency causes special requirements for common wall. When a wave passes through the barrier, a jump occurs in the derivative of the considered function $u(x_1, x_2)$, so, we will consider specific boundary conditions:

$$\begin{cases} u_+ = u_-, \\ u'_+ - u'_- = \alpha u, \end{cases} \quad (1)$$

where u'_{\pm} are vertical derivatives at the top and bottom of the wall. The conditions of such type appear if one considers the singular potential supported on hypersurface. These potentials have been intensively investigated during last two decades (see, e.g., [23–25]).

Problems with several windows may be very different. The number of windows can be finite or infinite; the “order of smallness” can vary for each window. We consider somewhat simple case – finite number of windows with the same order of smallness.

Let us have n coupling windows with the centers at the points $(x_q; 0)$, where $q = 1..n$. Each window has width $2a_q = 2a - \omega_m \omega_{m-1} \omega_{m+1}$. Parameter a is exactly common order of smallness. We will construct asymptotics in a . This also means that $\omega_q, q = 1..n$, describes the relative sizes of all the windows.

Unperturbed eigenfunctions of the transversal problem for the Laplace operator with semitransparency can be written as follows:

$$\chi_n(x) = \begin{cases} -C_n \sin(d_- \nu_n) \sin((x_2 - d_+) \nu_n), & x_2 > 0, \\ C_n \sin(d_+ \nu_n) \sin((x_2 + d_-) \nu_n), & x_2 < 0. \end{cases} \quad (2)$$

One can see that it satisfies conditions (1). The corresponding eigenvalues are denoted as ν_n and can be found from the equation $-\nu \operatorname{ctg}(d_+ \nu) - \nu \operatorname{ctg}(d_- \nu) = \alpha$. For investigating resonances, we need to choose “threshold” value. Threshold is such value of ν_n , that there are no summands with imaginary part exponent in Green’s function series which are lower than ν_n . Imaginary exponent corresponds to periodic summands which mean propagating waves. We will seek terms of asymptotic expansions close to the second threshold ν_2 .

“Perturbed” eigenvalue, also known as quasi-eigenfrequency, will be denoted as k_a . Difference between k_a and ν_2 is actually small value. We will use convenient expansion for its asymptotics:

$$\sqrt{\nu_2^2 - k_a^2} = \sum_{j=2}^{\infty} \sum_{i=0}^{[j/2]-1} k_{ji} a^j \ln^i \frac{a}{a_0}. \quad (3)$$

The Green function for waveguide is well-known [25] and appears as follows in our case:

$$G^{\pm}(x, y, k) = \sum_{n=1}^{\infty} \frac{\chi_n(x_2) \cdot \chi_n(y_2)}{2p_n} \cdot e^{-p_n |x_1 - y_1|}, \text{ where } p_n^{\pm} = p_n = \sqrt{\nu_n^2 - k_a^2}.$$

Finally, we can write down eigenfunctions for perturbed case near each window:

$$\begin{cases} \psi_a(x) = \sqrt{\nu_2^2 - k_a^2} \cdot \sum_{j=0}^{\infty} \sum_{q=1}^n a^j P_{j+1}^q \left(D_y, \ln \frac{a}{a_0} \right) G^+(x, y, k) \Big|_{y=(x_q;0)}, & x \in \Omega^+ \setminus \bigcup_{q=1}^n S_{a_0(a/a_0)^{1/2}}^q, \\ \psi_a(x) = \sum_{j=1}^{\infty} \sum_{i=0}^{[(j-1)/2]} v_{ji} \left(\frac{x}{a} \right) a^j \ln^i \frac{a}{a_0}, & x \in \bigcup_{q=1}^n S_{2a_0(a/a_0)^{1/2}}^q, \\ \psi_a(x) = -\sqrt{\nu_2^2 - k_a^2} \cdot \sum_{j=0}^{\infty} \sum_{q=1}^n a^j P_{j+1}^q \left(D_y, \ln \frac{a}{a_0} \right) G^-(x, y, k) \Big|_{y=(x_q;0)}, & x \in \Omega^- \setminus \bigcup_{q=1}^n S_{a_0(a/a_0)^{1/2}}^q. \end{cases} \quad (4)$$

Here, $S_{a_0(a/a_0)^{1/2}}^q$ is as sphere with a center at q -th window. Last important thing is differential operator P_j^q . It is described as follows:

$$P_1(D_y, \ln \frac{a}{a_0}) = a_{10}^{(1)} D_y^1, \quad D_y^n = \frac{\partial^n}{\partial n_y^n}, \quad P_m \left(D_y, \ln \frac{a}{a_0} \right) = \sum_{j=1}^{m-1} \sum_{i=0}^{[(j-1)/2]} a_{ji}^{(m)} \left(\ln \frac{a}{a_0} \right)^i D_y^{m-j+1}, \quad m \geq 2,$$

$$P_m^q(D_y, \ln \frac{a}{a_0}) = \alpha_q P_m(D_y, \ln \frac{a}{a_0}).$$

Here, α_q are very important coefficients which describe operator action in distribution between windows.

3. Calculating

Boundary problems for $v_{ji} \left(\frac{x}{a} \right)$ from (4) can be obtained in the following manner. We substitute the series (4) and (3) into the Helmholtz equation (for $k = k_a$) and then change variables $\xi = \frac{x}{a}$. The coefficients in the terms with the same powers of a and $\ln \frac{a}{a_0}$ should be equal. Hence, we obtain the following problems:

$$\Delta_{\xi} v_{ji} = - \sum_{p=0}^{j-3} \sum_{q=0}^{[p/2]} \Lambda_{pq} v_{j-p-2, i-q}, \quad \xi \in R^2 \setminus \gamma, \quad v_{ji} = 0, \xi \in \gamma, \quad (5)$$

where $\gamma = \{ \xi | \xi_2 = 0 \wedge \xi_1 \in (-\infty; -1] \cup [1; +\infty) \}$ and Λ_{pq} are the coefficients of the series:

$$k_a^2 = \sum_p \sum_q \Lambda_{pq} a^p \ln^q \frac{a}{a_0}.$$

As next step we need to introduce operator $M_{pq}(U)$ – it changes variables in expressions $U \left(\xi = \frac{x}{a}, \ln r = \ln \rho + \ln a \right)$ and filters summand with $a^p \ln^q \frac{a}{a_0} \varphi(\xi)$. Also, $M_p = \sum_q M_{pq}$, it is used to obtain all summands with a^p .

3.1. Calculating of k_{20}

Considering matching at q -th window we can obtain the following a -degree selections:

$$\begin{aligned} a^{-1} M_1 \left(\pm \sqrt{\nu_2^2 - k_a^2} \cdot \sum_{q=1}^n P_1^q G^{\pm}(x, y, k_a) \Big|_{y=(x_q;0)} \right) = \\ \pm \frac{a_{10}^{(1)} C_2^2 \nu_2^2 \sin^2(d_{\mp} \nu_2) \cos^2(d_{\pm} \nu_2)}{2} \cdot \sum_{p=1}^n \alpha_p \rho \sin \theta \mp \frac{1}{\pi} \alpha_q k_{20} a_{10}^{(1)} \rho^{-1} \sin \theta. \end{aligned} \quad (6)$$

An extremely important point to note – k -singularity has its place in all window summands but x -singularity exists only in current window, so we have $\sum_{p=1}^n \alpha_p$ for positive ρ degree and just α_q for negative degree being in context of q -th window.

In accordance with the lemma concerning the v_{ji} representation in the form of a linear combination of harmonic functions, we need to choose those functions as a summary of all windows. Function $f_1(z) = \frac{1}{2} (z + \sqrt{z^2 - 1})$ was

used for single window so we choose summary function as follows:

$$\widehat{f}_1(z) = \sum_{q=1}^n \alpha_q \omega_q f_1\left(\frac{z-x_q}{\omega_q}\right) = \begin{cases} \sum_{q=1}^n \alpha_q \omega_q \frac{z-x_q}{\omega_q} - \sum_{q=1}^n \alpha_q \frac{\omega_q^2}{4z} - \sum_{q=1}^n \alpha_q \frac{\omega_q^2 x_q}{4z^2} - \sum_{q=1}^n \alpha_q \left(\frac{\omega_q^2 x_q^2}{4} + \frac{\omega_q^4}{16}\right) \frac{1}{z^3} - \dots, z \rightarrow +\infty, \\ \sum_{q=1}^n \alpha_q \frac{\omega_q^2}{4z} + \sum_{q=1}^n \alpha_q \frac{\omega_q^2 x_q}{4z^2} + \sum_{q=1}^n \alpha_q \left(\frac{\omega_q^2 x_q^2}{4} + \frac{\omega_q^4}{16}\right) \frac{1}{z^3} + \dots, z \rightarrow -\infty. \end{cases}$$

For different coordinates, we will use notation $\widehat{f}_i(z) = \widehat{X}_i(z) + i\widehat{Y}_i(z)$. To match terms increasing on $\rho \rightarrow \infty$ in accordance with (6), we shall select $v_{10}(\xi)$ in such a way:

$$v_{10}(\xi) = \frac{a_{10}^{(1)} C_2^2 \nu_2^2 \sin^2(d_- \nu_2) \cos^2(d_+ \nu_2)}{2} \cdot \widehat{Y}_1(\xi) + \frac{a_{10}^{(1)} C_2^2 \nu_2^2 \sin^2(d_+ \nu_2) \cos^2(d_- \nu_2)}{2} \cdot \widehat{Y}_1(\xi^*).$$

Hence, we can match terms of order $\rho^{-1} \sin \theta$ for each window and get the system of equations:

$$\mp \frac{1}{\pi} \alpha_q k_{20} a_{10}^{(1)} = \pm \frac{a_{10}^{(1)} C_2^2 \nu_2^2 (\sin^2(d_- \nu_2) \cos^2(d_+ \nu_2) + \sin^2(d_+ \nu_2) \cos^2(d_- \nu_2))}{2} \cdot \left(\sum_{p=1}^n \alpha_p \frac{\omega_p^2}{4}\right) \Rightarrow$$

$$\sum_{p=1}^n \alpha_p c_{\omega_p} = \beta \alpha_q, \beta = \frac{-2k_{20}}{\pi C_2^2 \nu_2^2 [\sin^2(d_- \nu_2) \cos^2(d_+ \nu_2) + \sin^2(d_+ \nu_2) \cos^2(d_- \nu_2)]}$$

$$= \frac{-4k_{20}}{\pi C_2^2 \nu_2^2 [1 - \cos(2d_- \nu_2) \cos(2d_+ \nu_2)]}.$$

This system has nontrivial solution if:

$$\det \begin{pmatrix} c_{\omega_1} - \beta & c_{\omega_1} & \dots & c_{\omega_1} \\ c_{\omega_2} & c_{\omega_2} - \beta & \dots & c_{\omega_2} \\ \dots & \dots & \dots & \dots \\ c_{\omega_n} & c_{\omega_n} & \dots & c_{\omega_n} - \beta \end{pmatrix} = 0,$$

where $\frac{\omega_q^2}{4}$ is actually harmonic capacity of the corresponding segment in R^2 , so we will use sometimes a symbol: $c_{\omega_q} = \frac{\omega_q^2}{4}$. Determinant of this matrix is $(-\beta)^{n-1} \left(\left(\sum_{q=1}^n c_{\omega_q} \right) - \beta \right)$. Hence:

$$\beta = \sum_{q=1}^n c_{\omega_q} \Rightarrow \frac{-4k_{20}}{\pi C_2^2 \nu_2^2 [1 - \cos(2d_- \nu_2) \cos(2d_+ \nu_2)]} = \sum_{q=1}^n c_{\omega_q} \Rightarrow$$

$$k_{20} = -\frac{\pi C_2^2 \nu_2^2}{4} [1 - \cos(2d_- \nu_2) \cos(2d_+ \nu_2)] \sum_{q=1}^n c_{\omega_q}.$$

If you compare it with k_{20} for the single window case, you will see that the only difference is sum $\sum_{q=1}^n c_{\omega_q}$. It is actually something like “common size” of the windows, characterized by sum of capacities. For $n = 1$ it equals $\frac{1}{4}$.

3.2. Calculating of k_{30}

Procedure for k_{30} is absolutely the same. Selecting of a^2 gives us:

$$\pm a^{-2} M_2 \left(\sqrt{\nu_2^2 - k_a^2} \cdot \sum_{q=1}^n P_1^q G^\pm(x, y, k_a) |_{y=(x_q; 0)} \right) =$$

$$-\frac{a_{10}^{(1)} C_2^2 \sin^2(d_\mp \nu) \nu_2^3 \cos(d_\pm \nu_2) \sin(d_\pm \nu_2)}{8} \sum_{p=1}^n \alpha_p \rho^2 \cos 2\theta \mp \frac{1}{\pi} \alpha_q k_{30} a_{10}^{(1)} \rho^{-1} \sin(\theta), \tag{7}$$

$$\pm a^{-2} M_2 \left(\sqrt{\nu_2^2 - k_a^2} \cdot \sum_{q=1}^n a \cdot P_2^q G^\pm(x, y, k_a) \Big|_{y=(x_q, 0)} \right) = \frac{a_{10}^{(2)} C_2^2 \sin^2(d_\pm \nu_2) \nu_2^3 \cdot \sin(d_\pm \nu_2) \cos(d_\pm \nu_2)}{2} \sum_{p=1}^n \alpha_p \rho \sin \theta \mp \frac{1}{\pi} \alpha_q k_{30} a_{10}^{(2)} \rho^{-2} \cos 2\theta.$$

Harmonic function of the second order uses the same formula except one more multiplier ω_q and uses $f_2(z) = z \cdot f_1(z) = \frac{1}{2} (z^2 + z\sqrt{z^2 - 1})$:

$$\widehat{f}_2(z) = \sum_{q=1}^n \alpha_q \omega_q^2 f_2 \left(\frac{z - x_q}{\omega_q} \right) = \begin{cases} \sum_{q=1}^n \alpha_q \omega_q^2 \frac{z^2}{\omega_q^2} - \sum_{q=1}^n \alpha_q \omega_q^2 \frac{2x_q z}{\omega_q^2} - \sum_{q=1}^n \alpha_q \omega_q^2 \frac{\omega_q^2}{16z^2} - \sum_{q=1}^n \alpha_q \omega_q^2 \frac{2\omega_q^2 x_q}{16z^3} - \dots, z \rightarrow +\infty, \\ \sum_{q=1}^n \alpha_q \omega_q^2 \frac{\omega_q^2}{16z^2} + \sum_{q=1}^n \alpha_q \omega_q^2 \frac{2\omega_q^2 x_q}{16z^3} + \dots, z \rightarrow -\infty. \end{cases}$$

Unfortunately, it contains not only positive ρ degree, so we need to subtract corresponding additional summand using $\widehat{X}_1(\xi)$:

$$\begin{aligned} v_{20}(\xi) &= \frac{-a_{10}^{(1)} C_2^2 \sin^2(d_- \nu) \nu_2^3 \cos(d_+ \nu_2) \sin(d_+ \nu_2)}{8} \widehat{X}_2(\xi) \\ &\quad - \frac{a_{10}^{(1)} C_2^2 \sin^2(d_+ \nu) \nu_2^3 \cos(d_- \nu_2) \sin(d_- \nu_2)}{8} \widehat{X}_2(\xi^*) \\ &\quad - \frac{2a_{10}^{(1)} C_2^2 \sin^2(d_- \nu) \nu_2^3 \cos(d_+ \nu_2) \sin(d_+ \nu_2)}{8} \frac{\sum_{q=1}^n \alpha_q x_q}{\sum_{q=1}^n \alpha_q} \widehat{X}_1(\xi) \\ &\quad - \frac{2a_{10}^{(1)} C_2^2 \sin^2(d_+ \nu) \nu_2^3 \cos(d_- \nu_2) \sin(d_- \nu_2)}{8} \frac{\sum_{q=1}^n \alpha_q x_q}{\sum_{q=1}^n \alpha_q} \widehat{X}_1(\xi^*) \\ &\quad + \frac{a_{10}^{(2)} C_2^2 \sin^2(d_- \nu_2) \nu_2^3 \cdot \sin(d_+ \nu_2) \cos(d_+ \nu_2)}{2} \widehat{Y}_1(\xi) \\ &\quad - \frac{a_{10}^{(2)} C_2^2 \sin^2(d_+ \nu_2) \nu_2^3 \cdot \sin(d_- \nu_2) \cos(d_- \nu_2)}{2} \widehat{Y}_1(\xi^*). \end{aligned}$$

Equations system is similar to previous:

$$\begin{aligned} \mp \frac{1}{\pi} \alpha_q k_{30} a_{10}^{(1)} &= \pm \frac{a_{10}^{(2)} C_2^2 \sin^2(d_- \nu_2) \nu_2^3 \cdot \sin(d_+ \nu_2) \cos(d_+ \nu_2)}{2} \left(\sum_{p=1}^n \alpha_p \frac{\omega_p^2}{4} \right) \\ \mp \frac{a_{10}^{(2)} C_2^2 \sin^2(d_+ \nu_2) \nu_2^3 \cdot \sin(d_- \nu_2) \cos(d_- \nu_2)}{2} &\left(\sum_{p=1}^n \alpha_p \frac{\omega_p^2}{4} \right) \\ \Rightarrow \sum_{p=1}^n \alpha_p c_{\omega_p} &= \beta \alpha_q, \beta = \frac{-8k_{30}}{\pi C_2^2 \nu_2^3 [\sin(d_- \nu_2) \sin(d_+ \nu_2) \sin((d_- - d_+) \nu_2)]}. \end{aligned}$$

Determinant of this matrix is $(-\beta)^{n-1} \left(\left(\sum_{q=1}^n c_{\omega_q} \right) - \beta \right)$. Hence:

$$\begin{aligned} \beta &= \sum_{q=1}^n c_{\omega_q} \Rightarrow \frac{-8k_{30}}{\pi C_2^2 \nu_2^3 (\sin(d_- \nu_2) \sin(d_+ \nu_2) \sin((d_- - d_+) \nu_2))} = \sum_{q=1}^n c_{\omega_q} \Rightarrow \\ k_{30} &= \frac{-\pi C_2^2 \nu_2^3 (\sin(d_- \nu_2) \sin(d_+ \nu_2) \sin((d_- - d_+) \nu_2))}{8} \sum_{q=1}^n c_{\omega_q}. \end{aligned}$$

3.3. Calculating of k_{40}

As we previously noticed, equation (5) is homogeneous for $v_{10}(\xi)$, $v_{20}(\xi)$, but becomes more complicated for the next step. So we need to solve the Poisson equation:

$$\Delta_{\xi} v_{30} = -\frac{\pi^2}{d_{+}^2} v_{10}, \quad v_{30}(\xi) = 0, \quad \xi \in \gamma, \quad \gamma = \{\xi | \xi_2 = 0 \wedge \xi_1 \in (-\infty; -1] \cup [1; +\infty)\}.$$

The solution of this boundary problem can be presented as:

$$v_{30}(\xi) = \widehat{v}_{30}(\xi) + \widetilde{v}_{30}(\xi),$$

where $\widehat{v}_{30}(\xi)$ is solution of homogeneous Laplace equation satisfying the boundary conditions (as we seek for previous steps) and $\widetilde{v}_{30}(\xi)$ is particular solution of inhomogeneous Laplace equation satisfying the boundary conditions. M -operator expressions are not much different with single-window ones:

$$\begin{aligned} a^{-3} M_{30} \left(\pm \sqrt{\nu_2^2 - k_a^2} \cdot P_1 G^{\pm}(x, y, k_a) \Big|_{y=0} \right) &= \pm \sum_{p=1}^n \alpha_p \frac{a_{10}^{(1)} k_{20} C_1^2 \sin^2(d_{\mp} \nu_1) \nu_1^2 \cos^2(d_{\pm} \nu_1)}{2i \sqrt{\nu_2^2 - \nu_1^2}} \rho \sin \theta \\ &\pm \sum_{p=1}^n \alpha_p \cdot \frac{a_{10}^{(1)} C_2^2 \nu_2 \sin^2(d_{\mp} \nu) \cos(d_{\pm} \nu)}{2} \cdot \left[\frac{1}{24} \cos(d_{\pm} \nu_2) \nu_2^3 \rho^3 \sin 3\theta \pm \sin(d_{\pm} \nu) k_{20} \rho \cos \theta \right] \\ &\pm \sum_{p=1}^n \alpha_p \cdot a_{10}^{(1)} k_{20} g_x^{\pm} \rho \sin \theta \mp a_{10}^{(1)} \alpha_q \frac{1}{\pi} k_{40} \rho^{-1} \sin \theta, \end{aligned} \quad (8)$$

$$\begin{aligned} a^{-3} M_{30} \left(\pm \sqrt{\nu_2^2 - k_a^2} \cdot a \cdot P_2 G^{\pm}(x, y, k_a) \Big|_{y=0} \right) &= \\ &\mp \sum_{p=1}^n \alpha_p \cdot \frac{a_{10}^{(2)} C_2^2 \sin^2(d_{\mp} \nu_2) \nu_2^4 \cdot \sin^2(d_{\pm} \nu_2)}{8} \cdot \rho^2 \cos 2\theta \mp \frac{1}{\pi} \alpha_q k_{40} a_{10}^{(2)} \rho^{-2} \cos 2\theta, \end{aligned} \quad (9)$$

$$\begin{aligned} a^{-3} M_{30} \left(\pm \sqrt{\nu_2^2 - k_a^2} \cdot a^2 \cdot a_{10}^{(3)} D_3 G^{\pm}(x, y, k_a) \Big|_{y=0} \right) &= \\ &\pm \sum_{p=1}^n \alpha_p \cdot \frac{-a_{10}^{(3)} C_2^2 \sin^2(d_{\mp} \nu_2) \nu_2^4 \cos^2(d_{\pm} \nu_2)}{2} \cdot \rho \sin \theta \pm a_{10}^{(3)} \alpha_q \frac{\nu_2^2}{2\pi} k_{20} \rho^{-1} \sin \theta \pm a_{10}^{(3)} \alpha_q \frac{2}{\pi} k_{40} \rho^{-3} \sin 3\theta, \end{aligned} \quad (10)$$

$$\begin{aligned} a^{-3} M_{30} \left(\pm \sqrt{\nu_2^2 - k_a^2} \cdot a^2 \cdot a_{20}^{(3)} D_2 G^{\pm}(x, y, k_a) \Big|_{y=0} \right) &= \\ &= \sum_{p=1}^n \alpha_p \cdot \frac{a_{20}^{(3)} C_2^2 \sin^2(d_{\mp} \nu_2) \nu_2^3 \sin(d_{\pm} \nu_2) \cos(d_{\pm} \nu_2)}{2} \rho \sin \theta \mp \frac{1}{\pi} \alpha_q k_{30} a_{20}^{(3)} \rho^{-2} \cos 2\theta. \end{aligned} \quad (11)$$

The harmonic summary for $f_3(z) = \frac{1}{2} \left(z^3 + \frac{3}{2} \sqrt{z^2} + (\sqrt{z^2 - 1})^3 \right)$ can be presented as follows:

$$\begin{aligned} \widehat{f}_3(z) &= \sum_{q=1}^n \alpha_q \omega_q^3 f_3 \left(\frac{z - x_q}{\omega_q} \right) = \\ &\begin{cases} \sum_{q=1}^n \alpha_q \omega_q^3 \frac{z^3}{\omega_q^3} - \sum_{q=1}^n \alpha_q \omega_q^3 \frac{3x_q z^2}{\omega_q^3} + \sum_{q=1}^n \alpha_q \omega_q^3 \frac{3x_q^2 z}{\omega_q^3} + \sum_{q=1}^n \alpha_q \omega_q^3 \frac{3\omega_q}{16z} + \dots, z \rightarrow +\infty, \\ - \sum_{q=1}^n \alpha_q \omega_q^3 \frac{3\omega_q}{16z} - \dots, z \rightarrow -\infty. \end{cases} \end{aligned}$$

Here, we also obtain a set of positive degrees instead of one so we will need the same idea as for previous order. Separating summands from (8)–(11) with positive ρ degrees, we can obtain the following representation for $\widehat{v}_{30}(\xi)$:

$$\begin{aligned} \widehat{v}_{30}(\xi) &= \beta_{21} \widehat{X}_2(\xi) + \widetilde{\beta}_{21} \widehat{X}_2(\xi^*) + \beta_{11} \widehat{X}_1(\xi) + \widetilde{\beta}_{11} \widehat{X}_1(\xi^*) + \\ &\beta_{32} \widehat{Y}_3(\xi) + \widetilde{\beta}_{32} \widehat{Y}_3(\xi^*) + \beta_{22} \widehat{Y}_2(\xi) + \widetilde{\beta}_{22} \widehat{Y}_2(\xi^*) + \beta_{12} \widehat{Y}_1(\xi) + \widetilde{\beta}_{12} \widehat{Y}_1(\xi^*), \end{aligned}$$

where coefficients can be found:

$$\beta_{21} = \frac{-a_{10}^{(2)} C_2^2 \sin^2(d_{-} \nu_2) \nu_2^4 \cdot \sin^2(d_{+} \nu_2)}{8}, \quad \widetilde{\beta}_{21} = \frac{a_{10}^{(2)} C_2^2 \sin^2(d_{+} \nu_2) \nu_2^4 \cdot \sin^2(d_{-} \nu_2)}{8},$$

$$\beta_{11} = \frac{a_{10}^{(1)} k_{20} C_2^2 \nu_2 \sin^2(d_{-} \nu) \cos(d_{+} \nu) \sin(d_{+} \nu)}{2} + 2 \left(\frac{\sum_{q=1}^n \alpha_q x_q}{\sum_{q=1}^n \alpha_q} \right) \beta_{21},$$

$$\tilde{\beta}_{11} = \frac{a_{10}^{(1)} k_{20} C_2^2 \nu_2 \sin^2(d_+ \nu) \cos(d_- \nu) \sin(d_- \nu)}{2} + 2 \left(\frac{\sum_{q=1}^n \alpha_q x_q}{\sum_{q=1}^n \alpha_q} \right) \tilde{\beta}_{21},$$

$$\beta_{32} = \frac{a_{10}^{(1)} C_2^2 \nu_2^4 \sin^2(d_- \nu_2) \cos^2(d_+ \nu_2)}{48}, \quad \tilde{\beta}_{32} = \frac{a_{10}^{(1)} C_2^2 \nu_2^4 \sin^2(d_+ \nu_2) \cos^2(d_- \nu_2)}{48},$$

$$\beta_{22} = 3 \left(\frac{\sum_{q=1}^n \alpha_q x_q}{\sum_{q=1}^n \alpha_q} \right) \beta_{32}, \quad \tilde{\beta}_{22} = 3 \left(\frac{\sum_{q=1}^n \alpha_q x_q}{\sum_{q=1}^n \alpha_q} \right) \tilde{\beta}_{32},$$

$$\beta_{12} = \frac{a_{10}^{(1)} k_{20} C_1^2 \sin^2(d_- \nu_1) \nu_1^2 \cos^2(d_+ \nu_1)}{2i\sqrt{\nu_2^2 - \nu_1^2}} + a_{10}^{(1)} k_{20} g_x^+ - 3 \left(\frac{\sum_{q=1}^n \alpha_q x_q^2}{\sum_{q=1}^n \alpha_q} \right) \beta_{32} + 2 \left(\frac{\sum_{q=1}^n \alpha_q x_q}{\sum_{q=1}^n \alpha_q} \right) \beta_{22} - \frac{a_{10}^{(3)} C_2^2 \sin^2(d_- \nu_2) \nu_2^4 \cos^2(d_+ \nu_2)}{2} + \frac{a_{20}^{(3)} C_2^2 \sin^2(d_- \nu_2) \nu_2^3 \sin(d_+ \nu_2) \cos(d_+ \nu_2)}{2},$$

$$\tilde{\beta}_{12} = \frac{a_{10}^{(1)} k_{20} C_1^2 \sin^2(d_+ \nu_1) \nu_1^2 \cos^2(d_- \nu_1)}{2i\sqrt{\nu_2^2 - \nu_1^2}} + a_{10}^{(1)} k_{20} g_x^- - 3 \left(\frac{\sum_{q=1}^n \alpha_q x_q^2}{\sum_{q=1}^n \alpha_q} \right) \tilde{\beta}_{32} + 2 \left(\frac{\sum_{q=1}^n \alpha_q x_q}{\sum_{q=1}^n \alpha_q} \right) \tilde{\beta}_{22} - \frac{a_{10}^{(3)} C_2^2 \sin^2(d_+ \nu_2) \nu_2^4 \cos^2(d_- \nu_2)}{2} - \frac{a_{20}^{(3)} C_2^2 \sin^2(d_+ \nu_2) \nu_2^3 \sin(d_- \nu_2) \cos(d_- \nu_2)}{2}.$$

Particular solution of inhomogeneous equation can be obtained by integrating:

$$v_{10}(\xi) = \frac{a_{10}^{(1)} C_2^2 \nu_2^2 \sin^2(d_- \nu_2) \cos^2(d_+ \nu_2)}{2} \cdot \widehat{Y}_1(\xi) + \frac{a_{10}^{(1)} C_2^2 \nu_2^2 \sin^2(d_+ \nu_2) \cos^2(d_- \nu_2)}{2} \cdot \widehat{Y}_1(\xi^*),$$

$$\begin{aligned} & \tilde{v}_{30}(\xi) = -\nu_2^2 \frac{a_{10}^{(1)} C_1^2 \nu^2 \sin^2(d_- \nu) \cos^2(d_+ \nu)}{2} \\ & \times \begin{cases} \left(\sum_{q=1}^n \alpha_q \right) \frac{1}{8} \rho^3 \sin \theta + \left(\sum_{q=1}^n \alpha_q \frac{\omega_q^2}{8} \right) \rho \ln \rho \sin \theta - \frac{1}{8} \left(\sum_{q=1}^n \alpha_q \left(\frac{\omega_q^2 x_q^2}{4} + \frac{\omega_q^4}{16} \right) \right) \rho^{-1} \sin 3\theta - \dots, & \xi_2 > 0, \\ - \left(\sum_{q=1}^n \alpha_q \frac{\omega_q^2}{8} \right) \rho \ln \rho \sin \theta + \frac{1}{8} \left(\sum_{q=1}^n \alpha_q \left(\frac{\omega_q^2 x_q^2}{4} + \frac{\omega_q^4}{16} \right) \right) \rho^{-1} \sin 3\theta + \dots, & \xi_2 < 0, \end{cases} \\ & -\nu_2^2 \frac{a_{10}^{(1)} C_2^2 \nu_2^2 \sin^2(d_+ \nu_2) \cos^2(d_- \nu_2)}{2} \\ & \times \begin{cases} \left(\sum_{q=1}^n \alpha_q \frac{\omega_q^2}{8} \right) \rho \ln \rho \sin \theta - \frac{1}{8} \left(\sum_{q=1}^n \alpha_q \left(\frac{\omega_q^2 x_q^2}{4} + \frac{\omega_q^4}{16} \right) \right) \rho^{-1} \sin 3\theta - \dots, & \xi_2 > 0, \\ - \left(\sum_{q=1}^n \alpha_q \right) \frac{1}{8} \rho^3 \sin \theta - \left(\sum_{q=1}^n \alpha_q \frac{\omega_q^2}{8} \right) \rho \ln \rho \sin \theta + \frac{1}{8} \left(\sum_{q=1}^n \alpha_q \left(\frac{\omega_q^2 x_q^2}{4} + \frac{\omega_q^4}{16} \right) \right) \rho^{-1} \sin 3\theta + \dots, & \xi_2 < 0. \end{cases} \end{aligned}$$

Finally, we obtain full solution for $\xi_2 > 0$:

$$\begin{aligned}
 v_{30}(\xi) &= \beta_{21}\rho^2 \cos 2\theta + \beta_{11}\rho \cos \theta + \beta_{32}\rho^3 \sin 3\theta + \beta_{22}\rho^2 \sin 2\theta + \beta_{12}\rho \sin \theta \\
 &- \nu_2^2 \frac{a_{10}^{(1)} C_2^2 \nu_2^2 \sin^2(d_-\nu_2) \cos^2(d_+\nu_2)}{2} \times \left[\begin{aligned} &\left(\sum_{q=1}^n \alpha_q \right) \frac{1}{8} \rho^3 \sin \theta + \left(\sum_{q=1}^n \alpha_q \frac{\omega_q^2}{8} \right) \rho \ln \rho \sin \theta \\ &- \frac{1}{8} \left(\sum_{q=1}^n \alpha_q \left(\frac{\omega_q^2 x_q^2}{4} + \frac{\omega_q^4}{16} \right) \right) \rho^{-1} \sin 3\theta - \dots \end{aligned} \right] \\
 &- \nu_2^2 \frac{a_{10}^{(1)} C_2^2 \nu_2^2 \sin^2(d_+\nu_2) \cos^2(d_-\nu_2)}{2} \cdot \left[\begin{aligned} &\left(\sum_{q=1}^n \alpha_q \frac{\omega_q^2}{8} \right) \rho \ln \rho \sin \theta \\ &- \frac{1}{8} \left(\sum_{q=1}^n \alpha_q \left(\frac{\omega_q^2 x_q^2}{4} + \frac{\omega_q^4}{16} \right) \right) \rho^{-1} \sin 3\theta - \dots \end{aligned} \right] \\
 &+ \sum_{j=1}^{\infty} (\beta_{12} b_{1j}^+ + \tilde{\beta}_{12} b_{1j}^- + \beta_{22} b_{2j}^+ + \tilde{\beta}_{22} b_{2j}^- + \beta_{32} b_{3j}^+ + \tilde{\beta}_{32} b_{3j}^-) \rho^{-j} \sin j\theta \\
 &+ \sum_{j=1}^{\infty} (\beta_{11} a_{1j}^+ - \tilde{\beta}_{11} a_{1j}^- + \beta_{21} a_{2j}^+ + \tilde{\beta}_{21} a_{2j}^-) \rho^{-j} \cos j\theta.
 \end{aligned}$$

For $\xi_2 < 0$, one has:

$$\begin{aligned}
 v_{30}(\xi) &= \tilde{\beta}_{21}\rho^2 \cos 2\theta + \tilde{\beta}_{11}\rho \cos \theta - \tilde{\beta}_{32}\rho^3 \sin 3\theta - \tilde{\beta}_{22}\rho^2 \sin 2\theta - \tilde{\beta}_{12}\rho \sin \theta \\
 &- \nu_2^2 \frac{a_{10}^{(1)} C_2^2 \nu_2^2 \sin^2(d_-\nu_2) \cos^2(d_+\nu_2)}{2} \times \left[\begin{aligned} &- \left(\sum_{q=1}^n \alpha_q \frac{\omega_q^2}{8} \right) \rho \ln \rho \sin \theta + \\ &+ \frac{1}{8} \left(\sum_{q=1}^n \alpha_q \left(\frac{\omega_q^2 x_q^2}{4} + \frac{\omega_q^4}{16} \right) \right) \rho^{-1} \sin 3\theta + \dots \end{aligned} \right] \\
 &- \nu_2^2 \frac{a_{10}^{(1)} C_2^2 \nu_2^2 \sin^2(d_+\nu_2) \cos^2(d_-\nu_2)}{2} \times \left[\begin{aligned} &- \left(\sum_{q=1}^n \alpha_q \right) \frac{1}{8} \rho^3 \sin \theta - \left(\sum_{q=1}^n \alpha_q \frac{\omega_q^2}{8} \right) \rho \ln \rho \sin \theta + \\ &+ \frac{1}{8} \left(\sum_{q=1}^n \alpha_q \left(\frac{\omega_q^2 x_q^2}{4} + \frac{\omega_q^4}{16} \right) \right) \rho^{-1} \sin 3\theta + \dots \end{aligned} \right] \\
 &+ \sum_{j=1}^{\infty} (-\beta_{12} b_{1j}^+ - \tilde{\beta}_{12} b_{1j}^- - \beta_{22} b_{2j}^+ - \tilde{\beta}_{22} b_{2j}^- - \beta_{32} b_{3j}^+ - \tilde{\beta}_{32} b_{3j}^-) \rho^{-j} \sin j\theta \\
 &+ \sum_{j=1}^{\infty} (\beta_{11} a_{1j}^+ - \tilde{\beta}_{11} a_{1j}^- + \beta_{21} a_{2j}^+ + \tilde{\beta}_{21} a_{2j}^-) \rho^{-j} \cos j\theta.
 \end{aligned}$$

Matching terms of order $\rho^{-1} \sin \theta$, one obtains:

$$\begin{aligned}
 \mp a_{10}^{(1)} \alpha_q \frac{1}{\pi} k_{40} \pm a_{10}^{(3)} \alpha_q \frac{\nu_2^2}{2\pi} k_{20} &= \\
 \pm \nu_2^2 \frac{a_{10}^{(1)} C_2^2 \nu_2^2 [\sin^2(d_-\nu_2) \cos^2(d_+\nu_2) + \sin^2(d_+\nu_2) \cos^2(d_-\nu_2)]}{2} \cdot \left[\frac{3}{8} \left(\sum_{p=1}^n \alpha_p \left(\frac{\omega_p^2 x_p^2}{4} + \frac{\omega_p^4}{16} \right) \right) \right] \\
 \pm (\beta_{12} b_{11}^+ + \tilde{\beta}_{12} b_{11}^- + \beta_{22} b_{21}^+ + \tilde{\beta}_{22} b_{21}^- + \beta_{32} b_{31}^+ + \tilde{\beta}_{32} b_{31}^-) &\Rightarrow \\
 -a_{10}^{(1)} \alpha_q \frac{1}{\pi} k_{40} + a_{10}^{(3)} \alpha_q \frac{\nu_2^2}{2\pi} k_{20} &= \nu_2^2 \frac{3a_{10}^{(1)} C_2^2 \nu_2^2 S_+}{16} \cdot \left(\sum_{p=1}^n \alpha_p \left(\frac{\omega_p^2 x_p^2}{4} + \frac{\omega_p^4}{16} \right) \right) - \left(\sum_{p=1}^n \alpha_p \frac{3\omega_p^4}{16} \cdot \frac{a_{10}^{(1)} C_2^2 \nu_2^4 S_+}{48} \right) \\
 + \left(\sum_{p=1}^n \alpha_p \frac{\omega_p^2}{4} \right) &\left[\begin{aligned} &\frac{a_{10}^{(1)} k_{20} C_1^2 \nu_1^2}{2i \sqrt{\nu_2^2 - \nu_1^2}} S_+ + a_{10}^{(1)} (g_x^+ + g_x^-) \cdot k_{20} + \frac{a_{10}^{(1)} C_2^2 \nu_2^4}{16} S_+ \\ &+ \frac{a_{20}^{(3)} C_2^2 \nu_2^3}{2} (\sin^2(d_-\nu_2) \sin(d_+\nu_2) \cos(d_+\nu_2) - \sin^2(d_+\nu_2) \sin(d_-\nu_2) \cos(d_-\nu_2)) \\ &- 3 \left(\frac{\sum_{q=1}^n \alpha_q x_q^2}{\sum_{q=1}^n \alpha_q} \right) \frac{a_{10}^{(1)} C_2^2 \nu_2^4}{48} S_+ + 2 \left(\frac{\sum_{q=1}^n \alpha_q x_q}{\sum_{q=1}^n \alpha_q} \right) 3 \left(\frac{\sum_{q=1}^n \alpha_q x_q}{\sum_{q=1}^n \alpha_q} \right) \frac{a_{10}^{(1)} C_2^2 \nu_2^4}{48} S_+ \end{aligned} \right],
 \end{aligned}$$

where $S_{\pm} = \sin^2(d_-\nu_2) \cos^2(d_+\nu_2) \pm \sin^2(d_+\nu_2) \cos^2(d_-\nu_2)$.

As we can see this system of equations is not linear because of expressions like $\left(\frac{\sum_{p=1}^n \alpha_p x_p^2}{\sum_{p=1}^n \alpha_p} \right)$. That's why we

will consider only imaginary part of both sides and it will make system actually linear:

$$\begin{aligned} -a_{10}^{(1)} \alpha_q \frac{1}{\pi} \text{Im}k_{40} &= \left(\sum_{p=1}^n \alpha_p \frac{\omega_p^2}{4} \right) \left[-\frac{a_{10}^{(1)} k_{20} C_1^2 \nu_1^2}{2\sqrt{\nu_2^2 - \nu_1^2}} (\sin^2(d_- \nu_1) \cos^2(d_+ \nu_1) + \sin^2(d_+ \nu_1) \cos^2(d_- \nu_1)) \right] \Rightarrow \\ \beta \alpha_q &= \sum_{p=1}^n \alpha_p \frac{\omega_p^2}{4}, \quad \beta = \frac{2\sqrt{\nu_2^2 - \nu_1^2} \text{Im}k_{40}}{\pi k_{20} C_1^2 \nu_1^2 (\sin^2(d_- \nu_1) \cos^2(d_+ \nu_1) + \sin^2(d_+ \nu_1) \cos^2(d_- \nu_1))} \Rightarrow \\ \sum_{q=1}^n c_{\omega_q} &= \frac{2\sqrt{\nu_2^2 - \nu_1^2} \text{Im}k_{40}}{\pi k_{20} C_1^2 \nu_1^2 (\sin^2(d_- \nu_1) \cos^2(d_+ \nu_1) + \sin^2(d_+ \nu_1) \cos^2(d_- \nu_1))} \Rightarrow \\ \text{Im}k_{40} &= \frac{-\pi^2 C_1^2 \nu_1^2 C_2^2 \nu_2^2 (1 - \cos(2d_- \nu_1) \cos(2d_+ \nu_1)) (1 - \cos(2d_- \nu_2) \cos(2d_+ \nu_2))}{8\sqrt{\nu_2^2 - \nu_1^2}} \left(\sum_{q=1}^n c_{\omega_q} \right)^2. \end{aligned}$$

We can compare this formula with result from single-window case:

$$\text{Im}k_{40} = \frac{-\pi^2 C_1^2 \nu_1^2 C_2^2 \nu_2^2}{128\sqrt{\nu_2^2 - \nu_1^2}} (1 - \cos(2d_- \nu_1) \cos(2d_+ \nu_1)) (1 - \cos(2d_- \nu_2) \cos(2d_+ \nu_2))$$

and verify it is absolutely consistent, the difference is just in multiplier $\left(\sum_{q=1}^n c_{\omega_q} \right)^2$ characterizing common size of windows. As usual, it is the square of the coefficient appearing in the first order term.

4. Conclusion

The results for the imaginary part of the resonance allow us to pose the problem of minimizing/maximizing the lifetime of the resonance by changing the configuration of the windows, e.g., fixing the summary size of windows. The results pertaining to the real part of the resonance, give one an estimation of the shift of resonance with respect to the threshold. These results can be useful for the description of “quantum waveguide – quantum dot – quantum waveguide” systems. One can find such systems in different nanotechnology applications.

References

- [1] Lord Rayleigh O.M. The theory of Helmholtz Resonator. *Proceeding of Royal Society*, 1916, **638**, P. 265–275.
- [2] Morse F.M. Feshbach G. *Methods of Theoretical Physics*, V. 2. Foreign Literature Publishing House, 1960, 986 p.
- [3] Kiselev A.A., Pavlov B.S. The eigenfrequencies and eigenfunctions of the Laplace operator of the Neumann problem in a system of two coupled resonators. *Theor. Math. Phys.*, 1994, **100**(3), P. 354–366.
- [4] Gadyl'shin R.R. The existence and asymptotics of poles with a small imaginary part for the Helmholtz resonator. *Uspekhi of Mathematical Sciences*, 1997, **52**(313), P. 71–72.
- [5] Borisov D.I. Discrete spectrum of an asymmetric pair of waveguides coupled through a window. *Sb. Math.*, 2006, **197**(4), P. 475–504.
- [6] Achilleos V., Richoux O., et al. Acoustic solitons in waveguides with Helmholtz resonators: Transmission line approach. *Phys.Rev. E.*, 2015, **91**, P. 023204.
- [7] Martinez A., Nedelec L. Optimal lower bound of the resonance widths for a Helmholtz tube-shaped resonator. *J. Spectral Th.*, 2012, **2**, P. 203–223.
- [8] Gadyl'shin R.R. A two-dimensional analogue of the Helmholtz resonator with ideally rigid walls. *Diff. Uravn.*, 1994, **30**(2), P. 221–229. Translation in: *Diff. Eq.*, 1994, **30**(2), P. 201–209.
- [9] Gadyl'shin R.R. Influence of the position of the opening and its shape on the properties of a Helmholtz resonator. *Theor. Math. Phys.*, 1992, **93**, P. 1151–1159.
- [10] Borisov D., Exner P. Distant perturbation asymptotics in window-coupled waveguides. I. The non-threshold case. *J. Math. Phys.*, 2006, **47**(10), P. 113502(1-24).
- [11] Popov I. Asymptotics of bound states and bands for laterally coupled waveguides and layers. *J. Math. Phys.*, 2002, **43**, P. 215–234.
- [12] Borisov D.I., Gadyl'shin R.R. On the spectrum of the Laplacian with frequently alternating boundary conditions. *Theor. Math. Phys.*, 1999, **118**(3), P. 272–277.
- [13] Briet Ph., Dittrich J., Soccorsi E. Scattering through a straight quantum waveguide with combined boundary conditions. *J. Math. Phys.*, 2014, **55**, P. 112104.
- [14] Ilyin A.M. *Matching of the asymptotic expansions of solutions*. Science, Moscow, 1989, 336 p.
- [15] Exner P., Kreicirik D. Waveguides coupled through a semitransparent barrier: a Birman-Schwinger analysis. *Rev. Math. Phys.*, 2001, **13**, P. 307–334.
- [16] Exner P., Kreicirik D. Quantum waveguides with a lateral semitransparent barrier: spectral and scattering properties. *J. Phys. A*, 1999, **32**, P. 4475.

- [17] Popov I.Yu. The extension theory, domains with semitransparent surface and the model of quantum dot. *Proc. Royal Soc. London A.*, 1996, **452**(1950), P. 1505–1515.
- [18] Popov I.Y. Model of a quantum point as a cavity with semitransparent boundary. *Physics of the Solid State*, 1994, **36**(7), P. 1918–1922.
- [19] Popov I.Yu. The extension theory and the opening in semitransparent surface. *J. Math. Phys.*, 1992, **33**(5), P. 1685–1689.
- [20] Ikebe T., Shimada S. Spectral and scattering theory for the Scrodinger operator with penetrable wall potentials. *J.Math. Kyoto Univ.*, 1991, **31**(1), P. 219–258.
- [21] Popov I.Y., Trifanova E.S., Vorobiev A.M. 2D waveguides asymptotics of eigenvalue induced by a window in a semitransparent separating wall. *Bulletin of the Transilvania University of Brasov, Series III: Mathematics, Informatics, Physics*, 2021, **63**(1), P. 221–230.
- [22] Vorobiev A.M., Popov I.Y. Resonances in two-dimensional quantum waveguides separated by semitransparence wall with small window. *Technical Physics Letters*, 2021, **47**(9), P. 847–849.
- [23] Exner P., Kondej S., Lotoreichik V. Asymptotics of the bound state induced by delta-interaction supported on a weakly deformed plane. *J. Math. Phys.*, 2018, **59**, P. 013051.
- [24] Behrndt J., Exner P., et.al. Approximation of Schroedinger operators with delta-interactions supported on hypersurfaces. *Math. Nachr.*, 2017, **290**, P. 12151248.
- [25] Popov I.Yu. The operator extension theory, semitransparent surface and short range potential. *Math. Proc. Cambridge Phil. Soc.*, 1995, **118**, P. 555–563.
- [26] Tikhonov A.N., Samarskii A.A. *Equations of Mathematical Physics*. M.: Science, 1972, 531 p.

The effect of hydrolysis duration on the phase composition, texture, aggregation and agglomeration of ZrO₂ nanoparticles

Sh. O. Omarov

Ioffe Institute, Saint Petersburg, 194021, Russia

somarov@mail.ioffe.ru

PACS 81.20.-n, 61.46.+w, 81.10.-h, 64.70K

DOI 10.17586/2220-8054-2021-12-4-472-480

In this work, a number of ZrO₂ · nH₂O and ZrO₂ samples were synthesized by direct precipitation and hydrolysis with different duration (36 and 61 h) followed by neutralization and thermal treatment. The prepared samples were analyzed using DT-TGA, PXRD, N₂ physisorption and LD methods. The dependence of the size of crystallites and secondary particles, phase composition, texture, and particle morphology on the amount of zirconium hydrolyzed to form *m*-ZrO₂ is shown. The possibility of regulating the phase composition of ZrO₂ has been established while maintaining the specific surface area (110 – 120 m²/g), as well as creating a hierarchical system of micro-mesopores. The mechanism of the ZrO₂ · nH₂O formation during hydrolysis and precipitation is considered. The size of the critical nucleus is estimated (1.5 – 2 nm).

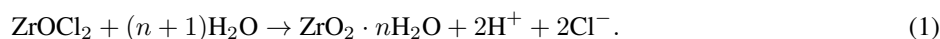
Keywords: zirconia, hydrolysis, phase composition, texture, aggregation, agglomeration, mechanism.

Received: 18 July 2018

1. Introduction

Zirconia has found application in the production of ceramic and catalysts, incl. those used in industrial applications [1–3]. It is considered that the tetragonal modification of ZrO₂ (*t*-ZrO₂) is preferable because it has a better porous structure, developed surface acidity, and defective structure. It was however shown [4, 5] that catalysts based on the monoclinic modification (*m*-ZrO₂) are more active but less stable by time on stream. Therefore, it is urgent to study in detail the possibility of obtaining *m*-ZrO₂ with a more developed porous structure and to study the possibility of obtaining and controlling the *t*-ZrO₂/*m*-ZrO₂ ratio.

Precipitation from aqueous solutions of salts is the main method for the synthesis of ZrO₂, during which nanosized X-ray amorphous hydrous zirconia (ZrO₂ · nH₂O) is formed. This is an effective method for the preparation of *t*-ZrO₂ nanocrystallites with a developed mesoporous structure, which is formed during thermal treatment at 350 – 450 °C. There are other methods: hydrolysis of aqueous solutions of salts [6–9], hydrothermal treatment [10], solution combustion [11], thermal decomposition of salts [12], heterophase conversion [13], etc. Matsui et al. [6–9] showed that a sol consisting of *m*-ZrO₂ nanoparticles (crystallites 2.2 – 4.9 nm, agglomerates 100 – 200 nm) is formed upon the long-term maintenance of a ZrOCl₂ solution at 100 °C during complete hydrolysis of the salt. The hydrolysis reaction proceeded as follows:



This method makes it possible to obtain phase-purified *m*-ZrO₂. However, the results on the porous structure are absent in the listed works, and in [5] and other similar studies, only the value of the specific surface area is given. Salt concentration, temperature and duration of hydrolysis are the most important parameters of synthesis [9]. Extraneous cations (Al³⁺, Ca²⁺) have no effect [7], while the presence of HCl, NaCl, NH₄OH allows regulation of the rate and completeness of hydrolysis, crystallite size and agglomerates of *m*-ZrO₂ due to a decrease in the effect of the electric double layer and an increase in heterocoagulation [6–8]. However, the intermediate states remained unexplored, when only a part of the primary forms of zirconium passed into the sol during complete hydrolysis. The residual solution can be neutralized with a base solution, thus allowing the phase composition of ZrO₂ to be adjusted.

In this work, the effect of the hydrolysis duration of a ZrOCl₂ solution, additionally neutralized with an NH₄OH solution, on the structural and morphological properties of ZrO₂ · nH₂O and ZrO₂ is analyzed. The phase composition, crystallite size, porous structure and agglomeration during neutralization are studied by a complex of physicochemical methods to establish the formation mechanism, and to assess the possibility of obtaining ZrO₂ with the required porous structure. The obtained results and the formation mechanism are discussed from the point of view of non-classical concepts of nucleation and crystal growth.

2. Experimental

2.1. Synthesis technique

A 0.2 M $ZrOCl_2$ solution was used as the initial solution. For this, 25.78 g of $ZrOCl_2 \cdot 8H_2O$ was dissolved in 200 ml of doubly distilled water and the volume of the solution was brought to 400 ml ($\rho = 1.027 \text{ g/cm}^3$). The hydrolysis was carried out in a three-necked borosilicate glass flask in a batch mode (8 h at $(100 \pm 1)^\circ\text{C}$ – 16 h at room temperature). The timing began when the solution temperature reached 95°C . Sol samples with a volume of 95 ml were taken after 36 ± 2 and 61 ± 3 h. The final hydrolysis time of the remaining sol was 126 ± 4 h. The resulting sols were neutralized by adding a 13 M ammonia solution ($\rho = 0.909 \text{ g/cm}^3$ at 20°C) to $\text{pH} = 9.1$. The preparation of $ZrO_2 \cdot nH_2O$ by direct precipitation from a 0.6 M $ZrOCl_2$ solution with a 13 M ammonia solution is described in [1].

Then the mother liquor was vacuum filtered using a Buchner funnel. The resulting mass was washed via decantation until there was no Cl^- ($\sim 0.2 \text{ L H}_2\text{O} / \text{g ZrO}_2$, controlled with 0.1 N AgNO_3). After washing, the mother liquor was squeezed out, and the resulting mass was dried for 4 h at 60°C and 1 h at 90°C . To study the pore structure and phase composition of ZrO_2 , the $ZrO_2 \cdot nH_2O$ samples were subjected to thermal treatment in a muffle furnace in the stepwise mode of 170°C , 0.5 h; 250°C , 0.5 h; $300 - 500^\circ\text{C}$, 0.5 h. The temperature growth rate was 4°C/min . The samples are denoted as $ZrO_2\text{-}P/H(x)\text{-}y$, where P – precipitation method, $H(x)$ – hydrolysis method and its duration, h , y – treatment temperature, $^\circ\text{C}$.

2.2. Characterization methods

Synchronous thermal analysis of $ZrO_2 \cdot nH_2O$ samples was conducted on a Shimadzu DTG-60A thermal analyzer. The weighed portion of a sample was 16 – 20 mg; the material of the crucibles and the reference was corundum; the heating rate was 10°C/min . The heat of crystallization data was used to determine the proportion of ZrO_2 that passed into the solid phase as a result of hydrolysis:

$$a_H = \left(1 - \frac{\Delta Q(ZrO_2 - H(x))}{\Delta Q(ZrO_2 - P)} \times 100\% \right). \quad (2)$$

Characteristics of the pore structure of $ZrO_2 \cdot nH_2O$ and ZrO_2 were identified via the low-temperature sorption of N_2 on a Quantachrome Autosorb 6iSA instrument at 77 K. Before analysis, the samples were degassed in vacuum for 1 h at 100°C (for $ZrO_2 \cdot nH_2O$) or 250°C (for ZrO_2). Specific surface area (S_{BET} , m^2/g) was calculated using the Brunauer–Emmett–Teller (BET) technique; total pore volume (V_Σ , cm^3/g) was determined from the limiting value of absorbed N_2 at $p/p_0 = 0.97$; pore size distribution was calculated according to the density functional theory [14].

The phase composition and crystalline size of the ZrO_2 samples were studied by powder X-ray diffraction on a Shimadzu XRD-6100 diffractometer (Cu anode, Ni filter) using $D:S:R = 0.5^\circ : 0.5^\circ : 0.15 \text{ mm}$ slits in the step of 0.02° with an acquisition time of 3 s per point. The volume fraction of the tetragonal phase ($t\text{-}ZrO_2$, V_t , vol.%) was calculated as described in [15]. The Scherrer equation ($K = 0.94$; $\lambda(\text{CuK}\alpha_1) = 0.15406 \text{ nm}$) was used to calculate the crystalline size of $t\text{-}ZrO_2$ (d_t , nm) and $m\text{-}ZrO_2$ (d_m , nm).

The size distribution of particles in the as-synthesized $ZrO_2 \cdot nH_2O$ sols and colloidal suspensions were investigated by laser diffraction (LD) on a “Shimadzu SALD-2300” particle size analyzer. For this, colloidal suspensions of the samples were prepared by mixing 80 mg of the product with 250 mL of distilled water and sonicating the mixture for 3 min by a 700 W ultrasonic disperser. The Refractive index was 1.85.

3. Results and discussion

3.1. Simultaneous TG-DTA

Fig. 1 and Table 1 shows results from simultaneous thermal analysis of $ZrO_2 \cdot nH_2O$ samples. Two regions can be distinguished from the differential thermal curves.

In the first region ($20 - 300^\circ\text{C}$), $ZrO_2 \cdot nH_2O$ underwent two steps of dehydration: the desorption of unbound water (Δm_1) and the removal of structural water during the thermal decomposition of oxyhydroxide (Δm_2) [16]. An increase in the hydrolysis duration leads to a non-monotonic increase in the amount of structural water and the total amount of water n (Table 1). Wherein the content of unbound water changes insignificantly. The $ZrO_2\text{-}H(36)$ sample has the highest hydration, and the $ZrO_2\text{-}H(126)$ sample has the lowest.

Crystallization of X-ray amorphous ZrO_2 ($a\text{-}ZrO_2$) obtained after dehydration of $ZrO_2 \cdot nH_2O$ occurs in the second region ($370 - 470^\circ\text{C}$). Here, weight loss (Δm_3) is also observed, which does not depend on the hydrolysis duration. The $ZrO_2\text{-}P$ sample obtained by precipitation is characterized by the maximum heat of crystallization of $a\text{-}ZrO_2$ (ΔQ). The crystallization peak of $a\text{-}ZrO_2$ for the $ZrO_2\text{-}H(126)$ sample is insignificant. The ΔQ value and the crystallization onset temperature (T_{init}) decrease with increasing the hydrolysis duration (Table 1). This regularity indicates an increase in the content of the hydrolysis product and, accordingly, a decrease in the content of $a\text{-}ZrO_2 \cdot nH_2O$, formed

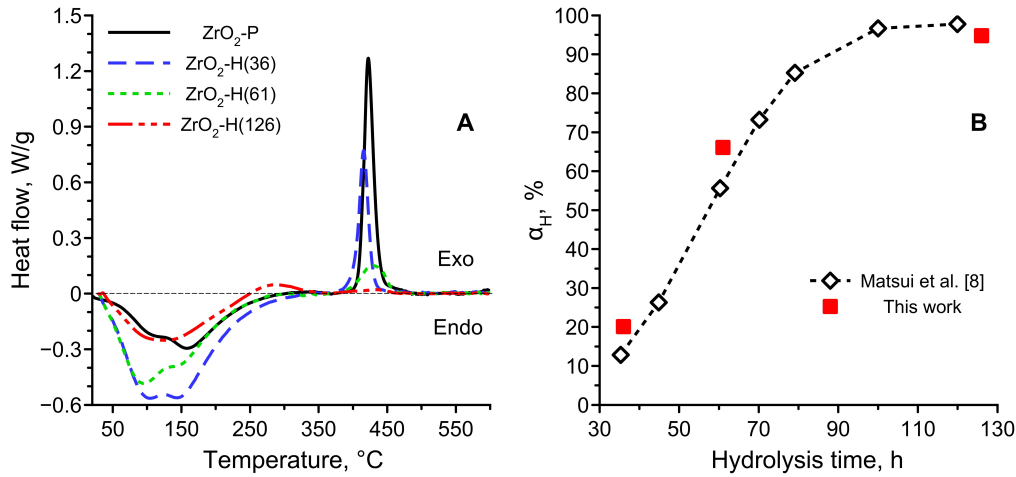


FIG. 1. DT-curves of samples (A) and results of determining the fraction of hydrolyzed zirconia

TABLE 1. Results from the simultaneous TG-DTA of $ZrO_2 \cdot nH_2O$

Sample	nH_2O^*	Weight loss, wt%			α - ZrO_2 crystallization	
		Δm_1	Δm_2	Δm_3	ΔQ , J/g ZrO_2	T_{init} , °C
		20 – 125 °C	125 – 300 °C	300 – 800 °C		
ZrO ₂ -P	1.16	2.4	9.7	2.4	130	411
ZrO ₂ -H(36)	1.54	3.6	11.6	3.2	102	402
ZrO ₂ -H(61)	1.20	4.0	7.4	3.4	43	397
ZrO ₂ -H(126)	0.80	2.1	5.2	3.2	~ 7	–

$$*n = \frac{6.85 \cdot \Delta m}{100 - \Delta m}, \text{ where } \Delta m - \text{total weight loss, wt\%}$$

during the neutralization of partially hydrolyzed solutions. The change in the heat of crystallization made it possible to estimate the amount of $ZrO_2 \cdot nH_2O$ (α_H) formed during complete hydrolysis (Fig. 1B). Comparison with the results [6–9], which determined α_H by chelation titration, shows a similar dependence and close absolute values of α_H .

3.2. Powder X-Ray diffraction

The results of X-ray diffraction are shown in Fig. 2 and Table 2. The ZrO₂-P sample obtained by precipitation is characterized by an X-ray amorphous state, which corresponds to the halo (Fig. 2A). The content of the poorly crystallized m -ZrO₂ phase in the resulting precipitates increased with longer hydrolysis durations. The formation of a mixture of m -ZrO₂ · nH_2O and α -ZrO₂ · nH_2O (hydrolysis duration of 36 and 61 h) was associated with the partial formation of m -ZrO₂ during hydrolysis of ZrOCl₂, as well as the precipitation from residual ZrOCl₂ upon neutralization with an ammonia solution, respectively. This was consistent with the results of TG-DTA: the content of the crystalline m -ZrO₂ increases with lengthening the hydrolysis duration. The crystallite size (coherent scattering region) of m -ZrO₂ increased with the hydrolysis duration reaching 3.4 nm (Table 2) upon hydrolysis for 126 h, which was consistent with prior results [8].

Significant changes in the phase composition and crystallite size of the ZrO₂-P sample occurred after thermal treatment at 450 °C, which corresponds to the completion of the α -ZrO₂ crystallization: a mixture of t - and m -ZrO₂ is formed with a predominance of t -ZrO₂ (Fig. 2B). The fraction of m -ZrO₂ increased, and the size of the crystallites of m -ZrO₂ and t -ZrO₂ decreased with longer hydrolysis times in the samples thermally-treated at 450 °C (Table 2).

The formation of metastable t -ZrO₂ during crystallization and its further polymorphic transformation into m -ZrO₂ is explained by the structural similarity of α -ZrO₂ and t -ZrO₂ [17], and the achievement of the critical crystallite size of about 30 nm, previously obtained [18] based on thermodynamic considerations about the influence of surface energy, respectively. However, the critical size of the t -ZrO₂ crystallite depends on the conditions of synthesis, and subsequent processing of ZrO₂ and can be much less than 30 nm [19]. The crystallite size of t -ZrO₂ is different for

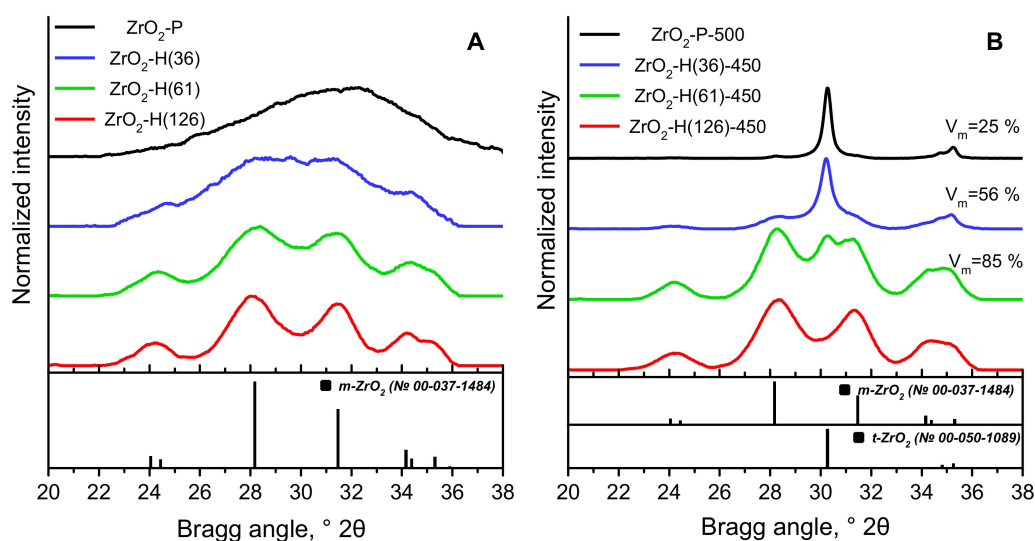


FIG. 2. XRD results of the as-prepared (A) and thermal treatment samples (B)

TABLE 2. m -ZrO₂ crystalline size (d_t given in parentheses)

Hydrolysis duration, h	Thermal treatment, °C					
	100	300	350	450	500	600
0 (precipitation)	< 2	–	–	–	13.9 (24.1)	–
36	2.1	–	3.6	5.3 (14.4)	–	–
61	3.1	–	3.9	5.5 (8.3)	–	–
126	3.4	3.7	3.8	4.2	4.4	5.8

samples that differ in the duration of hydrolysis and heat-treated at 450 – 500 °C (Table 2). The imposition of the kinetic factor proposed in [20], namely, only a part of the crystallites with a size above a critical value pass into a new phase, explain the observed decrease in d_t . The formation of m -ZrO₂ crystallites smaller than t -ZrO₂ can be explained by twinning [21].

An increase in the treatment temperature of ZrO₂-H(126) leads to a gradual increase in the size of m -ZrO₂ crystallites (Table 2). A noticeable change in d_m begins to occur at $T \geq 300^\circ\text{C}$, and a sharp increase occurs at 600 °C. After crystallization of a -ZrO₂, a stronger increase in the size of m -ZrO₂ crystallites occurs than with an increase in temperature from 100 to 350 °C in the case of samples with an intermediate duration of hydrolysis. This is due to the contribution of the t -ZrO₂ → m -ZrO₂ transition, which results in the formation of larger m -ZrO₂ crystallites.

4. Porous structure

The results of studying the texture of samples by the N₂ physisorption method are shown in Fig. 3 and Fig. 4. The isotherm for the ZrO₂-P-500 sample obtained by precipitation belongs to type IVa with an H4 hysteresis loop, which corresponds to a mesoporous structure according to IUPAC [14]. The contribution of the type I isotherm on the isotherms of the corresponding thermally treated samples increases with lengthening the hydrolysis duration. In this case, the hysteresis loops are retained and the contribution of the type IVa isotherm is present. The listed characteristics of the isotherms indicate the presence of micro- and mesopores in the texture of the samples. For the ZrO₂-H(61)-500 sample, a change in the type of hysteresis to H3 is observed, and for which it can be assumed that the pores are formed by aggregates of plot-like particles. In samples ZrO₂-H(126)-300 and ZrO₂-H(126)-500, the hysteresis loops are small; therefore, the texture is mainly represented by micropores.

The conclusions based on the isotherms are confirmed by the results of calculating the pore size distribution curves. Samples ZrO₂-P-500 and ZrO₂-H(36)-500, in the preparation of which the precipitation product predominated, are represented by small mesopores 2 – 10 nm. The proportion of micropores simultaneously increases with the

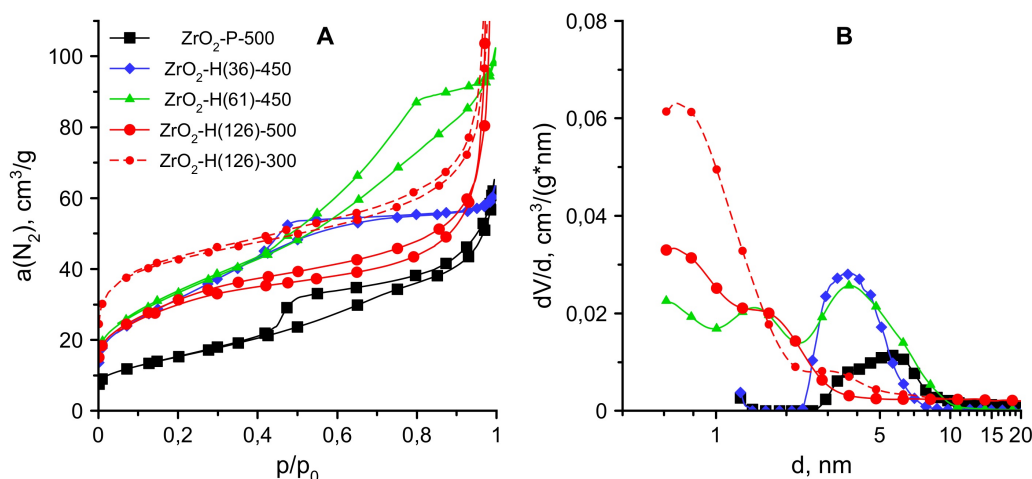


FIG. 3. N_2 physisorption isotherms (A) and pore size distribution (B) for ZrO_2 samples

contribution of hydrolysis to the formation of ZrO_2 (samples $ZrO_2-H(126)-300$ and $ZrO_2-H(126)-500$). The absorption of a large amount of nitrogen at $p/p_0 > 0.97$ is a feature of the sorption isotherms of the $ZrO_2-H(126)-300$ and $ZrO_2-H(126)-500$ samples. The corresponding pore size distribution curves show nonzero dV/d values at diameters greater than 5 nm (Fig. 3B) and the presence of a local maximum at 70 nm (not shown here). This may be due to the presence of secondary porosity formed by the gap between agglomerates (secondary particles).

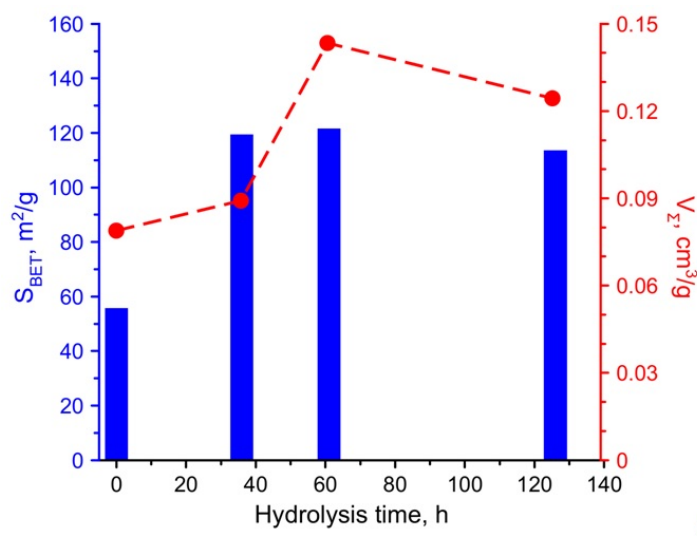


FIG. 4. Dependence of specific surface area and total pore volume vs hydrolysis duration for thermal treatment at 450 – 500 °C samples

The specific surface area of ZrO_2 increases with lengthening the hydrolysis duration (Fig. 4). A similar dependence is observed for V_{Σ} at $p/p_0 = 0.97$. The specific surface area of the $ZrO_2-H(126)$ sample obtained by complete hydrolysis decreases from 156 to 113 m^2/g , and the total pore volume from 0.149 to 0.124 cm^3/g with an increase in the treatment temperature from 300 to 500 °C. High S_{BET} and V_{Σ} correspond to loose packing of crystallites. The appearance in the phase composition of an amount of $m-ZrO_2$ comparable to the amount of $t-ZrO_2$ (sample $ZrO_2-H(36)-450$), and reduced size of $t-ZrO_2$ crystallites contribute to a noticeable increase in S_{BET} with lengthening the hydrolysis duration from 0 to 36 h (samples $ZrO_2-P-500$ and $ZrO_2-H(36)-450$, respectively). Poorly crystallized $m-ZrO_2$, which has a high S_{BET} (sample $ZrO_2-H(126)-450$), begins to make a greater contribution to S_{BET} with a further increase in the duration of hydrolysis to 61 h. The obtained S_{BET} values of $ZrO_2-H(36)-450$ and $ZrO_2-H(61)-450$ exceed the sum of S_{BET} of individual $t-ZrO_2$ and $m-ZrO_2$ samples $ZrO_2-P-500$ and $ZrO_2-H(126)-450$, respectively, taking into account their share in the phase composition.

There is an inverse proportionality between the crystallite size of the phases and S_{BET} according to the ratio:

$$d_{Ads} = \frac{A}{S_{BET} \times \rho}, \quad (3)$$

where ρ – density, A – coefficient depending on the shape of the crystallites. The calculation of d_{Ads} according to formula (3) and data on S_{BET} taking into account the density of the predominant phase (6.134 g/cm³ for *t*-ZrO₂ and 5.817 g/cm³ for *m*-ZrO₂) for different morphologies of particles ($A = 6$ for spherical, $A = 4$ for rod-shaped and $A = 2$ for plate-like particles) showed that d_{Ads} values closest to d_{XRD} for samples with a predominance of *m*-ZrO₂ are achieved under the assumption of a plate-like or rod-shaped particle and in the case of the predominance of *t*-ZrO₂ assuming a spherical shape (Table 3). The order of the d_{XRD} and d_{Ads} values is the same. Consequently, the specific surface area calculated from the N₂ sorption data is determined precisely by crystallites, and the formation of larger agglomerates and aggregates does not affect its value. It should be noted that the initial non-heat treated ZrO₂-P sample with $S_{BET} = 231$ m²/g has an equivalent particle size of 1.8 nm in the approximation of lamellar morphology ($\rho = 4.86$ g/cm³ [22]), which corresponds to the PXRD result on its X-ray amorphous state (Table 2).

TABLE 3. Particle size d_{SSA} values calculated using equation (3)

Sample	d_{Ads} ($A = 6$), nm	d_{Ads} ($A = 4$), nm	d_{Ads} ($A = 2$), nm
ZrO ₂ -P	5.3	3.6	1.8
ZrO ₂ -P-500	17.5	11.6	5.8
ZrO ₂ -H36-450	8.2	5.4	2.7
ZrO ₂ -H61-450	8.5	5.6	2.8
ZrO ₂ -H126-300	6.6	4.4	2.2
ZrO ₂ -H126-500	9.1	6.1	3.0

5. Laser diffraction

The resulting dispersed systems visually differed in sedimentation and coagulation stability. The ZrO₂ · *n*H₂O sol obtained by hydrolysis of a ZrOCl₂ solution for 126 h (ZrO₂-H(126) sol, Fig. 5) was characterized by a small size of secondary particles (agglomerates 210 nm) and a narrow size distribution. The sol of this sample was characterized by sedimentation and coagulation stability since noticeable signs of sedimentation were detected after several days, and ultrasonic treatment did not affect the given distribution. The results of laser diffraction for the ZrO₂-H(126) sol agreed with the results [6], where the TEM method showed the formation of agglomerates with a size of 170 nm upon hydrolysis of a 0.2 M ZrOCl₂ solution. For the sol obtained after 36 h of hydrolysis, the distributions could not be measured due to the low concentration of particles, while for the sol obtained after 61 h of hydrolysis, the distributions differ little from the distribution for ZrO₂-H(126), and the mean diameter was 0.20 μm. Active coagulation of the primary parts with the formation of nanoscale agglomerates occurred during the first 60 h of hydrolysis, at which 60% conversion of ZrOCl₂ to *m*-ZrO₂ · *n*H₂O was achieved. The obtained results partially agree with the results [23, 24], where it was shown by the DLS method that active growth of agglomerates was observed in the first 30 – 40 h of hydrolysis, and the time interval decreased to ~20 h with an increase in the initial concentration of the ZrOCl₂ solution.

Neutralization of the resulting sol with an ammonia solution is a common technique [5, 25], which makes it possible to simplify the subsequent washing of the precipitate from Cl⁻ and separation from the mother liquor. The addition of ammonia promotes additional coagulation of the sol, the formation of aggregates larger by an order (ZrO₂-H(126) suspension, Fig. 5), and the appearance of a bimodal distribution. The lack of coagulation stability of the ZrO₂-H(126) suspension led to a gradual coarsening of the aggregates, and the size distribution became close to that of the ZrO₂-P suspension. The aggregates of particles of the sample obtained by direct precipitation (ZrO₂-P suspension, Fig. 5) had an even larger size and retained a bimodal distribution.

6. Formation mechanism

According to [26, 27], during the dissolution of ZrOCl₂ because of hydrolysis and primary polymerization, zirconium is in solution mainly in two forms, between which there is a mobile equilibrium depending on pH: [Zr₄(OH)₈(H₂O)₁₆]⁸⁺ and [Zr₈(OH)₂₀(H₂O)₂₄]¹²⁺. The 0.2 M ZrOCl₂ solution used in this work had a pH equal to

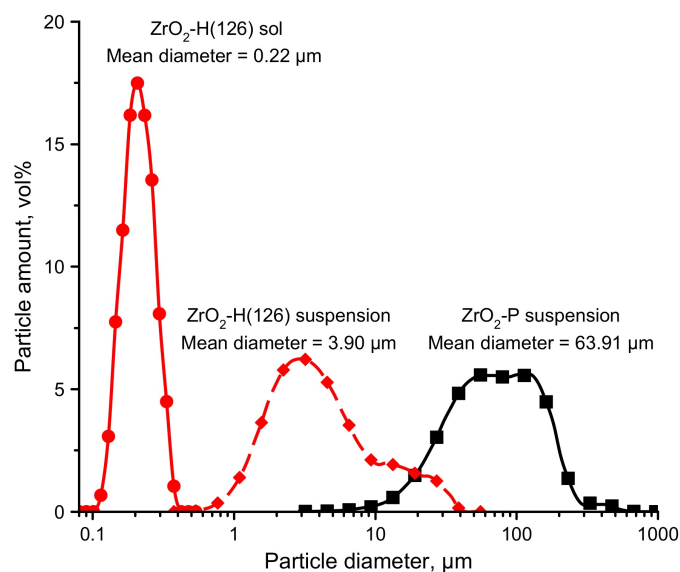


FIG. 5. Agglomerate and aggregate size distribution of the sol and suspensions

0.9 and 0.5 at 20 and 90 °C, respectively, which indicates the predominant presence of zirconium in $[\text{Zr}_4(\text{OH})_8(\text{H}_2\text{O})_{16}]^{8+}$ form. The pH of the resulting suspensions after 36, 61, and 126 h of hydrolysis was 0.4 – 0.5 at 20 °C. Consequently, the form $[\text{Zr}_4(\text{OH})_8(\text{H}_2\text{O})_{16}]^{8+}$ predominated at any time of hydrolysis.

The above data shows the following. X-ray amorphous $\text{ZrO}_2 \cdot n\text{H}_2\text{O}$ is formed during direct precipitation from a ZrOCl_2 solution and characterized by a plot-like morphology of primary particles, which are randomly folded into larger agglomerates and aggregates resulting from rapid coagulation. $\text{ZrO}_2 \cdot n\text{H}_2\text{O}$ crystallizes upon further heat treatment with the formation of predominantly *t*- ZrO_2 due to the inheritance of the structure of primary nanometer particles in $\text{ZrO}_2 \cdot n\text{H}_2\text{O}$, and the morphology of *t*- ZrO_2 crystallites is close to spherical. The porous structure is represented by micropores in *a*- $\text{ZrO}_2 \cdot n\text{H}_2\text{O}$ and mesopores in *t*- ZrO_2 .

Long-term hydrolysis of the ZrOCl_2 solution at 100 °C led to the formation of *m*- $\text{ZrO}_2 \cdot n\text{H}_2\text{O}$. A mixture of crystalline *m*- $\text{ZrO}_2 \cdot n\text{H}_2\text{O}$ and *a*- $\text{ZrO}_2 \cdot n\text{H}_2\text{O}$ with a predominance of the latter was formed after 36 h of hydrolysis and subsequent neutralization of the resulting sol with an ammonia solution. Monoclinic and tetragonal zirconia, respectively, were formed due to dehydration and crystallization during subsequent thermal treatment, and their ratio depends on the ratio of *m*- $\text{ZrO}_2 \cdot n\text{H}_2\text{O}$ and *a*- $\text{ZrO}_2 \cdot n\text{H}_2\text{O}$ in the initial precipitates. The observed excess of the content of *m*- ZrO_2 after heat treatment relative to its content in untreated mixtures of *m*- $\text{ZrO}_2 \cdot n\text{H}_2\text{O}$ and *a*- $\text{ZrO}_2 \cdot n\text{H}_2\text{O}$ maybe since *m*- ZrO_2 from *m*- $\text{ZrO}_2 \cdot n\text{H}_2\text{O}$ is a nucleus for the growth of new crystallites of *m*- ZrO_2 from *a*- $\text{ZrO}_2 \cdot n\text{H}_2\text{O}$ or accelerating the transition *t*- ZrO_2 to *m*- ZrO_2 [28].

The increased hydration of the $\text{ZrO}_2\text{-H}(36)$ sample detected by the TG-DTA method was associated with the fact that in the first 36 h of hydrolysis, the polymerization of $[\text{Zr}_4(\text{OH})_8(\text{H}_2\text{O})_{16}]^{8+}$ proceeded with the formation of a larger size polymer cluster and increased content of (OH) and (H₂O) due to olation and oxolation. A similar explanation for the induction period was suggested by Hu et al. [24] based on the results of a study of thermohydrolytic polymerization of a ZrOCl_2 solution by the SAXS method. An increase in the duration of hydrolysis led to the consumption of $[\text{Zr}_4(\text{OH})_8(\text{H}_2\text{O})_{16}]^{8+}$ and its oligomers for the growth of *m*- ZrO_2 crystallites, and a regular decrease in the hydration of the resulting product. The main growth of *m*- ZrO_2 crystallites occurred in the period from 36 to 61 h (Table 2), and the maximum CSR value was 3.4 nm. This stage is limiting. The addition of a base in the synthesis by direct precipitation seems to greatly accelerate the passage of the above steps. As a result, the olation and oxolation with the formation of oligomers are less deep, which determines the X-ray amorphous nature of the precipitation product.

The growth of agglomerates 100 – 300 nm proceeds in parallel with the process of crystallite growth. The size of the agglomerates did not change after 61 h of hydrolysis. Agglomerates were composed of plot-like and/or rod-shaped nanocrystallites of *m*- ZrO_2 and have a microporous structure. These results for the morphology of aggregates confirm the prior results of TEM by other authors [7, 24]. The plot-like and/or rod-shaped morphology of *m*- ZrO_2 particles indicated an oriented attachment of crystallites [29].

The final scheme of the sequence of the formation of $\text{ZrO}_2 \cdot n\text{H}_2\text{O}$ during hydrolysis and precipitation based on the data of this work is shown in Fig. 6.

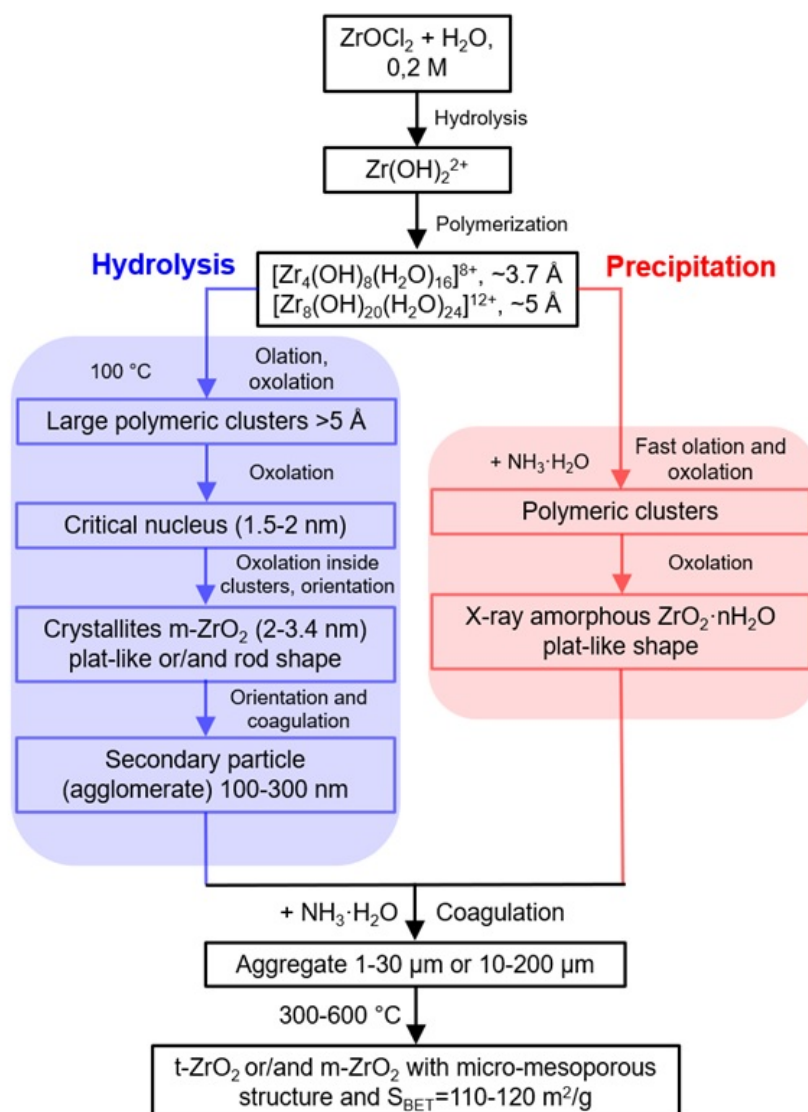


FIG. 6. Formation mechanism of $\text{ZrO}_2 \cdot n\text{H}_2\text{O}$ during hydrolysis and precipitation

The presence of polymeric zirconium hydroxocomplexes in the initial solution does not allow one to consider the formation of $\text{ZrO}_2 \cdot n\text{H}_2\text{O}$ within the framework of the classical theory of crystal growth. Comparison of the stages in Fig. 6 with nonclassical mechanisms of nucleation and growth of crystals shows that the formation of $m\text{-ZrO}_2$ during hydrolysis is the closest to the mechanism of aggregation nucleation [28]. Comparison of XRD data and adsorption-structural analysis indicated that the size of the $m\text{-ZrO}_2$ nucleus is in the range of 1.5 – 2 nm, which is 4 – 6 times greater than the gyration radius of the dominant $[\text{Zr}_4(\text{OH})_8(\text{H}_2\text{O})_{16}]^{8+}$ ($R_g = 3.7 \text{ \AA}$ [24, 27]). Rapid crystallite growth begins when the size of the $m\text{-ZrO}_2$ crystallite reaches 2.1 nm after 36 h of hydrolysis, and this value is the upper limit. The lower value depends on the size of the oligomers formed from $[\text{Zr}_4(\text{OH})_8(\text{H}_2\text{O})_{16}]^{8+}$ and its exact experimental determination by the used methods is impossible. The same range of possible critical nucleus size includes the equivalent particle size in $a\text{-ZrO}_2 \cdot n\text{H}_2\text{O}$ equal to 1.8 nm.

7. Conclusion

As a result of the work, the phase formation, texture, and morphology of $\text{ZrO}_2 \cdot n\text{H}_2\text{O}$ and ZrO_2 were studied depending on the hydrolysis duration of the ZrOCl_2 solution followed by neutralization of the sol. It was found that the above characteristics strongly depend on the completeness of the hydrolysis of ZrOCl_2 with the formation of poorly crystallized $m\text{-ZrO}_2$. The properties of $\text{ZrO}_2 \cdot n\text{H}_2\text{O}$ and the corresponding ZrO_2 obtained by hydrolysis are very different from the properties of $\text{ZrO}_2 \cdot n\text{H}_2\text{O}$ and the corresponding ZrO_2 obtained by direct precipitation, which is

due to the differences in the number of stages by which the formation of $ZrO_2 \cdot nH_2O$ occurs. The size of the critical nucleus was estimated. An important practical result was show the possibility of adjusting the ratio of *t*- and *m*- ZrO_2 with a constant high specific surface area exceeding the additive effect of individual *t*- and *m*- ZrO_2 . The possibility of creating a hierarchical porous micro-mesoporous structure was also shown, which is important for the preparation of catalytic materials based on ZrO_2 .

References

- [1] Omarov Sh.O., Pakhomov N.A. Varying the conditions of $ZrO_2 \cdot nH_2O$ precipitation and aging as a way of controlling the phase composition and texture of ZrO_2 . *Catal. Ind.*, 2021, **13**(1), P. 12–20.
- [2] Otroshchenko T., Radnik J., Schneider M., Rodemerck U., Linke D., Kondratenko E.V. Bulk binary ZrO_2 -based oxides as highly active alternative-type catalysts for non-oxidative isobutane dehydrogenation. *Chem. Commun.*, 2016, **52**, P. 8164–8167.
- [3] Omarov Sh.O., Vlasov E.A., et al. Physico-chemical properties of MoO_3/ZrO_2 catalysts prepared by dry mixing for isobutane alkylation and butene transformations. *Appl. Catal. B.*, 2018, **230**, P. 246–259.
- [4] Omarov Sh.O., Sladkovskiy D.A., Martinson K.D., Peurla M., Aho A., Murzin D.Yu., Popkov V.I. Influence of the initial state of ZrO_2 on genesis, activity and stability of Ni/ZrO_2 catalysts for steam reforming of glycerol. *Appl. Catal. A*, 2021, **616**, P. 118098.
- [5] Li J., Chen J., Song W., Liu J., Shen W. Influence of zirconia crystal phase on the catalytic performance of Au/ZrO_2 catalysts for low-temperature water-gas shift reaction. *Appl. Catal. A*, 2008, **334**, P. 321–329.
- [6] Matsui K., Ohga M. Formation mechanism of hydrous zirconia particles produced by the hydrolysis of $ZrOCl_2$ solutions. *J. Am. Ceram. Soc.*, 1997, **80**(8), P. 1949–1956.
- [7] Matsui K., Ohga M. formation mechanism of hydrous zirconia particles produced by the hydrolysis of $ZrOCl_2$ solutions: II. *J. Am. Ceram. Soc.*, 2000, **83**(6), P. 1389–1392.
- [8] Matsui K., Ohga M. Formation mechanism of hydrous zirconia particles produced by the hydrolysis of $ZrOCl_2$ solutions: III, kinetics study for the nucleation and crystal-growth processes of primary particles. *J. Am. Ceram. Soc.*, 2001, **84**(10), P. 2302–2012.
- [9] Matsui K., Ohga M. Formation mechanism of hydrous zirconia particles produced by the hydrolysis of $ZrOCl_2$ solutions: IV, effect of $ZrOCl_2$ concentration and reaction temperature. *J. Am. Ceram. Soc.*, 2002, **85**(3), P. 545–553.
- [10] Sharikov F.Yu., Almjashveva O.V., Gusarov V.V. Thermal analysis of formation of ZrO_2 nanoparticles under hydrothermal conditions. *Russ. J. Inorg. Chem.*, 2006, **51**(10), P. 1538–1542.
- [11] Raghavendra V.B., Naik S., Antony M., Ramalingam G., Rajamathi M., Raghavan S. Amorphous, monoclinic, and tetragonal porous zirconia through a controlled self-sustained combustion route. *J. Am. Ceram. Soc.*, 2011, **94**(6), P. 1747–1755.
- [12] Štefanić G., Musić S., Popović S., Furić K. Formation of ZrO_2 by the thermal decomposition of zirconium salts. *Croat. Chem. Acta.*, 1996, **69**, P. 223–239.
- [13] Zhukov A.V., Chizhevskaya S.V., Phyo P., Panov V.A. Heterophase synthesis of zirconium hydroxide from zirconium oxychloride. *Inorg. Mater.*, 2019, **55**(10), P. 994–1000.
- [14] Thommes M., Kaneko K., et al. Physisorption of gases, with special reference to the evaluation of surface area and pore size distribution (IUPAC Technical Report). *Pure Appl. Chem.*, 2015, **87**(9-10), P. 1051–1069.
- [15] Toraya H., Yoshimura M., Somiya S. Calibration curve for quantitative analysis of the monoclinic tetragonal ZrO_2 system by X-ray diffraction. *J. Am. Chem. Soc.*, 1984, **67**(6), P. C119–C121.
- [16] Sato T. The thermal decomposition of zirconium oxyhydroxide. *J. Therm. Anal. Calorim.*, 2002, **69**, P. 255–265.
- [17] Livage J., Doi K., Mazires C. Nature and thermal evolution of amorphous hydrated zirconium oxide. *J. Am. Ceram. Soc.*, 1968, **51**(6), P. 349–353.
- [18] Garvie R.C. The occurrence of metastable tetragonal zirconia as a crystallite size effect. *J. Phys. Chem.*, 1965, **69**(4), P. 1238–1243.
- [19] Almjashveva O.V., Lomanova N.A., Popkov V.I., Proskurina O.V., Tugova E.A., Gusarov V.V. The minimum size of oxide nanocrystals: phenomenological thermodynamic vs crystal-chemical approaches. *Nanosystems: Physics, Chemistry, Mathematics*, 2019, **10**(4), P. 428–437.
- [20] Mercera P.D.L., Van Ommen J.G., Doesburg E.B.M., Burggraaf A.J., Ross J.R.H. Zirconia as a support for catalysts. Evolution of the texture and structure on calcination in air. *Appl. Catal.*, 1990, **57**, P. 127–148.
- [21] Srinivasan R., Rice L., Davis B.H. Critical particle size and phase transformation in zirconia: transmission electron microscopy and X-ray diffraction studies. *J. Am. Ceram. Soc.*, 1990, **73**(11), P. 3528–3530.
- [22] Ceresoli D., Vanderbilt D. Structural and dielectric properties of amorphous ZrO_2 and HfO_2 . *Phys. Rev. B.*, 2006, **74**(12), P. 125108.
- [23] Hu M. Z.-C., Harris M.T., Byers C.H. Nucleation and growth for synthesis of nanometric zirconia particles by forced hydrolysis. *J. Coll. Int. Sci.*, 1998, **198**, P. 87–99.
- [24] Hu M. Z.-C., Zielke J.T., Byers C.H. Small-angle x-ray scattering studies of early-stage colloid formation by thermohydrolytic polymerization of aqueous zirconyl salt solutions. *J. Mater. Res.*, 1999, **14**(1), P. 103–113.
- [25] Zhao Y., Li W., Zhang M., Tao K. A comparison of surface acidic features between tetragonal and monoclinic nanostructured zirconia. *Catal. Comm.*, 2002, **3**, P. 239–245.
- [26] Clearfield A., Vaughan P.A. The crystal structure of zirconyl chloride octahydrate and zirconyl bromide octahydrate. *Acta Cryst.*, 1956, **9**, P. 555–558.
- [27] Walther C., Rothe J., Fuss M., Büchner S., Koltsov S., Bergmann T. Investigation of polynuclear Zr(IV) hydroxide complexes by nanoelectrospray mass-spectrometry combined with XAFS. *Anal. Bioanal. Chem.*, 2007, **388**, P. 409–431.
- [28] Almjashveva O.V., Gusarov V.V. Metastable clusters and aggregative nucleation mechanism. *Nanosystems: Physics, Chemistry, Mathematics*, 2014, **5**(3), P. 405–416.
- [29] Ivanov V.K., Fedorov P.P., Baranchikov A.Y., Osiko V.V. Oriented attachment of particles: 100 years of investigations of non-classical crystal growth. *Russian Chemical Reviews*, 2014, **83**(12), P. 1204–1222.

Study of magnetic and optical transitions in MFe_2O_4 (M=Co, Zn, Fe, Mn) with spinel structure

Nitika^{1,*}, Anu Rana¹, Vinod Kumar²

¹Department of Physics, SRM University, Delhi NCR, Sonapat, 131029, India

²Department of Physics, NSUT, Dwarka, New Delhi, 110078, India

*nitika270593@gmail.com

DOI 10.17586/2220-8054-2021-12-4-481-491

Spinel ferrite (MFe_2O_4) nanoparticles were successfully synthesized by the coprecipitation method. X-ray diffraction technique was employed for structural analysis. Single-phase cubic spinel structure with an average crystallite size ranging from 5 – 20 nm was obtained for the prepared ferrites. The Fourier transform infrared spectra exhibits an absorption band at 550 cm^{-1} , which is attributed to metal-oxygen bond vibrations at tetrahedral sites. The thermogravimetric analysis revealed the instability of $MnFe_2O_4$ and Fe_3O_4 above $500\text{ }^\circ\text{C}$ whereas $CoFe_2O_4$ is found to be the most stable ferrite. The hysteresis parameters demonstrate the superparamagnetic nature of the prepared nanoparticles with low coercivity except for $CoFe_2O_4$. The direct optical band gap energy derived from UV-visible spectra is calculated to be 2.82, 2.83, 2.81, and 2.44 eV for M=Co, Zn, Fe, and Mn respectively. The magnetic and optical properties show a strong dependence on cation site occupancy.

Keywords: Spinel ferrites, Fourier transform infrared spectroscopy, thermo-gravimetric analysis, hysteresis curve, optical properties.

Received: 10 May 2021

Revised: 27 July 2021

1. Introduction

Magnetic nanocrystalline bimetallic iron-based oxides are technologically important due to an excellent combination of structural, magnetic, and electrical properties. The transition metal oxides with formula MFe_2O_4 , also termed as magnetic spinels, have attracted research interest in recent years attributable to their significant stability, ease of synthesis, high magnetization, low toxicity, small coercivity, less remanent magnetization, and high electrical resistance. The tunable magnetic and electrical properties of ferrites have turned the prime focus of researchers towards their potential use in biomedical and electronic applications [1–11]. The unique physicochemical properties are dependent on the structure of the crystal. The occupancy of metal cations on both sites is governed by electrostatic, elastic, and crystal field stabilization energy. Following the cation distribution, ferrites can be classified into normal, inverse, and mixed spinel. In normal spinel, the divalent cations occupy tetrahedral sites (A-sites), whereas the trivalent cations occupy octahedral sites (B-sites). On the contrary, in inverse spinel structure, divalent cations occupy B-sites, while trivalent cations occupy the A-sites. In mixed spinels, the site occupancy is intermediate to that of normal and inverse spinel structure [12–15]. Among ferrites, $CoFe_2O_4$, $ZnFe_2O_4$, Fe_3O_4 , and $MnFe_2O_4$ nanoparticles have drawn appreciable attention due to their wide application range taking into consideration their magnificent properties. $CoFe_2O_4$ and Fe_3O_4 possess inverse spinel structures; $ZnFe_2O_4$ forms normal spinel ferrite, whereas $MnFe_2O_4$ represents mixed spinel ferrite with 80% predominantly inverse structure. Although significant research has been done which reports the physicochemical properties of all the above ferrites, a systematic and thorough investigation is imperative to study and compare the properties of transition metal nano-ferrites [16–22].

Naseri et al. [20] reviewed $ZnFe_2O_4$, $MnFe_2O_4$, and $CoFe_2O_4$ nanoparticles prepared by the thermal treatment method. The average particle size of prepared ferrites ranged from 15 nm to 21 nm with very low saturation magnetization (2 – 5 emu/g). The saturation magnetization values reported are not sufficient for their use in electronic devices and are not in agreement with previous reports [23–28]. Kolhatkar et al. [29] presented a review of magnetic nanoparticles focusing on magnetic properties. Pandervand et al. [30] studied XFe_2O_4 (X=Mn, Fe, Ni, Co, and Zn) nanoparticles prepared by coprecipitation and hydrothermal methods. The average particle size varied from 21 – 30 nm. The paper lacks any detailed discussion of magnetic behavior and its relation to the structure. Banerjee et al. [31] synthesized polyethylene glycol (PEG) coated transition metal ferrites and compared the observed properties. PEG coating increases saturation magnetization but is undesirable due to its nonbiodegradability and holds several drawbacks in the biomedical field [32, 33]. Moreover, insufficient literature exists highlighting the comparative study of optical and thermal properties. The properties of ferrites at the nanoscale are not well defined due to their dynamic behavior. Replication of experimental study is required to observe the patterns and trends in the behavior of the material and to conclude the findings based on sufficient evidence.

Therefore, in the present work, we investigate the properties of four different magnetic nanoparticles with varying spinel structures synthesized by the co-precipitation technique, which is a simple and cost-effective method with an eco-friendly route. The structural, magnetic, optical, and thermal properties of the obtained ferrites are studied and compared for a better understanding of structure-property relation from a specific application based-perspective.

2. Materials and methods

2.1. Synthesis method

Cobalt ferrite, zinc ferrite, ferrous ferrite, and manganese ferrite nanoparticles were prepared using the co-precipitation technique. Analytical grade chemical reagents used for preparation were $\text{FeSO}_4 \cdot 7\text{H}_2\text{O}$, $\text{Fe}(\text{NO}_3)_3 \cdot 9\text{H}_2\text{O}$, $\text{Zn}(\text{NO}_3)_2 \cdot 6\text{H}_2\text{O}$, $\text{MnCl}_2 \cdot 4\text{H}_2\text{O}$, and $\text{CoCl}_2 \cdot 6\text{H}_2\text{O}$. Separate homogeneous aqueous solutions of two precursors including $\text{Fe}(\text{NO}_3)_3 \cdot 9\text{H}_2\text{O}$ were prepared in distilled water with continuous stirring. The solutions were mixed, keeping the resultant solution at 70°C . Surfactant (oleic acid) was added to avoid agglomeration. After 30 min, aqueous NH_3 was added drop-wise with uninterrupted stirring to attain pH 11. The precipitates so formed were finally dried at 80°C on a hot plate followed by crushing using agate mortar. Further, the prepared samples were annealed at 300°C for 2 hrs to improve their crystalline properties. The physicochemical properties of obtained samples were studied using various characterization techniques.

2.2. Characterization tools

Powder X-ray diffraction measurements were performed in the 2θ range of $20 - 70^\circ$ with a scan rate of $5^\circ/\text{min}$ using $\text{Cu-K}\alpha$ radiation ($\lambda = 1.5406 \text{ \AA}$). Thermogravimetric analysis (TGA) was carried out to study mass loss at a heating rate of $10^\circ\text{C}/\text{min}$ by varying temperature from room temperature to 800°C in an aerobic atmosphere. FTIR spectra were recorded using a Perkin Elmer Frontier FTIR spectrophotometer in the range of $4000 - 450 \text{ cm}^{-1}$. Magnetic measurements were recorded using a Vibrating sample magnetometer (Lakeshore model 7400) at room temperature within the range of $\pm 1.5 \text{ T}$. The absorption spectra are obtained using an Ultraviolet spectrophotometer by Perkin Elmer (LAMBDA 950) in the range $200 - 1600 \text{ nm}$.

3. Results and Discussion

3.1. Structural analysis

Figure 1 shows the XRD pattern of CoFe_2O_4 (CNP), ZnFe_2O_4 (ZNP), Fe_3O_4 (FNP) and MnFe_2O_4 (MNP). The formation of a single-phase spinel cubic structure with an $\text{Fd}3\text{m}$ space group for all the samples is confirmed by the diffraction peaks (JCPDS #22-1086, #89-1010, #19-0629, #73-1964). The average crystallite size is calculated using the most intense peak belonging to the (311) plane by employing the Scherrer formula (1).

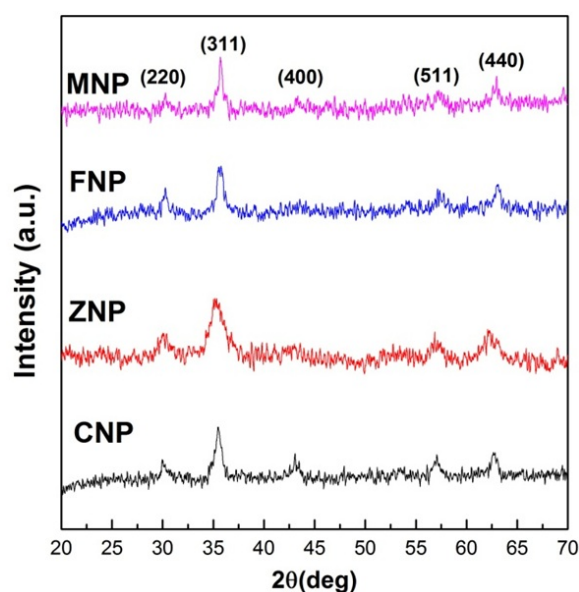


FIG. 1. XRD pattern of CoFe_2O_4 (CNP), ZnFe_2O_4 (ZNP), Fe_3O_4 (FNP), MnFe_2O_4 (MNP) nanoparticles

TABLE 1. Average crystallite size, lattice parameter, X-ray density, specific surface area, micro-strain and dislocation density for CNP, ZNP, FNP, and MNP

Sample	Average crystallite size D (nm)	Lattice Parameter a (Å)	X-ray Density ρ_x (g/cc)	Specific surface area S (m ² /g)	Micro-strain ε	Dislocation Density ρ_D (10 ¹⁵ m ⁻²)
CNP	11.35	8.381	5.29	99.85	0.003	4.82
ZNP	5.89	8.411	5.38	189.28	0.006	17.81
FNP	12.54	8.337	5.31	90.14	0.003	3.97
MNP	19.86	8.334	5.29	57.08	0.002	1.58

TABLE 2. Interionic distances and hopping lengths at A and B sites for CNP, ZNP, FNP and MNP

Sample	d_{AL} (Å)	d_{BL} (Å)	d_{AE} (Å)	d_{BE} (Å)	d_{BEU} (Å)	L_A (Å)	L_B (Å)
CNP	1.8871	2.0542	3.0817	2.8446	2.9643	3.6291	2.9631
ZNP	1.8939	2.0616	3.0927	2.8548	2.9749	3.6421	2.9737
FNP	1.8772	2.0434	3.0655	2.8297	2.9488	3.6100	2.9476
MNP	1.8765	2.0427	3.0644	2.8287	2.9477	3.6087	2.9465

$$D = \frac{K\lambda}{\beta \cos \theta}, \quad (1)$$

where D is the average crystallite size, K is Scherrer constant (0.9 for spherical crystallites with Cubic symmetry), λ is X-ray wavelength (1.5406 Å), β is FWHM of XRD peak in radians, θ is the diffraction angle. The lattice parameter (a) is calculated using (2) [34]:

$$a = d\sqrt{h^2 + k^2 + l^2}, \quad (2)$$

where d is interplanar spacing and h, k, l is the Miller indices. All the elementary information like X-ray density ρ_x , specific surface area (S), micro-strain (ε), and dislocation density ρ_D can be retrieved from the XRD pattern using the below-mentioned formulas (3-6):

$$\rho_x = \frac{ZM}{Na^3}, \quad (3)$$

$$S = \frac{6}{\rho_x D}, \quad (4)$$

$$\varepsilon = \frac{\beta \cos \theta}{4}, \quad (5)$$

$$\rho_D = \frac{15\varepsilon}{aD}, \quad (6)$$

where Z, M, N, β , and θ denote the number of atoms per unit cell, molecular weight, Avogadro's number, full width at half maximum, and diffraction angle respectively. The values obtained are tabulated in Table 1. Considering the preferred spinel structure, site occupancy, crystal field stabilization energy, and coordination number (CN), the ionic radii of all the cations can be chosen from the database of ionic radii [35]. The estimated ionic radii are 0.785 Å for Fe^{3+} ions at B sites, 0.63 Å for Fe^{3+} ions at A sites, 0.88 Å for Co^{2+} ions (as it occupies B sites with CN 6 being in the high spin state), 0.74 Å for Zn^{2+} ions (as it occupies A sites with CN 4 being in the high spin state), 0.92 Å for Fe^{2+} ions (as it occupies B sites with CN 6 being in the high spin state) and 0.80 Å for Mn^{2+} ions at A sites and 0.97 Å for Mn^{2+} ions at B sites [36–38]. The hopping lengths (L_A and L_B), interionic distances (i.e., M–O bond length at A site (d_{AL}), M–O bond length at B site (d_{BL}), tetrahedral and octahedral shared edge length (d_{AE} and d_{BE}), and unshared octahedral edge length (d_{BEU}) are calculated using the relations 7 – 13 [39–42].

$$L_A = \sqrt{3}a/4, \quad (7)$$

$$L_B = \sqrt{2}a/4, \quad (8)$$

$$d_{AL} = a\sqrt{3}(u - 0.25), \quad (9)$$

$$d_{BL} = a\sqrt{\left(3u^2 - \frac{11u}{4} + \frac{43}{64}\right)}, \quad (10)$$

$$d_{AE} = a\sqrt{2}(2u - 0.5), \quad (11)$$

$$d_{BE} = a\sqrt{2}(1 - 2u), \quad (12)$$

$$d_{BEU} = a\sqrt{4u^2 - 3u + \frac{11}{16}}, \quad (13)$$

where u is the oxygen positional parameter. The calculated values are listed in Table 2. From the variation observed in the interionic distances and hopping lengths, it can be inferred that the lattice parameter is strongly influenced by the distances between cations and anions. In the present study, all the cases possess different spinel structures; hence the lattice parameter cannot be compared. Although a cation distribution can be proposed by correlating the lattice parameter and the magnetic measurements which depend on the cations site occupancy. Former studies reveal that effective magnetism is observed in inverse and mixed spinel structures where A–B interactions are dominant. The average crystallite size, lattice parameter, and magnetic moments of the cations determine the magnetic properties of spinel ferrites [1].

3.2. Thermogravimetric analysis

Mass loss of prepared samples (TGA) and the first derivative of TGA (DTG) as a function of temperature are shown in Fig. 2. The thermal decomposition of CNP and ZNP takes place in two stages, whereas that of FNP and MNP takes place in three stages. The initial weight loss up to 250 °C is due to the loss of adsorbed water. This weight loss is approximately 6%, 2%, 6.6%, and 12% for CNP, ZNP, FNP, and MNP respectively which indicates surface water adsorption is highest for MNP and least for ZNP. The second mass loss up to 550 °C is due to the evaporation of surfactant used in the synthesis process. The boiling point of oleic acid used in the synthesis is 360 °C. Approximately 40%, 57%, 35%, and 34.8% mass loss is observed in this range corresponding to CNP, ZNP, FNP, and MNP respectively. This major loss indicates that nanoparticles prepared with the coprecipitation technique contained a large amount of organic compound. It can be inferred in the synthesis process, organic content increased in the order MNP < FNP < CNP < ZNP with a corresponding decrease in particle size. This phenomenon can be attributed to the increase in specific surface area in the order MNP < FNP < CNP < ZNP. The same trend has been reported and explained previously [43–45]. The third mass loss of 4% at 600 °C for FNP is due to the formation of secondary phases (α -Fe₂O₃ and γ -Fe₂O₃). The formation of these phases at higher temperatures is favorable due to its thermal stability above 570 °C [46]. A similar minor mass loss of 0.5% above 700 °C for MNP indicates the partial decomposition of MnFe₂O₄ to α -Mn₂O₃ and α -Fe₂O₃ [47, 48]. This signifies an increase in impurity phases in MNP at a higher temperature. As the temperature reaches 800 °C, the remaining mass% values of the samples were 51.6%, 42.2%, 52.3%, and 49.1% for CNP, ZNP, FNP, and MNP respectively. The analysis of all the TGA/DTG curves suggests thermal stability in the order CNP > ZNP > MNP > FNP.

3.3. Fourier transform infrared spectroscopy analysis

Figure 3 shows FTIR spectra of CNP, ZNP, FNP, and MNP respectively. The absorption bands between 3600 – 3300, 1700 – 1500 and 1000 – 1200 cm⁻¹ correspond to stretching and bending of H₂O molecules [49]. Low-intensity peaks are observed in the above-mentioned regions corresponding to ZNP indicating less surface water adsorption by the particles. Although the peaks for ZNP belonging to range 2800 – 2900 cm⁻¹ are more intense, indicating the presence of organic groups more than others. Oleic acid inhibits grain growth by binding the surface molecules which in turn induces strain [50]. The same has been proved in XRD and TGA analysis for ZNP. The peaks belonging to region 1300 – 1500 cm⁻¹ are attributed to the stretching and bending of the COO- group [51]. The presence of absorption band at frequency ~550 cm⁻¹ for all the samples is attributed to the intrinsic vibrations of the M–O bonds (M=Co, Zn, Fe, Mn) at tetrahedral sites which is the characteristic feature confirming the formation of spinel ferrite structures [52]. It is also observed that wavenumber corresponding to tetrahedral vibrations increases in the order FNP < ZNP < MNP < CNP respectively. The same trend has been observed in various reports [53]. This phenomenon particularly depends on the cation distribution, cation mass, and the ionic radii of the divalent cations.

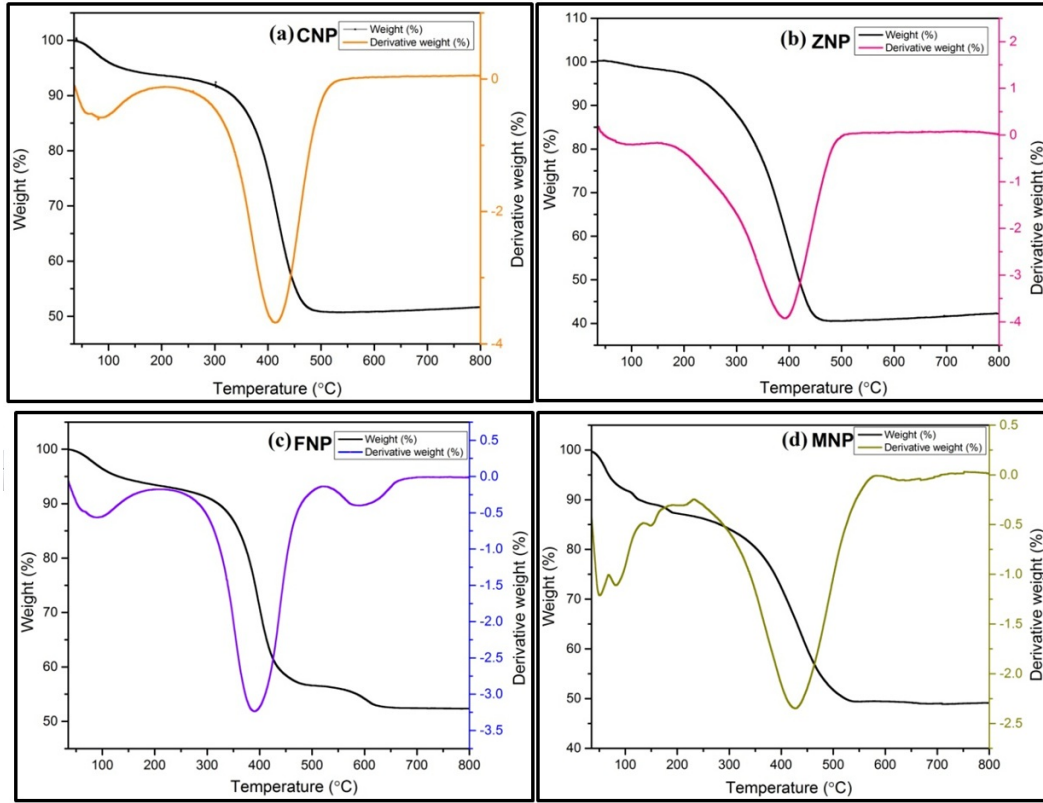


FIG. 2. TGA-DTG curve for (a) CNP (b) ZNP (c) FNP (d) MNP

TABLE 3. Magnetic parameters for CNP, ZNP, FNP, and MNP

Samples	M_S (emu/g)	H_C (Oe)	M_R (emu/g)	R	K(erg/Oe)	η_B (μ_B)
CNP	35.55	595.34	8.98	0.253	21593.22	1.493
ZNP	15.29	51.43	0.41	0.027	802.34	0.660
FNP	26.04	15.62	0.44	0.017	415.10	1.079
MNP	14.94	97.88	1.65	0.111	1492.59	0.617

3.4. Magnetic properties

Fig. 4 shows the magnetization curves for CNP, ZNP, FNP, and MNP recorded at room temperature. The values of saturation magnetization (M_S), coercivity (H_C), retentivity (M_R), squareness ratio (R), magnetic anisotropy constant (K), and magnetic moment (η_B) are tabulated in Table 3 [54]. The relation between magnetic anisotropy constant, squareness ratio, and magnetic moment is given below:

$$K = \frac{H_C M_S}{0.98}, \quad (14)$$

$$R = \frac{M_R}{M_S}, \quad (15)$$

$$\eta_B = \frac{(M \times M_S)}{5585}. \quad (16)$$

The variation of M_S follows the order CNP>FNP>ZNP>MNP. However, a very small difference exists between M_S of MNP and ZNP. Saturation magnetization is mainly governed by cation distribution and average crystallite size. Magnetic moments corresponding to different cations belonging to high spin state follows the order of $Mn^{2+}=Fe^{3+}(5.92 \mu_B)>Fe^{2+}(4.90 \mu_B)>Co^{2+}(3.87 \mu_B)>Zn^{2+}(0 \mu_B)$ [55,56]. The variation of M_S can be explained

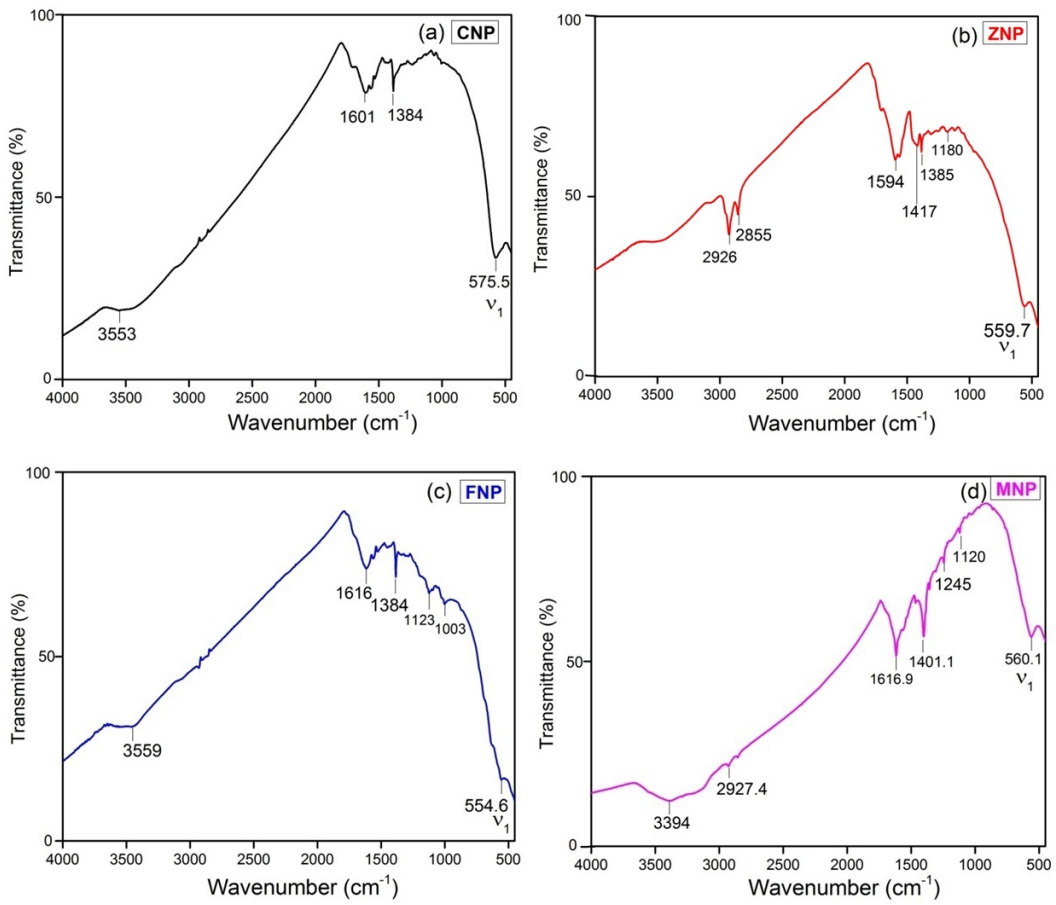


FIG. 3. FTIR Spectra for (a) CNP (b) ZNP (c) FNP (d) MNP

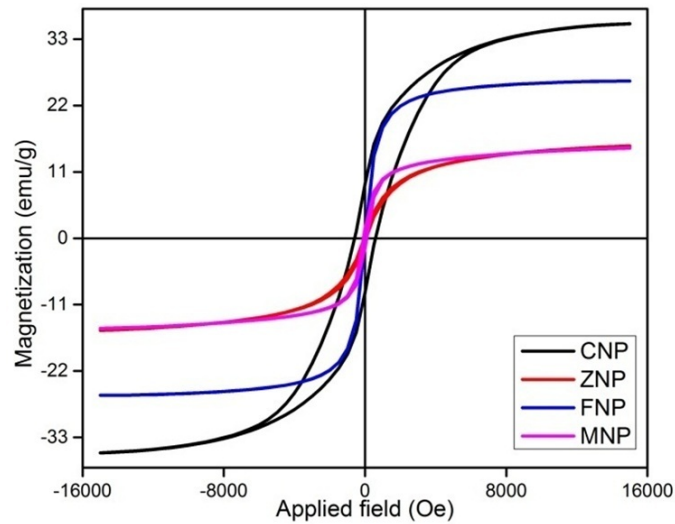


FIG. 4. Magnetic hysteresis curves for CNP, ZNP, FNP, and MNP

efficiently by taking into consideration their respective spinel structure and net magnetic moment. The net magnetization per formula unit is calculated using Neel's model where n_{net} is the difference between net magnetization at B-sites and net magnetization at A-sites [57]. CNP belongs to the inverse spinel structure, with a majority of Co^{2+} ions and Fe^{3+} ions occupying B-sites. This increases the net magnetic moment which is clear from the data in the table. FNP also belongs to inverse spinel structure, due to which net magnetization of B-sites is greater than that of A-sites, thereby yielding a high magnetic moment. A slight variation of the net magnetic moment for both the ferrites is due to the inversion degree. The fraction of Co^{2+} ions occupying B-sites in CNP is greater than that of Fe^{2+} ions in FNP. ZNP belongs to a normal spinel structure in which a maximum of non-magnetic Zn^{2+} ions occupy the A-sites. A small magnetic moment of $0.6 \mu_B$ agrees well with previous reports, which is correlated with a low fraction of Fe^{3+} ions in A-sites [12]. MNP belongs to a mixed spinel structure in which Mn^{2+} ions get distributed between both sites. Moreover, the magnetic moments of Mn^{2+} and Fe^{3+} are equal, resulting in very small magnetic moments. Small values of coercivity and retentivity for all the prepared ferrites except CNP indicate superparamagnetic nature. However, CNP exhibits ferromagnetic behavior. CNP possessed the highest coercivity with a highly anisotropic structure. The values of MR, HC, and K follow the same variation as M_S . The squareness ratio termed as Stoner–Wohlfarth value is less than 0.5 signifying uniaxial anisotropy influenced by lattice strain [58].

3.5. Optical properties

Figure 5 shows the absorption spectra of CNP, ZNP, FNP, and MNP demonstrating the absorption in the visible and near-infrared region. The absorption band of MNP shows a shoulder-like structure attributed to the absorption taking place due to surface states [59].

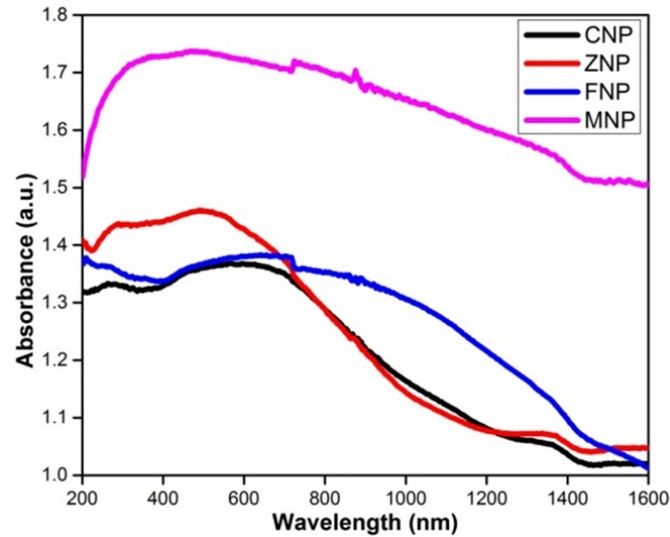


FIG. 5. Absorption spectra for CNP, ZNP, FNP, and MNP

The absorption spectrum is obtained due to the transition of the electrons from the valence band of O-2p to the conduction band of Fe-3d. The absorption in the visible region is highest in the case of MNP whereas it is least in the case of CNP. The optical band gap for direct transitions can be calculated using the Tauc plots by employing (17) (Fig. 6) [60]:

$$\alpha h\nu = A\sqrt{(h\nu - E_g)}, \quad (17)$$

where α is the absorption coefficient, $h\nu$ is the energy of the photon, E_g is the optical band gap and A is the proportionality constant.

The obtained values of optical band gaps are tabulated in Table 4. The optical bandgaps of prepared spinel ferrites varied from 2.44 – 2.83 eV. The tuning of bandgap signifies the potential of bandgap engineering in spinel ferrites. The variation observed in the optical band gap is explained by correlating it with average crystallite size. A decrease in average crystallite size increases the binding energy of valence electrons and parent atoms, which increases the bandgap energy [61]. The trend verifies Brass's effective mass model. The optical band gap is also influenced by the site occupancy of transition metal cation [56]. The spinel ferrites possess good absorption properties in the visible region which makes them suitable for optoelectronic devices. The study of optical properties is quite useful for photocatalytic reactions.

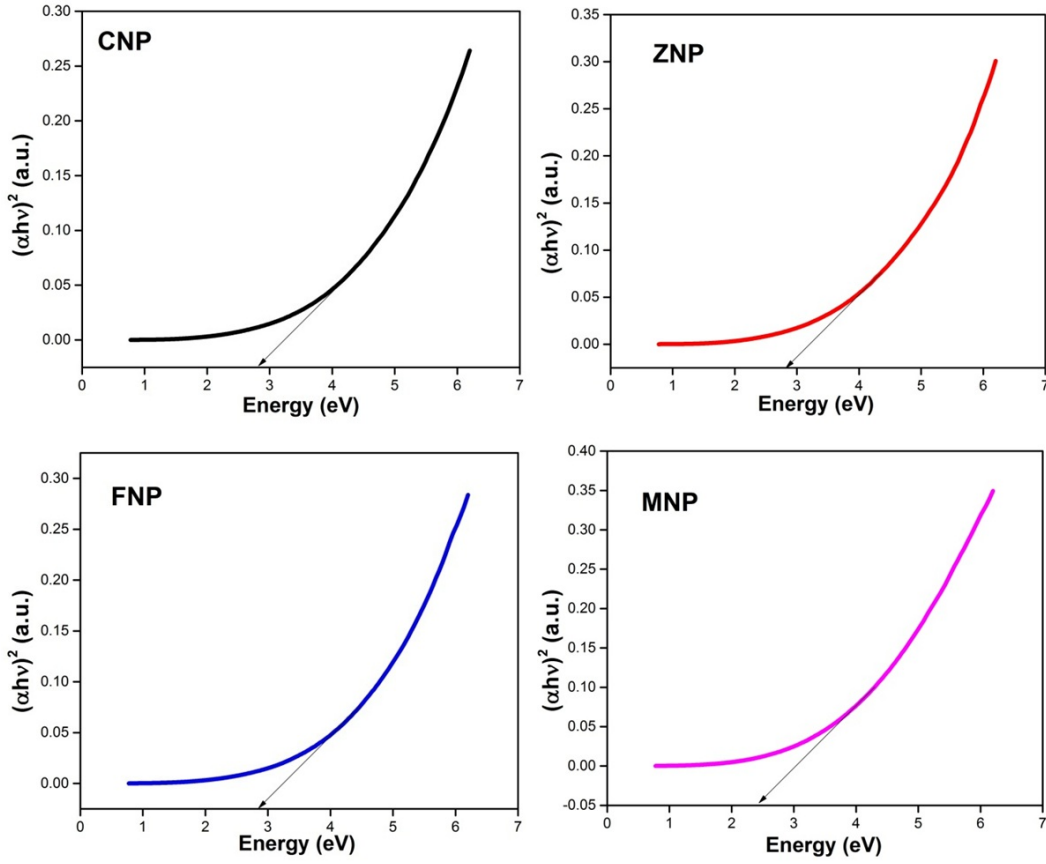


FIG. 6. Plot of $(\alpha h\nu)^2$ as a function of photon energy (eV) for CNP, ZNP, FNP, and MNP

TABLE 4. Optical bandgaps for CNP, ZNP, FNP, and MNP

Sample	Optical band gap (eV)	Refractive index (n)	Real dielectric constant (ϵ')	Imaginary dielectric constant (ϵ'')
CNP	2.82	2.40	3.97	6.47
ZNP	2.83	2.40	3.66	6.96
FNP	2.81	2.41	3.96	6.52
MNP	2.44	2.53	3.41	8.80

The Ravindra empirical relation can be employed to calculate optical parameters such as the refractive index (n), real and imaginary part of dielectric constant (ϵ' and ϵ'') [62, 63]. The values obtained using the below relations (18–21) are shown in Table 4:

$$n = A + (B \times E_g), \quad (18)$$

$$k = \frac{\alpha \lambda}{4\pi}, \quad (19)$$

$$\epsilon' = n^2 - k^2, \quad (20)$$

$$\epsilon'' = 2 \times n \times k, \quad (21)$$

where $A = 4.05 \text{ eV}^{-1}$, $B = -0.62 \text{ eV}^{-1}$, k is the extinction coefficient, α is the absorption coefficient and λ is the wavelength calculated from bandgap energy. The high value of the refractive index for MNP makes it suitable for antireflection coatings. It can be inferred that optical conductivity strongly depends on the absorption coefficient [64].

4. Conclusion

The physicochemical properties of spinel ferrites entirely depend on the crystal structure and cation distribution. In the present study, four different spinel ferrites belonging to normal, inverse, and mixed spinel structure were successfully synthesized using the chemical co-precipitation technique. XRD confirmed the formation of single-phase cubic spinel structures with average crystallite sizes of 11 nm, 6 nm, 13 nm, and 20 nm for $CoFe_2O_4$, $ZnFe_2O_4$, Fe_3O_4 , and $MnFe_2O_4$ respectively. The lattice parameter ranged from 8.334 – 8.411 Å. The specific surface area was highest for $ZnFe_2O_4$ and least for $MnFe_2O_4$ nanoparticles. TGA/DTG curves illustrated thermal stability in the order $CoFe_2O_4 > ZnFe_2O_4 > MnFe_2O_4 > Fe_3O_4$. The fundamental peak attributed to tetrahedral M–O bond vibrations was obtained around 550 cm^{-1} confirming the formation of spinel ferrites. All the ferrites exhibited superparamagnetic behavior except $CoFe_2O_4$. $CoFe_2O_4$ showed ferromagnetic behavior with high magnetic coercivity and anisotropy. The saturation magnetization and coercivity ranged from 14.94 emu/g to 35.55 emu/g and 15.62 – 595.34 Oe respectively. A strong dependence of optical properties on average crystallite size was observed. $MnFe_2O_4$ has the highest refractive index and imaginary dielectric constant but the least real dielectric constant. Optical conductivity depends on the absorption coefficient. The study of optical and magnetic properties is useful in determining the applications of the prepared ferrites in electrical and magnetic devices.

Acknowledgement

The author(s) received no financial support for the research, authorship, and/or publication of this article.

References

- [1] Galvão W.S., Neto D., Freire R.M., Fechine P.B. Super-paramagnetic nanoparticles with spinel structure: a review of synthesis and biomedical applications. *In solid state phenomena*, 2016, **241**, P. 139–176.
- [2] Valenzuela R. *Novel applications of ferrites*. Physics Research International, 2012.
- [3] Tatarchuk T., Bououdina M., Vijaya J.J., Kennedy L.J. Spinel ferrite nanoparticles: synthesis, crystal structure, properties, and perspective applications. *In International Conference on Nanotechnology and Nanomaterials*, 2016, August, P. 305–325.
- [4] Kombaiyah K., Vijaya J.J., Kennedy L.J., Bououdina M. Optical, magnetic and structural properties of $ZnFe_2O_4$ nanoparticles synthesized by conventional and microwave assisted combustion method: a comparative investigation. *Optik*, 2017, **129**, P. 57–68.
- [5] Brabers V.A.M. Progress in spinel ferrite research. *Handbook of magnetic materials*, 1995, **8**, P. 189–324.
- [6] Mathew D.S., Juang R.S. An overview of the structure and magnetism of spinel ferrite nanoparticles and their synthesis in microemulsions. *Chemical engineering journal*, 2007, **129**(1-3), P. 51–65.
- [7] Amiri M., Salavati-Niasari M., Akbari A. Magnetic nanocarriers: evolution of spinel ferrites for medical applications. *Advances in Colloid and Interface Science*, 2019, **265**, P. 29–44.
- [8] Bao N., Shen L., Wang Y., Padhan P., Gupta A. A facile thermolysis route to monodisperse ferrite nanocrystals. *Journal of the American Chemical Society*, 2007, **129**(41), P. 12374–12375.
- [9] Srinivas C., Kumar E.R., Tirupanyam B.V., Meena S.S., Bhatt P., Prajapat C.L., Sastry D.L. Study of magnetic behavior in co-precipitated Ni–Zn ferrite nanoparticles and their potential use for gas sensor applications. *Journal of Magnetism and Magnetic Materials*, 2020, **502**, P. 166534.
- [10] Kannapiran N., Muthusamy A., Renganathan B., Ganesan A.R., Meena S.S. Magnetic, electrical and gas sensing properties of poly (o-phenylenediamine)/ $MnCoFe_2O_4$ nanocomposites. *Applied Physics A*, 2020, **126**(12), P. 1–13.
- [11] Deepty M.Ch.S., Ramesh P.N., Mohan N.K., Singh M.S., Prajapat C.L., Sastry D.L. Evaluation of structural and dielectric properties of Mn^{2+} -substituted Zn-spinel ferrite nanoparticles for gas sensor applications. *Sensors and Actuators B: Chemical*, 2020, **316**, P. 128127.
- [12] Andersen H.L., Saura-Múzquiz M., Granados-Miralles C., Canévet E., Lock N., Christensen M. Crystalline and magnetic structure–property relationship in spinel ferrite nanoparticles. *Nanoscale*, 2018, **10**(31), P. 14902–14914.
- [13] Chand P., Vaish S., Kumar P. Structural, optical and dielectric properties of transition metal (MFe_2O_4 ; M= Co, Ni and Zn) nanoferrites. *Physica B: Condensed Matter*, 2017, **524**, P. 53–63.
- [14] Bid S., Pradhan S.K. Preparation of zinc ferrite by high-energy ball-milling and microstructure characterization by Rietveld’s analysis. *Materials Chemistry and Physics*, 2003, **82**(1), P. 27–37.
- [15] Rahman S., Nadeem K., Anis-ur-Rehman M., Mumtaz M., Naeem S., Letofsky-Papst I. Structural and magnetic properties of ZnMg-ferrite nanoparticles prepared using the co-precipitation method. *Ceramics International*, 2013, **39**(5), P. 5235–5239.
- [16] Maaz K., Mumtaz A., Hasanain S.K., Ceylan A. Synthesis and magnetic properties of cobalt ferrite ($CoFe_2O_4$) nanoparticles prepared by wet chemical route. *Journal of magnetism and magnetic materials*, 2007, **308**(2), P. 289–295.
- [17] Houshiar M., Zebhi F., Razi Z.J., Alidoust A., Askari Z. Synthesis of cobalt ferrite ($CoFe_2O_4$) nanoparticles using combustion, coprecipitation, and precipitation methods: A comparison study of size, structural, and magnetic properties. *Journal of Magnetism and Magnetic Materials*, 2014, **371**, P. 43–48.
- [18] Vinosha P.A., Mely L.A., Jeronsia J.E., Krishnan S., Das S.J. Synthesis and properties of spinel $ZnFe_2O_4$ nanoparticles by facile co-precipitation route. *Optik*, 2017, **134**, P. 99–108.
- [19] Zipare K., Dhupal J., Bandgar S., Mathe V., Shahane G. Superparamagnetic manganese ferrite nanoparticles: synthesis and magnetic properties. *Journal of Nanoscience and Nanoengineering*, 2015, **1**(3), P. 178–182.
- [20] Liu C., Zou B., Rondinone A.J., Zhang Z.J. Reverse micelle synthesis and characterization of superparamagnetic $MnFe_2O_4$ spinel ferrite nanocrystallites. *The Journal of Physical Chemistry B*, 2000, **104**(6), P. 1141–1145.
- [21] Gholizadeh A. A comparative study of physical properties in Fe_3O_4 nanoparticles prepared by coprecipitation and citrate methods. *Journal of the American Ceramic Society*, 2017, **100**(8), P. 3577–3588.

- [22] Kandpal N.D., Sah N., Loshali R., Joshi R., Prasad J. Co-precipitation method of synthesis and characterization of iron oxide nanoparticles, 2014.
- [23] Goodarz Naseri M., Saion E.B., Kamali A. An overview on nanocrystalline $ZnFe_2O_4$, $MnFe_2O_4$, and $CoFe_2O_4$ synthesized by a thermal treatment method. *International Scholarly Research Notices*, 2012.
- [24] Naik S.R., Salker A.V., Yusuf S.M., Meena S.S. Influence of Co^{2+} distribution and spin-orbit coupling on the resultant magnetic properties of spinel cobalt ferrite nanocrystals. *Journal of alloys and compounds*, 2013, **566**, P. 54–61.
- [25] Vasundhara K., Achary S.N., Deshpande S.K., Babu P.D., Meena S.S., Tyagi A.K. Size dependent magnetic and dielectric properties of nano $CoFe_2O_4$ prepared by a salt assisted gel-combustion method. *Journal of Applied Physics*, 2013, **113**(19), P. 194101.
- [26] Patange S.M., Desai S.S., Meena S.S., Yusuf S.M., Shirsath S.E. Random site occupancy induced disordered Néel-type collinear spin alignment in heterovalent $Zn^{2+}-Ti^{4+}$ ion substituted $CoFe_2O_4$. *RSC advances*, 2015, **5**(111), P. 91482–91492.
- [27] Yadav S.P., Shinde S.S., Bhatt P., Meena S.S., Rajpure K.Y. Distribution of cations in $Co^{1-x}Mn_xFe_2O_4$ using XRD, magnetization and Mössbauer spectroscopy. *Journal of Alloys and Compounds*, 2015, **646**, P. 550–556.
- [28] Hashim M., Shirsath S.E., Meena S.S., Mane M.L., Kumar S., Bhatt P., Şentürk E. Manganese ferrite prepared using reverse micelle process: Structural and magnetic properties characterization. *Journal of Alloys and Compounds*, 2015, **642**, P. 70–77.
- [29] Kolhatkar A.G., Jamison A.C., Litvinov D., Willson R.C., Lee T.R. Tuning the magnetic properties of nanoparticles. *International journal of molecular sciences*, 2013, **14**(8), P. 15977–16009.
- [30] Padervand M., Vossoughi M., Yousefi H., Salari H., Gholami M.R. An experimental and theoretical study on the structure and photoactivity of XFe_2O_4 ($X = Mn, Fe, Ni, Co, \text{ and } Zn$) structures. *Russian Journal of Physical Chemistry A*, 2014, **88**(13), P. 2451–2461.
- [31] Banerjee A., Blasiak B., Pasquier E., Tomaneck B., Trudel S. Synthesis, characterization, and evaluation of PEGylated first-row transition metal ferrite nanoparticles as T2 contrast agents for high-field MRI. *RSC advances*, 2017, **7**(61), P. 38125–38134.
- [32] Sebak A.A. Limitations of PEGylated nanocarriers: unfavourable physicochemical properties, biodistribution patterns and cellular and sub-cellular fates. *Int. J. Pharm.*, 2018, **10**, P. 6–12.
- [33] Patsula V., Horák D., Kučka J., Macková H., Lobaz V., Francová P., Šefc L. Synthesis and modification of uniform PEG-neridronate-modified magnetic nanoparticles determines prolonged blood circulation and biodistribution in a mouse preclinical model. *Scientific reports*, 2019, **9**(1), P. 1–12.
- [34] Cullity B.D. *Elements of X-ray Diffraction*. Addison-Wesley Publishing, 1956.
- [35] Shannon R.D. Revised effective ionic radii and systematic studies of interatomic distances in halides and chalcogenides. *Acta crystallographica section A: crystal physics, diffraction, theoretical and general crystallography*, 1976, **32**(5), P. 751–767.
- [36] Grimes N.W., Thompson P., Kay H.F. New symmetry and structure for spinel. *Proceedings of the Royal Society of London. A. Mathematical and Physical Sciences*, 1983, **386**(1791), P. 333–345.
- [37] Hwang L., Heuer A.H., Mitchell T.E. On the space group of $MgAl_2O_4$ spinel. *Philosophical Magazine*, 1973, **28**(1), P. 241–243.
- [38] Burdett J.K., Price G.D., Price S.L. Role of the crystal-field theory in determining the structures of spinels. *Journal of the American Chemical Society*, 1982, **104**(1), P. 92–95.
- [39] Areal C.O., Diaz E.G., Gonzalez J.R., Garcia M.V. Crystal chemistry of cadmium-zinc ferrites. *Journal of Solid State Chemistry*, 1988, **77**(2), P. 275–280.
- [40] Gillot B., Jemmali F. Dependence of electrical properties in iron–cobalt, iron–zinc ferrites near stoichiometry on firing temperature and atmosphere. *Physica status solidi (a)*, 1983, **76**(2), P. 601–608.
- [41] Pathan A.T., Mathad S.N., Shaikh A.M. Infrared spectral studies of nanostructured Co^{2+} -substituted Li-Ni-Zn ferrites. *International Journal of Self-Propagating High-Temperature Synthesis*, 2014, **23**(2), P. 112–117.
- [42] Mohammed K.A., Al-Rawas A.D., Gismelseed A.M., Sellai A., Widatallah H.M., Yousif A., Shongwe, M. Infrared and structural studies of $Mg_{1-x}Zn_xFe_2O_4$ ferrites. *Physica B: Condensed Matter*, 2012, **407**(4), P. 795–804.
- [43] Pereira C., Pereira A.M., Fernandes C., Rocha M., Mendes R., Fernández-García M.P., Freire C. Superparamagnetic MFe_2O_4 ($M = Fe, Co, Mn$) nanoparticles: tuning the particle size and magnetic properties through a novel one-step coprecipitation route. *Chemistry of Materials*, 2012, **24**(8), P. 1496–1504.
- [44] Si S., Kotal A., Mandal T.K., Giri S., Nakamura H., Kohara T. Size-controlled synthesis of magnetite nanoparticles in the presence of polyelectrolytes. *Chemistry of Materials*, 2004, **16**(18), P. 3489–3496.
- [45] Roca A.G., Marco J.F., Morales M.D.P., Serna C.J. Effect of nature and particle size on properties of uniform magnetite and maghemite nanoparticles. *The Journal of Physical Chemistry C*, 2007, **111**(50), P. 18577–18584.
- [46] Mahdavi M., Ahmad M.B., Haron M.J., Namvar F., Nadi B., Rahman M.Z.A., Amin J. Synthesis, surface modification and characterisation of biocompatible magnetic iron oxide nanoparticles for biomedical applications. *Molecules*, 2013, **18**(7), P. 7533–7548.
- [47] Aijun H., Juanjuan L., Mingquan Y., Yan L.I., Xinhua P. Preparation of nano- $MnFe_2O_4$ and its catalytic performance of thermal decomposition of ammonium perchlorate. *Chinese Journal of Chemical Engineering*, 2011, **19**(6), P. 1047–1051.
- [48] Stoia M., Păcurariu C., Muntean E.C. Thermal stability of the solvothermal-synthesized $MnFe_2O_4$ nanopowder. *Journal of Thermal Analysis and Calorimetry*, 2017, **127**(1), P. 155–162.
- [49] Umare S.S., Ningthoujam R.S., Sharma S.J., Shrivastava S., Kurian S., Gajbhiye N.S. Mössbauer and magnetic studies on nanocrystalline $NiFe_2O_4$ particles prepared by ethylene glycol route. *In ICAME*, 2007, P. 649–657.
- [50] Limaye M.V., Singh S.B., Date S.K., Kothari D., Reddy V.R., Gupta A., Kulkarni S.K. High coercivity of oleic acid capped $CoFe_2O_4$ nanoparticles at room temperature. *The Journal of Physical Chemistry B*, 2009, **113**(27), P. 9070–9076.
- [51] Nandiyanto A.B.D., Oktiani R., Ragadhita R. How to read and interpret FTIR spectroscopy of organic material. *Indonesian Journal of Science and Technology*, 2019, **4**(1), P. 97–118.
- [52] Pradeep A., Chandrasekaran G. FTIR study of Ni, Cu and Zn substituted nano-particles of $MgFe_2O_4$. *Materials Letters*, 2006, **60**(3), P. 371–374.
- [53] Bera P., Lakshmi R.V., Prakash B.H., Tiwari K., Shukla A., Kundu A.K., Barshilia H.C. Solution combustion synthesis, characterization, magnetic, and dielectric properties of $CoFe_2O_4$ and $Co_0.5M_0.5Fe_2O_4$ ($M = Mn, Ni, \text{ and } Zn$). *Physical Chemistry Chemical Physics*, 2020, **22**(35), P. 20087–20106.
- [54] Nikmanesh H., Kameli P., Asgarian S.M., Karimi S., Moradi M., Kargar Z., Salamati H. Positron annihilation lifetime, cation distribution and magnetic features of $Ni_{1-x}Zn_xFe_{2-x}Co_xO_4$ ferrite nanoparticles. *RSC Advances*, 2017, **7**(36), P. 22320–22328.

- [55] Carter C.B., Norton M.G. Using Magnetic Fields and Storing Data. *Ceramic Materials: Science and Engineering*, 2007, P. 598–618.
- [56] Szotek Z., Temmerman W. M., Ködderitzsch D., Svane A., Petit L., Winter H. Electronic structures of normal and inverse spinel ferrites from first principles. *Physical Review B*, 2006, **74**(17), P. 174431.
- [57] Néel L. Magnetic properties of ferrites; ferrimagnetism and antiferromagnetism. In *Annales de physique*, 1948, 12(3), P. 137–198.
- [58] Stoner E.C., Wohlfarth E.P. A mechanism of magnetic hysteresis in heterogeneous alloys. *Philosophical Transactions of the Royal Society of London. Series A*, 1948.
- [59] Joshi G.P., Saxena N.S., Mangal R., Mishra A., Sharma T.P. Band gap determination of Ni-Zn ferrites. *Bulletin of Materials Science*, 2003, **26**(4), P. 387–389.
- [60] Holinsworth B.S., Mazumdar D., Sims H., Sun Q.C., Yurtisigi M.K., Sarker S.K., Musfeldt J.L. Chemical tuning of the optical band gap in spinel ferrites: $CoFe_2O_4$ vs $NiFe_2O_4$. *Applied Physics Letters*, 2013, **103**(8), P. 082406.
- [61] Nitika, Rana A., Kumar V. Tailoring the Structural, Magnetic, Mechanical, and Thermal Properties of $CoFe_2O_4$ by Varying Annealing Temperature for High-Density Storage Devices. *ECS Journal of Solid State Science and Technology*, 2021.
- [62] Parishani M., Nadafan M., Dehghani Z., Malekfar R., Khorrami G.H.H. Optical and dielectric properties of $NiFe_2O_4$ nanoparticles under different synthesized temperature. *Results in physics*, 2017, **7**, P. 3619–3623.
- [63] Yuliantika D., Taufiq A., Hidayat A., Hidayat N., Soontaranon S. Exploring Structural Properties of Cobalt Ferrite Nanoparticles from Natural Sand. In *IOP Conference Series: Materials Science and Engineering*, 2019, April, **515**(1), P. 012047.
- [64] Pawar C.S., Gujar M.P., Mathe V.L. Optical properties of spin-deposited nanocrystalline Ni-Zn ferrite thin films processed by sol-gel. *Journal of Superconductivity and Novel Magnetism*, 2017, **30**(3), P. 615–625.

Synthesis and magnetic properties of cobalt ferrite nanoparticles formed under hydro and solvothermal conditions

B. V. Vasil'ev^{1,2}, R. Yu. Smyslov¹, D. A. Kirilenko^{3,4}, A. N. Bugrov^{1,2}

¹Institute of Macromolecular Compounds RAS, Bolshoy pr. 31, 199004 Saint Petersburg, Russia

²Saint Petersburg Electrotechnical University "LETI", ul. Professora Popova 5, 197376 Saint Petersburg, Russia

³Ioffe Institute RAS, Politekhnikeskaya ul. 26, 194021 Saint Petersburg, Russia

⁴ITMO University, Kronverskii avenue 49, 197101 Saint Petersburg, Russia

boris8152@gmail.com, urs@macro.ru, demid.kirilenko@mail.ioffe.ru, alexander.n.bugrov@gmail.com

PACS 75.20.-g; 75.75.+a

DOI 10.17586/2220-8054-2021-12-4-492-504

Cobalt ferrite nanoparticles were synthesized both in hydro and in solvothermal conditions from Co and Fe salts of different chemical nature (nitrates and chlorides) taken in a 1:2 cation ratio. Varying the chemical prehistory, synthesis temperature, isothermal holding time, and the reaction medium composition made it possible to obtain a set of $\text{Co}_x\text{Fe}_{3-x}\text{O}_4$ nanoparticles of different average diameters and isomorphous substitution degree x . The resulting nanoparticles' elemental composition, crystal structure, sizes, and magnetic properties were determined using EDX analysis, X-ray diffraction, transmission electron microscopy, and SQUID magnetometry. The temperature dependences of the coercivity, remanent magnetization, squareness on both the average diameter and the stoichiometry of nanoparticles are considered. $\text{Co}_x\text{Fe}_{3-x}\text{O}_4$ nanocrystals ranged from 11 to 29 nm were single magnetic domains and showed ferrimagnetic behavior at room temperature. The hardest magnetic nanoparticles with maximum squareness values in the high-temperature region were formed with $x = 0.79$ using solvothermal treatment of cobalt and iron nitrates at 250 °C, 7 MPa for 10 hours.

Keywords: single-domain cobalt ferrite, ferrimagnetic nanocrystals, size-controlled synthesis, stoichiometry, Rietveld refinement, coercive field, saturation magnetization, squareness.

Received: 19 October 2020

Revised: 9 August 2021

1. Introduction

Cobalt ferrite is well known as a hard magnetic material with a high coercive force (11.9 kOe) [1], moderate saturation magnetization (85 emu/g) [2], strong magnetocrystalline anisotropy (2.7×10^6 J/m), and high Curie temperature (520 °C) [3], which are combined with its increased mechanical hardness and chemical stability. This opens up opportunities for the potential use of CoFe_2O_4 in high-frequency applications [4], microwave devices [5], high-density magnetic storage materials [6], ferrofluids [7], as well as functional systems for hyperthermia [8], targeted drug delivery, and MRI diagnostics [9].

CoFe_2O_4 belongs to the single-phase structure of a cubic reverse spinel with the $Fd\bar{3}m$ space group, where one half of Fe^{3+} ions occupies tetrahedral vacancies (A-position), and the other populates octahedral interstices (B-position) along with Co^{2+} [10, 11]. In the case of cobalt ferrite nanoparticles, there is also a mixed spinel structure with the $(\text{Co}_z^{2+} \text{Fe}_{1-z}^{3+})^A[\text{Fe}_{1+z}^{3+} \text{Co}_{1-z}^{2+}]^B\text{O}_4$ formula, where z is the inversion degree of the corresponding metal ions [3, 12]. A change in x values of $\text{Co}_x\text{Fe}_{3-x}\text{O}_4$ particles strongly affects their magnetic properties since properties largely depend on the superexchange interaction between the tetrahedral and octahedral sublattices [3, 10, 13, 14]. So, for dispersions of cobalt ferrite nanoparticles obtained by the pH-controlled coprecipitation method, the coercive force (H_c) did not change monotonically depending on the stoichiometry. At first, H_c decreased up to the substitution degree of 0.2, then increased in the range $x = 0.2 - 0.6$, after which it again decreased at a higher concentration of Co^{2+} ($x = 0.8$). The saturation magnetization (M_s), on the contrary, increased to $x = 0.2$ and, having reached its maximum value of 61.78 emu/g, decreased with a further increase in the concentration of divalent cobalt in the spinel structure [3]. The coprecipitation method presented in another work [13] made it possible to obtain cobalt ferrite nanoparticles for which an increase in x from 0 to 1 promoted growth in H_c from 7.75 to 340.5 Oe and a decrease in M_s from 59.1 to 32.7 emu/g at room temperature. For $\text{Co}_x\text{Fe}_{3-x}\text{O}_4$ particles synthesized by thermal decomposition of precursors, starting with an substitution degree of 0.1 and ending with 0.7, the authors of [14] recorded an increase in the coercivity from 120 to 610 Oe, after which it began to decrease down to 325 Oe at $x = 1.5$. In turn, the M_s of these nanoparticles decreased as their composition approached stoichiometric since Co^{2+} has a lower magnetic moment than Fe^{3+} . In [10], during the formation of cobalt ferrite nanocrystals under hydrothermal conditions, a

similar tendency was observed in the variation of M_s and H_c , but the maximum value for the latter was reached at $x = 0.75$ and was 810 Oe. Thus, the substitution degree of Fe^{3+} by Co^{2+} in octahedral positions and the conditions of formation of cobalt ferrite nanoparticles affect their final magnetic characteristics.

In addition, to precise control of the composition and structure of CoFe_2O_4 , practical applications require the ability to regulate particle size at the nanoscale. It is known that fine tuning the size of cobalt ferrite nanocrystals in the single magnetic domain region can achieve extremely high values of the coercive force at room temperature [1, 15]. With an increase in the particle diameter, both the saturation magnetization and the coercive force rapidly accrue, but upon transition to the multidomain state, M_s reaches a plateau with a characteristic value of bulk CoFe_2O_4 , and H_c passes through a maximum. Depending on the synthesis conditions, the critical size (D_{cr}) of CoFe_2O_4 nanoparticles corresponding to the boundary of the single-domain region varies from 5 to 40 nm [14, 16–22]. For cobalt ferrite nanoparticles synthesized by the forced hydrolysis in polyol, D_{cr} was about 5 nm with a maximum coercivity of 14.5 kOe (5 K) and a saturation magnetization of 85 emu/g (5 K) [16]. The micellar microemulsion method [17] made it possible to obtain the maximum value of H_c (16 kOe) and provided a plateau for M_s (70 emu/g) at a particle size of 10 nm. In the case of approaches associated with thermal decomposition of precursors [14] and high temperature non-hydrolysis process combined with seed-mediated growth [18], the critical size was 12 nm with magnetic characteristics of 22.8 kOe, 69 emu/g (2 K), and 18 kOe, 82 emu/g (5 K), respectively. Larger D_{cr} were recorded for CoFe_2O_4 nanoparticles obtained by coprecipitation of cobalt and iron salts in the presence of oleic acid (28 nm) [19], hydrothermal synthesis with annealing (40 nm) [20], and the polymeric method via a thermal decomposition process (40 nm) [21]. A special place among the above methods is occupied by hydro(solvo)thermal synthesis due to relatively mild temperature conditions, the possibility of effective control of the composition, size, and morphology of the resulting nanoparticles, as well as due to the high purity and homogeneity degree of the resulting products [23–26].

Therefore, the main task of this work was to determine the effect of the nature of precursors, the composition of the reaction medium, the temperature and time of isothermal holding on the size, structure, and magnetic properties of cobalt ferrite nanoparticles formed under hydro(solvo)thermal conditions.

2. Experimental part

2.1. Synthesis of cobalt ferrite nanoparticles under hydrothermal conditions

$\text{Co}_x\text{Fe}_{3-x}\text{O}_4$ nanoparticles were obtained by coprecipitation of cobalt and iron hydroxides from aqueous solutions of their chlorides or nitrates, followed by dehydration under hydrothermal conditions. Based on the analysis of published data, the following procedure for synthesizing cobalt ferrite nanoparticles was developed.

Prepared solutions of $\text{Co}(\text{NO}_3)_2 \cdot 6\text{H}_2\text{O}$ (analytically pure, GOST 4328-77, Vekton, Russia) and $\text{Fe}(\text{NO}_3)_3 \cdot 9\text{H}_2\text{O}$ (chemically pure, CAS 10294-41-4, Vekton, Russia) or $\text{CoCl}_2 \cdot 6\text{H}_2\text{O}$ (analytically pure, GOST 4328-77, Vekton, Russia) and $\text{FeCl}_3 \cdot 9\text{H}_2\text{O}$ (chemically pure, CAS 10294-41-4, Vekton, Russia) were mixed for 2 hours. Then an aqueous solution of ammonia (NH_4OH) was added dropwise in an amount of 10 ml. The precipitate had formed at $\text{pH}=10$, it was repeatedly washed with distilled water until a negative reaction for chloride or nitrate ions and dried at 65 °C to constant weight. After cooling to room temperature, the resulting powder was crushed and transferred in an amount of 0.5 g to an autoclave with a teflon cell. 14.5 ml of distilled water was added to a weighed portion of a mixture of cobalt and iron hydroxides, and hydrothermal treatment was carried out. The holding time of the reaction mixture in the autoclave was 10 hours at a temperature of 200 °C and pressure of 7 MPa. Further, for nanoparticles of cobalt ferrite obtained from chlorides and nitrates under hydrothermal conditions, the abbreviations HC200 and HN200 will be used, respectively.

2.2. Synthesis of cobalt ferrite nanoparticles under solvothermal conditions

$\text{Co}(\text{NO}_3)_2 \cdot 6\text{H}_2\text{O}$ and $\text{Fe}(\text{NO}_3)_3 \cdot 9\text{H}_2\text{O}$ were each dissolved separately in 15 ml of ethylene glycol ($\text{C}_2\text{H}_6\text{O}_2$) and, after complete dissolution, were mixed. Then, 3.8 ml of ammonia in the form of a 25% aqueous solution as a precipitant ($\text{pH}=10$) were added and mechanically stirred for 1 hour. The resulting mixture was placed in an autoclave and kept for 5 hours at 250 °C or 10 hours at 100 – 250 °C, where the step was taken equal to 50 °C. The pressure in the reaction vessel during the synthesis was 7 MPa. After cooling to room temperature, the resulting black powder was centrifuged for 10 minutes at 8000 rpm. The precipitate of nanoparticles washed with alcohol was dried in air at 45 °C. Subsequently, for brevity, these samples will be designated as SN100, SN150, SN200, SN250⁵, and SN250¹⁰, where the number in the title block indicates the temperature, and the superscript indicates the synthesis time.

Using $\text{CoCl}_2 \cdot 6\text{H}_2\text{O}$ and $\text{FeCl}_3 \cdot 9\text{H}_2\text{O}$ to form cobalt ferrite nanoparticles under solvothermal conditions, the synthesis procedure was identical to that described above, and the name of the sample was taken as SC250.

TABLE 1. Parameters of the CoFe_2O_4 phase with a cubic cell $\alpha = \gamma = \beta = 90^\circ$

Sample	Unit cell parameters	Crystalline domain
	$a = b = c, \text{ \AA}$	$D, \text{ nm}$
HC200	8.3809 ± 0.0008	13.9 ± 0.5
HN200	8.3832 ± 0.0009	11.9 ± 0.5
SC250	8.3965 ± 0.0005	28.7 ± 0.5
SN250 ¹⁰	8.3992 ± 0.0008	24.8 ± 0.5
SN250 ⁵	8.3974 ± 0.0008	15.5 ± 0.5
SN200	8.4015 ± 0.0006	16.7 ± 0.5
SN150	8.4176 ± 0.0012	12.2 ± 0.5
SN100	–	–

2.3. Instruments and characterization

The size and shape of the cobalt ferrite nanoparticles obtained in this study were determined using a Jeol JEM-2100F transmission electron microscope at an accelerating voltage of 200 kV. Aqueous dispersions of CoFe_2O_4 nanopowders were deposited onto copper grids covered with graphene paper to obtain bright-field images.

X-ray diffraction (XRD) patterns of CoFe_2O_4 nanoparticles were obtained using a Rigaku SmartLab diffractometer with $\text{CoK}\alpha$ radiation. The survey was carried out in the 2θ range of angles from 5 to 90° with a scanning speed of $0.5^\circ/\text{min}$. The structure analysis of the obtained XRD patterns was carried out in the MAUD program [27] using the Rietveld method.

Energy dispersive X-ray (EDX) analysis was carried out to investigate the elemental composition of the obtained cobalt ferrite nanoparticles. EDX analysis was carried out on a TESCAN VEGA 3 SBH scanning electron microscope (TESCAN BRNO, Czech Republic) with an Advanced Aztec Energy energy-dispersive attachment for elemental microanalysis based on an X-act semiconductor energy dispersive detector (Oxford Instruments NanoAnalysis, Great Britain).

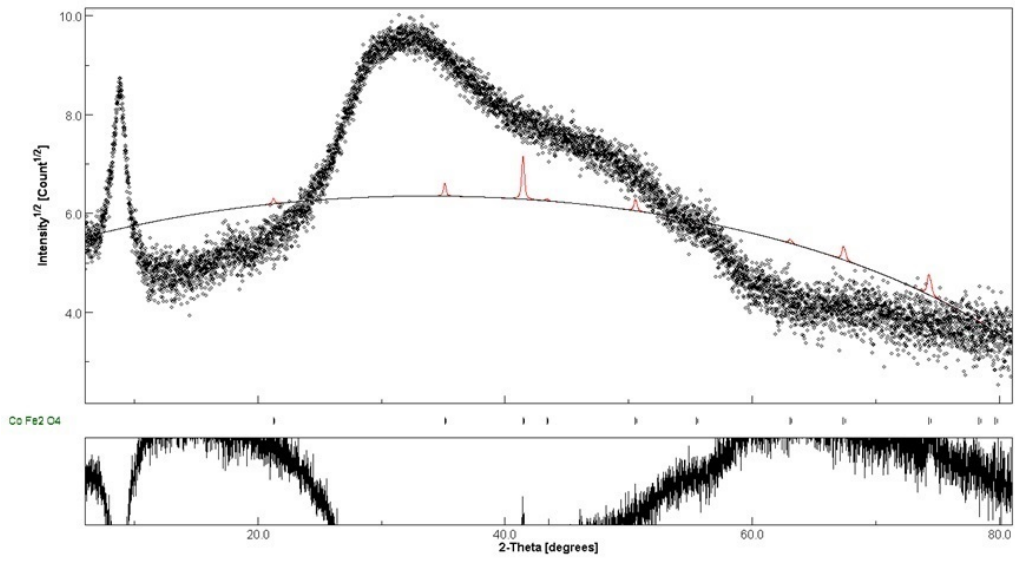
The study of the magnetic properties of the synthesized cobalt ferrite nanoparticles was carried out on a superconducting quantum interferometer (SQUID) MPMS SQUID VSM (Quantum Design) with a magnetic field up to 7 T.

3. Results and discussion

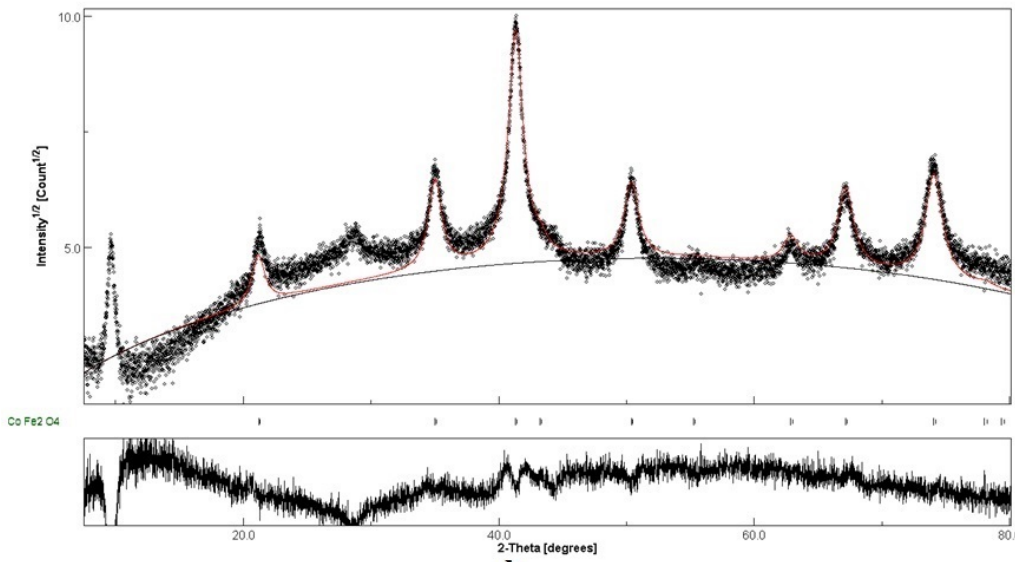
Qualitative X-ray phase analysis of nanoparticles obtained from salts (nitrates, chlorides) of cobalt and iron under hydro- and solvothermal conditions was carried out using the PDWin 4.0 software package (Burevestnik, Russia). Its results showed that HC200, HN200, SN150, SN200, SN250⁵, SN250¹⁰ and SC250 samples correspond to the crystal structure of CoFe_2O_4 (PDF card No. 3-864). No supplementary impurity phases were found during the analysis, except for the SN100 and SN150 nanoparticles. In their XRD patterns, in addition to the amorphous halo and peaks of partially crystallized cobalt ferrite in the 2θ region of 8° , a reflection corresponding to the double layered hydroxide (Co-Fe LDH) [28] was observed. This phase, passed into CoFe_2O_4 when the synthesis temperature increased to 200°C and higher (Fig. 1a,b,c). Analysis of powder XRD data (Fig. 1) using the Rietveld method made it possible to track the simultaneous changes in crystallite sizes and unit cell parameters (Table 1). For nanoparticles formed from cobalt and iron nitrates under solvothermal conditions, the crystallite size grew with an increase in the synthesis temperature, while the volume of a cubic unit cell, on the contrary, decreased. A longer isothermal holding of the reaction mixture also promoted an increase in the size of the $\text{Co}_x\text{Fe}_{3-x}\text{O}_4$ crystallites, but at the same time, had little effect on the unit cell parameters. The use of $\text{CoCl}_2 \cdot 6\text{H}_2\text{O}$ and $\text{FeCl}_3 \cdot 9\text{H}_2\text{O}$ as precursors for the synthesis of nanoparticles led to the compaction of the cubic unit cell and the formation of larger coherent scattering regions in comparison with the samples obtained from the corresponding nitrates (Table 1).

The same tendencies persist for cobalt ferrite nanoparticles obtained by hydrothermal synthesis (Fig. 1e,f). However, it should be noted that the average size of crystallites formed in an aqueous medium at elevated pressure and temperature is noticeably lower than that of their analogs obtained in ethylene glycol (Fig. 1c,e). The same can be said about the volume of the unit cell (Table 1).

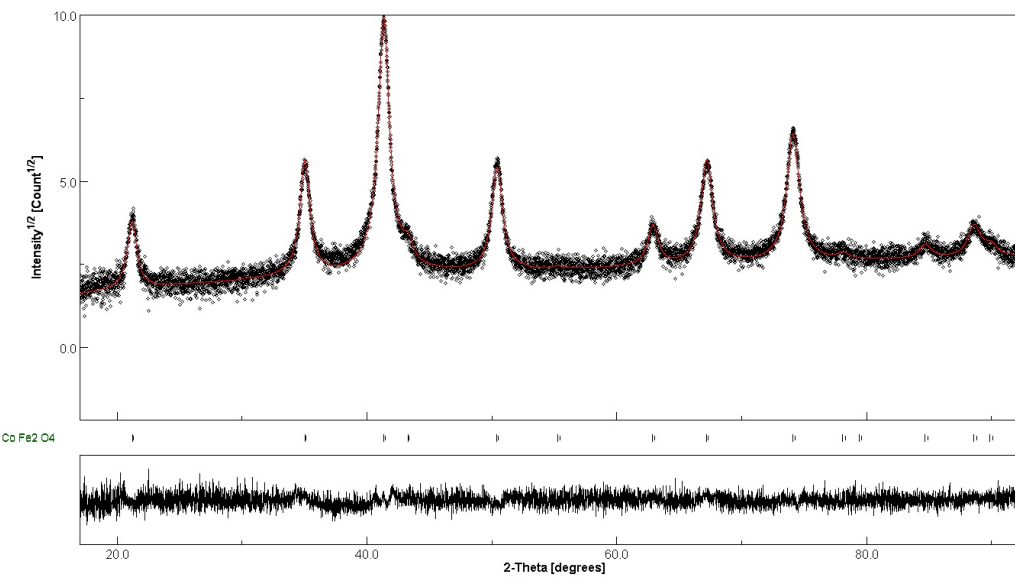
The value of microstresses for the synthesized $\text{Co}_x\text{Fe}_{3-x}\text{O}_4$ nanoparticles, regardless of their chemical prehistory and preparation method, was 0.0025 ± 0.0001 ($0.25 \pm 0.01\%$).



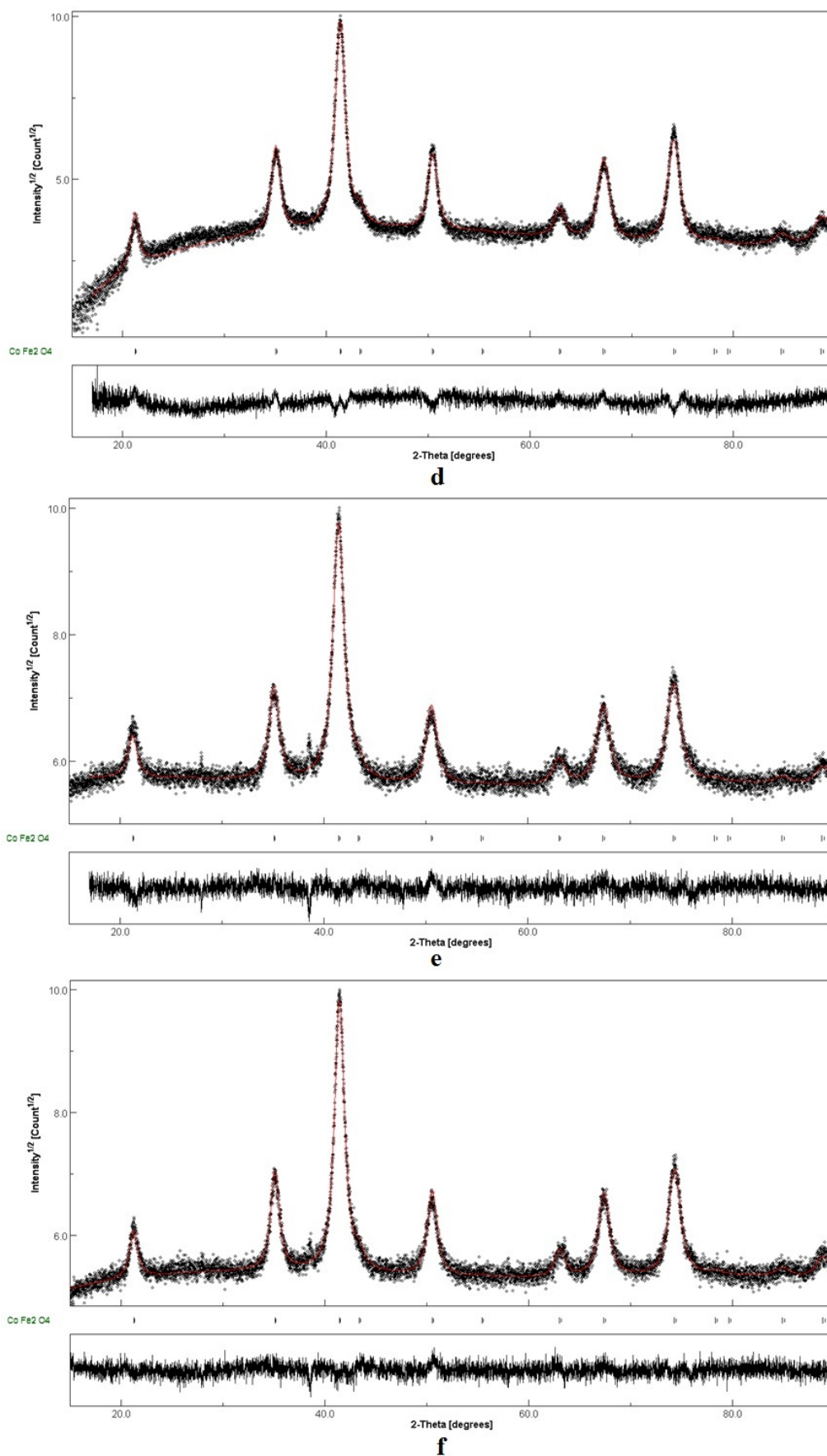
a



b



c

FIG. 1. XRD patterns of SN100 (a), SN150 (b), SN 200 (c), SN250⁵ (d), HN200 (e), HC200 (f) nanoparticles

The morphology of $\text{Co}_x\text{Fe}_{3-x}\text{O}_4$ nanoparticles synthesized by the hydro- and solvothermal method from various precursors is shown in TEM micrographs (Fig. 2a). Cobalt ferrite nanoparticles are mostly quasi-spherical, although a small number of large crystals in the form of plates and octahedra are observed. In Fig. 2b, the diameter data of quasi-spherical nanoparticles as histograms are statistically treated using a lognormal distribution. Data processing was performed in the program OriginPro 2021b (built 9.8.5.201). The lognormal distribution usually describes the size of the synthesized nanoparticles well. In our case, it is better than the normal one. Besides, the obtained data are shown as Half Violin with data points in the left size (Fig. 2c). The size distribution of nanoparticles turned out to be relatively wide and asymmetric for all the selected synthesis conditions (Fig. 2b,c). It should be noted that the maxima in the size histograms corresponding to the average diameter of nanoparticles, within the limits of the method errors, are comparable to the crystallite sizes determined from the XRD data (Fig. 2b,c, Table 1). Thus, this confirms the earlier conclusion that the formation of smaller $\text{Co}_x\text{Fe}_{3-x}\text{O}_4$ nanoparticles is facilitated by the hydrolysis of nitrates of the corresponding metals, followed by the dehydration of oxyhydroxides under hydrothermal conditions.

Elemental analysis showed that the content of cobalt in the products of solvothermal synthesis carried out at 100 °C did not exceed 0.5% and, therefore, no $\text{Co}_x\text{Fe}_{3-x}\text{O}_4$ phases were formed (Table 2). This was also confirmed by the XRD data (Fig. 1a). In the case of an increase in the synthesis temperature to 150 °C, a mixed spinel with a stoichiometric coefficient $x = 0.535$ was formed. Higher temperatures of isothermal holding of cobalt and iron salts under both hydro and solvothermal conditions increased the degree of substituting Fe^{3+} ions in octahedral positions by Co^{2+} but the stoichiometric composition was still not achieved (Table 2).

TABLE 2. Elemental analysis of nanoparticles

Sample	Ratio	at. %			Stoichiometric ratio ¹	
	$\kappa = [\text{Co}]/[\text{Fe}]$	Co	Fe	O	x	$1 - x$
HC200	0.401	12.18	30.4	57.42	0.858	0.142
HN200	0.396	8.97	22.66	68.37	0.851	0.149
SC250	0.384	10.3	26.8	62.9	0.833	0.167
SN250 ¹⁰	0.357	8.31	23.26	68.43	0.790	0.210
SN250 ⁵	0.307	9.79	31.92	58.29	0.704	0.296
SN200	0.353	9.25	26.23	64.52	0.782	0.218
SN150	0.217	4.24	19.54	76.22	0.535	0.465
SN100	0.026	0.5	19.24	80.26	0.076	0.924

¹The formula for calculating the stoichiometric coefficient:

$$\kappa = \frac{x}{3-x} \Leftrightarrow x = \frac{3\kappa}{1+\kappa}; \kappa = \frac{[\text{Co}]}{[\text{Fe}]}; \text{Co}_x\text{Fe}_{3-x}\text{O}_4 \Leftrightarrow (\text{CoFe}_2\text{O}_4)_x(\text{Fe}_3\text{O}_4)_{1-x}$$

Studies of the synthesized cobalt ferrite nanoparticles using SQUID magnetometry showed that their magnetization curves have hysteresis loops regardless of the type of precursor used, as well as the chosen conditions of hydrolysis and dehydration (Fig. 3, Table 3). The only exception was SN250⁵ for which almost superparamagnetic behavior (low coercive force and zero remanent magnetization) was observed at room temperature (Table 3). This may be due to the short synthesis time during which the magnetic domains do not yet have time to form and the magnetic properties of nanoparticles are practically absent [29] (Fig. 3b). It should also be noted that “constricted” hysteresis loops were recorded for cobalt ferrite nanoparticles obtained under hydrothermal conditions or in an organic solvent at temperatures of 150 and 200 °C (Fig. 3a,c), which are typical for a mixture of soft and hard magnetic materials [1, 30]. In this case, such a “necking” in the central part of the M-H loop can be explained by a small amount of superparamagnetic single-domain particles in ferrimagnetic $\text{Co}_x\text{Fe}_{3-x}\text{O}_4$ nanocrystals.

The coercive force (H_c), saturation magnetization (M_s), remanent magnetization (M_r) were determined from the M-H curves at 400, 300, and 5 K for the resulting nanoparticles (Fig. 3, Table 3). The values of H_c and M_s as a function of the average nanoparticle diameter (D) are shown in Fig. 4a,b for a series of crystallites obtained under solvothermal conditions (S) from cobalt and iron nitrates at different temperatures. It was found that the coercive force grew with an increase in the size of the formed $\text{Co}_x\text{Fe}_{3-x}\text{O}_4$ crystallites. It is known from the literature that, for spherical cobalt ferrite nanoparticles, H_c grows with an increase in their diameter to a specific critical single-domain size, after which the coercivity begins to decrease against the background of further enlargement of crystallites [31]. The maximum H_c is associated with the transition from a magnetic single-domain regime to a multidomain one: from the coherent

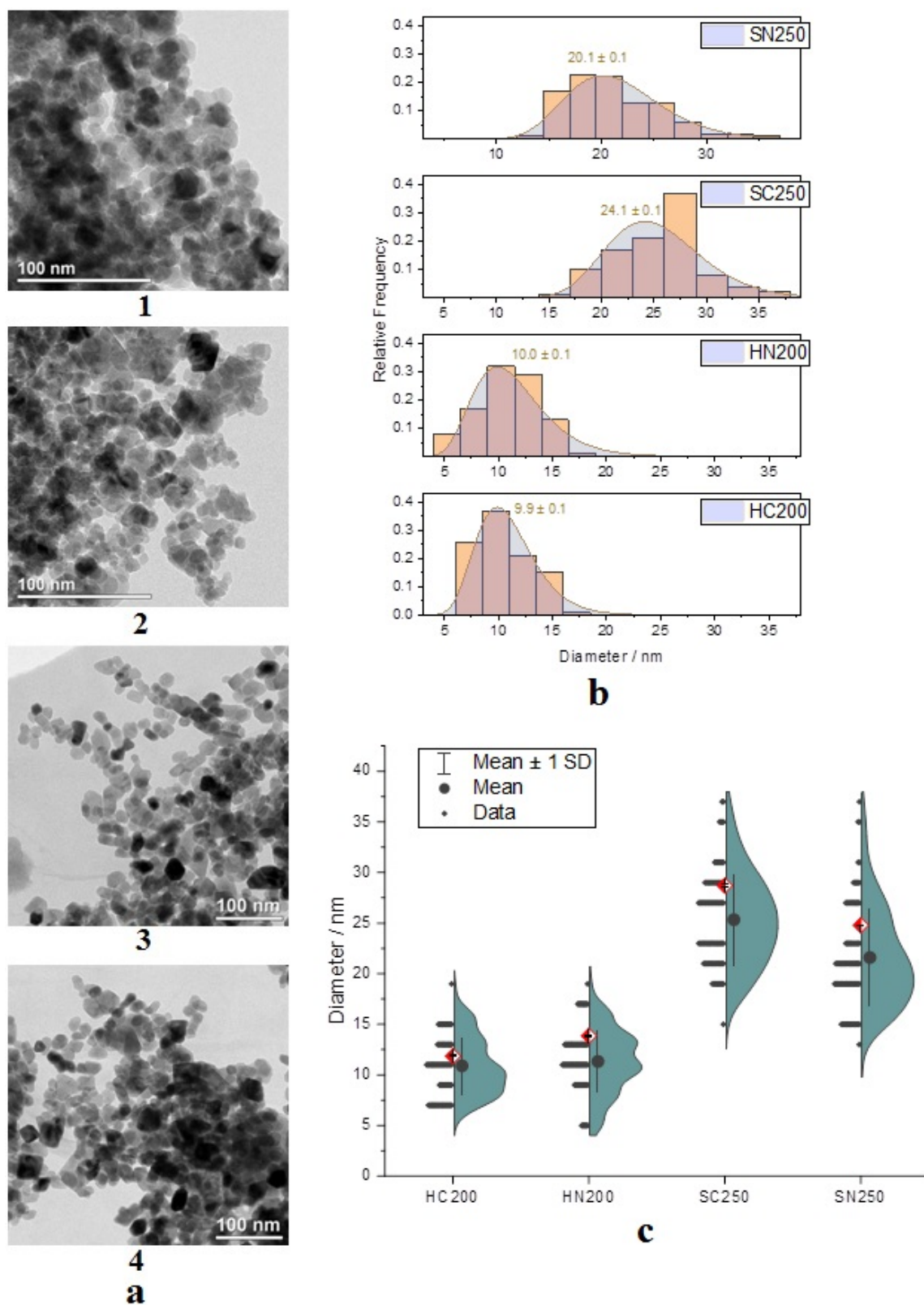


FIG. 2. TEM micrographs (a), histograms of size distribution (b) and Half Violin with data points (c) for SN250¹⁰ (1), SC250 (2), HN200 (3) and HC200 (4) nanoparticles

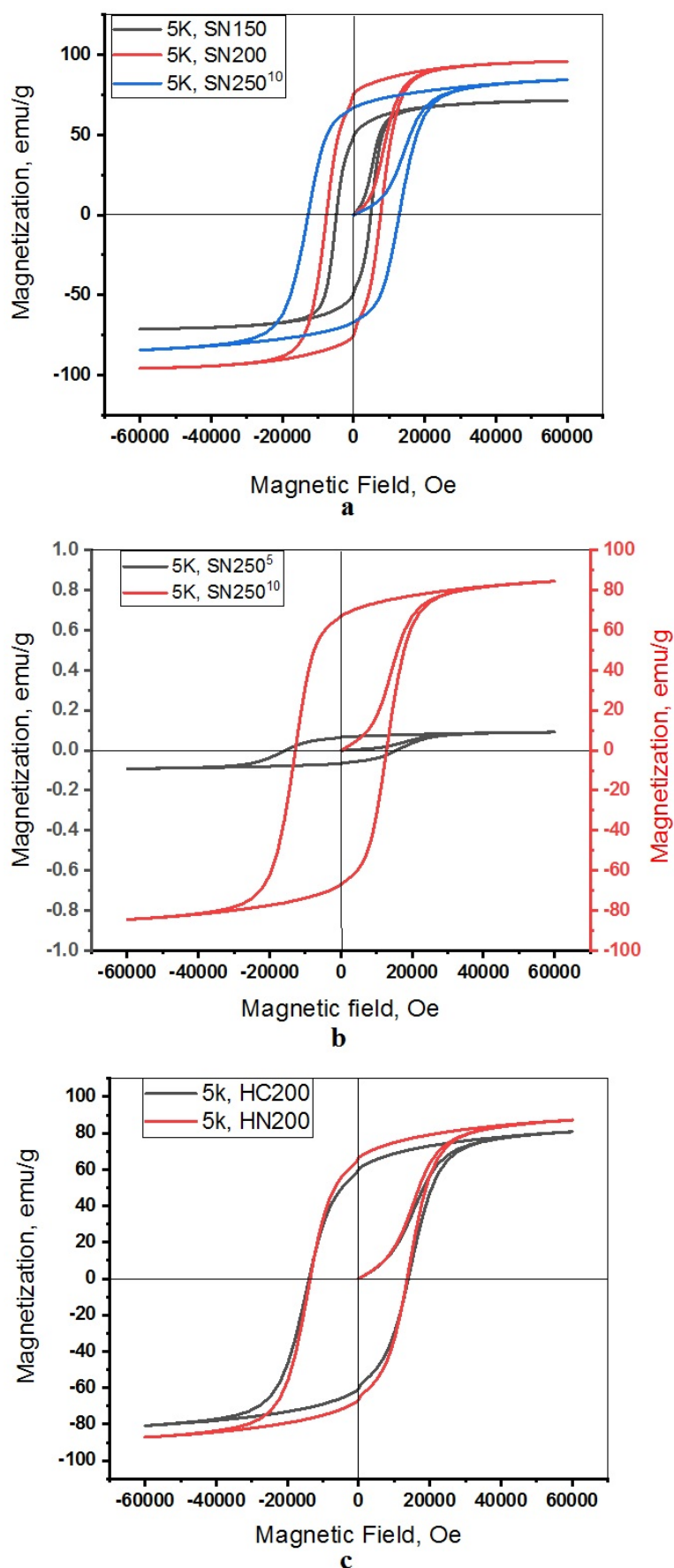


FIG. 3. The low-temperature magnetic hysteresis (M-H) loops for $\text{Co}_x\text{Fe}_{3-x}\text{O}_4$ nanoparticles synthesized under solvo-(a,b) and hydrothermal conditions (c)

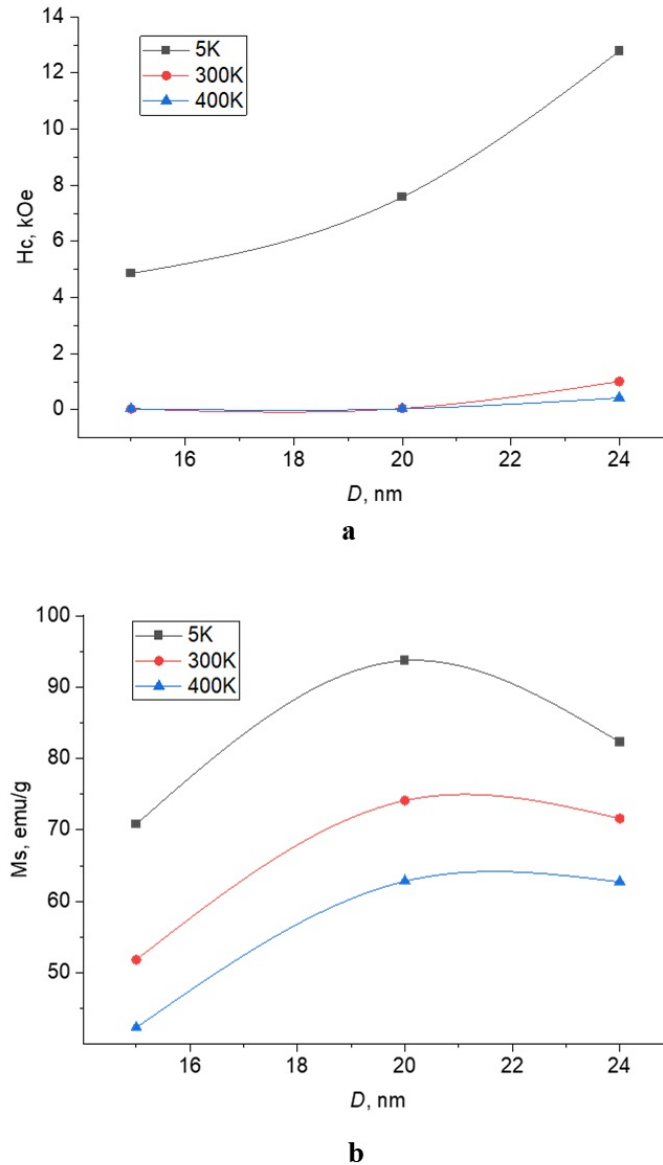


FIG. 4. Particle size dependences of (a) coercivity, (b) saturation magnetization for SN150, SN200, and SN250 samples of $\text{Co}_x\text{Fe}_{3-x}\text{O}_4$ nanoparticles measured at 5, 300, 400 K

to incoherent rotation of spins (twisting rotation and motion of domain walls) [21]. Since we record an increase in the coercivity in the size range from 10 to 24 nm and do not reach the maximum, we assume that all nanoparticles obtained in the S series are single-domain. The saturation magnetization plotted as a function of size at 400, 300, and 5 K shows its initial increase with growing D , but above a specific size, it tends to be a kind of plateau with values comparable to those of bulk CoFe_2O_4 (Fig. 4b) [16]. The increase in M_s with diameter for single-domain particles can be understood by considering the core-shell model [16, 31, 32]. An oriented magnetic domain is considered as a core, and disordered spins on the surface due to imperfect coordination of surface atoms create a shell, the so-called surface “dead magnetic layer” [21]. As the particle size increases, the ratio of the shell thickness to the volume of the domain (core) decreases, which leads to an increase in M_s . When particles approach the multidomain state, the growth of the magnetization values stops.

Low remanent magnetization and almost zero squareness at room temperature for SN150 and SN200 nanoparticles may mean their superparamagnetic behavior is replaced by ferrimagnetic behavior with an increase in the synthesis temperature to 250 °C. According to the Stoner-Wohlfarth model, the fixed M_r/M_s values for synthesized single-domain particles are within the range of values characteristic of non-interacting three-dimensional random particles

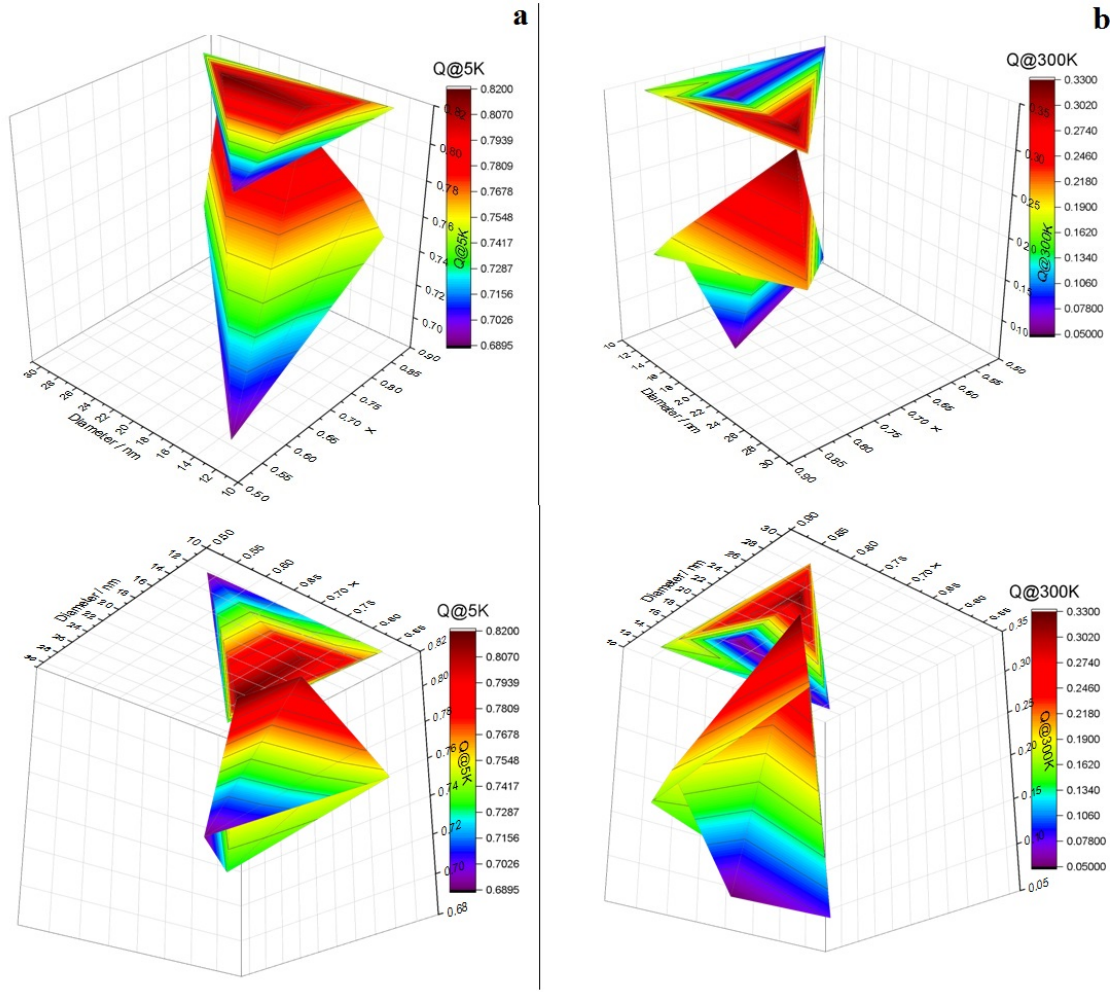


FIG. 5. Dependence of the magnetization hysteresis loop squareness on the stoichiometry of the elemental composition and nanoparticle size at 5 (a) and 300 K (b)

with uniaxial anisotropy [26]. Only samples SN250 and SC250 are knocked out of the available row. The M_r and M_r/M_s values measured at 5 K turned out to be larger than the values estimated at 300 and 400 K. For this, a possible reason may be associated with the increased ratio of magnetic anisotropy to thermal energy at low temperatures [21].

Figure 5 shows surfaces of the squareness (Q) dependence of the hysteresis loops for the magnetization of synthesized cobalt ferrite nanoparticles (Table 3) on their stoichiometry and size:

$$Q = \frac{M_r}{M_s} = f(x, D),$$

where M_r is the remanent magnetization, M_s is the saturation magnetization, x is the stoichiometric coefficient of the composition of $\text{Co}_x\text{Fe}_{(3-x)}\text{O}_4$ nanoparticles (Table 2), D is the size of $\text{Co}_x\text{Fe}_{(3-x)}\text{O}_4$ nanoparticles obtained from TEM data.

Part of Fig. 5, corresponding to the coordinate plane (x, D), shows the projection of the two-dimensional surface of the quantity Q in the form of a color map. It was determined that the maximum squareness of 0.82 at 5 K of the hysteresis loop is at a composition stoichiometry x of about 0.77 – 0.80 and a particle diameter in the range of 16 – 25 nm. At 300 K, the maximum Q value of about 0.33 is observed at the same x and a nanoparticle size of 25 nm.

The analysis of the magnetic properties of $\text{Co}_x\text{Fe}_{3-x}\text{O}_4$ nanoparticles obtained under hydro or solvothermal conditions, depending on the nature of the anion of the salt used, concludes that there is no noticeable difference between them at low temperatures. At 300 K and higher, for nanoparticles obtained from Co and Fe nitrates, the values of H_c , M_r are higher than those for their analogs SC250 and HC200.

The magnetic parameters strongly depend on the distribution of cations (Co^{2+} , Fe^{2+} , Fe^{3+}) between the tetrahedral and octahedral positions. Fe^{3+} and Co^{2+} ions can occupy tetrahedral vacancies (A-positions) or octahedral

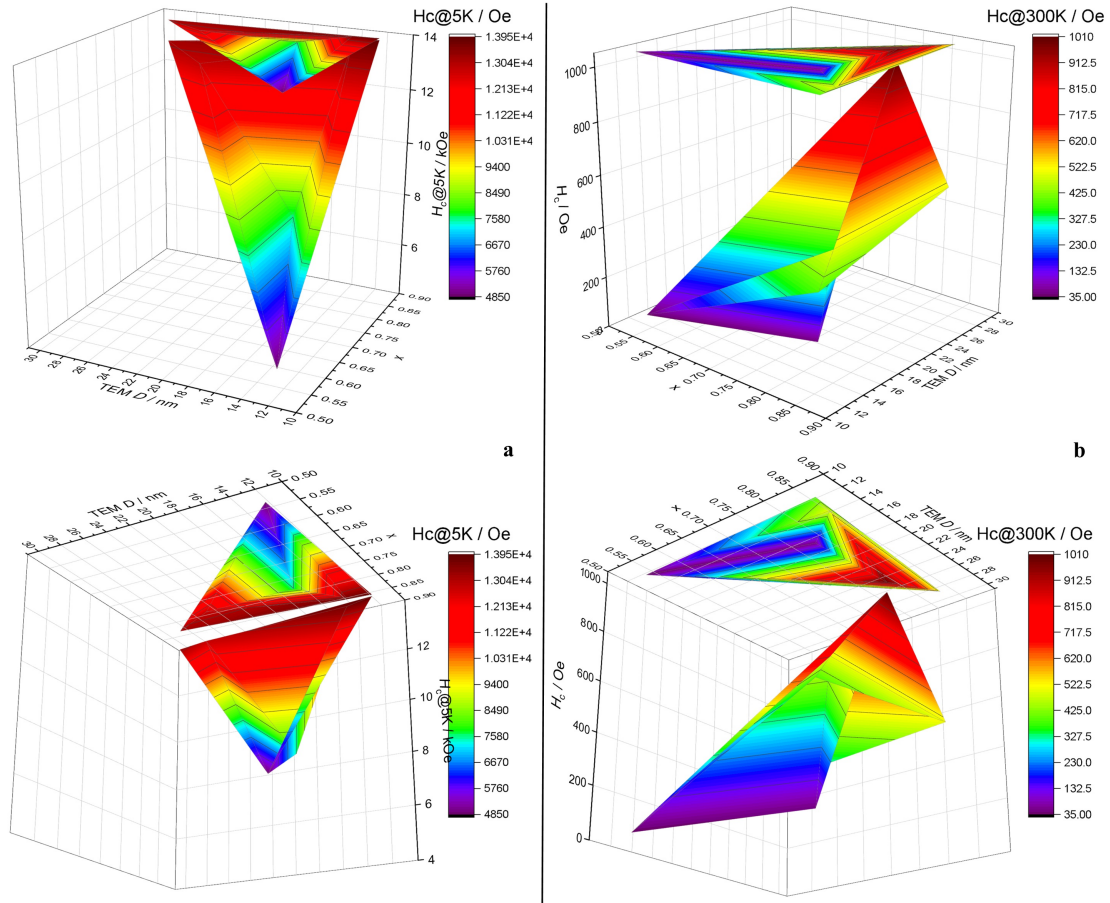


FIG. 6. Dependence of the coercive force on the stoichiometry of the elemental composition and size of cobalt ferrite nanoparticles at 5 (a) and 300 K (b)

TABLE 3. Magnetic characteristics of $\text{Co}_x\text{Fe}_{3-x}\text{O}_4$ nanoparticles depending on their chemical and thermal prehistory

Sample	Temperature											
	5 K				300 K				400 K			
	$Q^{1)}$	M_r , emu/g	M_s , emu/g	H_c , Oe	Q	M_r , emu/g	M_s , emu/g	H_c , Oe	Q	M_r , emu/g	M_s , emu/g	H_c , Oe
HC200	0.75	60.2	80.8	13935	0.16	11	68.2	385	0.04	2.2	58.6	46
HN200	0.77	66.7	87.2	13657	0.19	13.8	72.7	499	0.06	3.6	61.4	86
SC250	0.73	69.5	95	13210	0.21	16.8	79.9	504	0.04	3.1	70.4	56
SN250 ¹⁰	0.82	67.1	82.3	12783	0.33	23.9	71.6	1007	0.21	12.9	62.7	421
SN250 ⁵	–	0.07	0.09	15635	–	0.01	0.08	276	–	–	0.06	–
SN200	0.81	75.7	93.7	7583	0.05	4	74.1	47	0.07	4.5	62.8	33
SN150	0.69	49.1	70.8	4856	0.08	4.1	51.8	35	0.08	3.3	42.3	36

¹⁾squareness of magnetization hysteresis loops for $\text{Co}_x\text{Fe}_{3-x}\text{O}_4$ nanoparticles: $Q = \frac{M_r}{M_s}$

interstices (B-positions) in a cation-substituted spinel $(\text{Co}_z^{2+} \text{Fe}_{1-z}^{3+})^A [\text{Fe}_{1+z}^{3+} \text{Co}_{1-z}^{2+}]^B \text{O}_4$, where z is the extrinsic site inversion [3, 33]. The change of the magnetization in the ferrimagnetic spinel can be explained by the antiparallel interaction between the moments of the cations in the A and B positions. The magnetic moment of the Co^{2+} ion ($3 \mu\text{B}$) is less than that of the Fe^{2+} ($4 \mu\text{B}$) and Fe^{3+} ($5 \mu\text{B}$) ions. At low degrees of inversion, Co^{2+} ions prefer to substitute for Fe^{3+} ions in the A-sites, which decreases the magnetic moment of the tetragonal regions and increases the total magnetic moment. The exchange interaction A–O–B remains stronger than A–O–A and B–O–B. However, the exchange interactions A–O–B weaken with an increase in the degree of substitution of Fe^{3+} ions on Co^{2+} in the A-sites. Because of the latter, the magnetic moments of the tetrahedral and octahedral positions align antiparallel to each other.

The increase in the coercive force seen in Fig. 6a is associated at 5 K with an increase in the stoichiometric ratio. The H_c extremum of 13 – 15 kOe is observed at x in the range of 0.82 – 0.85, while the particle diameter varies over a wide range of 12 – 28 nm. However, at 300 K, an H_c maximum is equal to *ca.* 1 kOe, observed at 0.79 for nanoparticles with a diameter of 25 nm (Fig. 6b), which agrees with the literature data [10, 14].

4. Conclusions

The synthesis of cobalt ferrite, an essential step towards creating new efficient ferrimagnetic nanoparticles, requires control over many physicochemical parameters. When synthesizing cobalt ferrite nanoparticles by the solvo(hydro)thermal method, varying the temperature, nature of the solvent, and counterions for cobalt(II) and iron(III) makes it possible to create $\text{Co}_x\text{Fe}_{3-x}\text{O}_4$ nanoparticles with different stoichiometric ratios. Analysis of the data obtained allowed us to conclude that changes in the conditions for the synthesis of particles from Fe^{3+} and Co^{2+} lead to significant changes in the nanoparticles' properties. These properties include the contribution of the superparamagnetic fraction, the degree of spinel inversion, the average size of nanoparticles, coercivity, and saturation magnetization. The results obtained can be used to develop scientific recommendations for developing state-of-the-art materials for medical applications and in engineering. Further research is needed to understand the relationship between the solvo(hydro)thermal synthesis conditions, the structure of the nanoparticles formed, and their functional (magnetic) properties.

Acknowledgement

X-ray diffraction experiments were performed on the Engineering Center equipment of the St. Petersburg State Technological Institute (Technical University). TEM studies were carried out in the Federal Joint Research Center "Material science and characterization in advanced technology" funded by the Ministry of Education and Science of the Russian Federation.

References

- [1] Perales-Pérez O., Cedeño-Mattei Y. Optimizing processing conditions to produce cobalt ferrite nanoparticles of desired size and magnetic. *Magnetic Spinel - Synthesis, Properties and Applications*, Mohindar Singh Seehra, IntechOpen, 2017.
- [2] López-Ortega A., Lottini E., Fernandez C.D.J., Sangregorio C. Exploring the magnetic properties of cobalt ferrite nanoparticles for the development of a rare-earth-free permanent magnet. *Chem. Mater.*, 2015, **27**, P. 4048–4056.
- [3] Kumar P., Pathak S., Singh A., Kuldeep, Khanduri H., Wang X., Basheed G.A., Pant R.P. Optimization of cobalt concentration for improved magnetic characteristics and stability of $\text{Co}_x\text{Fe}_{3-x}\text{O}_4$ mixed ferrite nanomagnetic fluids. *Mater. Chem. Phys.*, 2021, **265**, P. 124476.
- [4] Goh S.C., Chia C.H., Zakaria S., Yusoff M., Haw C.Y., Ahmadi Sh., Huang N.M., Lim H.N. Hydrothermal preparation of high saturation magnetization and coercivity cobalt ferrite nano crystals without subsequent calcinations. *Mater. Chem. Phys.*, 2010, **120**, P. 31–35.
- [5] Labchir N., Hannour A., Aithssi A., Vincent D., Ganster P., Ihlal A. Controlled electrochemical growth and magnetic properties of CoFe_2O_4 nanowires with high internal magnetic field. *J. Alloys Compd.*, 2021, **868**, P. 159196.
- [6] Sugimoto M. The past, present, and future of ferrites. *J. Am. Ceram. Soc.*, 1999, **82**, P. 269.
- [7] Karthick R., Ramachandran K., Srinivasan R. Study of Faraday effect on $\text{Co}_{1-x}\text{Zn}_x\text{Fe}_2\text{O}_4$ nanoferrofluids. *Nanosystems: Physics, Chemistry, Mathematics*, 2016, **7**(4), P. 624–628.
- [8] Manohar A., Geleta D.D., Krishnamoorthi C., Lee J. Synthesis, characterization and magnetic hyperthermia properties of nearly monodisperse CoFe_2O_4 nanoparticles. *Ceramics International*, 2020, **46**(18), P. 28035-28041.
- [9] Javed F., Abbas M.A., Asad M.I., Ahmed N., Naseer N., Saleem H., Errachid A., Lebaz N., Elaissari A., Ahmad N.M. Gd^{3+} doped CoFe_2O_4 nanoparticles for targeted drug delivery and magnetic resonance imaging. *Magnetochemistry*, 2021, **7**, P. 47.
- [10] Li Y., Lu X., Yang S., Duan W., Zhang Y., Zhou C., Li K., Zhang Y., Shi Q. Synthesis of monodisperse ferromagnetic $\text{Co}_x\text{Fe}_{3-x}\text{O}_4$ colloidal particles with magnetically tunable optical properties. *CrystEngComm*, 2019.
- [11] Shirsath S.E., Liu X., Yasukawa Y., Li S., Morisako A. Switching of magnetic easy-axis using crystal orientation for large perpendicular coercivity in CoFe_2O_4 thin film. *Scientific Reports*, 2016, **6**, P. 30074.
- [12] Long N.V., Yang Y., Teranishi T., Thi C.M., Cao Y., Nogami M. Related magnetic properties of CoFe_2O_4 cobalt ferrite particles synthesised by the polyol method with NaBH_4 and heat treatment: new micro and nanoscale structures. *RSC Adv.*, 2015, **5**, P. 56560–56569.
- [13] Yasemian A.R., Kashi M.A., Ramazani A. Exploring the effect of Co concentration on magnetic hyperthermia properties of $\text{Co}_x\text{Fe}_{3-x}\text{O}_4$ nanoparticles. *Mater. Res. Express*, 2020, **7**, P. 016113.
- [14] Dehsari H.S., Asadi K. The impact of stoichiometry and size on magnetic properties of cobalt-ferrite nanoparticles. *J. Phys. Chem. C*, 2018.

- [15] Gandha K., Elkins K., Poudyal N., Liu J.P. Synthesis and characterization of CoFe_2O_4 nanoparticles with high coercivity. *Journal of Applied Physics*, 2015, **117**, P. 17A736.
- [16] Artus M., Tahar L.B., Herbst F., Smiri L., Villain F., Yaacoub N., Gren'ecche J.-M., Ammar S., Fi'evet F. Size-dependent magnetic properties of CoFe_2O_4 nanoparticles prepared in polyol. *J. Phys.: Condens. Matter.*, 2011, **23**, P. 506001.
- [17] Liu C., Rondinone A.J., Zhang Z.J. Synthesis of magnetic spinel ferrite CoFe_2O_4 nanoparticles from ferric salt and characterization of the size-dependent superparamagnetic properties. *Pure Appl. Chem.* 2000, **72**(1,2), P. 37.
- [18] Song Q., Zhang Z.J. Correlation between spin-orbital coupling and the superparamagnetic properties in magnetite and cobalt ferrite spinel nanocrystals. *J. Phys. Chem. B*, 2006, **110**, P. 11205–11209.
- [19] Maaz K., Mumtaz A., Hasanain S.K., Ceylan A. Synthesis and magnetic properties of cobalt ferrite (CoFe_2O_4) nanoparticles prepared by wet chemical route. *J. Magn. Magn. Mater.*, 2007, **30**(8), P. 289–295.
- [20] Shyamaldas, Bououdina M., Manoharan C. Dependence of structure/morphology on electrical/magnetic properties of hydrothermally synthesised cobalt ferrite nanoparticles. *Journal of Magnetism and Magnetic Materials*, 2020, **493**, P. 165703.
- [21] Das A., Bestha K.K., Bongurala P., Gorige V. Correlation between size, shape and magnetic anisotropy of CoFe_2O_4 ferrite nanoparticles. *Nanotechnology*, 2020, **31**, P. 335716.
- [22] Kumar Y., Sharma A., Ahmed Md.A., Mali S.S., Hong C.K., Shirage P.M. Morphology-controlled synthesis and enhanced energy product (BH)_{max} of CoFe_2O_4 nanoparticles.
- [23] Fayazzadeh S., Khodaei M., Arani M., Mahdavi S.R., Nizamov T., Majouga A. Magnetic properties and magnetic hyperthermia of cobalt ferrite nanoparticles synthesized by hydrothermal method. *Journal of Superconductivity and Novel Magnetism*, 2020, **3**(3), P. 2227–2233.
- [24] Almjasheva O.V., Gusarov V.V. Prenucleation formations in control over synthesis of CoFe_2O_4 nanocrystalline powders. *Russian Journal of Applied Chemistry*, 2016, **89**(6), P. 851–856.
- [25] Dippong T., Levei E.A., Cadar O. Recent advances in synthesis and applications of MFe_2O_4 (M = Co, Cu, Mn, Ni, Zn) nanoparticles. *Nanomaterials*, 2021, **11**, P. 1560.
- [26] Kuznetsova V., Almjasheva O., Gusarov V.V. Influence of microwave and ultrasonic treatment on the formation of CoFe_2O_4 under hydrothermal conditions. *Glass Physics and Chemistry*, 2009, **35**(2), P. 205–209.
- [27] Lutterotti L., Bortolotti M., Ischia G., Lonardelli I., Wenk H.-R. Rietveld texture analysis from diffraction images. *Z. Kristallogr., Suppl.*, 2007, **26**, P. 125–130.
- [28] Barashok K.I., Panchuk V.V., Semenov V.G., Almjasheva O.V., Abiev R.Sh. Formation of cobalt ferrite nanopowders in an impinging-jets microreactor. *Nanosystems: Physics, Chemistry, Mathematics*, 2021, **12**(3), P. 30–310.
- [29] Yuan Y., Wei S., Liang Y., Wang B., Wang Y. Effect of solvothermal reaction-time on microstructure and microwave absorption properties of cobalt ferrite. *Materials*, 2020, **13**, P. 5331.
- [30] Zhao L., Zhang H., Xing Y., Song S., Yu S., Shi W., Guo X., Yang J., Lei Y., Cao F. Studies on the magnetism of cobalt ferrite nanocrystals synthesized by hydrothermal method. *J. Solid State Chem.*, 2008, **181**, P. 245–252.
- [31] Lu R.E., Chang K. G., Fu B., Shen Y.J., Xu M.W., Yang S., Song X.P., Liu M., Yang Y.D. Magnetic properties of different CoFe_2O_4 nanostructures: nanofibers versus nanoparticles. *J. Mater. Chem. C*, 2014, **2**, P. 8578.
- [32] Ansari S.M., Sinha B.B., Phase D., Sen D., Sastry P.U., Kolekar Y.D., Ramana C.V. Particle size, morphology, and chemical composition controlled CoFe_2O_4 nanoparticles with tunable magnetic properties via oleic acid based solvothermal synthesis for application in electronic devices. *ACS Appl. Nano Mater.*, 2019, **2**, P. 182–1843.
- [33] Raghvendra Yadav S., Havlica J., Masilko J., Kalina L., Hajdúchová M., Enev V., Wasserbauer J., Kuřitka I., Kozakova Z. Structural, cation distribution, and magnetic properties of CoFe_2O_4 spinel ferrite nanoparticles synthesized using a starch-assisted sol–gel auto-combustion method. *Journal of Superconductivity and Novel Magnetism*, 2015, **28**, P. 1851–1861.

Preparation and X-ray luminescence of $\text{Ba}_{4\pm x}\text{Ce}_{3\pm x}\text{F}_{17\pm x}$ solid solutions

D. S. Yasyrkina, S. V. Kuznetsov, A. A. Alexandrov, S. Kh. Batygov, V. V. Voronov, P. P. Fedorov
 Prokhorov General Physics Institute of the Russian Academy of Sciences, Moscow, Russia
 darya.yasyrkina@gmail.com

DOI 10.17586/2220-8054-2021-12-4-505-511

Single-phase $\text{BaF}_2:\text{Ce}$ solid solutions containing 30 – 40 mol. % cerium with the simultaneous entry of potassium into the crystal lattice in an amount of 0.7 – 0.8 mol. % were prepared by coprecipitation from aqueous nitrate solutions with potassium fluoride as the fluorinating agent. The cerium X-ray luminescence intensity increases in response to increasing cerium concentration contrary to the concentration quenching effect.

Keywords: barium fluoride, cerium, X-ray luminescence.

Received: 21 July 2021

1. Introduction

Barium fluoride is a well-known heavy scintillator with two X-ray luminescence bands. The 220-nm band exhibits a very short decay time (0.8 ns), and a broad exciton band peaking around 300 nm has a decay time of 600 – 800 ns [1, 2]. In cerium-doped barium fluoride, exciton luminescence transforms to cerium ion luminescence induced by $d-f$ electron transitions in Ce^{3+} ion [3–8]. The highest luminescence light yield occurs when the CeF_3 concentration is approximately 0.1 mol. %. At higher cerium concentrations, the luminescence intensity declines dramatically due to the concentration quenching phenomenon [9]. The decline was observed both for single crystals and for $\text{BaF}_2:\text{Ce}^{3+}$ optical ceramics [10–15]. The concentration decay effect was assigned to defect cluster formation in fluorite-type lattices upon formation of $\text{Ba}_{1-x}\text{Ce}_x\text{F}_{2+x}$ solid solutions [9]. The composition corresponding to the highest luminescence light yield is the one with the highest concentration of free $\text{Ce}^{3+}-\text{F}^-$ dipoles in the BaF_2 lattice [16]. In addition, barium fluoride dissolves up to 52 mol. % CeF_3 , which radically changes the physical properties of its crystals, in particular, appreciably increases their density [17, 18].

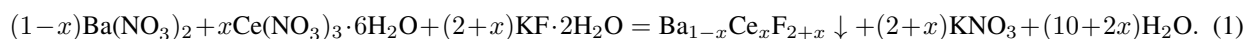
A natural strategy to gain X-ray luminescence in high-cerium $\text{Ba}_{1-x}\text{Ce}_x\text{F}_{2+x}$ solid solutions is to destroy defect clusters to release $\text{Ce}^{3+}-\text{F}^-$ free dipoles. This can be fulfilled by doping the solid solution with univalent cations, e.g., potassium. Potassium fluoride is frequently used to prepare precursors of fluoride optical ceramics [19–23]. It was due to the use of potassium fluoride in the synthesis of precursors that X-ray luminescence was induced in BaCeF_5 ceramics [24].

The goals of this work were to prepare $\text{Ba}_{1-x}\text{Ce}_x\text{F}_{2+x}$ solid solutions by coprecipitation from aqueous nitrate solutions with KF as the precipitating agent and to study X-ray luminescence of Ce^{3+} ions.

2. Experimental section

The initial reagents were used $\text{Ce}(\text{NO}_3)_3 \cdot 6\text{H}_2\text{O}$ (99.99% pure, Lanhit, Moscow, Russia), $\text{Ba}(\text{NO}_3)_2$ (specialty grade, Vekton, St. Petersburg, Russia), $\text{KF} \cdot 2\text{H}_2\text{O}$ (reagent grade, the Fluoride Salts Plant, Russia), and bidistilled water. The potassium fluoride was stored in a desiccator. The reagents were used as received.

Samples were prepared by coprecipitation from aqueous solutions [25] by reaction (1):



Barium nitrate and cerium nitrate solutions (0.08 mol/L each) were mixed, and the mixed solution was added drop by drop to a 0.16 M potassium fluoride solution under vigorous stirring on a magnetic stirrer. The potassium fluoride was used in a 7% excess over the stoichiometry. Once dropwise addition was over, the resulting suspension was stirred for 2 hours. After a precipitate settled, the mother solution was decanted, and the precipitate was washed with bidistilled water. Nitrate leaching was monitored by the diphenylamine test. The as-washed precipitate was air-dried at 45 °C. The cerium fluoride content in samples ranged from 30 to 55 mol. %. X-ray phase analysis of samples were carried out on Bruker D8 ADVANCE diffractometer using $\text{CuK}\alpha$ radiation. The unit cell parameters and coherent scattering domain (CSD) sizes were calculated in the TOPAS software ($R_{wp} < 10$). The size of the particles and the morphology of the samples were studied by means of Carl Zeiss NVision 40 scanning electron microscope (Germany) with an Oxford Instruments XMAX microprobe analyzer (UK) (80 mm²) for energy dispersive X-ray spectroscopy. The particle size was averaged over 25 particles in the ImageJ software. The X-ray luminescence (XRL) spectra of the prepared samples were measured on a laboratory installation built of an X-ray source (tungsten anode) and an FSD-10

mini-spectrometer (Optofiber LLC, Moscow, Russia). A test sample was placed onto the holder horizontally under the beam of the X-ray source operating at a voltage of 40 kV and a current of 35 mA. The XRL signal was collected by a waveguide and transferred to the FSD-10 spectrometer. The luminescence was recorded in the 200 – 1000 nm range of the spectrum.

3. Results and discussion

Prior studies [26–29] imply that the coprecipitation of barium and cerium fluorides from aqueous solutions by various precipitating agents yields two-phase samples (pure barium fluoride and a fluorite phase containing 30 – 45 mol. % CeF_3). Single-phase samples can be prepared at 32–58 mol. % CeF_3 with hydrofluoric acid or ammonium fluoride as the precipitating agent [28].

X-ray diffraction patterns for samples with as-batch cerium concentrations of 30.0, 35.0, 40.0, 42.5, 45.0, 47.5, 50.0, and 55.0 mol. % shows on Fig. 1. X-ray diffraction experiments showed that our syntheses of solid solutions yielded single-phase powders with the fluorite structure containing 30 – 40 mol. % cerium. When the cerium concentration increased to 42.5 mol. %, a second (CeF_3 -based) phase appeared, and its X-ray reflection intensity increased as the cerium concentration increased further (Fig. 1).

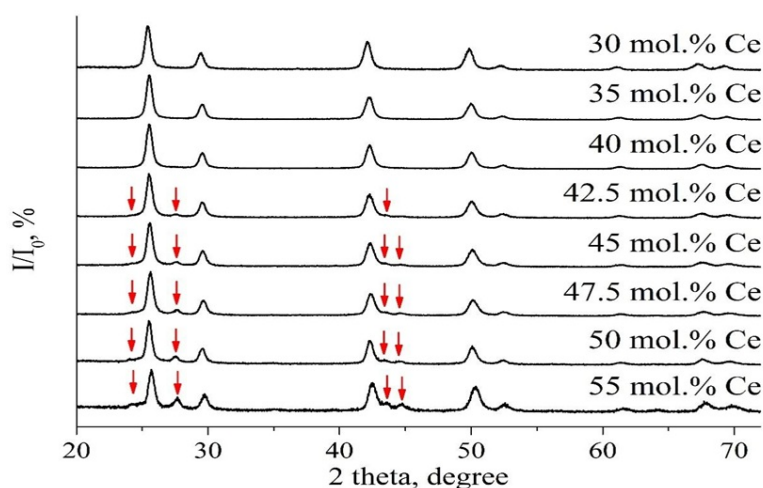


FIG. 1. X-ray diffraction patterns of $\text{BaF}_2\text{-CeF}_3$ samples with various cerium concentrations (the peaks marked with arrow refer to the CeF_3 tysonite phase)

Table 1 displays the calculated unit cell parameters and CSDs of prepared samples. An inspection of the tabulated values shows that, as the cerium concentration increases, the unit cell parameter of the fluorite phase decreases systematically due to the cerium radius being smaller than the barium radius [31].

The unit cell parameter versus rare-earth-ion concentration relationship for $\text{Ba}_{1-x}\text{Ce}_x\text{F}_{2+x}$ fluorite solid solutions borrowed from [30] was used to estimate the cerium concentration as

$$a = a_0 + kx, \quad (2)$$

where $a_0 = 6.2000 \text{ \AA}$ is the BaF_2 unit cell parameter and $k = -0.36$ (Table 2). The estimated compositions were richer in cerium compared to the as-batch compositions for single-phase samples and were depleted in cerium for biphasic samples.

Figure 2 shows the SEM images of single-phase samples. The mean particle sizes in these samples were 15 nm, in match with the CSD calculations (Table 1).

The EDX results reveal that potassium does enter the solid solution lattice when the as-batch cerium concentration is 35.0 or 40.0 mol. % (Table 2). Despite the additional entrance of potassium, there is a satisfactory match between the estimates by Eq. (2) and EDX measurements. Between the as-analyzed and as-batch concentrations, there is a reasonable match.

X-ray luminescence spectra for single-phase $\text{Ba}_{1-x}\text{Ce}_x\text{F}_{2+x}$ samples presented on Fig. 3.

An inspection of the X-ray luminescence spectra elucidated an increase in intensity of the 347-nm cerium luminescence in response to increasing cerium concentration.

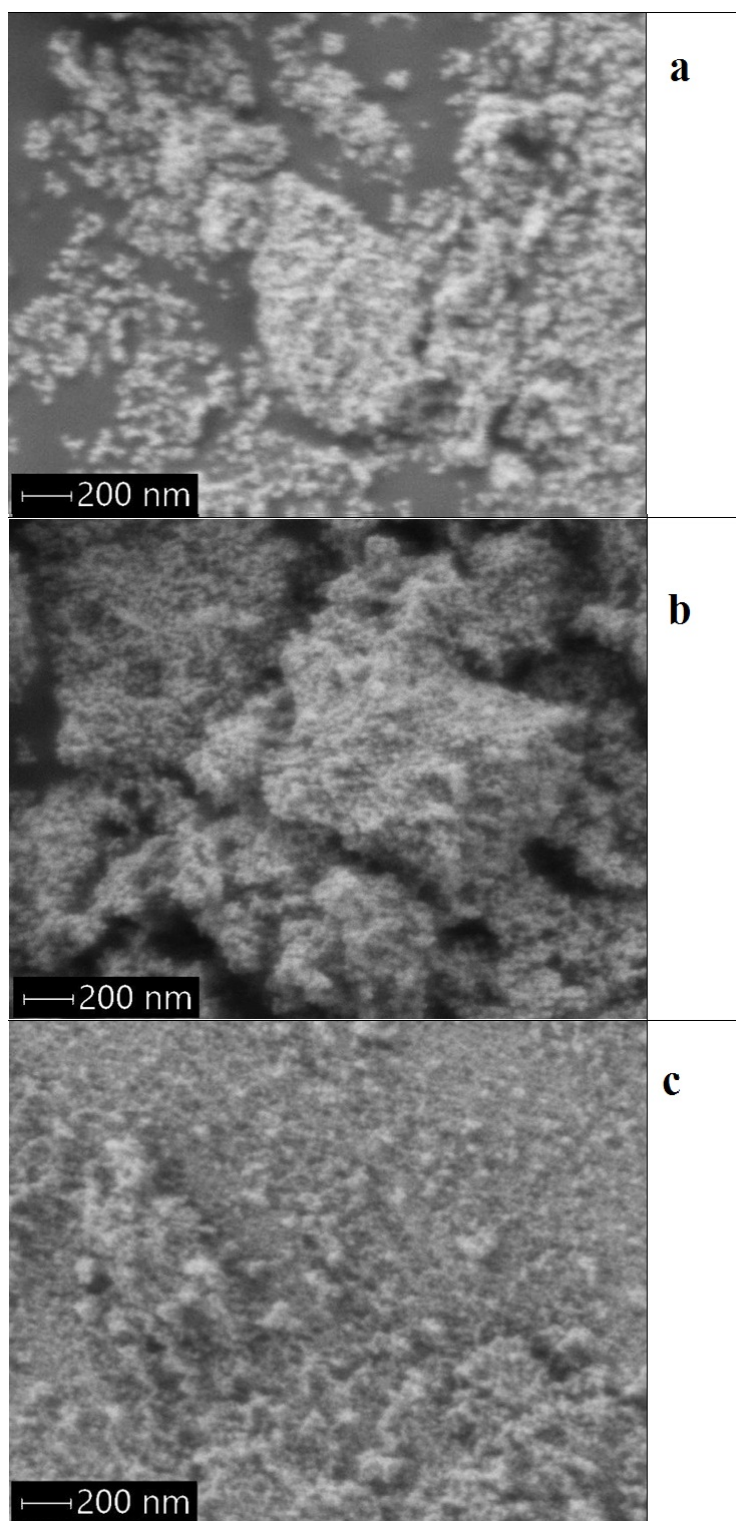


FIG. 2. SEM images of $Ba_{1-x}Ce_xF_{2+x}$ samples containing (a) 30.0 mol. %, (b) 35.0 mol. %, and (c) 40.0 mol. % nominal composition

TABLE 1. Unit cell parameters and CSDs of prepared samples

Nominal composition	Phase	Unit cell parameter, Å	CSD, nm
Ba _{0.70} Ce _{0.30} F _{2.30}	Fluorite	6.071(1)	18(1)
Ba _{0.65} Ce _{0.35} F _{2.35}	Fluorite	6.059(1)	19(1)
Ba _{0.60} Ce _{0.40} F _{2.40}	Fluorite	6.050(1)	17(1)
Ba _{0.575} Ce _{0.425} F _{2.425}	Fluorite	6.054(1)	16(1)
	presence a tysonite phase		
Ba _{0.55} Ce _{0.45} F _{2.45}	Fluorite	6.048(1)	16(1)
	presence a tysonite phase		
Ba _{0.525} Ce _{0.475} F _{2.475}	Fluorite	6.046(1)	16(1)
	presence a tysonite phase		
Ba _{0.50} Ce _{0.50} F _{2.50}	Fluorite	6.039(1)	15(1)
	presence a tysonite phase		
Ba _{0.45} Ce _{0.55} F _{2.55}	Fluorite	6.035(1)	15(1)
	presence a tysonite phase		

TABLE 2. Estimated compositions of prepared samples

Nominal composition	As calculated from the unit cell parameter	As probed by EDX
Ba _{0.70} Ce _{0.30} F _{2.30}	Ba _{0.642} Ce _{0.358} F _{2.358}	Ba _{0.645} Ce _{0.355} F _{2.355}
Ba _{0.65} Ce _{0.35} F _{2.35}	Ba _{0.608} Ce _{0.392} F _{2.392}	Ba _{0.594} Ce _{0.398} K _{0.008} F _{2.390}
Ba _{0.60} Ce _{0.40} F _{2.40}	Ba _{0.583} Ce _{0.417} F _{2.417}	Ba _{0.563} Ce _{0.430} K _{0.007} F _{2.423}
Ba _{0.575} Ce _{0.425} F _{2.425}	Ba _{0.594} Ce _{0.406} F _{2.406}	————
Ba _{0.55} Ce _{0.45} F _{2.45}	Ba _{0.578} Ce _{0.422} F _{2.422}	————
Ba _{0.525} Ce _{0.475} F _{2.475}	Ba _{0.572} Ce _{0.428} F _{2.428}	————
Ba _{0.50} Ce _{0.50} F _{2.50}	Ba _{0.553} Ce _{0.447} F _{2.447}	————
Ba _{0.45} Ce _{0.55} F _{2.55}	Ba _{0.542} Ce _{0.458} F _{2.458}	————

The unit cell parameter of the fluorite solid solution changes due to the interplay of two factors: the substitution of barium by a smaller cerium ion [31] and the entrance of an additional (interstitial) fluoride ion for providing charge compensation as



Individual dipoles are observed only for low cerium concentrations in the solid solutions. The formation of *nmn* dipoles of trigonal symmetry is characteristic of low concentrations of cerium in the BaF₂ matrix [16, 32].

The association of dipoles in the barium fluoride matrix occurs with an increase in the cerium concentration, which leads to the formation of defect clusters. There is, as yet, no common structural description in terms of defect clusters for concentrated Ba_{1-x}Ce_xF_{2+x} solid solutions in spite of numerous structural studies for chemically similar Ba_{1-x}La_xF_{2+x} [33–40] solid solutions. An essential factor for a reliable interpretation of the results is the concentration range over which fluorite phases are formed in low-temperature syntheses of solid solutions in BaF₂–RF₃ systems. High-temperature syntheses in these systems yield ordered fluorite-related phases of Ba₄R₃F₁₇ stoichiometry [18, 42–45]. These phases were found in all BaF₂–RF₃ systems for R = Ce–Lu, Y when their phase equilibria were studied [18, 42, 46]. Kieser and Greis [46] prepared an ordered Ba₄Ce₃F₁₇ phase by heat-treating a disordered solid solution of the appropriate concentration at 400 °C. The fluorite-related Ba₄R₃F₁₇ phases are distinguished by a trigonal distortion of the fluorite-type lattice caused by spatial ordering of R₆F₃₇ clusters [44]. Accordingly, the synthesis of single-phase fluorite solid solutions containing 30 – 40 mol. % cerium may be regarded as the synthesis of a Ba_{4±x}Ce_{3±x}F_{17±x} phase, whose ordering is not manifested at the nanoscale level [47–51]. It is quite natural to suggest that R₆F₃₇ clusters exist in the structure of this phase, substituting for parts of the Ba₆F₃₂ lattice in accordance

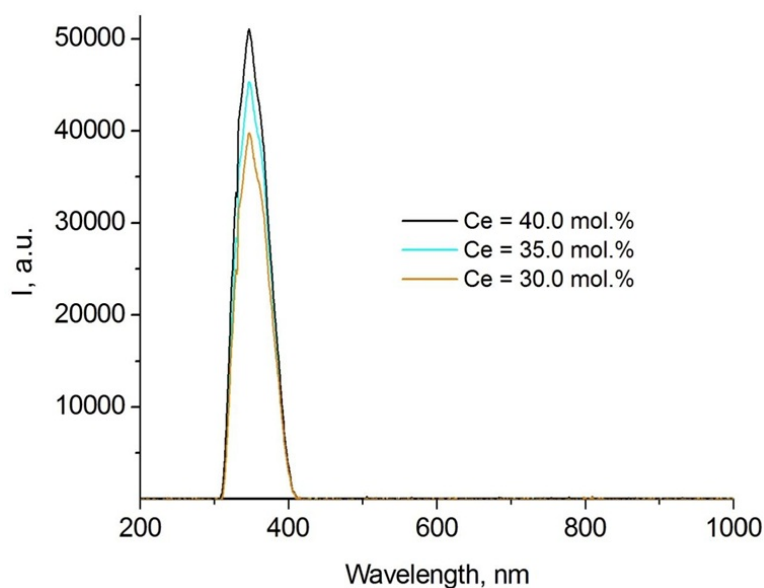


FIG. 3. X-ray luminescence spectra of single-phase $Ba_{1-x}Ce_xF_{2+x}$ solid solution samples

with the isomorphic substitution scheme advanced by Bevan et al. [52]. The shift of the X-ray luminescence peak from 330 to 347 nm may serve as an argument for this suggestion. The observation of X-ray luminescence in the prepared samples both by us and by Chen and Wu [24] may be regarded as the verification of the expected increase in free dipole concentration due to additional entrance of potassium in the barium fluoride host.

The concerted entrance of univalent and trivalent cations to form solid solutions is typical of the fluorite lattice [53]. Potassium was systematically observed to enter the host fluorite lattice in nanofluorides synthesized by coprecipitation of solid solutions [19]. In the $NaF-BaF_2-GdF_3$ ternary system, univalent sodium enters the lattice of the $Ba_4Gd_3F_{17}$ phase thereby extending its existence area [54].

4. Conclusions

A range of single-phase $Ba_{1-x}Ce_xF_{2+x}$ ($x = 0.30 - 0.40$) solid solutions, with an average particle size of 15 nm, prepared by coprecipitation from aqueous solutions, has been determined. It has been suggested that these solid solutions actually have a more complex composition, namely, $Ba_{4\pm x}Ce_{3\pm x}F_{17\pm x}$. The X-ray luminescence intensity in the solid solution samples increased in response to cerium concentration, increasing from 30 to 40 mol. % without concentration quenching. The absence of concentration decay was most likely due to potassium (0.7 – 0.8 mol. %) entering the crystal lattice, and thus, precluding cerium-based cluster formation.

References

- [1] Rodnyi P.A. Core-valence luminescence scintillators. *Radiat. Meas.*, 2004, **38**, P. 343–352.
- [2] Seliverstov D.M., Demidenko A.A., Garibin E.A., Gain S.D., Gusev Yu. I., Fedorov P.P., Kosyanenko S.V., Mironov I.A., Osiko V.V., Rodnyi P.A., Smirnov A.N., Suvorov V.M. New fast scintillators on the base of BaF_2 crystals with increased light yield of 0.9 ns luminescence for TOF PET. *Nuclear Instruments and Methods in Physics Research*, 2012, **695**, P. 369–372.
- [3] Visser R., Dorenbos P., van Eijk C.W.E., Meijerink A., Blasse G. Energy transfer processes involving different luminescence center in $BaF_2:Ce$. *J. Phys. Condens. Matter*, 1993, **5**, P. 1659–1680.
- [4] Sobolev B.P. Multicomponent crystals based on heavy metal fluorides for radiation detectors. *Barcelona: Institut d'Estudis Catalans*, 1995, P. 265.
- [5] Wojtowicz A.J., Szupryczynski P., Glodo J., Drozdowski W., Wisniewski D. Radioluminescence and recombination processes in $BaF_2:Ce$. *J. Phys.: Condens. Matter*, 2000, **12**, P. 4097–4124.
- [6] van Eijk C.W.E., et al. Inorganic-scintillator development. *Nucl. Instrum. Meth.: Phys. Res.*, 2001, **460**(1), P. 1–14.
- [7] Dorenbos P., et al. The Effects of La^{3+} and Ce^{3+} Dopants on the Scintillation Properties of BaF_2 Crystals. *Radiat. Effects Defects Solids*, 2000, **119-121**(1), P. 87–92.
- [8] Janus S., Wojtowicz A.J. Scintillation light yield of $BaF_2:Ce$. *Opt. Mater.*, 2009, **31**, P. 523–526.
- [9] Batygov S.Kh., Fedorov P.P., Kuznetsov S.V., Osiko V.V. Luminescence of $Ba_{1-x}Ce_xF_{2+x}:Ce^{3+}$ Crystals. *Doklady Physics*, 2016, **61**(1), P. 50–54.
- [10] Rodnyi P.A., Gain S.D., Mironov I.A., Garibin E.A., Demidenko A.A., Seliverstov D.M., Gusev Yu.I., Fedorov P.P., Kuznetsov S.V. Spectral-kinetic characteristics of crystals and nanoceramics based on BaF_2 and $BaF_2:Ce$. *Phys. Solid State*, 2010, **52**(9), P. 1910–1914.

- [11] Fedorov P.P., Ashurov M.Kh., Boboyarova Sh.G., Boibobeva S., Nuritdinov I., Garibin E.A., Kuznetsov S.V., Smirnov A.N. Absorption and Luminescence Spectra of CeF₃-Doped BaF₂ Single Crystals and Nanoceramics. *Inorganic Materials*, 2016, **52**(2), P. 213–217.
- [12] Batygov S.Kh., Bolyasnikova L.S., Garibin E.A., Demidenko V.A., Doroshenko M.E., Dykelskii K.V., Luginina A.A., Osiko V.V., Fedorov P.P. BaF₂:Ce³⁺ scintillation ceramics. *Doklady Physics*, 2008, **53**(9), P.485–488.
- [13] Fedorov P.P., Kuznetsov S.V., Osiko V.V. Elaboration of nanofluorides and ceramics for optical and laser applications. *Photonic and Electronic Properties of Fluoride Materials*, 2016, **513**, P. 7-31.
- [14] Luginina A.A., Baranchikov A.E., Popov A.I., Fedorov P.P., Preparation of barium monohydrofluoride BaF₂HF from nitrate aqueous solutions. *Materials Res. Bull.*, 2014, **49**(1), P. 199–205.
- [15] Luo J., Ye L., Xu J. Preparation and properties of Ce³⁺:BaF₂ transparent ceramics by vacuum sintering. *J. Nanoscience and Nanotechnology*, 2016, **16**, P. 3985–3989.
- [16] Fedorov P.P. Association of point defects in nonstoichiometric M_{1-x}R_xF_{2+x} fluorite-type solid solutions. *Bull. Soc. Cat. Cien.*, 1991, **12**(2), P. 349–381.
- [17] Sobolev B.P. The Rare Earth Trifluorides. P.2. Introduction to materials science of multicomponent metal fluoride crystals. *Barcelona: Institut d'Estudis Catalans*, 2000, P. 460.
- [18] Sobolev B.P., Tkachenko N.L. Phase diagrams of BaF₂-(Y, Ln)F₃ systems. *J. Less-Common Metals*, 1982, **85**(2), P. 155–170.
- [19] Kuznetsov S.V., Aleksandrov A.A., Fedorov P.P. Optical Fluoride Nanoceramics. *Inorganic Materials*, 2021, **57**(6), P. 555–578.
- [20] Liu Z., Jia M., Yi G., Mei B., Jing Q., Liu P. Fabrication and microstructure characterizations of transparent Er:CaF₂ composite ceramic. *J. Am. Ceram. Soc.*, 2019, **102**(1), P. 285–293.
- [21] Li J., Chen X., Tang L., Li Y., Wu Y. Fabrication and properties of transparent Nd-doped BaF₂ ceramics. *J. Am. Ceram. Soc.*, 2019, **102**(1), P. 178–184.
- [22] Yi G., Li W., Song J., Mei B., Zhou Z., Su L. Structural, spectroscopic and thermal properties of hot-pressed Nd:(Ca_{0.94}Gd_{0.06})F_{2.06} transparent ceramics. *J. Eur. Ceram. Soc.*, 2018, **38**(9), P. 3240–3245.
- [23] Zhou Z., Mei B., Song J., Li W., Yang Y., Yi G. Effects of Sr²⁺ content on microstructure and spectroscopic properties of Nd³⁺ doped Ca_{1-x}Sr_xF₂ transparent ceramics. *J. Alloys Compd.*, 2019, **811**, P. 152046.
- [24] Chen X., Wu Y. High Concentration Ce³⁺ doped BaF₂ transparent ceramics. *J. Alloys Compd.*, 2020, **817**.
- [25] Fedorov P.P., Kuznetsov S.V., Mayakova M.N., Voronov V.V., Ermakov R.P., Baranchikov A.E., Osiko V.V. Coprecipitation from aqueous solutions to prepare binary fluorides. *Russian J. Inorg. Chem.*, 2011, **56**(10), P. 1525–1531.
- [26] Kuznetsov S.V., Fedorov P.P., Voronov V.V., Samarina K.S., Ermakov R.P., Osiko V.V., Synthesis of Ba₄R₃F₁₇ (R stands for Rare-Earth Elements) Powders and Transparent Compacts on Their Base. *Rus. J. Inorg. Chem.*, 2010, **55**(4), P. 484–493.
- [27] Batygov S.Kh., Mayakova M.N., Kuznetsov S.V., Fedorov P.P., X-ray luminescence of BaF₂:Ce³⁺ powders. *Nanosystems: Physics, Chemistry, Mathematics*, 2014, **5**(6), P. 752–756.
- [28] Mayakova M.N., Voronov V.V., Iskhakova L.D., Kuznetsov S.V., Fedorov P.P. Low-temperature phase formation in the BaF₂-CeF₃ system. *J. Fluorine Chem.*, 2016, **187**, P. 33–39.
- [29] Fedorov P.P., Mayakova M.N., Kuznetsov S.V., Voronov V.V., Ermakov R.P., Samarina K.S., Popov A.I., Osiko V.V. Co-Precipitation of Yttrium and Barium Fluorides from Aqueous Solutions. *Mat. Res. Bull.*, 2012, **47**, P. 1794–1799.
- [30] Fedorov P.P., Sobolev B.P. Concentration dependence of unit-cell parameters of phases M_{1-x}R_xF_{2+x} with the fluorite structure. *Sov. Phys. Crystallogr.*, 1992, **37**(5), P. 651–656.
- [31] Shannon R.D. Revised effective ionic radii and systematic studies of interatomic distances in halides and chalcogenides. *Acta Cryst.*, 1976, **32**, P. 751–767.
- [32] Murin I.V., Gunsser W. Relaxation methods for the study of ion transport in halide systems. *Solid State Ionics*, 1992, **53-56**, P. 837–842.
- [33] Den Hartog H.W., Langevoort J.C. Ionic thermal current of concentrated cubic solid solutions of SrF₂:LaF₃ and BaF₂:LaF₃. *Phys. Rev. B.*, 1981, **24**(6), P. 3547–3554.
- [34] den Hartog H.W., Pen K.F., Meuldijk J. Defect structure and charge transport in solid solutions Ba_{1-x}La_xF_{2+x}. *Phys. Rev. B*, 1983, **28**(10), P. 6031–6040.
- [35] Wapenaar K.E.D., Van Koesveld J.L., Schoonman J. Conductivity enhancement in fluorite-structured solid solutions. *Solid State Ionics*, 1981, **2**, P. 145–154.
- [36] Andersen N.H., Clausen K.N., Kjems J.K., Schoonman J. A study of the disorder in heavily doped Ba_{1-x}La_xF_{2+x} by neutron scattering, ionic conductivity and specific heat measurements. *J. Phys. C: Sol. St. Phys.*, 1986, **19**, P. 2377–2389.
- [37] Alexandrov V.B., Otroshchenko L.P., Fykin L.E., Bydanov N.N., Sobolev B.P. Features of the defective structure of Ba_{0.5}Ce_{0.5}F_{2.5} fluorite solid solution according to the neutronographic study of single crystals. *Cryst. Reports.*, 1989, **34**(6), P. 1997–1501 (in Russian).
- [38] Otroshchenko L.P., Alexandrov V.B., Muradyan L.A., Sarin B.A., Sobolev B.P. Neutron diffraction study of the features of fluorine ions incorporation into Ba_{1-x}R_xF_{2+x} solid solutions. *Bull. Soc. Cat. Cien.*, 1991, **12**(2), P. 383–391.
- [39] Sobolev B.P., Golubev A.M., Otroshchenko L.P. et al. *Crystallography Rep.*, 2003, **48**(6), P. 1012.
- [40] Aminov L.K., Kurkin I.N., Kurzin S.P., Gromov I.A., Mamin G.V., Rakhmatullin R.M. Detection of cuboctahedral clusters in mixed crystals by the EPR method. *Physics of the Solid State*, 2007, **49**(11), P. 1990–1993 (in Russian).
- [41] Maksimov B.A., Solans Kh., Dudka A.P., Genkina E.A., Font-Badria M., Buchinskaya I.I., Loshmanov A.A., Golubev A.M., Simonov V.I., Font-Altaba M., Sobolev B.P. The Fluorite-matrix-based Ba₄R₃F₁₇ (R=Y, Yb) crystal structure. Ordering of cations and specific features of the anionic motif. *Crystallography Rep.*, 1996, **41**, P. 50–57.
- [42] Sobolev B.P. The Rare Earth Trifluorides. P.1. The high temperature chemistry of the rare earth trifluorides. *Barcelona: Institut d'Estudis Catalans*, 2000, P. 520.
- [43] Grover V., Arhary S.N., Patwe S.S.J., Tyagi A.K. Synthesis and characterization of Ba_{1-x}Nd_xF_{2+x} (0.00 ≤ x ≤ 1.00). *Mat Res. Bull.*, 2003, **38**, P. 1101–1111.
- [44] Zolotova K.N., Kolbanev I.V., Ardashnikova E.I., Abakumov A.M., Dolgikh V.A. Interactions in the NdF₃-Nd₂O₃-MF₂ (M=Ba, Sr) systems. *Russ. J. Inorg. Chem.*, 2011, **56**, P. 1623-1631.
- [45] Fedorov P.P., Luginina A.A., Popov A.I. Transparent Oxyfluoride Glass Ceramics. *J. Fluorine Chem.*, 2015, **172**, P. 22–50.
- [46] Kieser M., Greis O. Preparation and properties of fluorite-related superstructure phases Ba₄RE₃F₁₇ with RE = Ce-Nd, Sm-Lu, and Y. *Z. anorg. allg. Chem.*, 1980, **469**, P. 164–171.

- [47] Karbowski M., Cichos J., Does BaYF₅ nanocrystals exist? – The BaF₂-YF₃ solid solution revisited using photoluminescence spectroscopy. *J. Alloys Compd.*, 2016, **673**, P. 258–264.
- [48] Kuznetsov S.V., Nizamutdinov A.S., Mayakova M.N., Voronov V.V., Madirov E.I., Khadiev A.R., Spassky D.A., Kamenskikh I.A., Yapryntsev A.D., Ivanov V.K., Marisov M.A., Semashko V.V., Fedorov P.P. Synthesis and down conversion of luminescence of Ba₄Y₃F₁₇:Yb:Pr solid solutions for photonics. *Nanosystems: Phys., Chem., Math.*, 2019, **10**(2), P. 190–198.
- [49] Li T., Li Y., Luo R., Ning Zh., Zhao Y., Liu M., Lai X., Zhong Ch., Wang Ch., Zhang J., Bi J., Gao D. Novel Ba(Gd_{1-x}Y_x)_{0.78}F₅: 20 mol % Yb³⁺, 2 mol % Tm³⁺ (0 ≤ x ≤ 1.0) solid solution nanocrystals: A facile hydrothermal controlled synthesis, enhanced upconversion luminescent and paramagnetic properties. *J. Alloys Comp.*, 2018, **740**, P. 1204–1214.
- [50] Nizamutdinov A.S., Kuznetsov S.V., Madirov E.I., Voronov V.V., Khadiev A.R., Yapryntsev A.D., Ivanov V.K., Semashko V.V., Fedorov P.P. UV to IR down-conversion luminescence in novel Ba₄Y₃F₁₇:Yb:Ce solar spectrum sensitizer for silicon solar cells. *Optical Materials*, 2020, **108**, P. 110185.
- [51] Kuznetsov S.V., Nizamutdinov A.S., Madirov E.I., Voronov V.V., Tsoy K.S., Khadiev A.R., Yapryntsev A.D., Ivanov V.K., Kharintsev S.S., Semashko V.V. Near infrared down-conversion luminescence. of Ba₄Y₃F₁₇:Yb³⁺:Eu³⁺ nanoparticles under ultraviolet excitation. *Nanosystems: Phys., Chem., Math.*, 2020, **11**(3), P. 316–323.
- [52] Bevan D.J.M., Strahle J., Creis O. The crystal structure of tveitite, an ordered yttriofluorite mineral. *J. Solid State Chem.* 1982, **44**(1), P. 75–81.
- [53] Rozhnova Yu. A., Kuznetsov S.V., Luginina A.A., Voronov V.V., Ryabova A.V., Pominova D.V., Ermakov R.P., Usachev V.A., Kononenko N.E., Baranchikov A.E., Ivanov V.K., Fedorov P.P. New Sr_{1-x-y}R_x(NH₄)_yF_{2+x-y} (R = Yb, Er) solid solution as precursor for high efficiency up-conversion luminophor and optical ceramics on the base of strontium fluoride. *MatChemPhys.*, 2016, **172**, P. 150–157.
- [54] Pavlova L.N., Fedorov P.P., Ol'khovaya L.A., Ikrami D.D., Sobolev B.P. Ordering of heterovalent solid solution with the fluorite structure in the NaF-BaF₂-GdF₃ system. *Crystallogr. Rep.*, 1993, **38**(2), P. 221–224.

Properties of Prussian Blue filled membrane mini-reactor in Cs(I) adsorption processes

A. Ioshin¹, E. Polyakov¹, I. Volkov¹, E. Denisov²

¹Institute of Solid State Chemistry, 91, Pervomaiskaya str., Ekaterinburg, 620990, Russia

²Ural Federal University named after the first President of Russia B. N. Yeltzin, Physical-technical Institute, 28, Mira str., Ekaterinburg, 620002, Russia

polyakov@ihim.uran.ru

PACS 47.56.+r, 68.43.-h

DOI 10.17586/2220-8054-2021-12-4-512-519

We present the results of investigation of Cs(I) ion mass-transfer from outer solution into the inner part of membrane mini-reactor (MR), which is a centimeter-sized hermetically sealed pocket made of polyethylene terephthalate track membrane and filled with Prussian Blue (PB) colloidal solution. The mean size of colloidal particles was 74 ± 20 nm (98.4%) and ξ -potential was $-(33 \pm 6)$ mV. The pore diameter of the track membrane in the experiments varied from 50 to 50000 nm. It was found that the construction and properties of PB filled MR allow one to realize an extremely high distribution coefficient of $(1.50 \pm 0.05) \cdot 10^6$ ml/g with respect to Cs(I), which is characteristic of colloid-sized PB. Adsorption is a diffusion-controlled process localized in the pores of TM, which can be fulfilled in solution without agitation.

Keywords: Membrane, reactor, Prussian Blue, Cs(I), adsorption, kinetics.

Received: 27 June 2021

1. Introduction

The development of methods for the decontamination of materials, technogenic and natural objects and soil on the principles of minimal intervention in the environment becomes an increasingly more topical problem of radioecology in view of the growing share of nuclear power engineering in the energy balance of the Russian Federation and other countries, as well as complication of atomic power engineering technologies and methods for recovery and processing of uranium and rare-earth elements [1–6]. The decontamination approach based on the introduction of sorbents into radionuclide polluted soil that are able to block the transition of radionuclides into vegetation owing to their competitive sorption has been actively discussed in recent years [7]. The sorbent remains in soil in dispersed form. This complicates its removal and makes further geochemical fate of highly active sorbent particles uncertain over the long term. The chemical mechanism of deactivation of contaminated material (hereinafter called material) by sorbent purifier (hereinafter called sorbent) placed into aqueous electrolyte solution has been considered by the authors in terms of competitive sorption in the system “material – aqueous solution – sorbent” [8, 9]. The application of competitive sorption for the isolation of radionuclide from soil with minimal intervention in the environment is possible in the case of membrane separation of sorbent and purified material. For example, the introduction of sorbent in the composition of compact chemical reactor, whose walls are made of sorbent-impermeable membrane material allowing the outer solution to pass through, makes it possible to separate the internal sorbent or its suspension from particle mass transfer outside the reactor walls while retaining chemical contact of sorbent with external environment through membrane wall pores. Such membrane reactor with linear dimensions 5 – 20 mm (mini-reactor [8]) filled with selective sorbent [10], can provide spontaneous sorption extraction of ions from solution with subsequent mechanical removal of mini-reactor with spent sorbent from solution or suspension [11, 12]. Owing to a large range of pore sizes, track membranes are suitable as a semipermeable material of mini-reactor walls. They allow the sorbent in the form of colloidal solution (1 – 100 nm) or suspension [12] to be placed inside the reactor.

The aim of this work was to determine the functional properties of membrane mini-reactor filled with nanoparticles in the form of a colloidal solution during sorption of microelements from solution. We considered the effects of membrane area, pore size, hydrodynamic regime of membrane wall contact with solution and temperature on the sorption properties and application of sorbent filled mini-reactor in the processes of sorption of microelements from aqueous solutions during convection and/or diffusion mass transfer of sorbate through reactor wall. The study was concerned with the system “¹³⁷CsCl – electrolyte solution – Prussian Blue colloid (PB)”, for which high values of distribution coefficient of cesium ion, $K_d \sim 10^6$ ml/g are typical according to the data of sorption statics [9, 10, 13].

2. Experiment

In the investigation, we used membrane reactors having a form of square or rectangular envelopes with edge length ranging from 15 to 25 mm (Fig. 1). The envelopes were made of a Lavsan (polyethylene-terephthalate) track membrane [14, 15] with pore size in the interval 0.1 – 50 μm using the technique described in [12]. Prussian Blue (Ecsorb) [13] was used as sorbent. According to X-ray diffraction analysis of the sorbent, the PB powder had a dark-blue color and was a phase with space group $F 4/m - 3 2/m$ with lattice parameters (\AA): $a = b = c = 10.1723$, angles (deg.) $a = b = g = 90.0000$ and composition $\text{Fe}_3[\text{Fe}(\text{CN})_6]_2 \cdot 14\text{H}_2\text{O} - 97.8 \text{ wt.}\%$. The size of dry aggregated PB particles was 30 – 60 μm . The average size of primary particles (average value of coherent scattering region) was 14.7 nm. The impurity phase was the basic sulfate $\text{K}_2\text{Fe}(\text{SO}_4)$, space group $R - 3 2/m$ with lattice parameters (\AA): $a = 7.29250$, $b = 7.2925$, $c = 17.2094$, angles (deg.) $a = b = 90.0000$, $g = 120.0000$, content – 2.2 wt.%. The hydrodynamic diameter of PB particles was determined using the dynamic light scattering method on a Zetasizer Nano ZS instrument (Malvern Instruments Ltd.). The measurements were performed at 25 $^\circ\text{C}$. Samples were taken from the upper part of examined suspension volume. According to light scattering data, the average diameter D_h of PB particles in initial suspension was $(145 \pm 67) \text{ nm}$ (90.2 mol. % of the whole concentration), ξ -potential was equal to $-(27 \pm 4.0) \text{ mV}$. Approximately 9.8 mol. % PB particles were $(600 \pm 230) \text{ nm}$ in size and had the same ξ -potential. After dilution and ultrasonic dispersion, the PB solution with a concentration of 100 mg/l consisted of particles with $D_h = (70 \pm 20) \text{ nm}$ (98 mol. % of the whole concentration of PB suspension), ξ -potential = $-(33 \pm 6) \text{ mV}$, Fig. 1B.

The kinetic regime of microelement (CsCl) mass transfer was analyzed using a facility, whose design allowed one to control and vary the lateral flow velocity of the electrolyte with microelement (sorbate) relative to the membrane reactor outer wall. The diagram of this facility is presented in Fig. 2; it included a glass cup (Fig. 2B), in which 500 ml electrolyte solution (hydrochloric solution with $\text{pH} = 4.1$) and an aliquot (2.5 ml) of standard solution of cesium ions (CsCl) with a concentration of 100 mg/l were poured. During radiometric measurement of sorbate concentration, only an aliquot of radiochemically pure $^{137}\text{CsCl}$ solution was added to the electrolyte. After homogenizing a sorbate composition by stirring, a 5 ml solution was sampled to establish the initial concentration of cesium ions in the working solution by mass-spectrometry (ELAN 9000) [16], or g-spectrometry methods on an MKS-AT1315 gamma-spectrometer (Atomtekh) with a NaI(Tl) $63 \times 63 \text{ mm}$ detector [17]. The counting rate interval was 0.4 – 150 Bq. The membrane pore diameter, mini-reactor edge area and PB mass inside the reactor we varied depending on the experiment objective.

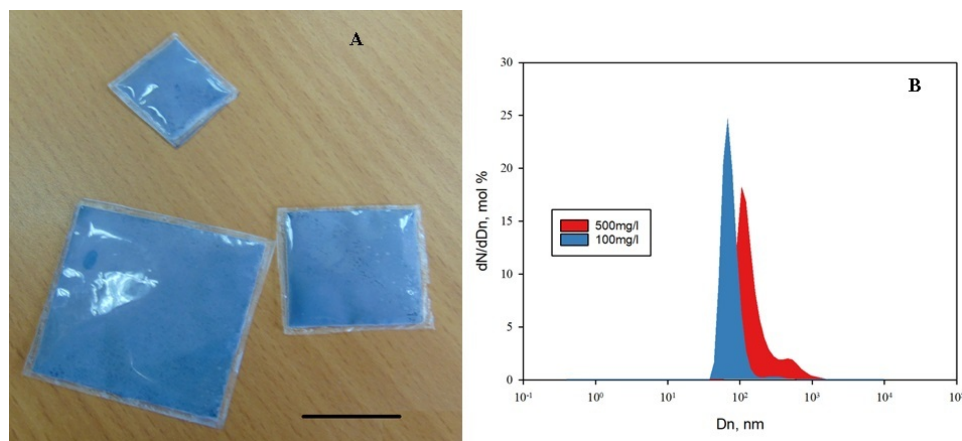


FIG. 1. (A) Appearance of membrane mini-reactors made of track membrane with pore diameter 100 nm and thickness 50 μm filled with PB sorbent powder [13]. The line in the Figure is 1.0 cm. (B) Empirical size (D_n) distribution of PB particles in the initial solution with PB concentration 500 mg/l and in diluted solution with PB concentration 100 mg/l after 30 min irradiation in ultrasonic field with frequency 40 kHz and power 50 W, $\text{pH} = 7.1$

When studying the hydrodynamic regime of sorption statics with the use of membrane mini-reactor, a perforated high-pressure polyethylene cylinder with radius (r) and apertures of 4 mm in diameter (Fig. 2A) was placed into container (1) of the setup, Fig. 2B. The cylinder was coaxially jointed with the mixer using a flexible drive. During the experiment, the membrane mini-reactor with a sorbent, placed inside the cylinder, took the position near the cylinder side wall, in the zone of the maximal angular (W_{liq}) and linear (L_{liq}) velocity of sorbate lateral motion relative to the container walls.

The angular velocity of cylinder rotation W_0 (1/min) was measured by means of a laser tachometer and varied during the experiments in the range 20 – 560 1/min. At certain time intervals from the beginning of experiment, aliquots of sorbate solution were sampled from the container to measure the microelement concentration. Before elemental analysis, the aliquot was diluted with 0.1 M HCl solution and the concentration of cesium ions in it was measured. In addition, the behavior of PB powder in solution was studied without the use of the membrane mini-reactor at $W_0 = 550$ 1/min.

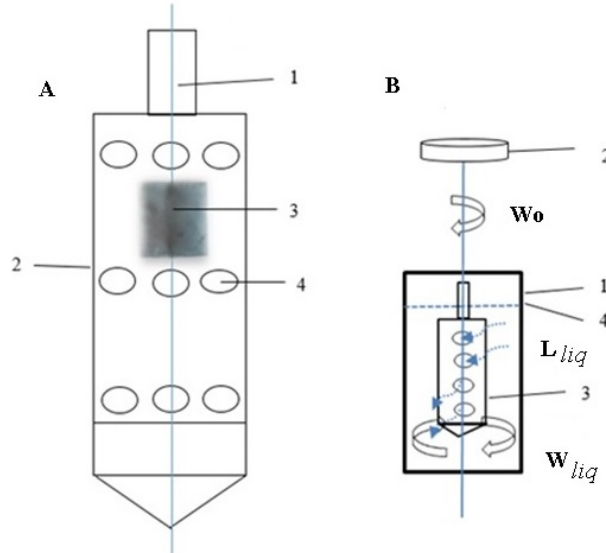


FIG. 2. The layout drawing (A) and diagram of laboratory setup (B) for measuring the linear flow rate of HCl–CsCl–H₂O electrolyte solution relative to the membrane mini-reactor wall surface. (A): 1 – rod for fixing a mixer motor to the axis of top driving rotor; 2 – 100 cm³ cylinder made of high-pressure polyethylene with perforated walls for passage of sorbate solution; 3 – mini-reactor located inside the cylinder; 4 – aperture in the cylinder for passage of sorbate solution during axial rotation of the cylinder with solution, diameter 0.4 cm. (B): 1 – glass container with 500 cm³ sorbate solution; 2 – top driving rotor with reducing unit and laser meter of the number of rotor revolutions; 3 – rotating cylinder with perforated walls and a mini-reactor inside; 4 – sorbate solution level. Arrows – direction of sorbate solution flow during rotation of cylinder with a mini-reactor

The dependence between the angular W_0 and linear L_{liq} velocities of sorbate motion inside the rotating perforated cylinder (Fig. 2) was estimated using a previously described technique [18]. Vertical marking of length (mm) was done on the plastic cylinder so that the point of origin coincides with the upper level of sorbate solution in the container; the scale goes down with a spacing of 5 mm. The cylinder was immersed into the container with distilled water. After 15 – 20 sec operation of the mixer with perforated cylinder, the position of water meniscus (Δh) in the cylinder was registered relative to the scale zero. The angular rotation velocity of the cylinder W_0 (1/min) was determined using a laser tachometer and converted into angular velocity W (1/s) according to formula:

$$W = W_0 \cdot \frac{2\pi}{60}. \quad (1)$$

The angular rotation velocity of liquid in the perforated cylinder W_{liq} (1/s) was calculated by eq. (2), [18]:

$$W_{liq} = \sqrt{\frac{\Delta h \cdot 2 \cdot g}{r^2}}, \quad (2)$$

where Δh is the height of the parabolic water meniscus determined from the scale (cm), g is the free fall acceleration 981.0 (cm/s²) and r is the cylinder radius, 1.425 (cm). Then the average linear velocity of sorbate solution at the cylinder wall, L_{liq} , (cm/s) was determined from formula (3):

$$L_{liq} = W_{liq} \cdot r. \quad (3)$$

Figure 3A shows the dependence between the angular and linear rotation velocities of sorbate solution in the cylinder, from which the value of L_{liq} was used for the estimation of hydrodynamic sorption regime with participation of mini-reactor.

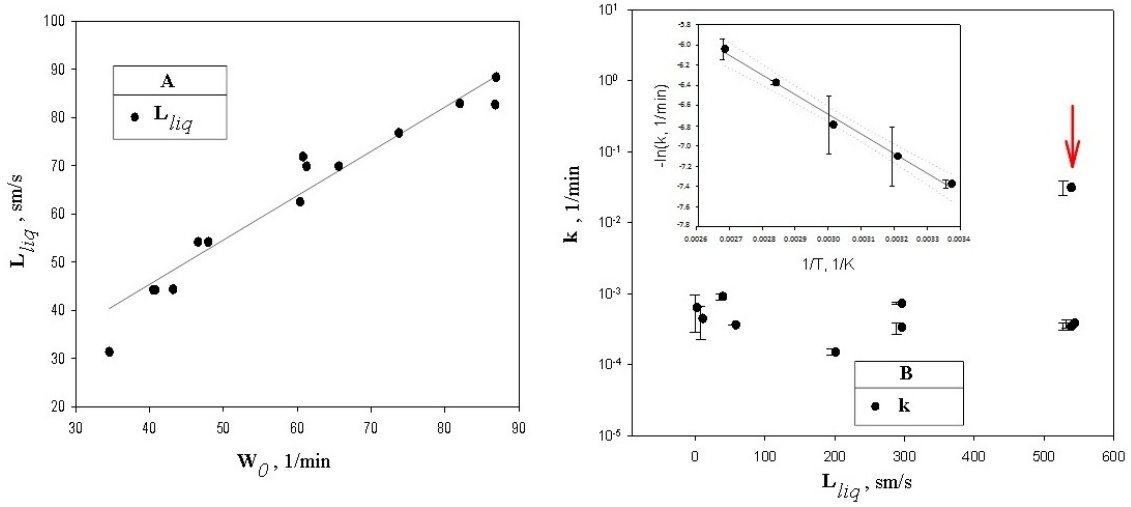


FIG. 3. A: Empirical dependence between angular (W_0 , 1/min) and linear (L_{liq} , sm/s) velocity of electrolyte solution motion near the cylinder wall in the setup. Fig. 2. B: correlation between the velocity coefficient (k) of irreversible first-order reaction of Cs(I) ion sorption by PB powder in the mini-reactor and the linear velocity L_{liq} of solution near the mini-reactor wall. The mini-reactor edge area $S = 6.5$ cm², pH=4.1, 22 °C. The point with coordinates $k = 5 \cdot 10^{-2}$ 1/min and $L_{liq} = 550$ cm/s, referring to the experiment with PB powder without mini-reactor, is marked by the arrow. Inset: the Cs(I) sorption velocity coefficient logarithm as a function of reciprocal temperature for pH=4.0, $L_{liq} = 120$ cm/s

In order to determine the degree of sorption of microelement by the sorbent in the mini-reactor (D), we used the known relationship:

$$D = \frac{(I_i - I_f)}{I_i}, \quad (4)$$

where I_i and I_f are the initial and final concentration (specific activity during measurement of ¹³⁷Cs in the region of photopeak of 660 keV) of microelement in solution. The equilibrium value of concentration/specific activity of solution (I_∞) was calculated from the equation of sorption reaction kinetics, whereupon we found the equilibrium value of sorption D_∞ from eq. (4) and the equilibrium distribution coefficient K_d (ml/g):

$$K_d = \frac{D_\infty}{(1 - D_\infty)} \cdot \frac{V}{m}, \quad (5)$$

where V is the volume of solution in the container, ml, and m is the sorbent sample in the mini-reactor, g.

The variation in the fraction of cesium absorbed by the membrane mini-reactor with the sorbent as a function of contact time of the system “mini-reactor–sorbate” revealed that the dependence of sorption on the contact time (t), Fig. 4, corresponds to the kinetics of the irreversible first-order reaction of Cs(I) ion sorption

$$D = a \cdot (1 - \exp(-k \cdot t)), \quad (6)$$

where a is the dimension coefficient and k is the sorption reaction velocity coefficient, 1/min. The equilibrium adsorption isotherm of cesium ions at pH4.1 and 22 °C is described by the single-sort Langmuir model with the cesium ion distribution coefficient K_d (ml/g) = $(1.50 \pm 0.05) \cdot 10^6$ and sorption capacity G (mmol/g) = $(9.80 \pm 0.80) \cdot 10^{-3}$.

The diffusion kinetics of competitive sorption of cesium ions in the system “SiO₂-CsCl-H₂O||PB” (MR|| is the symbol of membrane mini-reactor) was studied by the space-limited method. 200 ml of the solution containing 0.25 mg/l cesium with HCl pH = 4.1 were poured in 500 ml flasks made of chemically resistant glass with a ground stopper. 3.0 g of silica gel powder of 100 – 200 μm fraction (SiO₂) were added to the flasks and agitated for 48 h on a magnetic mixer until sorption equilibrium in the system was established [8, 19]. Then the agitation was discontinued and a membrane mini-reactor with surface area 10 cm² and 100 mg PB sample inside was placed in each flask. The cesium ion distribution between sorbents and solution in a chosen flask was analyzed at certain intervals. The solution from the flask was filtered through a “blue tape” paper filter, the filter cake (SiO₂) was treated for 8 h using 40 ml 5M sodium hydroxide.

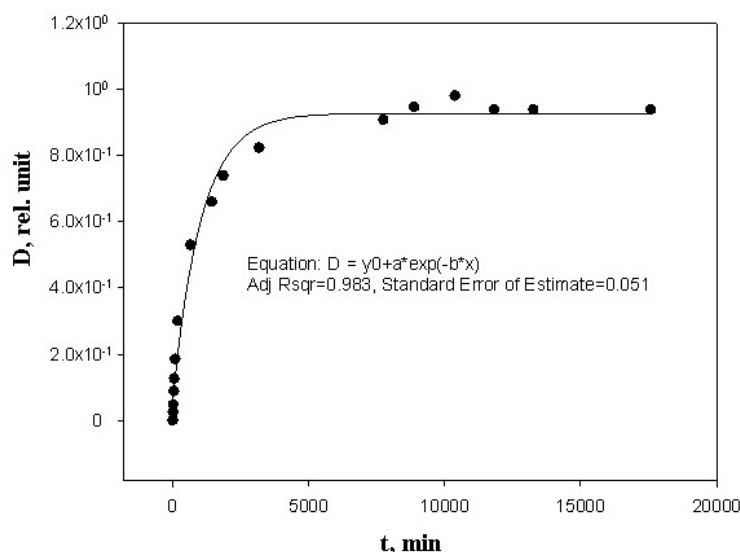


FIG. 4. The fraction (D) of $^{137}\text{Cs(I)}$ sorbed by PB powder filled mini-reactor vs. contact time, t . The cesium concentration in the sorbent was determined using γ -spectrometry from the 662 keV line of the equilibrium pair ^{137}Cs – ^{137}Ba . The solution contained an acetate buffer with pH=7. The sorbent mass in the mini-reactor with $S = 6.5 \text{ cm}^2$ and pore size $d = 1.0 \mu\text{m}$ was 200 mg, 22 °C. The line was plotted using the regression equation of the irreversible first-order reaction of Cs(I) sorption: $a = (0.926 \pm 0.006) \text{ r.u.}$, $b = (1.030 \pm 0.05) \cdot 10^{-3}, 1/\text{min}$, determination coefficient $R^2 = 0.997$

The membrane mini-reactor was opened and treated for 8 h with the use of 20 ml 5M solution of sodium hydroxide. In the “background” experiment, cesium ion sorption by PB filled membrane mini-reactor was controlled depending on the contact time of the reactor with the solution in the absence of silica gel. Based on cesium ion concentration measurement, we determined the dependence of cesium content in silica gel, aqueous solution and PB on the contact time of phases.

3. Experimental results

The experimental relationship between cesium ion sorption velocity coefficient (k) by PB in membrane mini-reactor and the linear velocity of sorbate solution (L_{liq}), Fig. 3B, shows that the kinetic regime of sorption does not depend on the sorbate ion mass transfer rate from the solution bulk to the membrane reactor surface. The Arrhenius dependence of the velocity coefficient on temperature gives a sorption activation energy value ($1.62 \pm 0.03, \text{ kJ/mol}$) which agrees with the average activation energy of cesium ion diffusion in aqueous salt solutions [19,20], Fig. 3B. The limiting stage of cesium ion mass transfer in PB inside the mini-reactor is external diffusion in the bulk of electrolyte. This follows from the fact that the sorption velocity coefficient according to eq. (6) changes linearly with the contact area of the membrane reactor edges (S) with outer solution, Fig. 5. The sorption velocity coefficient is proportional to the membrane pore cross-sectional area at relatively small pore sizes ($d < 5 \mu\text{m}$), Fig. 6. With further enhancement of the pore diameter, the sorption velocity coefficient increases abruptly due to transition from diffusion to convection transfer in membrane pores [20]. Comparison of the obtained data shows that the slowest mass transfer process is localized in the pore space of reactor membrane. The values of cesium sorption velocity coefficient obtained in sorption experiments with sorbent with and without application of membrane reactor are shown in Fig. 3B for $L_{liq} = 550 \text{ cm/s}$ for comparison. The difference in the sorption velocity coefficients is about two orders of magnitude, which also confirms the diffusion character of sorbate mass transfer mechanism in PB in case of membrane regime of sorption.

The diffusion character of the limiting stage of cesium ion sorption by PB in the membrane mini-reactor allows one to use this regime for sorption of microquantities of cesium ions without convective stirring of sorbent suspension and sorbate solution. To verify this assumption, we studied the kinetics of spontaneous cesium ion mass transfer in the heterogeneous system “ $\text{SiO}_2\text{--CsCl--H}_2\text{O} \parallel \text{PB}$ ”, in which silica (SiO_2) powder was preliminarily sorption-saturated

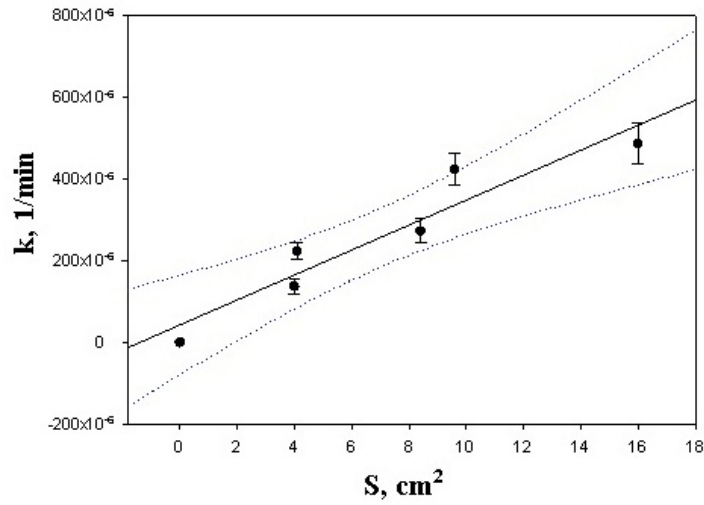


FIG. 5. Velocity coefficient (k , 1/min) of Cs(I) sorption by PB powder filled membrane mini-reactor vs. the surface area of mini-reactor edges (S). pH = 4.1, $S = 7.3 \text{ cm}^2$, $d = 1.0 \text{ }\mu\text{m}$, $L_{liq} = 50 \text{ cm/s}$ 23 °C

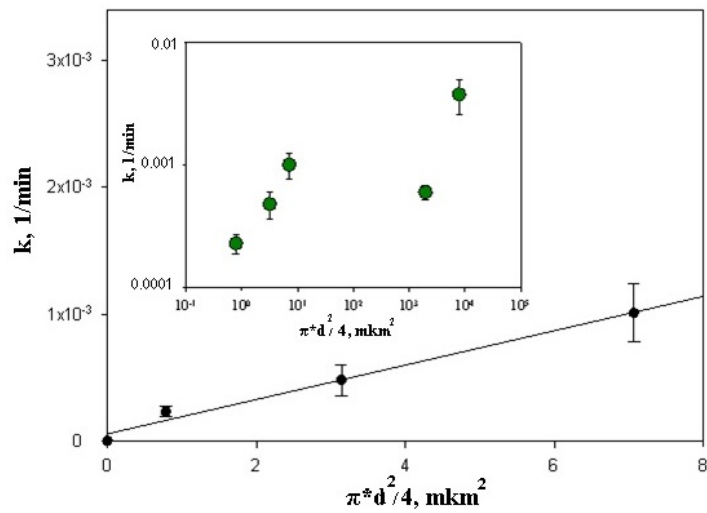


FIG. 6. Cs(I) sorption velocity coefficient (k , 1/min) by PB powder filled membrane mini-reactor vs. membrane pore diameter (d). pH=4.1, $S = 7.3 \text{ cm}^2$, $L_{liq} = 5.0 \text{ cm/s}$, 22 °C

with cesium ions. The data on cesium ion distribution between phases show that the dependence of cesium concentration on the contact time of phases agrees with the kinetic model of irreversible mass transfer by the first-order reaction of cesium ion sorption, Fig. 7.

The lines connecting the points in Fig. 7 were fitted by estimating the coefficients of the experimental dependence of cesium concentration in solution $Cs(\text{solution})$, silica $Cs(\text{SiO}_2)$ and sorbent in the membrane reactor $Cs(\text{PB})$ using the least squares method [19]. From Fig. 7 it is possible to estimate the average sorption relaxation time, $t \sim 2 \cdot 10^4 \text{ min}$, corresponding to the cesium ion mass transfer coefficient, $\frac{1}{t} \sim 5 \cdot 10^{-5} \text{ 1/min}$, which is in agreement with cesium ion diffusion mass transfer coefficient in the PB filled mini-reactor, Fig. 6.

4. Conclusion

Thus, the results of studying the functional properties of PB sorbent filled membrane mini-reactor with respect to cesium ions revealed that the sorption kinetics are determined by external diffusion transfer of sorbate ions through membrane wall pores and are described by the first-order reaction equation for cesium ions. The sorption velocity coefficient is proportional to the geometrical surface area of membrane mini-reactor and the total area of membrane

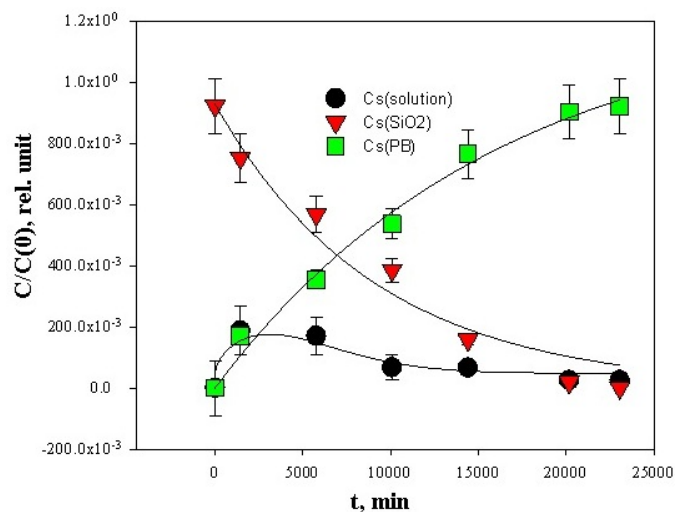


FIG. 7. The isotherm of competitive cesium sorption kinetics in the system “SiO₂-CsCl-H₂O|| PB” without agitation. The initial cesium concentration in SiO₂ saturated ($8.5 \cdot 10^{-7}$ mol/l) membrane mini-reactor with pore diameter $d = 0.1 \mu\text{m}$, edge surface 10.0 cm², PB concentration in mini-reactor 100 mg/l, pH 4.1, 23 °C

wall pores and does not depend on the linear velocity of sorbate solution motion relative to the membrane reactor wall. When the diameter of membrane pores becomes larger than 25 μm , the sorption velocity coefficient increases, probably, because the mass transfer mechanism through membrane pores changes from diffusion to convection type. The average sorption relaxation time of cesium ions, determined from competitive sorption experiment in the system “SiO₂-CsCl-H₂O|| PB” without agitation, corresponds to the cesium ion sorption velocity coefficient in diffusion regime.

Acknowledgement

The study was carried out in accordance with the Institute budgetary financing plans No AAAAA18-118111290051-4. The authors declare that they have no conflict of interest while performing this work.

References

- [1] Moskvina L.N., Krivobokov V.V., Efimov A.A. Low-waste process for chemical decontamination of primary circuits of water-cooled nuclear power installations using ion-exchange methods for treatment of decontaminating solutions. *Radiochemistry*, 2010, **52**(6), P. 584–591.
- [2] Kulagina T.A., Shelenkova V.V. Methods for decontamination of surfaces with nuclear pollution. *Zhurnal Sibirskogo federalnogo universiteta. Ser.: Tekhnika i tekhnologii*, 2017, **10**(3), P. 352–363. [in Russ.]
- [3] Voronik N.I., Toropova V.V. Polymer formulations for “dry” decontamination of the equipment and premises of nuclear power plants. *Radiochemistry*, 2017, **59**(2), P. 188–192.
- [4] Polyakov E.V. Competitive sorption as a method for environment decontamination. *Priroda*, 2015, **7**(1199), P. 88–89. [in Russ.]
- [5] Rakhimova O.V. *Processing and decontamination of radioactive waste of loparite concentrate chlorination*. PhD thesis. Berezniki: PNITU, Perm, Genesis, 2012, 173 p [in Russ.]
- [6] Polyakov E.V. Physicochemistry of humate complexes as a basis of “green chemistry” in radioecology. Thesis of the 7th Russian Conference on Radiochemistry “Radiochemistry-2012”. Dimitrovgrad: OOO VDV PAK, 2012, 343 [in Russ.]
- [7] Voronina A.V., Semenishchev V.S., M Blinova .O., Sanin P.Ju. Methods for Decrease of Radionuclides Transfer from Soil to Agricultural Vegetation. Gupta D. (Ed.) Walther C. *Radionuclides in the Environment*. Springer, Cham, 2015, P. 186–204.
- [8] Polyakov E.V., Ioshin A.A., Volkov I.V. Competitive Adsorption as a Physicochemical Ground for Self-Sufficient Decontamination Areas from Radioactive Pollutants. [Ed.] Voronina A., Gupta D. *Remediation Measures for Radioactively Contaminated Areas*. Cham: Springer, 2019, 2020.
- [9] Polyakov E.V., Volkov I.V., Khlebnikov N.A., Tsukanov R.R., Ioshin A.A. Competitive sorption as a method for decontamination of materials. *Radiokhimiya*, 2015, **57**(2), P. 149–153. [in Russ.]
- [10] Polyakov E.V., Volkov I.V., Khlebnikov N.A. Competitive sorption of cesium and other microelements onto iron(III) hexacyanoferrate(II) in the presence of humic acids. *Radiochemistry*, 2015, **57**(2), P. 172–177.
- [11] Ioshin A.A., Polyakov E.V., Volkov I.V. The possibilities of removal of heavy metals and radionuclides from aqueous solutions in sorbent packaged membrane reactor. “Solid State Chemistry and Functional Materials-2016”. All-Russian Conference, Ekaterinburg: UrO RAN, 2016, P. 144–145. [in Russ.]
- [12] Polyakov E.V., Ioshin A.A., Volkov I.V. Method for removal of toxic metals and radionuclides from aqueous solutions. ISSC UB RAS. Priority No. 2016114919 RF, Bull. 30, 3p [in Russ.]
- [13] Remez, V.P. ECSORB 2016. ECSORB. [In Internet] Mediasite, 10 08 2016. [Cited: 31.08.2019] <http://www.eksorb.com/about/history/>

- [14] Gerasimov A.A. Dubna cluster – Areas – Track membranes. Dubna cluster. [In Internet], 2013, [Cited: 14.08.2019] http://dubna-cluster.ru/areas/track_membranes/. [in Russ.]
- [15] Adak S., L. L. Daemen, Hartl M., Williams D., Summerhill J., Nakotteet H. Thermal expansion in 3d-metal prussian blue analogs – A survey study. *Journal of Solid State Chemistry*, 2011, **184**(11), P. 2854–2861.
- [16] Polyakov E.V., Volkov I.V., Surikov V.T., Perelyaeva L.A., Shveikin G.P. Dissolution of monazite in humic solutions. *Radiochemistry*, 2010, **52**(4), P. 429–434.
- [17] Betenekov N.D., Denisov E.I., Sharygin L.M. Influence of molybdenum speciation on its recovery with hydroxide sorbents. *Radiochemistry*, 2016, **58**(1), P. 63–71.
- [18] Acherkan N.S. *Machinery handbook*. Moscow: MASHGIZ, 1955–1961. V. 2, P. 616–618. [in Russ.]
- [19] Nosov A.V., Krylov A.L., Kiselev V.P., Kazakov S.V. *Modeling of migration of radioactive substances in surface water*. [Ed.] Arutyunyan R.V. Moscow: Nuclear Safety Institute (IBRAE) RAS. Nauka, 2010, p. 253.
- [20] Robinson R.A., Stoks R.H. *Electrolyte solutions*. London, Butterworths Scientific Publications, 1959, p. 645

Tuning of interfacial interactions in poly(isoprene) ferroelastomer by surface modification of embedded metallic iron nanoparticles

A. P. Safronov^{1,2}, T. V. Terziyan¹, A. V. Petrov³, I. V. Beketov^{1,2}

¹Ural Federal University, Institute of Natural Sciences and Mathematics,
Yekaterinburg, 19 Mira Str., 620002, Russia

²Institute of Electrophysics UB RAS, Yekaterinburg, 106 Amundsen Str., 620016, Russia

³Uralplast LLC, Yekaterinburg, 7 Schorsa Str., 620142, Russia

alexander.safronov@urfu.ru, tatiana.terzian@urfu.ru, beketov@iep.uran.ru, avp@labural.com

DOI 10.17586/2220-8054-2021-12-4-520-527

Zero-valent metallic iron nanoparticles (NPs) with modified surface were embedded in poly(isoprene) (PI) and the enthalpy of interfacial adhesion in resulted ferroelastomers was evaluated. Iron NPs were synthesized by the method of electrical explosion of wire (EEW) in inert gas. Modification of their surface was performed by the *in situ* liquid treatment of the active condensed NPs in the EEW installation. The enthalpy of mixing of poly(isoprene) with Fe NPs was determined using thermochemical cycle based on the isothermal calorimetry measurement of the enthalpy of dissolution of PI/Fe composites in chloroform at 25°C. Using these values the enthalpy of adhesion of PI to the surface of modified Fe NPs was evaluated using Langmuir-type isotherm. It was shown that the enthalpy of adhesion strongly depends on the properties of the surface of Fe NPs and its modification. It was the lowest in the case of oxidized Fe NPs and the highest for Fe NPs which surface was modified by pre-deposited polymeric shells.

Keywords: nanocomposites, zero-valent iron nanoparticles, ferroelastomers, surface modification, enthalpy of adhesion.

Received: 25 June 2021

Revised: 23 July 2021

1. Introduction

Zero valent iron nanoparticles have received considerable interest because of their potential applications in many diverse fields, including ferrofluids, biomedical materials, sensors, catalysts, magnetic and electro-conductive materials [1–5]. In many cases nanoparticles are incorporated into polymeric composites [2–5]. In particular, it is the case of magnetically active polymeric composites – ferroelastomers, which combine the elasticity of a polymer with the magnetic properties of embedded solid magnetic particles [5]. These materials provide the advantage of remote control of their mechanical characteristics by the application of the external magnetic field. The integral performance of ferroelastomers depends on the combination of their mechanical and magnetic responses. Meanwhile, these two aspects are in some respect controversial. The increase in the load of solid magnetic particles improves the magnetic properties of a ferroelastomer, but at the same, time it can decrease its mechanical strength. The weak point for the ultimate tensile stress in a composite is the polymer/solid interface. Hence, enhancement of the adhesion at the polymer/solid interface can be a solution to the problem. The major route to provide this is the modification of embedded solid magnetic particles.

There are two main ways to modify the surface of inorganic particles [6]. The first is accomplished through surface absorption of small molecules or polymers, the second method is based on covalent bonding of a modifier to the groups existing at the surface of the particles. Typically, surface adsorption is related to various surfactants like oleic acid and its salts [7–9]. Covalent bonding, as well as surface graft-polymerization, requires the presence of chemically active groups at the solid surface, like hydroxyls [10–13]. The surface of zero-valent metal nanoparticles, however, is lacking active functional groups, and in this case, the modification by covalent bonding becomes a complex multi-step procedure [14, 15].

A combination of the adsorption and bonding mechanisms of modification of zero-valent metal nanoparticles was reported in references [16, 17]. Modification was a one step process performed *in situ* during the synthesis of 3d metal nanoparticles by the method of the electrical explosion of wire (EEW). This is a highly productive method based on the evaporation of the metal wire by the high voltage electrical discharge with consequent condensation of spherical particles in inert gas [18, 19]. As-synthesized particles were immersed in a liquid solution of a modifier, which was deposited at the interface by chemical bonding, initiated by the active surface of metal particles.

The effect of the modification of the surface of solid particles on their adhesion to a polymer can be evaluated by the thermodynamic approach, which gives the enthalpy of formation of nanocomposite as a measure for the enthalpy

of adhesion at solid/polymer interface. This approach was successfully elaborated in our earlier studies concerning composites based on various polymers filled with metal and metal oxide nanoparticles [20–22].

The objective of the present work was to study the influence of the surface modification of metallic iron nanoparticles on the enthalpy of their interaction with poly(isoprene) in ferroelastomer. This polymeric matrix may be considered on one hand as a good model for the interaction of the amorphous polymer in an equilibrium conformational state with the surface of metal nanoparticles. On the other hand, poly(isoprene) is the commercially available polymer widely used in rubber industry in general and for the production of ferroelastomers in particular.

2. Experimental part

2.1. Synthesis and surface modification of Fe MNPs

The method of the electrical explosion of wire (EEW) was used for the synthesis of metallic iron magnetic nanoparticles (Fe NPs). The detailed description of EEW equipment designed at Institute of Electrophysics of RAS (Yekaterinburg, RF) is given elsewhere [18, 19]. The method is based on the evaporation of a portion of a metal wire by the electrical high voltage discharge in the explosion chamber filled with an inert gas. Further condensation of the expanding metal vapors resulted in the formation of spherical NPs. The applied voltage was 30 KV and the length of the exploded portion of wire was 90 mm. The wire was continuously fed to the explosion chamber. The high voltage source was concurrently recharged after each explosion, and the process was repeated in the pulsed manner. It resulted in the rapid production of NPs (200 g/h). The reaction chamber was filled with a circulating 70:30 mixture of Ar and N₂ which provided the working gas pressure of 0.12 MPa.

The *in-situ* liquid-phase modification of MNPs was made by the immersing of the as-prepared Fe NPs in hexane, toluene, 0.6 % solution of oleic acid in hexane, and 1 % solutions of poly(isoprene) (PI) and poly(styrene) (PS) in toluene in the special hopper attached to the EEW installation and filled with the inert gas mixture. The details of the modification are given elsewhere [16, 17]. All the modifiers were obtained from commercial suppliers and used without further purification.

As it was shown earlier [16], hexane is an inert liquid for the active surface of the as-prepared Fe NPs, and if kept under hexane, the metallic surface of Fe MNPs remained intact. It makes such samples highly pyrophoric. In order to make them stable in the air controlled oxidation should be performed to provide the oxide shell 1.5–3 nm in thickness on the surface of Fe MNPs [23]. Toluene is not inert to the as-prepared Fe NPs. Aromatic hydrocarbons condense on the surface of 3d metal NPs producing the layer of polycyclic aromatic hydrocarbons. The details of the deposition and its mechanism are given elsewhere [16]. The treatment of Fe NPs by the solutions of oleic acid, poly(isoprene), poly(styrene) provided the deposition of these modifiers on the surface. The deposited layer was 3–5 nm (TEM) in thickness and protected NPs from further oxidation.

The batches of modified Fe NPs taken for the study and their selected parameters are given in Table 1. Subsequently the batches will be addressed according to the marks listed in this table.

TEM images of the obtained Fe NPs are presented in Fig. 1. The particles are spherical and non-agglomerated. Particle size distribution obtained by the image analysis is lognormal with a median value of 59 nm and a logarithmic dispersion of 0.478. Fig. 1B presents the image of the protective oxide layer on the surface of NPs from batch Fe_{O_x}.

The specific surface area of the NPs was determined by the low temperature adsorption of nitrogen using Micromeritics TriStar 3000 analyzer. Phase composition of NPs was characterized by XRD (Bruker D8 DISCOVER). TEM and HTEM were performed using a JEOL JEM2100 microscope operating at 200 kV.

2.2. Preparation of poly(isoprene) ferroelastomers

Poly(isoprene) was the commercial product (RF – GOST 14925-79 corr. 1-8). The weight average molecular weight of PI MW=5.4×10⁵ was measured by viscometry in benzene solution at 25 °C ($K_{\eta} = 5.02 \times 10^{-4} \text{ dm}^3/\text{g}$, $a = 0.675$).

Nanocomposites based on PI with embedded Fe NPs were prepared by casting onto the glass substrate. First, the 5 % stock solution of PI in toluene was prepared and equilibrated. Then, the weighted amounts of Fe NPs were dispersed in 15 mL of stock solution to prepare mixed suspensions. They were homogenized in the Cole Parmer ultrasound processor at 20 KHz and 300 W for 10 min in a pulse/pause regime (pulse – 15 sec, pause – 10 sec). In all the cases except pyrophoric Fe₀ air-dry powders of NPs were taken. Fe₀ was used in the form of the hexane suspension. The load of modified Fe NPs in the suspension varied to provide 10, 20, 30, 40, 50, 60, 70, 80, 90 % of the filler in finally obtained ferroelasts. Homogenized suspensions of intact and modified Fe NPs in toluene solution of PI were cast onto the Petri dishes and dried to the constant weight *in vacuo* at 25 °C.

TABLE 1. Batches of modified Fe NPs and their selected parameters: specific surface area S_{BET} , content of carbon and crystalline phase composition

No	Batch	Preparation	S_{BET} (m ² /g)	Carbon content (%)	Crystalline phases (%)
1	Fe ₀	Intact Fe NPs kept under hexane	8.4	0.08	αFe:97.7 γFe: 2.3
2	Fe _{Ox}	Controlled oxidation	8.5	0.08	αFe:95.0 γFe:1.9 Fe ₂ O ₃ :3.1
3	Fe _T	Modification by liquid toluene	7.8	0.25	αFe:88.6 γFe:6.7 Fe ₂ O ₃ :4.7
4	Fe _{OA}	Modification by 0.6 % solution of oleic acid in hexane	8.4	0.39	αFe:97.5 γFe:62.5
5	Fe _{PI}	Modification by 1 % solution of poly(isoprene) in toluene	7.8	0.56	αFe:89.5 γFe:6.3 Fe ₂ O ₃ :4.2
6	Fe _{PS}	Modification by 1 % solution of poly(styrene) in toluene	7.8	0.45	αFe:89.8 γFe:6.5 Fe ₂ O ₃ :3.7

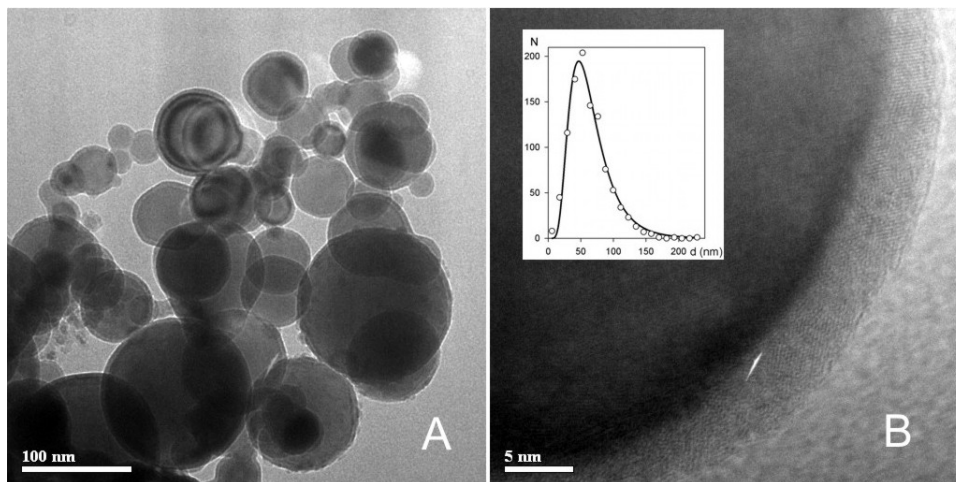


FIG. 1. (A) – TEM image of Fe NPs produced by EEW and taken as a filler for the composite. (B) – HTEM image of Fe_{Ox}NP with the protective oxide layer on the surface. Inset – particle size distribution (1043 particles)

2.3. Calorimetric measurements

The enthalpies of the processes incorporated in the thermochemical cycle were measured in isothermal conditions at 25 °C using Calvet 3D calorimeter SETARAM C80. Ampoule mixing cells were elaborated. The weighted amounts (ca 20 – 90 mg) of Fe NPs, or PI, or composite with certain Fe NPs content were placed into a thin glass ampoule (ca 0.5 cm³) and dried to a constant weight. Then the ampoules were sealed, placed in a special holder, which was mounted in the stainless steel cell (10 cm³), and loaded with 5 mL of chloroform. Two assembled cells were located in the ports of the calorimeter set at 25 °C. Thermal equilibration took ca. 2 – 3 hrs and was monitored by the baseline. When the baseline drift fell below 0.01 mW within 30 min, the calorimetric experiment in one of the cells was started by breaking the ampoule in chloroform. The other cell was the reference. The heat evolution was observed for ca 60 min until the equilibrium baseline was reestablished. Then, the experiment in the second cell was performed in a similar way. Typically measured heat effects fell within 0.1 – 5 J range, depending on the load in the ampoule. The relative error of measurements of the heats of dissolution and the heats of wetting was estimated in 5 % for the heat effects ranging from 0.1 to 0.5 J and 2 % for the heat effects in the 0.5 – 5 J range.

3. Results and discussion

The enthalpy of formation of filled polymer composite, which depends on the interaction at the solid/polymer interface cannot be measured in the direct calorimetric experiment, as the solid particles do not spontaneously mix with polymer matrix. In such cases, the enthalpy can be determined by the proper combination of the steps, which can be performed in the calorimeter. These steps for the evaluation of the enthalpy of formation of the polymeric nanocomposite with embedded solid particles are presented schematically in Fig. 2 [20].

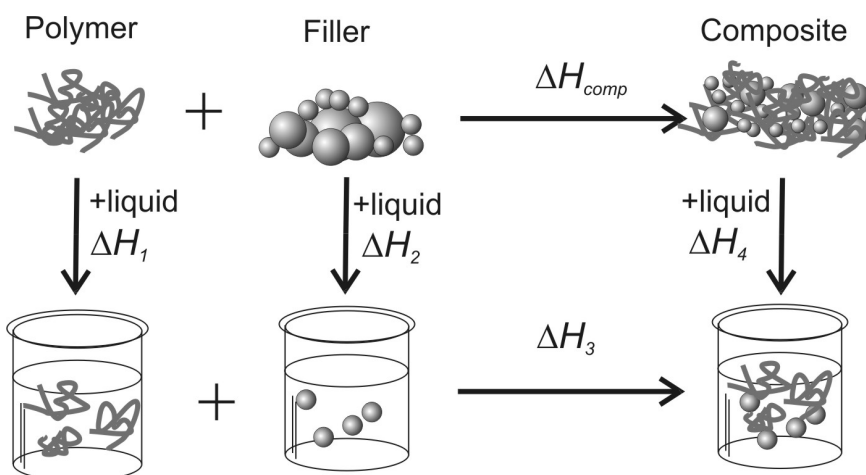


FIG. 2. Thermochemical cycle for the determination of the enthalpy of formation of a polymer composite

The target thermodynamic function in the thermochemical cycle (Hess cycle) in Fig. 2 is ΔH_{comp} – the enthalpy of formation of composite from its constituents. However, the mixing of a composite cannot be performed in the calorimetric cell; the composite with the definite filler content should be prepared separately. In order to evaluate ΔH_{comp} , one should go through consequent steps of the cycle in Fig. 2, which is based on the interaction of the components and the composite with an appropriate liquid. This liquid should be a good solvent for the polymer and should provide full dissolution of the polymer and the composite. In the present study, we used chloroform for such a liquid, as it is a good solvent for poly(isoprene) and for all its composites.

In the first step of the cycle, the enthalpy of dissolution (ΔH_1) of a polymer in a large extent of liquid was measured. At the same step, but in a separate experiment, the powdered filler was wetted by the same liquid with the enthalpy effect ΔH_2 . In the second step of the cycle the polymer solution was mixed with the suspension of the filler with the heat effect ΔH_3 . In the final step of the cycle, the solvent should be eliminated to give the composite with the definite filler content. Obviously, it was the reversal of the dissolution of the composite in the large extent of the liquid with the enthalpy effect ΔH_4 . Finally, the enthalpy of formation of the composite was calculated as the linear combination of enthalpy effects for these steps:

$$\Delta H_{comp} = \omega_1 \Delta H_1 + \omega_2 \Delta H_2 + \Delta H_3 - \Delta H_4, \quad (1)$$

TABLE 2. The enthalpy of dissolution in chloroform at 25 °C for poly(isoprene) ferroelastomers with embedded Fe NPs with intact and modified surface

ω_2	Enthalpy of dissolution of a composite, ΔH_4 (J/g)									
	0.1	0.2	0.3	0.4	0.5	0.6	0.7	0.8	0.9	1.0*
Fe ₀	-7.63	-6.75	-5.91	-5.05	-4.18	-3.34	-2.52	-1.79	-1.32	-4.86
Fe _{Ox}	-7.38	-6.40	-5.40	-4.47	-3.42	-2.73	-1.95	-1.34	-0.94	-1.05
Fe _T	-7.21	-6.03	-4.88	-3.62	-2.24	-1.05	-0.15	0.47	0.60	-4.27
Fe _{OA}	-7.20	-6.06	-5.08	-4.27	-3.44	-2.70	-1.96	-1.34	-0.95	-1.47
Fe _{PI}	-7.44	-6.58	-5.76	-4.92	-4.05	-3.19	-2.42	-1.76	-2.18	-21.07
Fe _{PS}	-7.64	-6.88	-6.13	-5.36	-4.58	-3.75	-2.96	-2.45	-2.92	-21.29

*The value of ΔH_4 at $\omega_2 = 1$ is the enthalpy of wetting of a filler ΔH_2

**The value of the enthalpy of dissolution on poly(isoprene), ΔH_1 , was equal to -8.39 J/g. This was the same in all cases.

where ω_1 , ω_2 are the weight fractions of the polymer (PI) and the filler (Fe MNPs) in the composite, which normalize ΔH_{comp} value per 1 g of the composite. The resulted value of ΔH_{comp} obtained in the thermochemical cycle corresponds to the temperature, at which the calorimetric measurements were made; and it was 25 °C in the present study.

Table 2 gives the values of the enthalpy of dissolution of poly(isoprene) in chloroform (ΔH_1), the enthalpy of wetting of Fe NPs with chloroform (ΔH_2), and the enthalpy of dissolution of composites (ΔH_4) with different Fe NPs content (ω_2). They were measured in calorimeter in the entire composition range for the composites filled with zero-valent metallic iron NPs with the intact and modified surface. ΔH_3 values in all the cases fell within the experimental error and are not listed.

The values given in Table 2 were used for calculating the enthalpy of formation of nanocomposites with embedded Fe NPs according to equation (1). They are plotted against the weight fraction of Fe NPs in Fig. 3. The values of the enthalpy of formation (ΔH_{comp}) are negative for all the nanocomposites; it means that the interaction between PI matrix and Fe NPs is energetically favorable. In all the cases, the concentration dependence is the smooth curve with minimum. It is clear that the modification of Fe NPs strongly affects ΔH_{comp} values. The largest absolute values were obtained for the ferroelastomers with Fe_{PI} and Fe_{PC} NPs, which were modified by the polymeric layer at the surface. The lowest absolute values of ΔH_{comp} correspond to Fe_{Ox} NPs with the passivating oxide layer on the surface. Qualitatively, these results indicate that the modification of the surface of Fe NPs improves interaction with PI matrix as a rule. The quantitative consideration needs more detailed treatment of the concentration plots for ΔH_{comp} .

The enthalpy of interaction at the interface is the result of the numerous elementary molecular contacts among the base-units of a polymer and the solid surface. If these contacts are short-range and independent (no cooperative forces are involved), then the total enthalpy of interaction will be proportional to the number of elementary contacts established at the interface. The number of such contacts is proportional to the fraction of the surface occupied by the base-units of a polymer. If the entire surface of the solid particle is filled with base-units of a polymer, then the enthalpy of interfacial interaction comes to saturation. Such a consideration leads to a Langmuir-type [24] equation for the enthalpy of adhesion at the polymer/solid interface:

$$\Delta H_{adh} = \Delta H_{adh}^{\infty} \frac{KC_P}{1 + KC_P}. \quad (2)$$

Here, ΔH_{adh} is the enthalpy of all contacts established by monomeric units with the surface of NPs at certain concentration of polymer, ΔH_{adh}^{∞} is the enthalpy of all the contacts in the saturated layer, K is the effective constant of the formation of an adhesive contact, C_P is the concentration of a polymer (PI) in g per 1 m² of the solid surface.

The function (ΔH_{adh}) and the variable (C_P) are related to the enthalpy of formation of composite and to the weight fraction of the filler by the obvious equations:

$$\Delta H_{adh} = \frac{\Delta H_{comp}}{\omega_2 S_{BET}}, \quad (3)$$

$$C_P = \frac{1 - \omega_2}{\omega_2 S_{BET}}. \quad (4)$$

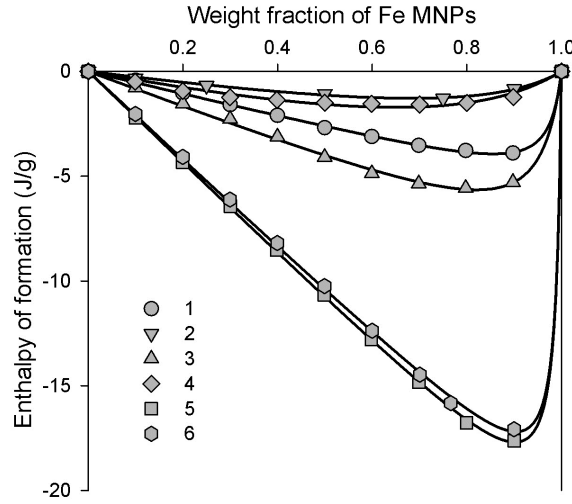


FIG. 3. Dependence of the enthalpy of formation of poly(isoprene) ferroelastomers on the content of Fe NPs with the intact and modified surface for systems filled with 1 – Fe_0 , 2 – Fe_{O_x} , 3 – Fe_T , 4 – Fe_{O_A} , 5 – Fe_{PI} , 6 – Fe_{PS} . The solid curves are the result of the interpolation by equation (5)

TABLE 3. Parameters of adhesion: ΔH_{adh}^∞ and K for the interaction of poly(isoprene) with the surface of the intact and modified Fe MNPs in poly(isoprene) ferroelastomers

Batch	Fe_0	Fe_{O_x}	Fe_T	Fe_{O_A}	Fe_{PI}	Fe_{PS}
ΔH_{adh}^∞ (J/m ²)	-0.64	-0.32	-1.08	-0.48	-2.79	-2.69
K (m ² /g)	299.0	41.6	164.0	29.0	655.0	697.0

Substitution of equations (3), (4) in equation (2) gives the relation of the experimentally determined value of ΔH_{comp} to the parameters of equation (2) – ΔH_{adh} and K :

$$\Delta H_{comp} = \Delta H_{adh}^\infty \frac{K(1 - \omega_2)\omega_2 S_{BET}}{K(1 - \omega_2) + \omega_2 S_{BET}}. \quad (5)$$

Figure 4 presents the model concentration dependencies of ΔH_{comp} calculated for different parameter sets. One can see that the curves have the same shape as the experimental plots presented in Fig. 3. In general, ΔH_{adh}^∞ governs the scale of the enthalpy changes, while K determines the position of the minimum on the curves. Large values of K correspond to the strong adhesion at the interface and it shifts the minimum of ΔH_{comp} to the large weight fraction of NPs in the composition (compare curves 1 and 2 in Fig. 4). This occurs because the adhesion layers become saturated at the relatively low levels of polymer content. If the adhesion is weak (i.e., low K), a large amount of the polymer is required to saturate the adhesion layers and the minimum of ΔH_{comp} is shifted to low fraction of NPs in the composition. If ΔH_{adh}^∞ is constant, the increase of K not only shifts the curve to the higher content of NPs but makes the minimum deeper. It is the result of the normalization of ΔH_{comp} value to 1 g of the composition. At high K the enthalpy of interaction corresponds to the relatively small amount of the polymer and it enlarges the negative values of ΔH_{comp} .

At a constant K , the negative values of ΔH_{comp} linearly increase with ΔH_{adh}^∞ as each adhesion contact with surface becomes stronger (compare curves 2 and 3 in Fig. 4).

Experimental values of ΔH_{comp} in Fig. 3 were fitted by equation (5) to get adhesion parameters ΔH_{adh}^∞ and K for PI ferroelastomers under study. Lines in Fig. 3 correspond to this interpolation. It is clearly seen that simple Langmuir model fits well the experimental results for the enthalpy of formation of nanocomposites.

Table 3 gives the parameters ΔH_{adh}^∞ and K obtained by fitting the concentration plots of ΔH_{comp} (Fig. 3) by equation (5).

The weakest is the adhesion of PI to the surface of Fe_{O_x} NPs with the passivating oxide layer. The absolute ΔH_{adh}^∞ value is twice lower than the value for the non-passivated Fe_0 with intact metal surface. This means that the passivation of metallic Fe NPs by its oxidation is unfavorable for the adhesion of PI. On the contrary, adhesion of PI to Fe_T NPs is almost twice stronger than that to the intact metallic surface. In reference [16], it was shown that the treatment of the intact surface of 3d metal by the aromatic liquids resulted in the formation of polycyclic aromatic

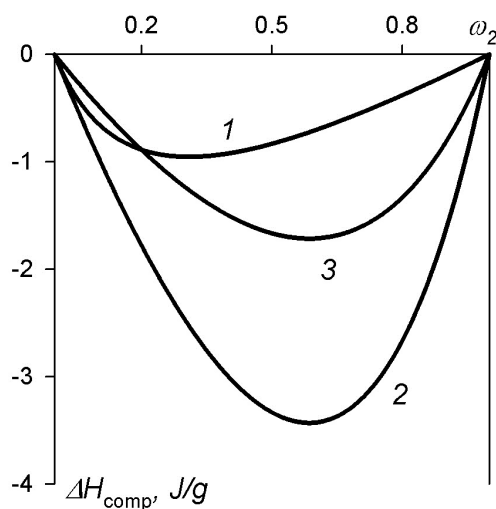


FIG. 4. The model concentration dependencies of ΔH_{comp} calculated for: (1) $K = 2 \text{ m}^2/\text{g}$, $\Delta H_{adh}^{\infty} = -1 \text{ J/m}^2$; (2) $K = 20 \text{ m}^2/\text{g}$, $\Delta H_{adh}^{\infty} = -1 \text{ J/m}^2$; (3) $K = 20 \text{ m}^2/\text{g}$, $\Delta H_{adh}^{\infty} = -0.5 \text{ J/m}^2$

hydrocarbons (PAH) on the surface. According to the results presented in Fig. 3 and Table 3, the layer of PAH substantially improves the adhesion of PI to the metallic surface of Fe MNPs. PI is a non-polar polymer with p-bonds in its monomeric units. Molecular orbitals on the double bonds more likely will interact with the delocalized electrons, which are present in the metal and in the benzene rings of PAH, than with the ionic crystalline oxide structure.

The strongest adhesion was obtained for the composites with Fe NPs modified by polymeric layers. Both polymeric modifiers – PI and PS contain π -electron density in their monomeric units and can effectively interact with PI matrix. Furthermore, it is well-known [25] that the macromolecules in the polymeric shells on the surface contain numerous loops and free tails, which substantially enhance the possibilities of the adhesion of PI matrix by interdiffusion.

Unexpectedly, Fe_{OA} showed rather poor adhesion to the PI matrix. It was lower than that for the intact Fe_0 but still stronger than for Fe_{Ox} . Oleic acid is commonly known as a good dispersant for the suspensions of metal and metal oxide particles in the non-polar liquids [1]. Its activity is based on the formation of the oriented adsorption layers on the surface of the particles. Usually, metal surfaces are oxidized, and thus, the mechanism of oleic acid adsorption on the metal and on the metal oxide is likely the same. The polar heads of the oleic acid stick to the polar surface of the oxide, while hydrocarbon tails form the hydrophobic shell around the particle. However, this is not the case for the Fe_{OA} NPs studied in the present work. Modification by oleic acid was performed on the intact metal surface not exposed to the air, which might not favor the formation of the oriented layer. No such layer on the surface of Fe NPs was found by HTEM in our previous work [23]. Oleic layer on the surface was amorphous and the polar carboxyl residues of oleic acid were facing any direction. Therefore these polar groups might as well be exposed to PI matrix in the composite, and might effectively diminish the adhesion.

The trends in K values (Table 3) generally follow the trends in ΔH_{adh}^{∞} . This means that strong molecular contacts provide higher adherence at the interface. However, K being the effective constant of the formation of adhesion contact relates to the free energy of the adhesion, which includes not only the enthalpy, but also the entropy contribution. Most likely it is the reason for the deviations from the linear correlation between ΔH_{adh}^{∞} and K (e.g. in the case of Fe_0 , see Table 3).

4. Conclusions

The evaluation of the interaction energy at the interface between the polymeric matrix and dispersed solid particles is crucial for the development of the advanced composite polymeric materials. Specifically, it relates to the elastic composites with embedded magnetic nanoparticles – ferroelastomers. In the present study, we have used thermodynamic approach based on the thermochemical cycle to evaluate the enthalpy of formation of poly(isoprene) ferroelastomers with metal Fe NPs. We have taken Fe NPs with different surface treatment to study the influence of the surface modification on the enthalpy of interaction between poly(isoprene) matrix and the surface of embedded Fe NPs. In all the nanocomposites studied, the enthalpy of interaction between poly(isoprene) and Fe NPs was negative; it indicated adhesion between components at the polymer/solid interface. The dependence of the enthalpy of interaction on the NP's content in poly(isoprene) ferroelastomers is a smoothly shaped curve with a minimum. The simple Langmuir-type model was shown to be a good choice for the quantitative description of the experimental data

and provided solid grounds for the consideration of the role of surface modification on poly(isoprene)/Fe interaction in the elastic nanocomposites.

The negative values of the enthalpy of adhesion increase almost ten-fold in a series Fe_{O_x} (oxidized surface) – Fe_{OA} (deposited oleic acid) – Fe_0 (intact metal surface) – Fe_T (deposited polycyclic aromatics) – $FePI$ (deposited poly(isoprene)) = Fe_{PS} (deposited poly(styrene)). It supports the delocalization of π -electrons as the likely source for the interaction at the interface. Poly(isoprene) contains unsaturated double bond in each monomeric unit in the macromolecule. The intact Fe surface can participate in such delocalization due to the electronic gas in the metal lattice. The adhesion with poly(isoprene) matrix further improves when the intact Fe surface is covered by organic deposits with unsaturated electronic structures (double bonds, benzene rings). Meanwhile, if the metal surface is covered by oxide shell with ionic crystal lattice, the adhesion of poly(isoprene) diminishes. In a whole, the obtained results revealed that the in-situ surface modification of zero-valent iron nanoparticles in the EEW synthesis allowed controlled tuning of molecular adhesion at polymer/solid interface.

Acknowledgement

The research was supported by Russian Science Foundation grant 20-12-00031.

References

- [1] Li L., Hu J., Shi X., Fan M., Luo J., Wei X. Nanoscale zero-valent metals: a review of synthesis, characterization, and applications to environmental remediation. *Environ Sci Pollut Res*, 2016, **23**, P. 17880–17900.
- [2] Yang T.-I., Brown R.N.C., Kempel L. C., Kofinas P. Magnetodielectric properties of polymer- Fe_3O_4 nanocomposites. *J Magn Magn Mater*, 2008, **320**(31), P. 2714–2720.
- [3] Jamal E.M.A., Joy P.A., Kurian P., Anantharaman M.R. Synthesis of nickel rubber nanocomposites and evaluation of their dielectric properties. *Mater Sci Eng B-Adv*, 2009, **156**(13), P. 24–31.
- [4] Kong I., Ahmad S. H., Abdullah M. H., Hui D., Yusoff A.N., Puryanti D. Magnetic and microwave absorbing properties of magnetite thermo-plastic natural rubber nanocomposites. *J Magn Magn Mater*, 2010, **322**(21), P. 3401–3409.
- [5] Stepanov G.V., Chertovich A.V., Kramarenko E.Yu. Magnetorheological and deformation properties of magnetically controlled elastomers with hard magnetic filler. *J Magn Magn Mater*, 2012, **324**(21), P. 3448–3451.
- [6] Kango S., Kalia S., Celli A., Njuguna J., Habibi Y., Kumar R. Surface modification of inorganic nanoparticles for development of organic–inorganic nanocomposites – a review. *Progress Polym Sci*, 2013, **38**, P. 1232–1261.
- [7] Yuan W., Yuan J., Zhou L., Wu S., Hong X. Fe_3O_4 @poly(2-hydroxyethyl methacrylate)-graft-poly(3-caprolactone) magnetic nanoparticles with branched brush polymeric shell. *Polymer*, 2010, **51**, P. 2540–2547.
- [8] Pich A., Bhattacharya S., Ghosh A., Adler H.-J.P. Composite magnetic particles: 2. Encapsulation of iron oxide by surfactant-free emulsion polymerization. *Polymer*, 2005, **46**, P. 4596–4603.
- [9] Campanella A., Di Z., Luchini A., Paduano L., Klapper A., Herlitschke M., Petracic O., Appavou M.S., Müller-Buschbaum P., Frielinghaus H., Richter D. Nanocomposites composed of HEUR polymer and magnetite iron oxide nanoparticles: Structure and magnetic response of the hydrogel and dried state. *Polymer*, 2015, **60**, P. 176–185.
- [10] Móczó J., Pukánszky B. Polymer micro and nanocomposites: Structure, interaction, properties. *J Ind Eng Chem*, 2008, **14**, P. 535–563.
- [11] Liu D., Pourrahimi A.M., Olsson R.T., Hedenqvist M.S., Gedde U.W. Influence of nanoparticle surface treatment on particle dispersion and interfacial adhesion in low-density polyethylene/aluminium oxide nanocomposites. *Eur Polym J*, 2015, **66**, P. 67–77.
- [12] Chou F.-Y., Shih C.-M., Tsai M.-C., Chiu W.-Y., Lue S.J. Functional acrylic acid as stabilizer for synthesis of smart hydrogel particles containing a magnetic Fe_3O_4 core. *Polymer*, 2012, **53**, P. 2839–2846.
- [13] Gelbrich T., Marten G.U., Schmidt A.M. Reversible thermoflocculation of magnetic core-shell particles induced by remote magnetic heating. *Polymer*, 2010, **51**, P. 2818–2824.
- [14] Chen J., Du K., Chen X., Li Y., Huang J., Wu Y., Yang C., Xia X. Influence of surface microstructure on bonding strength of modified polypropylene/aluminum alloy direct adhesion. *Appl Surf Sci*, 2019, **489**, P. 392–402.
- [15] Barroso-Bujans F., Serna R., et al. Grafting of poly(acrylic acid) onto an aluminum surface. *Langmuir*, 2009, **25**(16), P. 9094–9100.
- [16] Beketov I.V., Safronov A.P., Bagazeev A.V., Larrañaga A., Kurlyandskaya G.V., Medvedev A.I. In situ modification of Fe and Ni magnetic nanopowders produced by the electrical explosion of wire. *Journal of Alloys and Compounds*, 2014, **586**, P. S483–S488.
- [17] Safronov A.P., Kurlyandskaya G.V., Chlenova A.A., Kuznetsov M.V., Bazhin D.N., Beketov I.V., Sanchez-Illarduya M.B., Martinez-Amesti A. Carbon deposition from aromatic solvents onto active intact 3d metal surface at ambient conditions. *Langmuir*, 2014, **30**, P. 3243–3253.
- [18] Kotov Yu.A. Electric explosion of wires as a method for preparation of nanopowders. *Journal of Nanoparticle Research*, 2003, **5**, P. 539–550.
- [19] Kurlyandskaya G.V., Bhagat S.M., Safronov A.P., Beketov I.V., Larranaga A. Spherical magnetic nanoparticles fabricated by electric explosion of wire. *AIP Advances*, 2011, **1**, P. 042122.
- [20] Petrov A.V., Safronov A.P., Terziyan T.V., Beketov I.V. Effect of the nature of a polymer matrix on the enthalpy of adhesion interactions in composites filled with nickel nanoparticles. *Polym Sci Ser A*, 2012, **54**(11), P. 840–848.
- [21] Terziyan T.V., Safronov A.P., Petrov A.V., Panteleeva M.V., Beketov I.V. Thermodynamics of interfacial interactions in composites based on nanodispersed NiO and methacrylic acid derivatives. *Polym Sci Ser A*, 2014, **56**(1), P. 63–71.
- [22] Terziyan T.V., Safronov A.P., Zalyaeva E.R., Beketov I.V., Lakiza N.V. Thermochemical analysis of the interaction between interfaces in composites containing nanodispersed powders of Al and Al_2O_3 . *Russian Journal of Physical Chemistry A*, 2020, **94**(12), P. 2508–2513.
- [23] Safronov A.P., Bagazeev A.V., Demina T.M., Petrov A.V., Beketov I.V. Active surface modification for iron nanopowders produced by wire electrical explosion. *Nanotechnologies in Russia*, 2012, **7**, P. 5–6.
- [24] Hiemenz P.C., Rajagopalan R., *Principles of Colloid and Surface Chemistry*. Marcel Dekker, New York, 1997, 651 p.
- [25] Takahashi A., Kawaguchi M. The structure of macromolecules adsorbed on interfaces. *Adv Polym Sci*, 1982, **46**, P. 1–65.

Conjugation of curcumin with Ag nanoparticle for improving its bioavailability and study of the bioimaging response

Runjun Sarma^{1*}, Monoj Kumar Das², Lakshi Saikia³, Anand Ramteke², Ratul Saikia⁴

¹Department of Physics, Mehr Chand Mahajan DAV College for Women, Sector 36, Chandigarh, India

²Cancer Genetics and Chemoprevention Research Group, Department of Molecular Biology and Biotechnology, Tezpur University, Tezpur, Assam 784028, India

³Material Science and Technology Division, CSIR-North East Institute of Science and Technology, Jorhat, Assam 785006, India

⁴Biological Science and Technology Division, CSIR-North East Institute of Science and Technology, Jorhat, Assam 785006, India

*runjun2018chd@gmail.com

DOI 10.17586/2220-8054-2021-12-4-528-535

We report here the production of curcumin conjugated polyvinylpyrrolidone (PVP)-capped Ag nanoparticles for potential biological applications. Evidence for the efficient conjugation of hydrophobic curcumin to the synthesized nanoparticles (NPs) is expected from UV-Vis, zeta potential and Fourier transform infrared (FT-IR) analysis. Curcumin conjugated to PVP-capped Ag NPs is observed to gain high water solubility and bioavailability in a biological environment without diminishing its therapeutic properties. The presence of the main therapeutic group, the diarylheptanoid chromophore of curcumin, indicates the existence of its medicinal behavior in the curcumin-Ag NPs complex. Moreover, the fluorescence efficiency of PVP capped Ag NPs in the breast cancer cellular medium have been found to be significantly enhanced (by factor of ~ 2.37) with curcumin conjugation. The production of bioavailable curcumin provides an opportunity to expand the clinical repertoire of this efficacious agent without hampering the environment and human health.

Keywords: therapeutic, bioavailability, imaging, curcumin, PVP.

Received: 15 March 2021

Revised: 22 July 2021

1. Introduction

Curcumin (Turmeric), a bio-active polyphenol component of *Curcuma longa* L., has attracted significant interest in biological research owing to its unique therapeutic properties such as anti-inflammatory, antibacterial, antioxidant, antifungal, anti-carcinogenic etc. [1, 2]. Moreover, it has been found that curcumin is extremely safe even at very high doses in animals as well as in humans [3, 4]. Therefore, curcumin exhibits tremendous potential to be used for the treatment and prevention of various human diseases. However, despite the possibility for the use of curcumin as a therapeutic agent in vivo, poor aqueous solubility (i.e. 0.0004 mg/mL at pH 7.3) limits its use as a drug for the prevention or treatment of various diseases. This results in low intrinsic activity, poor absorption and rapid elimination/clearance from the living body [1].

Until now, various methods have been reported to explore the potential applications of curcumin in various biological fields. Nanoparticles, liposomes, micelles, and phospholipid complexes have been used to improve permeability and circulation of curcumin in vivo. However, it has been observed that though the bio-availability improves upon conjugation, the main therapeutic group of this molecule gets engaged in the conjugation thereby decreasing its availability for therapeutic activity in a biological system [5]. In this regard, the conjugation of curcumin in the nanoparticle-polymer composite may be an alternative and easier approach to enhance its water solubility as well as bioavailability without diminishing its therapeutic property [6].

On the other hand, in recent years, metallic nanoparticles (NPs) in general and silver NPs (Ag NPs) in particular have attracted considerable interest in various applications such as therapeutic [7], drug delivery [8], antimicrobial [9] and medical imaging [10]. This is due to their unique physical, chemical, optical and biological properties [11].

We report here on the formation of water-soluble and biocompatible curcumin conjugated Ag NPs. Polyvinylpyrrolidone (PVP) will be used to conjugate Ag NPs with curcumin (Ag-PVP-C) to make it bioavailable without harming its medicinal activity. Then the optical, vibrational, and morphological properties of the synthesized metallic NPs will be considered. Moreover, the modification of these properties with conjugation of therapeutic agent curcumin will be

studied. Finally, a critical evaluation with respect to cellular (MDA-MB-231 breast cancer cells) uptake of the PVP-capped Ag NPs/Ag-PVP-CNPs (curcumin conjugated PVP-capped Ag NPs) will be carried out through fluorescence imaging data.

2. Experimental details

2.1. Synthesis of PVP capped Ag nanoparticles (Ag NPs)

Silver nitrate (AgNO_3) has been used as a metal precursor and borohydride (NaBH_4) as reducing agent for the preparation of Ag NPs. At first, 1 % PVP (MW 40000) solution was prepared by dissolving 0.1 g of PVP in 10 mL distilled water and stirred it for 30 min. Then 10 mL volume of 1 mM stock solution of AgNO_3 was prepared by dissolving 0.00169 g silver salt in 10 mL distilled water. From the stock solution, 10 mL of 0.4 mM solution was prepared and added to the PVP solution. After 15 minutes of stirring, 2 mL of 0.2 mM sodium borohydride (NaBH_4), freshly prepared in ice cold water, was added to the above mixture in a drop wise manner. With the addition of NaBH_4 , the color of the solution turned to light yellow indicating the formation of the Ag NPs by reduction of Ag^{2+} to Ag^0 . The solution was then cooled to room temperature.

2.2. Synthesis of curcumin conjugated PVP capped Ag nanoparticles (Ag-PVP-C NPs)

Conjugation of curcumin with PVP-capped Ag NPs was carried out by dissolving 30 mg of curcumin in 10 mL of acetone. Acetone was used for as the solubility of curcumin is highest in acetone as compared to other commonly used organic solvents, such as methyl ethyl ketone, ethyl acetate, methanol, ethanol, 1,2-dichloroethane, isopropanol, ether etc.

5 mL curcumin solution was then added to 10 mL solution of the as synthesized PVP-capped Ag NPs, under stirring at 100 °C temperature. The reaction was allowed to continue for up to 2 h to get curcumin conjugated-PVP capped Ag NPs (Ag-PVP-C).

2.3. Characterization techniques

The structural characterization of the Ag NPs and Ag-PVP-C NPs complex was performed by using a high-resolution transmission electron microscopy (HRTEM) (Model: JEM-2100, JEOL, USA) at NEHU, Shillong, India, working at an accelerating voltage of 200 kV. The optical absorption study was performed by the UV-Visible absorption spectroscopy (UV 2450, Shimadzu Corporation). The zeta potential was measured using a Malvern Zetasizer (Model Nano ZS, NSW, Australia). Furthermore, IR-active vibrational features were assessed through Fourier transform infrared (FT-IR) (Nicolet model Impact-410) studies. Ag NPs and Ag-PVP-C NPs complexes were used as cancer cell probes by using a fluorescent microscope (Model: Leica DM300, USA) equipped with a cooled color CCD camera (Model DP71).

3. Results and discussions

We discuss below the analysis of PVP capped Ag NPs (Ag NPs) and curcumin conjugated-PVP capped Ag NPs (Ag-PVP-C) characterized by different techniques.

3.1. Morphological analysis through transmission electron microscopy studies

High resolution transmission electron microscopy (HRTEM) was used to study themorphological behavior of the as-synthesized PVP capped Ag NPs and curcumin conjugated PVP-capped Ag NPs. The HRTEM micrographs of the PVP capped Ag NPs are shown in Fig. 1(a). The average size (diameter) of the NPs was found to be ~ 2 nm with nearly spherically symmetric structure. Further, good crystallinity of the sample could be predicted from the clear lattice fringes (upper left inset of Fig. 1(a)). The typical interplanar spacing (d) was estimated to be ~ 0.2 nm which is close to the value (0.23 nm) reported in an earlier work [12]. The perfect periodicity of lattice atoms was mostly witnessed in the central region (approx. at a distance within ~ 0.7 nm from the center) while missing atoms and planes are generally observable close to the surface of the Ag nanoparticle. The orientation of the planes of the upper right side of a particle changes the orientation with regard the lower side planes ((lower left inset of Fig. 1(a)). This may suggest the existence of some edge dislocation occurring as a result of undeveloped lattice planes at the nanoparticle surface.

The HRTEM image of curcumin conjugated-PVP capped Ag NPs (Ag-PVP-C NPs) is shown in Fig. 1(b). The average size of the Ag-PVP-C NPs are found to be ~ 4.25 nm in diameter. It can be observed that Ag NPs are surrounded by PVP. Similar behavior has also been observed for PVP-capped Au NPs conjugated to curcumin [13].

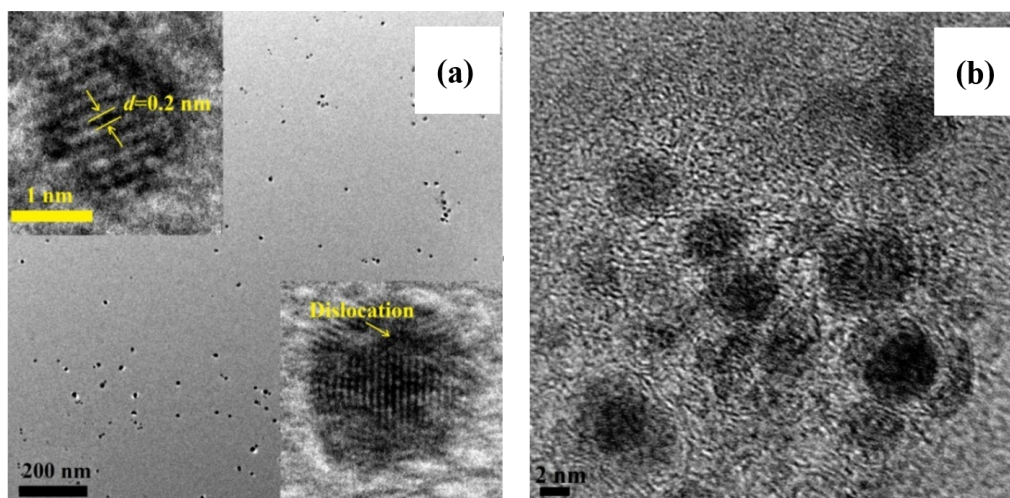


FIG. 1. HRTEM image of (a) PVP capped Ag NPs. The enlarged, isolated NPs are shown as upper left and lower right insets with indicating interplanar spacing and dislocation; respectively. (b) HRTEM image of curcumin conjugated-PVP capped Ag NPs (Ag-PVP-C)

3.2. UV-Vis spectra of PVP capped Ag NPs, curcumin (C) and Ag-PVP-C NPs

The UV-Vis absorption spectra of PVP capped Ag NPs, curcumin and Ag-PVP-C NPs are depicted in Fig. 2. As can be found, Ag NPs shows SPR peak at ~ 400 nm arising from the collective oscillation of free conduction electrons induced by an interacting electromagnetic field (Fig. 2(a)).

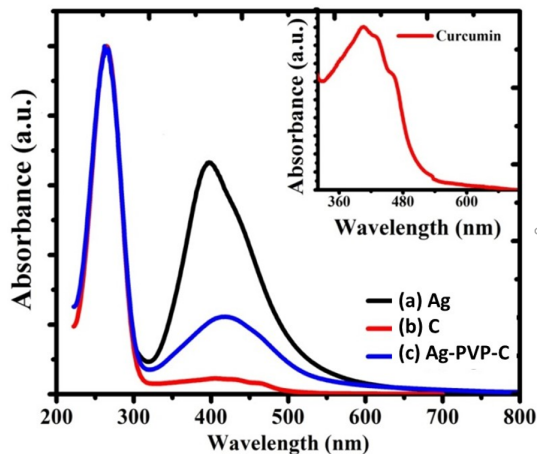


FIG. 2. Optical absorption of (a) PVP capped Ag NPs (Ag); (b) Curcumin(C); (c) Curcumin conjugated-PVP capped Ag NPs (Ag-PVP-C)

Curcumin generally shows a strong and intense absorption band in the ranges of 350 – 480 nm and 200 – 280 nm. In our case (Fig. 2(b)), the absorption spectrum in the region of 350 – 480 nm is very broad, having a number of absorption bands. The presence of more than one shoulder i.e. at ~ 406 , ~ 429 and ~ 462 nm, (shown in enlarged in the inset of the figure) indicates the possible presence of more than one isomeric form in the ground state of curcumin [14, 15]. Moreover, it is to be noted that the peak observed at ~ 429 nm is a signature of the basic diarylheptanoid chromophore group of curcumin [6, 16], the main therapeutic group of this molecule. One characteristic absorption band of curcumin, which corresponds to the transfer of $\pi-\pi^*$ electrons in the benzene ring, is noticed at ~ 263 nm.

The UV-Vis spectra of curcumin conjugated PVP-capped Ag NPs (Ag-PVP-C) (Fig. 2(c)) clearly shows two distinct peaks at ~ 263 and ~ 418 nm. The peak observed at ~ 418 nm is red shifted by 18 nm from original SPR peak at 400 nm as observed in curcumin free PVP capped Ag NPs. Whereas, this peak is blue shifted by ~ 11 nm from the curcumin absorption peak at ~ 429 nm related to the diarylheptanoid chromophore group. The presence of this peak

at Ag-PVP-C complex demonstrates that curcumin retains its diarylheptanoid chromophore group while conjugating to PVP capped Ag NPs, which is much needed in antimicrobial applications [6, 17].

3.3. Molecular vibrations in PVP capped Ag NPs, curcumin (C) and Ag-PVP-C NPs

Figure 3 shows the FTIR spectra of PVP capped Ag NPs, curcumin (C) and curcumin conjugated-PVP capped Ag NPs (Ag-PVP-C).

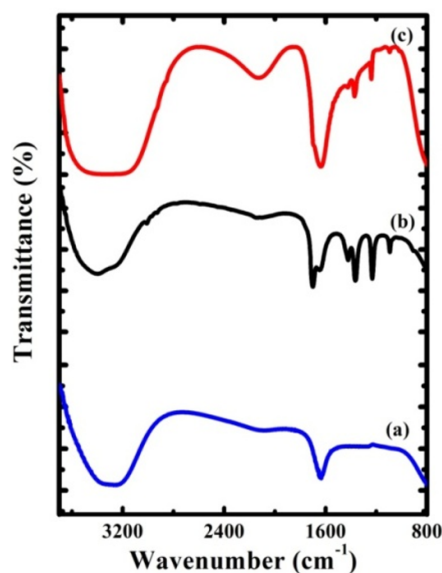


FIG. 3. FTIR spectra of (a) PVP capped Ag NPs; (b) Curcumin (C); (c) Curcumin conjugated PVP capped Ag NPs (Ag-PVP-C)

Figure 3(a) shows the FTIR spectra of the PVP-capped Ag NPs. A broad band centered around 3412 cm^{-1} attributed to the stretching vibration of -OH group. The absorption band of the C=O bond at 1663 cm^{-1} for pure PVP was shifted to 1643 cm^{-1} for Ag NPs capped by PVP. This decrease in wavenumber for the C=O absorption may result from bond weakening via partial donation of oxygen lone pair electrons of PVP to the vacant orbitals of the silver [18]. Whereas, the wavenumber observed at $\sim 1270\text{ cm}^{-1}$ was due to bond vibrations of the N=H-O complex [19]. Thus, the FTIR spectra reveal the molecular interaction between Ag and PVP chain.

To determine the specific sites of interaction between PVP-capped Ag NPs and curcumin, FTIR spectra of both curcumin (Fig. 3(b)) and curcumin conjugated-PVP capped Ag NPs (Ag-PVP-C) (Fig. 3(c)) have been studied. The FTIR bands for stretching vibration of -OH group in curcumin is observed at 3398 cm^{-1} . This -OH vibration absorption (at $\sim 3321\text{ cm}^{-1}$) observed for curcumin conjugated PVP-capped Ag NP is not sharp as obtained for curcumin. This may be due to the hydrogen-bond intermolecular interaction between O-H of curcumin and C=O of PVP around Ag NP [20].

The FTIR band due to the in-plane bending of two phenolic and one enolic hydroxyl groups of the curcumin are observed at 1360 (phenolic) 1227 (phenolic) and 962 cm^{-1} (enolic). The absence of a band at 962 cm^{-1} (due to enolic group of curcumin) for the Ag-PVP-C compound may suggest the interaction of Ag NPs through this site also [21]. Generally, metal coordination of curcumin occurs through the enolic group, where the enolic proton is replaced by the metal ion and the *o*-methoxy phenolic moiety remains intact in the complexes [22].

The band at 1428 cm^{-1} observed in curcumin corresponds to the olefinic in-plane bending vibrations of the heptadiene chain of curcumin. Similarly, the absorption at, 1091 cm^{-1} is due to aromatic C-O-C vibration of curcumin. These bands at 1428 and 1091 cm^{-1} shown by curcumin as stated above were shifted to 1424 and 1178 cm^{-1} ; respectively on conjugation of curcumin to PVP capped Ag NPs. This indicates the presence of intact curcumin moiety in the Ag-PVP-C complex [21]. The shifting of aromatic C-O-C vibration in Ag-PVP-C NP signifies the symmetry change related to benzene rings of curcumin [17]. The presence of basic diarylheptanoid group is confirmed from the FTIR band at 1424 cm^{-1} in Ag-PVP-C NPs. This is the chromophore group of curcumin which is required in the antimicrobial application. Thus, FTIR spectra confirm that curcumin retains its diarylheptanoid chromophore group while conjugating to PVP capped Ag NPs and hence preserving its therapeutic properties.

3.4. Measurement of zeta potential

The stability of a colloidal system could be predicted from the value of the zeta potential. An increased value of zeta potential (*+ve* or *-ve*) signifies the enhancement of repulsive behavior between the particles and thus results a more stable colloidal dispersion. The respective values of zeta potential of PVP-capped Ag NPs (Ag NPs) and curcumin conjugated PVP-capped Ag NPs (Ag-PVP-C) were observed to be -16.5 and -33.7 mV. The larger value of zeta potential in Ag-PVP-C clearly indicates the efficient conjugation of curcumin to PVP capped Ag NPs while simultaneously enhancing its stability in the colloidal solution.

3.5. PVP capped Ag NPs (Ag NPs) and curcumin conjugated-PVP capped Ag NPs (Ag-PVP-C NPs) as cancer cell probe

Imaging snapshots of MDA-MB-231 cancer cells treated with PVP capped Ag NPs and curcumin conjugated PVP-capped Ag NPs are shown in Fig. 4(a) and (b), respectively. The snapshots suggest high biocompatibility and fluorescent behavior of both PVP capped Ag NPs and curcumin conjugated PVP capped Ag NPs in the cancer cellular environment.

Using image J-1.46r software® the quantitative analysis of the fluorescence of the NPs was predicted presuming complete localization of the NPs inside the cell as discussed in previous reports [23,24]. Fig. 4(c,d) highlight the areas of interest (A, B, C, D etc.) and the selected background areas (region without fluorescence; bk1, bk2, bk3 etc.) of fluorescent images marked with encircled regions. The corrected total counts of fluorescence (CTCF) intensity values were calculated using the relation:

$$\text{CTCF} = \text{Integrated Density} - (\text{Area} \times \text{mean fluorescent of background setting}),$$

here, the 'integrated density' (IntDen) of a fluorescent image is the sum of the values of the pixels in the selected regions. Fig. 4(e) signifies a comparative view on representative histograms of the average CTCF and average IntDen obtained for different NPs system. It predicts biocompatibility and fluorescent behavior of the NPs on being used for the treatment of cancer cells. Moreover, the fluorescence intensity indicates the level of the internalization of NPs by the cells. It could be observed that, the fluorescence efficiency (CTCF) of curcumin conjugated-PVP capped Ag NPs in the cancer cellular medium is ~ 2.37 times more than that the value obtained for curcuminfree PVP-capped Ag NPs. Thus, the cellular uptake and bioimaging aspects of metallic Ag NPs were significantly affected by the conjugation with the therapeutic agent curcumin. Similar response for the curcumin conjugated NPs is also reported earlier [25]. Though the surface charge/zeta potential of NPs significantly impact the cellular uptake mechanism, there are different opinions regarding uptake rate of cationic and anionic NPs by the cells [26–30]. Moreover, there may be direct permeation of the NPs in to the cell irrespective of the surface charge of the NPs [31].

Fröhlich, in a review article [29], discusses the role of surface charge of the NPs on cytotoxicity, cellular uptake, and their localization in the intracellular region. It was concluded that nonphagocytic cells have the ability to uptake cationic NPs to a higher extent, while phagocytic cells favor anionic NPs. Apart from the surface charge, there are different factors such as size, shape, type of material, charge density, surface hydrophobicity, concentration and stabilizing agents that influence the cellular uptake process of a NP.

MDA-MB-231 breast cancer cells have the potential to function as phagocytes. They exhibit phagocytic activity (engulfing and digesting) on the normal cells [32, 33]. Cellular uptake of PVP-capped anionic Ag NPs occur in the MDA-MB-231 breast cancer cells in endosomes and then in the amphisomes (of the MDA-MB-231 breast cancer cells) [34]. However, there is aggregation/degradation of the PVP-capped Ag NPs inside the cancer cells. In the present case, we can expect preferential internalization of the curcumin conjugated PVP-capped Ag NPs (zeta potential -33.7 mV) by phagocytic MDA-MB-231 breast cancer cells. As obtained from zeta potential curcumin conjugated PVP-capped Ag NPs show better colloidal stability preventing their aggregation and hence the degradation. Moreover, PVP-capped Ag NPs may increase the photostability of curcumin and hence reduce photobleaching resulting higher fluorescence of the curcumin conjugated PVP-capped Ag NPs inside the cells [35].

An electrostatic repulsive force between anionic NPs and the negatively charged cell membrane can hinder the efficiency of NPs binding to the cell. This electrostatic repulsion can be suppressed by changing the capping/conjugated material and the size of the NPs [36]. In this context, detailed of both PVP-capped Ag NPs and curcumin conjugated PVP-capped Ag NPs which are anionic particles, are needed to determine the existence or extent of influence of electrostatic repulsive behavior on the cellular uptake rates in the breast cancer cells considered in our study. However, at present, a comprehensive assessment of this topic is beyond the present scope [37]. Though anionic NPs are characterized by limited interaction ability, they are attractive for biomedical applications due to very low cytotoxic effects as compared to the cationic ones. There are various reports which describe successful internalization of anionic NPs to cells [36, 38–40].

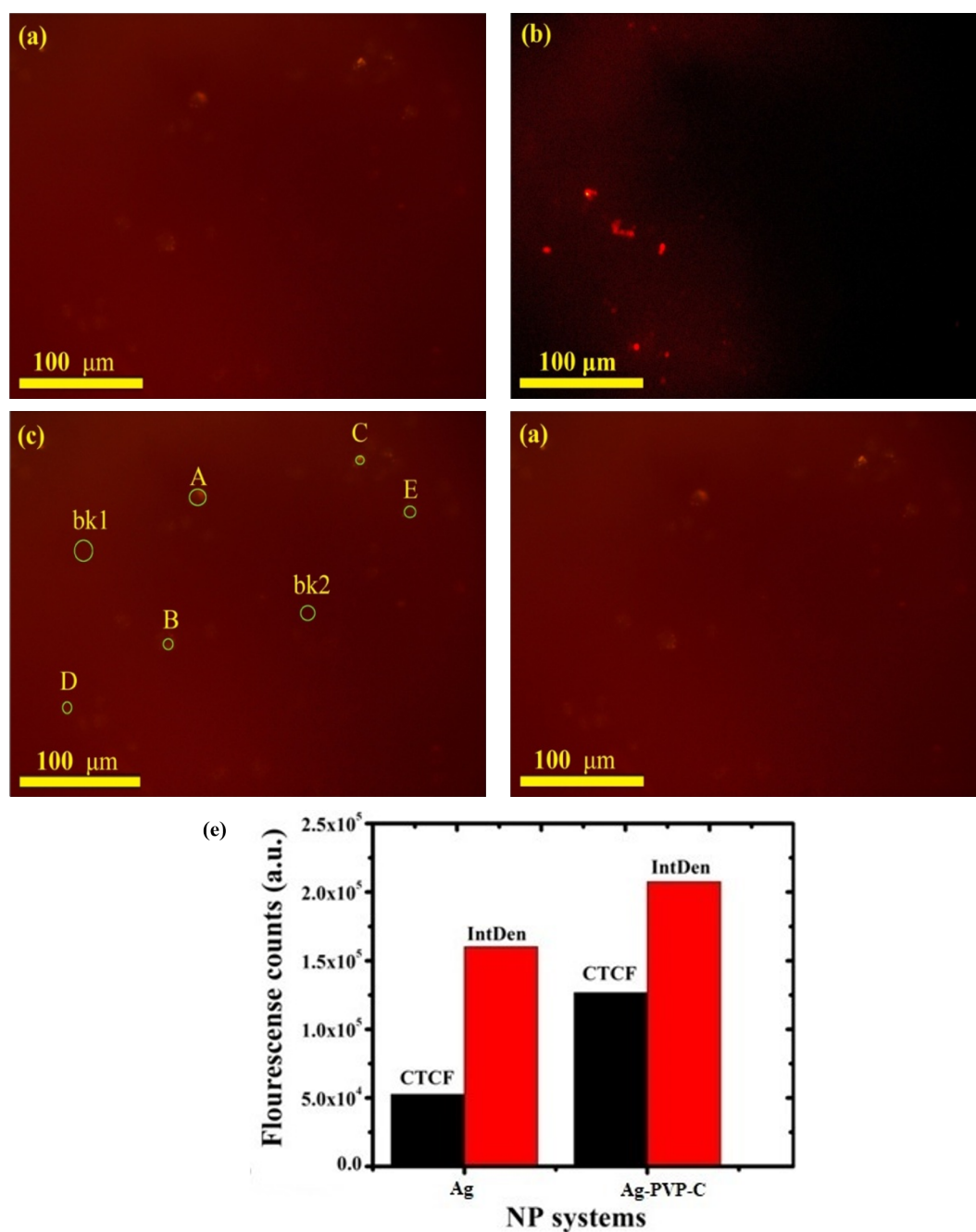


FIG. 4. Fluorescent imaging (using violate filter) of cancer cells with (a) Ag NPs (b) Ag-PVP-C complex. Figure (c), (d) show selected fluorescent and background areas of fluorescent images respectively ($\lambda_{ex} \sim 300$ nm). Histograms representing the average value of IntDen and CTCF of different types of NP systems is shown in Figure (e)

4. Conclusion

PVP-capped silver nanoparticles were synthesized and characterized for structural, optical and vibrational properties. The influence of curcumin on the aforementioned properties have been studied by conjugating curcumin to PVP-capped Ag NPs. Curcumin was found to be water soluble and retained its therapeutic properties upon conjugation with PVP capped Ag NPs. While used as a cancer cell imaging probe, curcumin conjugated PVP-capped Ag NPs showed higher fluorescence response as compared to the curcumin free ones. The production of water soluble and biocompatible curcumin expands the clinical range of this efficacious agent without hampering the environment and human health. In addition, the curcumin conjugated PVP-capped Ag NPs exhibited fluorescent properties, which is believed to cater to a broad spectrum of diverse applications in biological and pharmacological activities such as bio-imaging, targeted drug delivery, biosensing, examination of intracellular processes etc.

Acknowledgements

The author R. Sarma is thankful to the Department of Biotechnology (DBT), Ministry of Science & Technology, New Delhi for financial support under DBT-RA scheme Department of Biotechnology, government of India, New Delhi (Project No. GAP0740). The authors are also thankful to the Material Science Division, CSIR-NEIST, Jorhat for providing nanoparticle synthetic lab facility, UV-Vis and Zeta potential measurement, and Director, CSIR-NEIST, Jorhat for providing the necessary facilities in the institute, and Dr. Manash Jyoti Kashyap, for his extensive help in editing the article. The authors gratefully acknowledge Analytical Chemistry Group, CSIR-NEIST for FTIR analysis and SAIF-NEHU, Shillong for HR-TEM measurements.

References

- [1] Anand P., et al. Bioavailability of curcumin: problems and promises. *Molecular pharmaceuticals*, 2007, **4** (6), P. 807–818.
- [2] Senft C., et al. The nontoxic natural compound Curcumin exerts anti-proliferative, anti-migratory, and anti-invasive properties against malignant gliomas. *BMC cancer*, 2010, **10** (1), P. 491.
- [3] Lao C.D., et al. Dose escalation of a curcuminoid formulation. *BMC complementary and alternative medicine*, 2006, **6** (1), P. 10.
- [4] Qureshi S., Shah A., Ageel A. Toxicity studies on *Alpinia galanga* and *Curcuma longa*. *Planta medica*, 1992, **58** (2), P. 124–127.
- [5] Daniel S., et al. Through metal binding, curcumin protects against lead- and cadmium-induced lipid peroxidation in rat brain homogenates and against lead-induced tissue damage in rat brain. *Journal of inorganic biochemistry*, 2004, **98** (2), P. 266–275.
- [6] Gangwar R.K., et al. Conjugation of curcumin with PVP capped gold nanoparticles for improving bioavailability. *Materials Science and Engineering C*, 2012, **32** (8), P. 2659–2663.
- [7] Gopinath P., et al. Implications of silver nanoparticle induced cell apoptosis for in vitro gene therapy. *Nanotechnology*, 2008, **19** (7), 075104.
- [8] Wu W., et al. Smart core-shell hybrid nanogels with Ag nanoparticle core for cancer cell imaging and gel shell for pH-regulated drug delivery. *Chemistry of Materials*, 2010, **22** (6), P. 1966–1976.
- [9] Shahverdi A.R., et al. Synthesis and effect of silver nanoparticles on the antibacterial activity of different antibiotics against *Staphylococcus aureus* and *Escherichia coli*. *Nanomedicine: Nanotechnology, Biology and Medicine*, 2007, **3** (2), P. 168–171.
- [10] Kravets V., et al. Imaging of biological cells using luminescent silver nanoparticles. *Nanoscale research letters*, 2016, **11** (1), P. 30.
- [11] Tran Q.H., Le A.-T. Silver nanoparticles: synthesis, properties, toxicology, applications and perspectives. *Advances in Natural Sciences: Nanoscience and Nanotechnology*, 2013, **4** (3), 033001.
- [12] Jyoti K., Baunthiyal M., Singh A. Characterization of silver nanoparticles synthesized using *Urtica dioica* Linn. leaves and their synergistic effects with antibiotics. *Journal of Radiation Research and Applied Sciences*, 2016, **9** (3), P. 217–227.
- [13] Gangwar R.K., et al. Conjugation of curcumin with PVP capped gold nanoparticles for improving bioavailability. *Materials Science and Engineering C*, 2012, **32** (8), P. 2659–2663.
- [14] Patra D., Barakat C. Synchronous fluorescence spectroscopic study of solvatochromic curcumin dye. *Spectrochimica Acta Part A: Molecular and Biomolecular Spectroscopy*, 2011, **79** (5), P. 1034–1041.
- [15] Masek A., Chrzescijanska E., Zaborski M. Characteristics of curcumin using cyclic voltammetry, UV-vis, fluorescence and thermogravimetric analysis. *Electrochimica Acta*, 2013, **107**, P. 441–447.
- [16] Masuda T., et al. Chemical studies on antioxidant mechanism of curcuminoid: analysis of radical reaction products from curcumin. *Journal of agricultural and food chemistry*, 1999, **47** (1), P. 71–77.
- [17] Hatamie S., et al. Complexes of cobalt nanoparticles and polyfunctional curcumin as antimicrobial agents. *Materials Science and Engineering C*, 2012, **32** (2), P. 92–97.
- [18] Ajitha B., et al. Role of capping agents in controlling silver nanoparticles size, antibacterial activity and potential application as optical hydrogen peroxide sensor. *RSC Advances*, 2016, **6** (42), P. 36171–36179.
- [19] Zhang Z., Zhao B., Hu L. PVP protective mechanism of ultrafine silver powder synthesized by chemical reduction processes. *Journal of Solid State Chemistry*, 1996, **121** (1), P. 105–110.
- [20] Machmudah S., et al. Formation of Fine Particles from Curcumin/PVP by the Supercritical Antisolvent Process with a Coaxial Nozzle. *ACS omega*, 2020, **5** (12), P. 6705–6714.
- [21] Sindhu K., et al. Curcumin conjugated gold nanoparticle synthesis and its biocompatibility. *RSC Advances*, 2014, **4** (4), P. 1808–1818.
- [22] Priyadarsini K. The Chemistry of Curcumin: From Extraction to Therapeutic Agent. *Molecules*, 2014, **19** (12), P. 20091.
- [23] Sarma R., Mohanta D. Luminescence and bio-imaging response of thio-glycolic acid (TGA) and sodium dodecyl sulfate (SDS)-coated fluorescent cadmium selenide quantum dots. *Journal of Luminescence*, 2015, **161**, P. 395–402.
- [24] Burgess A., et al. Loss of human Greatwall results in G2 arrest and multiple mitotic defects due to deregulation of the cyclin B-Cdc2/PP2A balance. *Proceedings of the National Academy of Sciences*, 2010, **107** (28), P. 12564–12569.

- [25] Nguyen H.N., et al. Curcumin as fluorescent probe for directly monitoring in vitro uptake of curcumin combined paclitaxel loaded PLA-TPGS nanoparticles. *Advances in Natural Sciences: Nanoscience and Nanotechnology*, 2016, **7** (2), P. 025001.
- [26] Patil S., et al. Protein adsorption and cellular uptake of cerium oxide nanoparticles as a function of zeta potential. *Biomaterials*, 2007, **28** (31), P. 4600–4607.
- [27] Zhao M.-X., Zeng E.-Z. Application of functional quantum dot nanoparticles as fluorescence probes in cell labeling and tumor diagnostic imaging. *Nanoscale research letters*, 2015, **10** (1), P. 171.
- [28] Foroozandeh P., Aziz A.A. Insight into Cellular Uptake and Intracellular Trafficking of Nanoparticles. *Nanoscale research letters*, 2018, **13** (1), P. 339.
- [29] Fröhlich E. The role of surface charge in cellular uptake and cytotoxicity of medical nanoparticles. *International journal of nanomedicine*, 2012, **7**, P. 5577–5591.
- [30] Jeon S., et al. Surface Charge-Dependent Cellular Uptake of Polystyrene Nanoparticles. *Nanomaterials (Basel, Switzerland)*, 2018, **8** (12), P. 1028.
- [31] Nakamura H., Watano S. Direct Permeation of Nanoparticles Across Cell Membrane: A Review. *Powder and Particle*, 2018, **35**.
- [32] Ivers L.P., et al. Dynamic and influential interaction of cancer cells with normal epithelial cells in 3D culture. *Cancer Cell International*, 2014, **14** (1), P. 108.
- [33] Monks J., et al. Epithelial cells as phagocytes: apoptotic epithelial cells are engulfed by mammary alveolar epithelial cells and repress inflammatory mediator release. *Cell Death & Differentiation*, 2005, **12** (2), P. 107–114.
- [34] Swanner J., et al. Silver nanoparticles selectively treat triple-negative breast cancer cells without affecting non-malignant breast epithelial cells in vitro and in vivo. *FASEB BioAdvances*, 2019, **1** (10), P. 639–660.
- [35] Abdellah A.M., et al. Green synthesis and biological activity of silver-curcumin nanoconjugates. *Future medicinal chemistry*, 2018, **10** (22), P. 2577–2588.
- [36] Mendoza M., et al. Nanoparticles and organized lipid assemblies: from interaction to design of hybrid soft devices. *Soft Matter*, 2019, **15** (44).
- [37] Doherty G.J., McMahon H.T. Mechanisms of Endocytosis. *Annual Review of Biochemistry*, 2009, **78** (1), P. 857–902.
- [38] Zhang X., et al. Effects of surface charges of gold nanoclusters on long-term in vivo biodistribution, toxicity, and cancer radiation therapy. *International journal of nanomedicine*, 2016, **11**, P. 3475–3485.
- [39] Alexis F., et al. Factors Affecting the Clearance and Biodistribution of Polymeric Nanoparticles. *Molecular Pharmaceutics*, 2008, **5** (4), P. 505–515.
- [40] Bodewein L., et al. Differences in toxicity of anionic and cationic PAMAM and PPI dendrimers in zebrafish embryos and cancer cell lines. *Toxicology and Applied Pharmacology*, 2016, **305**, P. 83–92.



NANOSYSTEMS:

PHYSICS, CHEMISTRY, MATHEMATICS

INFORMATION FOR AUTHORS

The journal publishes research articles and reviews, and also short scientific papers (letters) which are unpublished and have not been accepted for publication in other magazines. Articles should be submitted in English. All articles are reviewed, then if necessary come back to the author to completion.

The journal is indexed in Web of Science Core Collection (Emerging Sources Citation Index), Chemical Abstract Service of the American Chemical Society, Zentralblatt MATH and in Russian Scientific Citation Index.

Author should submit the following materials:

1. Article file in English, containing article title, the initials and the surname of the authors, Institute (University), postal address, the electronic address, the summary, keywords, MSC or PACS index, article text, the list of references.
2. Files with illustrations, files with tables.
3. The covering letter in English containing the article information (article name, MSC or PACS index, keywords, the summary, the literature) and about all authors (the surname, names, the full name of places of work, the mailing address with the postal code, contact phone number with a city code, the electronic address).
4. The expert judgement on possibility of publication of the article in open press (for authors from Russia).

Authors can submit a paper and the corresponding files to the following addresses: nanojournal.ifmo@gmail.com, popov1955@gmail.com.

Text requirements

Articles should be prepared with using of text editors MS Word or LaTeX (preferable). It is necessary to submit source file (LaTeX) and a pdf copy. In the name of files the English alphabet is used. The recommended size of short communications (letters) is 4-6 pages, research articles– 6-15 pages, reviews – 30 pages.

Recommendations for text in MS Word:

Formulas should be written using Math Type. Figures and tables with captions should be inserted in the text. Additionally, authors present separate files for all figures and Word files of tables.

Recommendations for text in LaTeX:

Please, use standard LaTeX without macros and additional style files. The list of references should be included in the main LaTeX file. Source LaTeX file of the paper with the corresponding pdf file and files of figures should be submitted.

References in the article text are given in square brackets. The list of references should be prepared in accordance with the following samples:

- [1] Surname N. *Book Title*. Nauka Publishing House, Saint Petersburg, 2000, 281 pp.
- [2] Surname N., Surname N. Paper title. *Journal Name*, 2010, **1** (5), P. 17-23.
- [3] Surname N., Surname N. Lecture title. In: Abstracts/Proceedings of the Conference, Place and Date, 2000, P. 17-23.
- [4] Surname N., Surname N. Paper title, 2000, URL: <http://books.ifmo.ru/ntv>.
- [5] Surname N., Surname N. Patent Name. Patent No. 11111, 2010, Bul. No. 33, 5 pp.
- [6] Surname N., Surname N. Thesis Title. Thesis for full doctor degree in math. and physics, Saint Petersburg, 2000, 105 pp.

Requirements to illustrations

Illustrations should be submitted as separate black-and-white files. Formats of files – jpeg, eps, tiff.



NANOSYSTEMS:

PHYSICS, CHEMISTRY, MATHEMATICS

Журнал зарегистрирован

Федеральной службой по надзору в сфере связи, информационных технологий и массовых коммуникаций
(свидетельство ПИ № ФС 77 - 49048 от 22.03.2012 г.)
ISSN 2220-8054

Учредитель: федеральное государственное автономное образовательное учреждение высшего образования

«Санкт-Петербургский национальный исследовательский университет информационных технологий, механики и оптики»

Издатель: федеральное государственное автономное образовательное учреждение высшего образования

«Санкт-Петербургский национальный исследовательский университет информационных технологий, механики и оптики»

Отпечатано в Учреждении «Университетские телекоммуникации»

Адрес: 197101, Санкт-Петербург, Кронверкский пр., 49

Подписка на журнал НФХМ

На первое полугодие 2022 года подписка осуществляется через
ОАО «АРЗИ», подписной индекс Э57385